
Emergent Gauge Fields in Systems with Competing Interactions

DISSERTATION
ZUR ERLANGUNG DES WISSENSCHAFTLICHEN GRADES
DOCTOR RERUM NATURALIUM
(DR. RER. NAT.)

vorgelegt
dem Bereich Mathematik und Naturwissenschaften
der Technischen Universität Dresden
von
Dipl. Phys. Matthias GOHLKE
geboren am 18.11.1987 in Frankfurt (Oder)

Eingereicht am: 20. Juli 2018

Angefertigt am
Max Planck Institut für die Physik komplexer System



Gutachter:

1. Prof. Dr. Roderich Moessner
2. Prof. Dr. Frank Pollmann
3. Prof. Dr. Matthias Vojta

Contents

1	Introduction	1
2	Emergent Gauge Fields	5
2.1	Introduction	5
2.2	Emergent Maxwell's Equation in (Spin-)Ice	5
2.2.1	Ice-Rules	6
2.2.2	Pauling's residual entropy of Ice	8
2.2.3	Emergent Maxwell's Electrostatics	9
2.2.4	Fractionalization and Magnetic Monopoles	12
2.2.5	Magnetization Plateaus	14
2.2.6	Kasteleyn Transition of Dimers	15
2.3	Emergent \mathbb{Z}_2 -Gauge Theory in the Kitaev Model	19
2.3.1	Kitaev model	19
2.3.2	Static \mathbb{Z}_2 Fluxes	20
2.3.3	Exact solution via Majorana operators	21
2.3.4	The Spectrum of the Fermion Problem	23
2.3.5	The Kitaev Model in a Magnetic Field: Perturbation Theory	25
2.3.6	Topological Order and Anyonic Excitations	27
2.3.7	Dynamical Spin-Structure Factor	28
2.3.8	Kitaev Materials	30
3	Methods	33
3.1	Matrix Product States	34
3.1.1	Schmidt Decomposition	35
3.1.2	Infinite Matrix Product States	37
3.1.3	Entanglement	38
3.1.4	Matrix Product Operators	40
3.1.5	Density Matrix Renormalisation Group	41
3.1.6	Extension to Two-Dimensional Lattices	43
3.2	Transfer Matrix Spectrum	43

3.2.1	Implementation	44
3.2.2	Example: Anisotropic XY-Heisenberg Chain	45
3.3	Matrix Product Operator Based Time-Evolution	46
3.3.1	Protocol for Time-Evolution	46
3.3.2	Represent the Time-Evolution Operator as MPO	47
3.3.3	Example: Anisotropic XY-Heisenberg Chain	50
4	Kitaev-Heisenberg Model	51
4.1	Introduction	51
4.2	Ground State Phase Diagram	52
4.3	Dynamical Spin Structure Factor	57
4.4	Conclusion	61
5	Kitaev-Gamma Model	63
5.1	Introduction	63
5.2	Ground State Phase Diagram	64
5.3	Transfer Matrix Spectrum	67
5.3.1	Kitaev Limit	69
5.3.2	K - Γ Model	69
5.4	Majorana Mean Field Theory	73
5.5	Two-Majorana Spectrum, iDMRG vs. MFT	76
5.5.1	Anisotropic Coupling	78
5.6	Conclusion	79
6	Kitaev-Model in [111] Magnetic Field	81
6.1	Introduction	81
6.2	Model	83
6.3	Ground State Phases	84
6.3.1	Topological Phase	85
6.3.2	Intermediate Regime	91
6.3.3	Polarized Phase	94
6.4	Dynamical Spin-Structure Factor	94
6.4.1	Topological Phase	97
6.4.2	Polarized Phase	98
6.5	Conclusion	100
7	Topological Magnons in Kitaev Magnets at High Fields	103
7.1	Introduction	103
7.2	Linear Spin Wave Theory and the Non-Trivial Chern Number	104
7.3	Include Magnon-Magnon Interactions: Comparison with DMRG	108

7.4	Chirality on a Slab Geometry	111
7.5	Extension to the JKTT'-Model	113
7.6	Conclusion	113
8	Polarization Plateaus in Hexagonal Water Ice	115
8.1	Introduction	115
8.2	Hexagonal Ice I_h Structure and Model	117
8.3	Directed Loop Monte Carlo Sampling	118
8.4	Polarization Plateaus	120
8.5	Kasteleyn Transition for Dimers on a Square Lattice	126
8.6	Correlations and Static Structure Factor	128
8.7	Conclusion	134
9	Conclusion and Outlook	137
	Acknowledgments	157

Chapter 1

Introduction

Interactions between the microscopic constituents of a solid—a many-body system—can lead to novel phases and exotic physical phenomena. In this context, the fractional quantum hall effect [1] is a paradigmatic example, in which strong electron-electron interactions lead to a new collective state of the electrons. This collective state exhibits a topological degeneracy and provides a *vacuum* for unusual excitations carrying fractions of the elemental charge of an electron [2]. The collective ground state of a many-body system may also be described by emergent gauge fields such as the Chern-Simons theory for the fraction quantum hall effect [3, 4]. In the context of this thesis, a prominent example for an emergent gauge field is water ice or spin ice, a magnetic variant of the former, where local constraints result in emergent Maxwell’s equations [5].

The concept of frustration provides the ground for such exotic phenomena. It can prevent a many-body system from establishing long-range order down to the lowest temperatures due to competing interactions. In particular, the contributions to the energy of the interactions cannot all be minimised simultaneously. If the lattice structure alone precludes Néel order expected for a primarily antiferromagnetic coupling, the frustration is said to be *geometrical*. Considering antiferromagnetically coupled spins with interactions along links of a lattice with odd-length loops, e.g. triangles, such interactions can never all be satisfied simultaneously. A second source of frustration arises from competing exchange interactions, hence the name *exchange* frustration. It is caused by strongly anisotropic exchange or if the exchange competes between nearest and next-nearest neighbors. In any case, strong frustration can give rise either to unconventional order or even to disordered and liquid-like phases of matter. In the latter case, any spontaneous symmetry breaking is suppressed such that the system remains paramagnetic, yet highly correlated. Thence, such a state was coined a *collective paramagnet* by Villain in 1979 [6] or a *spin liquid*.

Historically, common hexagonal water ice is the paragon of geometric frustration. In the 1930s experiments by Giauque et al. [7] revealed a discrepancy in the entropy

between spectroscopic measurements and when integrating over the specific heat. This discrepancy stems from an extensive residual entropy as has been explained by Pauling [8]. His explanation is based on the *ice-rules* that were proposed by Bernal and Fowler [9]: the proton configuration is disordered, but subject to local constraints leaving a set of ground states whose size grows exponentially with system volume. This implies the extensive residual entropy. Two decades later, it was noted by Anderson [10] that the ice-rules are applicable to certain magnetic systems, providing a first glimpse on materials named spin ice more recently [11–13].

Besides the extensive ground state degeneracy exhibited by classical models, it is their excitations that possess exotic features. The excitations in spin ice—by breaking the ice-rule constraint locally—may be considered as monopoles, which can only be created pairwise out of a single spin flip. By flipping consecutive spins, the monopoles get separated without further breaking any constraints. Thence, the cost of energy for separating the two monopoles is purely determined by their interaction and turns out to be bounded: the spin flip *fractionalizes* into two *deconfined* magnetic monopoles. The monopoles interact with each other following an *emergent* Coulomb law, that *emerges* from the interplay of the constituents forming the many-body ground state. Such a Coulomb law is a priori of purely entropic origin, but it is enhanced energetically by a dipolar exchange of the spins as occurs in spin ice compounds. As a consequence, the monopoles can be described as quasiparticles with an entropic or magnetic charge [14] instead of an electric one. Once again, the many-body ground state provides the vacuum for exotic quasiparticles—magnetic monopoles—not found elsewhere.

A second origin of frustration appears due to strong coupling between spin and orbital degrees of freedom. The particular hybridization of orbitals of neighboring atoms allows for spatially anisotropic spin exchange between magnetic ions and results in effective so-called compass models [15]. One example that has attracted a lot of interest in the last decade is the two-dimensional Kitaev model [16]. It exhibits strongly anisotropic Ising exchange between spin- $\frac{1}{2}$ degrees of freedom. As such, the interactions are subject to frustration and their constituents enter a quantum spin liquid ground state. A quantum spin liquid, first introduced by Anderson in 1973 [17] in the context of *resonating valence bonds*, describes a novel zero-temperature phase of matter without any spontaneous symmetry breaking, but distinct from a simple paramagnet with long-ranged entangled constituents.

As with (spin-)ice, it is the excitations that harbor many interesting properties: a local spin excitation fractionalizes into free gapless Majorana fermions and static fluxes, the vison excitations of a \mathbb{Z}_2 -gauge field. Generally, fractional quasi-particles confined to two dimension have the remarkable feature that they do not need to exhibit boson or fermion exchange statistics [18]. Upon exchange of quasi-particles, the many-body wave function describing the ground state can either acquire a general $e^{i\phi}$ phase,

or exchanges may even be non-commuting. Such fractional quasi-particles are called *anyons* [19], *abelian* in the former and *non-abelian* in the latter case. The existence of anyons in two or higher dimension is generally associated with topological order [20]. A system is in a topologically ordered phase, if its ground state degeneracy depends only on the genus of the manifold it is placed on. The topological sector—one of the degenerate ground states—can only be changed upon a global action on the system. Any local perturbation would not change the topological sector, which motivates the idea of topologically protected qubits and topological quantum computation [21].

The absence of any order parameter in strongly frustrated systems—due to not breaking any symmetry spontaneously—immediately raises the question about possible experimental probes of spin-liquids and their fractional excitations. Dynamic probes, like inelastic neutron scattering or Raman scattering, provide an experimental method to detect signatures of fractionalised quasiparticles. The energy and momentum transferred in a scattering event is split between the fractional quasiparticles, generically resulting in a broad continuum in the spectra.

On the theory side, computing such dynamical signatures beyond one spatial dimension is generally a difficult task. Only in rare instances—as for the Kitaev model [22]—is it possible to derive an exact solution for the spectrum. However, once a more general model is studied, advanced numerical methods are needed. In this thesis, numerical methods like density matrix renormalisation group [23] and matrix product states [24–26] are used extensively to study strongly frustrated magnets and their dynamics in a non-perturbative way. As some of the techniques used have been developed very recently, an introduction of the methods is presented in chapter 3.

A major part of the thesis covers the Kitaev model and the effect of additional spin-exchanges relevant in Kitaev-like frustrated magnets or how a magnetic field acts on the spin liquid. The interplay of the Kitaev exchange with these additional spin-exchanges gives rise to many different phases, among them spin liquids, but also long range ordered phases. The main questions addressed here concern the stability of the quantum spin liquid phase, its excitations and dynamical signatures within the spin liquid, but also in adjacent phases.

A high-energy continuum has been observed in inelastic neutron measurements of α - RuCl_3 [27, 28], a magnetic material which is believed to exhibit Kitaev exchange. In this context, it has been suggested that α - RuCl_3 may be considered to be a proximate spin-liquid compound. In a first attempt to address the high-energy continuum, the dynamics of the Kitaev-Heisenberg model are investigated in chapter 4. For small Heisenberg exchange, but sufficiently strong to enter an ordered phase adjacent to the Kitaev spin liquid, significant weight of dynamical spectra is shifting to a high-energy continuum not easily explainable utilizing conventional methods. In this view, the Kitaev-Heisenberg model may resemble similar high-energy features as found experi-

mentally, however, the nature of the high-energy continuum is still debated.

Likewise, the precise couplings of α - RuCl_3 are still subject of ongoing discussion. The symmetric off-diagonal Γ -exchange has been suggested also to be of relevant magnitude and it is studied in chapter 5. A large part of the Kitaev- Γ phase diagram contains a quantum paramagnetic phase. A recently established mapping between the complex eigenvalues of the transfer matrix and the excitation spectrum is utilized and reveals coherent excitations of the quantum paramagnetic phase. The lower edge of the excitation spectrum moves coherently in momentum space in a well-defined fashion as a function of Γ/K , implying a non-trivial nature of these excitations.

Even more recently, many experiments have been carried out on α - RuCl_3 in a magnetic field. Thence, it is of general interest to study the effect of a magnetic field on the Kitaev spin liquid beyond perturbation theory. As discussed in chapter 6, an enigmatic, possibly gapless, phase at intermediate fields exists that is only present for antiferro-type Kitaev exchange. The critical field, when transitioning into the high-field polarized phase, differs by an order in magnitude depending on the sign of the Kitaev exchange. Furthermore, dynamical signatures of the topological and the field-polarized phases close to the transition are studied. In the former, the magnetic field allows the fluxes to hop and to acquire dispersion. Consequently, the dynamical spin-structure factor attains mores structure. The gap to the lower edge of the spectrum reduces towards the transition into the intermediate phase. In the latter, the magnon modes of the polarized phase flatten and reduce in energy towards the transition until they get obscured by interactions with the multi-magnon continuum. Remarkably, the gap between the ground state and the continuum appears to close across the entire reciprocal space.

Chapter 7 addresses the magnon modes in the high-field polarized phase separately. They are found to be topologically non-trivial. The non-zero Chern numbers of the magnon bands are extracted using linear spin wave theory and magnonic edge states are observed numerically to underline the topological nature of the magnons.

In the second part, a classical minimal model of water ice is studied, in particular the effect of how its extensive ground state degeneracy is lifted by an external field (cf. Ch. 8). Field directions exist for which the remaining degrees of freedom map to an effective dimer model. Dimers are objects that occupy two neighboring sites of a lattice. None of the lattice sites shall be un- or doubly occupied. Such a model does not exhibit long-range order if the dimers have a similar probability to occupy different bonds. A transition of Kasteleyn-type into an ordered state occurs when a bond or orientation is preferred sufficiently strongly.

Chapter 2

Emergent Gauge Fields

2.1 Introduction

This chapter introduces two physical models that exhibit frustration and whose constituent form a collective many-body ground state with an emergent gauge theory. Historically, the first gauge theory occurs in Maxwell equations describing electromagnetism. One refers to a gauge theory, if a model or physical description contains a certain redundancy in its degrees of freedom. Take Maxwell's equations as an example, they remain invariant under a transformation of the vector field by the gradient of a scalar field, $\mathbf{A} \rightarrow \mathbf{A}' + \partial a$. In fact, Maxwell's equations describe an $U(1)$ gauge theory. We will encounter a lattice version of Gauss law, one of Maxwell's equation, in the first model presented in section 2.2. There, Gauss law emerges from the interplay of the constituents subject to the *ice rules*, a local constraint on the allowed configurations, cf. Sec. 2.2.1. As the name suggests, such ice rules are essential in explaining the proton configuration in common hexagonal ice, but also in a particular set of magnetic compounds named spin ice.

The second part, Sec. 2.3, reviews the Kitaev model, which incorporates strongly anisotropic Ising exchanges between spin- $\frac{1}{2}$ degrees of freedom. An extensive set of commuting plaquette operators defines a static \mathbb{Z}_2 -gauge field. A free Majorana fermion hopping problem remains to be solved. In this view, the spin degrees of freedom fractionalize into static \mathbb{Z}_2 fluxes—or equivalently visons of the \mathbb{Z}_2 -gauge field—and free Majorana fermions. Returning to the original spin language, the ground state of the Kitaev model is a quantum spin liquid.

2.2 Emergent Maxwell's Equation in (Spin-)Ice

In this section, frustration in ice-like systems will be studied, such as common hexagonal water ice I_h , but also the cubic water ice I_c and its magnetic variant, spin ice on

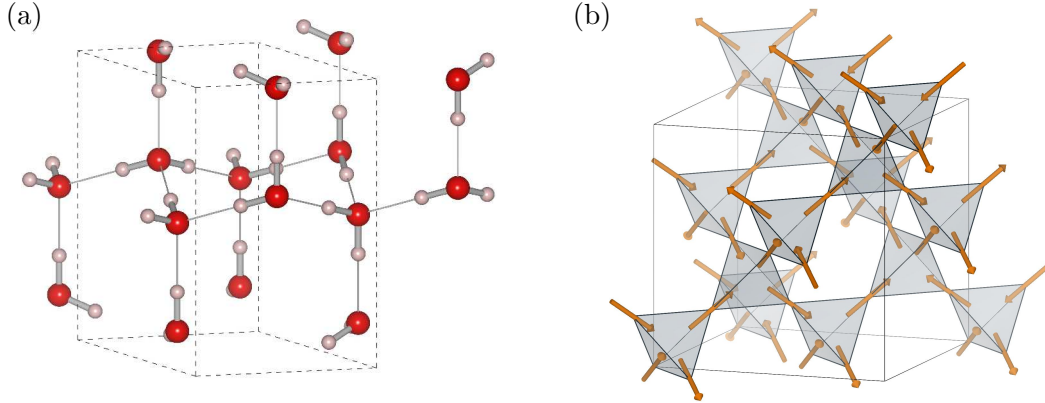


Figure 2.1: Structure of hexagonal ice I_h with one arbitrary proton configuration satisfying the ice rules.

the pyrochlore lattice. The first subsection 2.2.1 states the *ice rules*, both for water ice as well as spin ice. A consequence of these ice rules is an extensive ground state degeneracy, i.e. with an extensive residual entropy. A remarkably accurate yet simple estimate of this entropy has been given by Pauling [8] and is presented in Sec. 2.2.2. Fluctuations between different ground states of the extensively degenerate set form a classical spin-liquid ground state with the spins satisfying emergent Maxwell's equation, see 2.2.3. The lowest energy excitations will break the ice-rules locally, revealing rich microscopic structure including fractionalization and emergent magnetic monopoles, cf. 2.2.4. Applying an external field, either magnetic in the case of spin ice or electric for water ice, generically lifts the ground state degeneracy. As we will see in 2.2.5, magnetization plateaus occur and depending on the particular field direction, the transition into an ordered, fully polarized phase may be of Kasteleyn-type. The Kasteleyn transition is a finite temperature transition between an ordered phase at low temperature without any fluctuations into a high-temperature phase exhibiting fluctuations due to excitations that span the whole system.

2.2.1 Ice-Rules

Let us first describe the structure of the common water ice I_h [29]. Ice I_h has a bipartite lattice with a hexagonal primitive cell containing four oxygen atoms and eight protons, cf. Fig. 2.1.¹ The oxygen atoms form a tetrahedral structure of $P6_3/mmc$ symmetry with four nearest neighbor oxygen atoms. The following symmetries exist: a sixfold rotation axis, a twofold rotation axis perpendicular to the z-axis, and a horizontal reflection plane. Within the unit cell, eight distinct oxygen-oxygen links exist having one proton each. Each proton has two valid positions arranged symmetrically around

¹Structure illustrations are done using VESTA. [30]

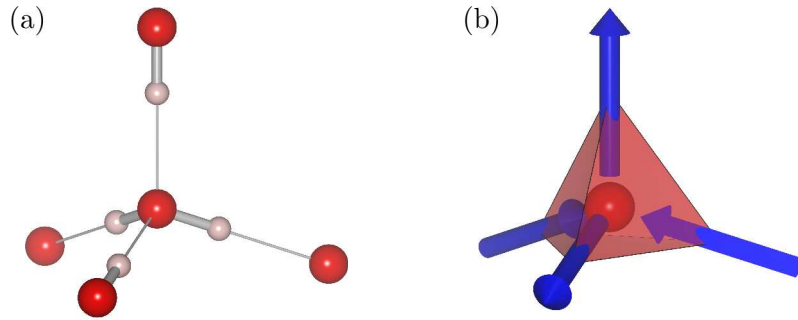


Figure 2.2: A single tetrahedron of (a) water ice with an arbitrary configuration respecting the ice rules, and (b) corresponding spin configuration as would appear in spin ice.

the midpoint of a link. The low energy state of the proton is described by the *ice rules* [9]:

- (I1) On each link between two neighboring oxygen atoms resides one proton. It can either be covalently bonded with the left oxygen having a hydrogen atom with the right oxygen ($\text{O-H}\cdots\text{O}$) or vice versa ($\text{O}\cdots\text{H-O}$).
- (I2) Two protons are covalently bonded to each oxygen forming H_2O molecules at each vertex in a natural way.

These rules give rise to an exponentially growing number of possible configurations implying an extensive degeneracy and finite entropy [8] as will be shown below. Furthermore, the ice rules prevent the protons from ordering. Water ice is therefore considered to be a paragon of geometrical frustration.

Remarkably, a magnetic equivalent of these ice rules exist in magnets with a pyrochlore structure. Already in 1956 Anderson noted a connection between certain magnetic compounds and the proton ordering problem of water ice in the context of spinels and ferrites [10]. More than three decades later, $\text{Ho}_2\text{Ti}_2\text{O}_7$ [11] and $\text{Dy}_2\text{Ti}_2\text{O}_7$ [12] are the first pyrochlore spin ice compounds investigated experimentally. The pyrochlore structure is composed of corner-sharing tetrahedra formed by the magnetic ions, e.g., Dy^{3+} or Ho^{3+} , with a large magnetic moment. Due to the crystal field, the magnetic dipoles are aligned parallel (or antiparallel) to the links between the center of two neighboring tetrahedra. The low-energy subspace of the dipoles is given by the famous *two-in-two-out* rule of spin ice:

- (M) Of the four magnetic moments, or classical spins, of a tetrahedron, two point in and two out.

Both sets of ice rules are equivalent in the low-energy sector. Let's assume the ice rule (I1) is already satisfied. Then (I2) and (M) are essentially equivalent. The

relative positions of the protons with respect to the center of the Oxygen–Oxygen link correspond to the magnetic moments stemming from magnetic ions placed at the center of such a link.

If we are considering perfect lattices, defects are introduced by breaking the corresponding ice rule. By flipping a single spin, the two-in-two-out rule is violated at two neighboring tetrahedra, one of which has one spin pointing inwards and three out, whereas at the other tetrahedron the spins point three-in-one-out. These defects turn out to be magnetic monopoles for reasons that become clear in section 2.2.4. Here we can already observe that flipping subsequent spins along a string does violate the two-in-two-out rule only at the ends of the string. Thus, moving the defects does not cost any additional energy due to the ice rules.

For the sake of completeness, a second kind of defect is possible in water ice only by violating (I1). A single Oxygen–Oxygen link could either be doubly occupied or not occupied at all. These defects are called Bjerrum-defects [31] and will not be discussed further.

As we have seen that the low-energy description of water ice and spin ice is equivalent, we will only use the language in terms of spin ice below with its magnetic moments or classical Ising spins. At any time, the spin can simply be replaced by the corresponding proton in one of the two possible sites and the water ice picture is restored.

2.2.2 Pauling’s residual entropy of Ice

The ice-rules leave an extensive degeneracy of the ground states leading to a residual finite entropy. When considering a single tetrahedron with four Ising spins, out of the 16 different configurations six remain respecting the ice rules. However, fixing the configuration at one tetrahedron, diminishes the number of possible configurations at neighboring tetrahedra. Hence, Pauling uses the following counting argument [8]. The lattice of tetrahedra is bipartite with a sublattice A and B. Considering first sublattice A, six configurations per tetrahedron are valid. Next considering a tetrahedron on sublattice B, all 16 configurations would appear if we were only fixing the configurations on A. Thus, an additional factor 6/16 enters and we arrive at the following number W_N of configurations

$$W_N = 6^{\frac{N}{2}} \left(\frac{6}{16} \right)^{\frac{N}{2}} = \left(\frac{3}{2} \right)^N, \quad (2.1)$$

where N is the number of tetrahedra. The number of degenerate states is growing exponentially leaving an extensive entropy of

$$S_N = k_B \log W_N = N k_B \log \frac{3}{2}, \quad (2.2)$$

which is the famous Pauling residual entropy of ice.

Corrections to this estimate occur due to loops [32], but turn out to be small. In particular, an exact solution for the two-dimensional ice on the square lattice exists [33]. Pauling's line of arguing carries over to the square ice enabling a direct comparison to the exact value

$$W_{\text{Pauling}} = \frac{3}{2} \quad \text{vs.} \quad W_{\text{sq. ice}} = \left(\frac{4}{3}\right)^{\frac{3}{2}} = 1.5396007\dots, \quad (2.3)$$

where $W = \lim_{N \rightarrow \infty} W_N^{(1/N)}$ is the number of configurations per vertex or per two spins, respectively.

An exact solution does not exist in three dimension. However, estimates suggest that corrections due to loops are even smaller for ice and pyrochlore spin than for square ice. Using a series expansion, Nagle obtains an estimate of $W = 1.50685 \pm 0.00015$ [32], Extracted via numerical integration, Isakov et al. obtain $W = 1.5071 \pm 0.0003$ [34], and very recently, Vanderstraeten et al. [35] employed *Projected Entangled Pair States* getting $W = 1.5074562$.

2.2.3 Emergent Maxwell's Electrostatics

We may consider the Heisenberg model with classical spins placed on the links of a pyrochlore (or ice I_h) lattice²

$$H_{\text{Heis.}} = -J \sum_{\langle i,j \rangle} \mathbf{S}_i \cdot \mathbf{S}_j, \quad (2.4)$$

which exhibits a disordered ground state with correlations decaying algebraically as $\mathcal{O}(\frac{1}{r^3})$ [37, 38]. The degrees of freedom of the Heisenberg spins can be reduced to Ising spins due to the crystal field providing the same ice-like rules as for water ice.

Let us rewrite the spin configuration of spin ice or the proton configuration of water ice to obtain a simplified model. In spin ice, spins are placed at the corners of corner-sharing tetrahedra or, equivalently, the midpoints of links connecting the midpoint of neighboring tetrahedra. Thus, the spins are placed on the nodes of a pyrochlore lattice (the midpoints of the tetrahedra form a diamond lattice). A spin is oriented (anti-)parallel to such a link and is described by

$$\mathbf{S}_i = s_i \hat{\mathbf{e}}_i, \quad (2.5)$$

where $s_i = \pm 1$ is an Ising variable and the direction of the link i itself is given by the unit vector $\hat{\mathbf{e}}_i$ with the convention to point from sublattice A to B,

²Spin ice compounds have a dipolar coupling, which is suppressed in this discussion. Isakov et al. [36] showed that the dipolar term leads to the same ice-rule ground-state manifold in the $T \rightarrow 0$ limit.

For water ice, a proton is placed at $\mathbf{r}_i = \mathbf{R}_i + \delta s_i \hat{\mathbf{e}}_i$, where \mathbf{R}_i denotes its midpoint and δ is the displacement from the midpoint along a link. The only variable remaining is the Ising-like variable $s_i = \pm 1$. By construction ice rule (I1)—only one proton per link—is satisfied. Using the notation of an electric dipole, we arrive at $\mathbf{d}_i = s_i \delta \hat{\mathbf{e}}_i$. This description provides a one-to-one mapping of the corresponding low-energy degrees of freedom of water ice or of spin ice to Ising variables s .

Using (2.5), the Hamiltonian H_{Heis} in Eq. 2.4 simplifies to a minimal model of Ising spins s_i first discussed by Anderson [10]

$$H = \frac{J}{6} \sum_{\langle i,j \rangle} s_i s_j + c = \frac{J}{6} \sum_{\alpha} L_{\alpha}^2 + c. \quad (2.6)$$

where c is a constant and $L_{\alpha} = \sum_{i \in \boxtimes_{\alpha}} s_i$ represent a sum of Ising spins on a single tetrahedron \boxtimes_{α} .

In the limit of small temperature $J \gg T$ the ice rule (I2)—or (M), respectively—get restored as

$$L_{\alpha} = \eta_{\alpha} \sum_{i \in \boxtimes_{\alpha}} s_i = 0, \quad (2.7)$$

where $\eta_{\alpha} = \pm 1$ is a sign prefactor depending on whether the tetrahedron is an up or down tetrahedron.³ Equation (2.7) represents the lattice version of a divergence-free condition known as Gauss law. Consider a volume \mathcal{V} : the sum of all s_i of links cut by its surface $\partial\mathcal{V}$, $\Phi_{\mathcal{V}} = \sum_{\langle i \rangle \in \partial\mathcal{V}} s_{ij}$, defines a flux through $\partial\mathcal{V}$ and is identical zero.

Let us introduce the spin field (proportional to the magnetization) of a tetrahedron [5, 39]

$$\mathbf{\Omega}_{\alpha} = \sum_{i \in \boxtimes_{\alpha}} \mathbf{S}_i \quad (2.8)$$

in terms of the oriented spins \mathbf{S}_i , cf. Eq. (2.5). A single tetrahedron can have six different configurations resulting in the different local spin fields [39] $\mathbf{\Omega}_{\alpha} = (\pm 1, 0, 0)$, $(0, \pm 1, 0)$, or $(0, 0, \pm 1)$.

The next step is to transfer to a continuum description by coarse-graining over tetrahedra in the neighborhood $\mathbf{\Omega}_{\alpha} \mapsto \mathbf{\Omega}(\mathbf{r})$, such that $\mathbf{\Omega}(\mathbf{r})$ varies continuously. Upon such a coarse-graining, equation (2.7) turns into the continuum variant of Gauss law

$$\nabla \cdot \mathbf{\Omega} = 0. \quad (2.9)$$

Thus, $\mathbf{\Omega}$ can be described by introducing a gauge field \mathbf{A} with $\mathbf{\Omega} = \nabla \times \mathbf{A}$.

We may consider a section of the lattice and fix the flux through its surface. The entropy, which is the number of accessible configurations or microstates subject to

³Or in other words, whether the tetrahedron belongs to sublattice A or B of the diamond lattice, which is dual to the pyrochlore lattice. The atoms of the pyrochlore lattice are situated at the midpoints of the bonds of the diamond lattice.

the flux condition, is expected to maximize for zero flux and, equivalently, vanishing total magnetization. If instead a non-zero flux is chosen, the number of accessible configurations decreases. Following renormalisation group ideas, one may consider a general action with operators $\mathbf{\Omega}^2$, $\mathbf{\Omega}^4$, $(\nabla \cdot \mathbf{\Omega})^2$, etc. respecting the symmetries (here isotropy). After a renormalisation procedure, $\mathbf{\Omega}^2$ is the most relevant operator. Thence, the probability for a given field $\mathbf{\Omega}$ is conjectured to be [39–41]

$$P[\mathbf{\Omega}] \propto e^{-\frac{1}{V} \int_V d^3\mathbf{r} \frac{\kappa}{2} |\mathbf{\Omega}|^2}, \quad (2.10)$$

around the zero flux configuration, and given $\nabla \cdot \mathbf{\Omega} = 0$ is satisfied. The constant κ reflects the stiffness of fluctuations, which has to be extracted by other means, e.g., by Monte-Carlo simulations. As a remark, Eq. (2.10) represents Gaussian fluctuations of the field.⁴

From (2.10) follows a free-energy of purely entropic origin

$$\frac{F}{T} = S = \frac{1}{V} \int_V d^3\mathbf{r} \frac{\kappa}{2} |\mathbf{\Omega}|^2. \quad (2.11)$$

Upon Fourier transforming, we arrive at

$$\frac{F}{T} = \sum_{\mathbf{k}} \frac{\kappa}{2} |\mathbf{\Omega}(\mathbf{k})|^2. \quad (2.12)$$

Assuming that the free energy is split evenly across all the components $\Omega_\mu(\mathbf{k})$ of the spin field, one arrives at a correlator $\langle \Omega_\mu(-\mathbf{k}) \Omega_\nu(\mathbf{k}) \rangle = \delta_{\mu\nu} / \kappa$. However, we still have to account for Gauss law, which after a Fourier transform reads $\mathbf{k} \cdot \mathbf{\Omega}(\mathbf{k}) = 0$. Thence, by projecting out the correlations that do not satisfy Gauss law, the correlator is

$$\langle \Omega_\mu(-\mathbf{k}) \Omega_\nu(\mathbf{k}) \rangle = \frac{1}{\kappa} \left(\delta_{\mu\nu} - \frac{k_\mu k_\nu}{|\mathbf{k}|^2} \right). \quad (2.13)$$

Fourier transforming back to direct space yields

$$\langle \Omega_\mu(\mathbf{r}) \Omega_\nu(0) \rangle = \frac{4\pi}{\kappa} \left(\frac{r^2 \delta_{\mu\nu} - 3r_\mu r_\nu}{r^5} \right) \quad (2.14)$$

for large r . Equation 2.14 reveals the structure of dipole-dipole correlations [42, 43]. The correlations decay algebraically with a power law $\propto \frac{1}{r^3}$. Such systems are said to be in a *Coulomb phase*.

Furthermore, we note the anisotropy in the correlations, which give rise to so called

⁴A priori, one might also invoke the Central Limit Theorem (CLT) to obtain Eq. (2.10) as argued in [41]. The CLT states that the sum of independent identically distributed random variables approaches a Gaussian distribution. However, $\mathbf{\Omega}(\mathbf{r})$ are not independent, but correlated variables. In fact, as follows below, the correlations $\langle \Omega(\mathbf{r}) \Omega(0) \rangle$ decay even algebraically satisfying a power law.

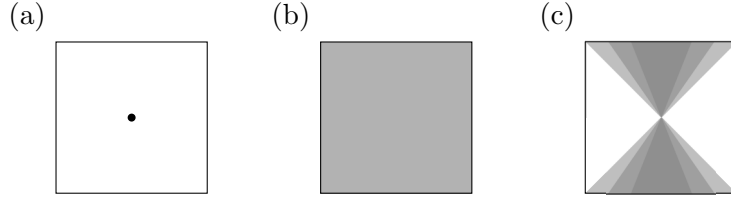


Figure 2.3: Typical scattering features. (a) Bragg peak occurring from a lattice, (b) homogeneous diffuse scattering due to (white) noise, and (c) pinch-point with a bow-tie like intensity. The latter occurs if local constraints like the ice rules lead to an anisotropic scattering profile..

bow tie intensity profiles around pinch points. The second term of Eq. 2.13 has two different limits at $k = 0$. E.g. take the component $\langle \Omega_x(-\mathbf{k})\Omega_x(\mathbf{k}) \rangle = \frac{1}{\kappa} \left(\delta_{xx} - \frac{k_x k_x}{|\mathbf{k}|^2} \right)$, which is zero along k_x , but acquires a finite value for \mathbf{k} perpendicular to k_x . Typical scattering features including bow ties are illustrated in Fig. 2.3. These pinch points are not bound to appear at $\mathbf{k} = 0$. The precise lattice structure and the form factors will shift them to integer multiples of the reciprocal lattice vectors. Such pinch points with a bow tie intensity were first noted by Youngblood et al. [44–46] in the context of ice-rule ferroelectrics. Scattering experiments on spin-ice compounds using polarized neutron provide clearly recognizable pinch points [47].

2.2.4 Fractionalization and Magnetic Monopoles

Given a spin-configuration satisfying the ice rules, the simplest local excitation is a single spin flip. Such a spin flip leads to a violation of the ice rules at two neighboring tetrahedra such that instead of two-in-two-out, there is one tetrahedron with three-in-one-out and one with one-in-three-out. The lattice divergence, cf. Eq. 2.7, acquires a finite values

$$L_\alpha = -L_\beta = \pm 1$$

of opposite sign on the tetrahedron. The defects can now hop to different sites without further violating the ice rules by flipping consecutive spins. It is in that sense, that the initial excitation—the single spin flip—is fractionalized into monopole and anti-monopole [14]. Those monopoles can only be created pairwise upon a local excitation. Creating a single defect would require to flip consecutive spins along a line reaching the boundary. Thence, the monopoles are *topological defects*.

Remarkably, the interaction between monopoles follows a *Coulomb law* of purely entropic origin [41]

$$\frac{F_{\text{int.}}(\mathbf{r}_1, \mathbf{r}_2)}{T} = \frac{\kappa q_1 q_2}{4\pi |\mathbf{r}_2 - \mathbf{r}_1|}, \quad (2.15)$$

where κ is the stiffness first introduced in Eq. (2.10) and $q_{1,2} = \pm q_m$ are the charges of magnetic (anti-)monopoles.

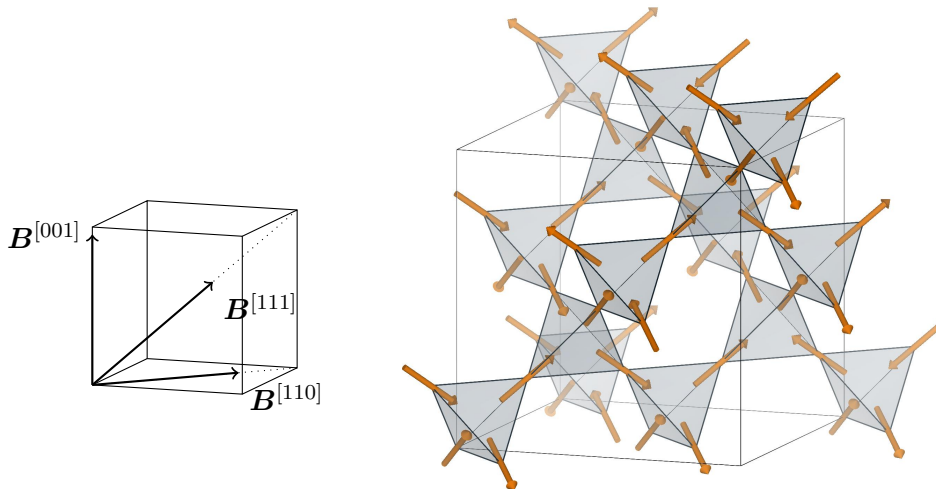


Figure 2.4: Edge-sharing tetrahedra of Pyrochlore spin ice with relevant field directions: $B^{[001]}$, $B^{[110]}$, and $B^{[111]}$.

A model that allows to quantify q_m introduces *dumbbells* of charges for each spin [14] exploiting the basic principle of electrostatics that two opposite charges form a dipole. The *dumbbell model* maps to the dipolar spin-ice model including a (energetic) dipolar interaction, the latter not being discussed here. Nonetheless, the dumbbell model provides a clear picture of fractionalization and magnetic monopoles. Each spin gets replaced by a pair of opposite charges at adjacent tetrahedra. Four charges are placed within each tetrahedron. The energy of the configuration of dipoles is given (up to order $\mathcal{O}(1/r^5)$) by the pairwise Coulomb interaction between the charges [14]

$$V_{\alpha\beta} = \begin{cases} \frac{\mu_0}{4\pi} \frac{Q_\alpha Q_\beta}{|\mathbf{r}_\alpha - \mathbf{r}_\beta|} & (\mathbf{r}_\alpha \neq \mathbf{r}_\beta) \\ \frac{1}{2} v_0 Q_\alpha^2 & (\mathbf{r}_\alpha = \mathbf{r}_\beta) \end{cases}, \quad (2.16)$$

where Q is the total charge on a single tetrahedron, and v_0 a constant on-site repulsion. In the limit of v_0/T large, a charge neutrality $\forall \alpha : Q_\alpha = 0$ is enforced. Then the two-in-two-out rule is satisfied.

Flipping a spin leads to two oppositely charged tetrahedra adjacent to the flipped spin. Additional to the cost of the spin flip, the interaction energy of the two charges is then given by the Coulomb term in (2.16). The energy to separate the two charges is bounded and thence the monopoles are deconfined. This coulombic monopole-monopole interaction is verified to agree with the dipolar spin-ice model by a direct numerical simulation [14].

2.2.5 Magnetization Plateaus

Generally, applying a field will lift the ground state degeneracy caused by the ice rules. However, due to the spatial orientation of the spins, different scenarios depending on the direction of the field exist. The degeneracy may either be lifted fully leading to saturated magnetization, or only partially. A review can be found in Ref. [48, Ch. 12.5.1] and in [49].

Magnetic Field along [110]

A field along [110] pins two of the four spins, one-in-one-out, on a tetrahedron. One-dimensional chains of spins perpendicular to the field remain. Those chains, if the spins satisfy the ice rules, have only two possible orientations irrespective of the number of spins a chain contain. Thence, the remaining entropy is subextensive. For a cubic system with linear dimension L the entropy is $S \propto L^2 \propto N^{\frac{2}{3}}$. Inter-chain exchange is expected for spin-ice compounds due to dipolar couplings and drive the system into an ordered state [50].

Magnetic Field along [001]

In a field along a cubic axis, e.g., [001], each spin has a projection of the same magnitude onto the field direction. In a sufficiently large ratio of magnetic field and temperature, $B_{[001]}/T$, a single, fully polarized state remains that satisfies the ice-rules. Let us consider an excitation out of the fully polarized state. Upon flipping a single spin, the ice rules are violated at the tetrahedra adjacent to the flipped spin. In order to restore the ice rules anywhere in the bulk, the defects have to be transported to the surface⁵ by flipping consecutive spins. Due to the fully polarized state with all spins pointing in field direction, one defect can only transported opposite to the field and the second defect only in field direction. The excitation out of the fully polarized state consists of a string of consecutive spins and spans the entire system. The energy of such a string defect grows with the linear dimension of the system. Consequently, string defects are completely suppressed at sufficiently large $B_{[001]}/T$. On the other side at low $B_{[001]}/T$, if even only one such string defect exists, its precise trajectory through the system can fluctuate freely enabling a gain of entropy.

The critical condition can be obtained following a simple argument involving the free energy. Let us consider the fully polarized configuration and add a string defect. Its internal energy is $U/N = \mu \mathbf{S} \cdot \mathbf{B}_{[100]} = 2\mu B/\sqrt{3}$ per spin flipped. On the other hand, two spins can be flipped at each tetrahedron accumulating an entropy of $S/N = \log 2$.

⁵Or if periodic boundary conditions are considered, one defect can be threaded around the system until it meets and annihilates the second defect. As a result, a loop of spins has been flipped and the ice rules are restored anywhere.

We can now ask, whether creating such a random chain of flipped spins results in an increase or decrease of the free energy, $F = U - ST$. The change of the free energy per spin is

$$\Delta F/N = 2\mu B/\sqrt{3} - T \log 2. \quad (2.17)$$

If the free energy increases, $\Delta F > 0$, spin flips are suppressed and no fluctuation occur. The spins remain in the fully polarized state. But if the free energy decreases, $\Delta F < 0$, spin flips occur and the (local) magnetization fluctuates. The critical ratio $(B_{[001]}/T)_{\text{crit}}$ is obtained from the condition $\Delta F = 0$ and is given as [51]

$$\left(\frac{T}{B}\right)_{\text{crit}} = \frac{2\mu}{\sqrt{3} \log 2}. \quad (2.18)$$

Such an asymmetric transition, fluctuation-free below the critical temperature and exhibiting fluctuations above, is known from hardcore dimer models and is named a Kasteleyn transition, see also next Sec. 2.2.6. More precisely, pyrochlore spin ice in a magnetic field along [001] exhibits a three-dimensional variant of such Kasteleyn transition [51].

Magnetic Field along [111]

A field along [111] pins one of the four spins, which has the major projection along the field. The pinned spins form a triangular lattice, while the remaining degrees of freedom lie on decoupled Kagomé layers with alternating triangles of two-in-one-out or one-in-two-out. Due to its similarity to the ice rules, such a state has been named *Kagomé ice* [52, 53]. Its residual entropy is reduced, but remains extensive [10, 54].

The magnetization of the Kagomé ice state is only saturated partially. Upon further increasing the field and once the Zeeman energy exceeds the energy scale of violating the ice-rule, an alternating three-in-one-out or one-in-three-out state is favored. The different energy scales involved lead to a magnetisation plateau with the Kagomé ice state over a finite range of the field strength. Matsuhira et al. [52] reported such a magnetization plateau in $\text{Dy}_2\text{Ti}_2\text{O}_7$.

The Kagomé ice state maps to a full covering of hard-core dimers on a honeycomb lattice [54, 55]. Upon tilting the field, a second way of reaching saturation without breaking the ice rules is provided. Tilting the field reduces the degrees of freedom in the Kagomé layers until eventually a Kasteleyn transition [56] into an ordered state occurs. Again, depending on the energy scales, a magnetization plateau is expected.

2.2.6 Kasteleyn Transition of Dimers

A Kasteleyn transition [56] is a particular classical transition between an ordered and a disordered phase of a dimer tiling on a planar graph. A dimer is an object that occupies

two neighboring sites. Any site shall be occupied, but none doubly occupied. Placing a dimer on an edge (or link) may cost or gain energy, which is reflected in assigning Boltzmann weights to the edges. The honeycomb and the square lattice graphs are of particular interest in the thesis at hand. A mathematical introduction can be found in the lecture notes by Kenyon [57] and in the earlier literature [58, 59].

Generally, the goal is to provide an expression for the partition function [56]

$$\mathcal{Z} = \sum_{\{n_1, n_2, \dots, n_N\}} g(n_1, n_2, \dots, n_N) z_1^{n_1} z_2^{n_2} \dots z_N^{n_N} , \quad (2.19)$$

where the Boltzmann weight $z_i = e^{-\beta E_i}$ belongs to edge i with an occupation number $n_i = \{0, 1\}$. $g()$ is a generating function. Kasteleyn has proven that \mathcal{Z} can be written in terms of a Pfaffian [56]

$$\mathcal{Z} = |\text{Pf } K| \quad (2.20)$$

of a skew-symmetric matrix K . The Pfaffian of a skew-symmetric matrix is defined via the determinant as $(\text{Pf } A)^2 = \det A$. The matrix K is the directed adjacency matrix of a graph—here lattices—with weights z_i and an additional phase factor ϕ_i . ϕ_i has to be chosen such that a loop around a face with $0 \pmod 4$ edges acquires a negative sign and a positive sign around a face with $2 \pmod 4$ edges [56]. This ensures, that all the terms generated in $\text{Pf } K$ have the same sign and Eq. (2.20) is valid.

A simplification exists for bipartite lattices. If the nodes of the lattice are numbered such that the nodes of sublattice A get indices $\{0, 1, \dots, N/2 - 1\}$ and the nodes of B indices $\{N/2, \dots, N - 1\}$, then K has the structure

$$K = \begin{pmatrix} 0 & \tilde{K} \\ -\tilde{K}^T & 0 \end{pmatrix} . \quad (2.21)$$

Here, \tilde{K} denotes the Kasteleyn matrix, which is the (reduced) adjacency matrix. Rows of the adjacency matrix represent nodes of sublattice A and columns represent nodes of B. In contrast to K , the reduced \tilde{K} is not defined with respect to a directed lattice.

Since $\det K = (\det -\tilde{K}^T)(\det \tilde{K}) = (\det \tilde{K})^2$,⁶ Eq. (2.20) simplifies to

$$\mathcal{Z} = |\det \tilde{K}| . \quad (2.22)$$

Our interest lies in computing the partition function for dimers on lattices that are infinite, bipartite, and planar (for convenience put on a torus). A lengthy mathematical construction [60] arrives at

$$\frac{1}{N} \log \mathcal{Z} = \frac{1}{(2\pi i)^2} \int_{\mathcal{C}_1} \frac{dw}{w} \int_{\mathcal{C}_2} \frac{dz}{z} \log \left(\det \tilde{K}(w, z) \right) , \quad (2.23)$$

⁶The minus sign vanishes due to the number of nodes being even.

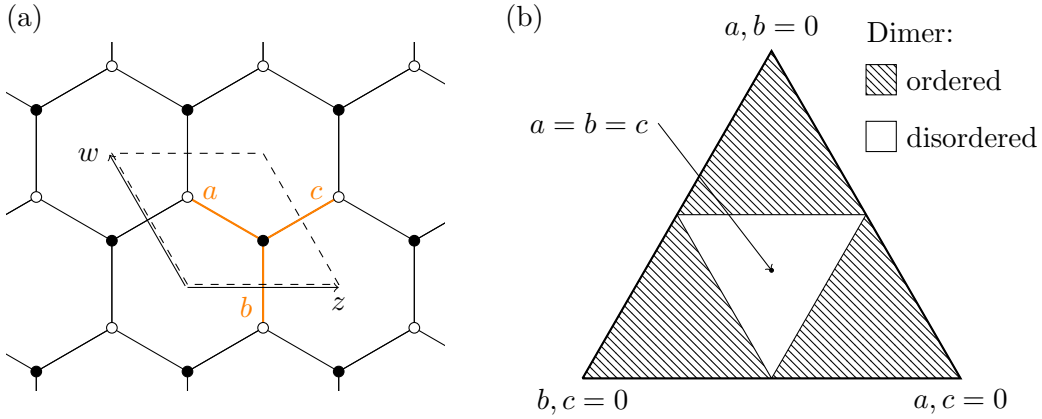


Figure 2.5: (a) Sketch of a single unit cell for the honeycomb lattice with weights as used in $\tilde{K}(w, z)$ in the main text. (b) Phase diagram of dimers on the edges of a honeycomb lattice.

where $\tilde{K}(w, z)$ is the Kasteleyn matrix of a fundamental domain or simply unit cell. Links to adjacent unit cells—by translating along lattice vectors, i.e. $\mathbf{G} = m\mathbf{a} + n\mathbf{b}$ —obtain a factor w^m, z^n . The integration is carried out over a closed loop $|w| = 1$ in the complex plane, and analogously $|z| = 1$.

Dimers on the Honeycomb Lattice

Let us first consider close-packed hardcore dimers on an honeycomb lattice. Each of the edges has a Boltzmann weights a , b , or c assigned to it with parallel edges having the same weight. Following the convention of the unit cell and the weights pictured in Fig. 2.5, we get the following Kasteleyn 'matrix' $\tilde{K}(w, z) = a + bw + cz$ [57], which is just a scalar since the lattice is bipartite and the unit cell contains only two sites. Thence,

$$\frac{1}{N} \log \mathcal{Z}_H = \frac{1}{(2\pi i)^2} \int_{C_1} \frac{dw}{w} \int_{C_2} \frac{dz}{z} \log \left(a + \frac{b}{w} + cz \right). \quad (2.24)$$

This integral is quickly computed for $a > b + c$ (or permutations thereof) as the function has only one pole within the integration contour. One can apply the residue theorem to obtain

$$\frac{F}{N} = \frac{1}{N} \log \mathcal{Z} = \begin{cases} \log a & (a > b + c) \\ \log b & (b > a + c) \\ \log c & (c > a + b) \end{cases} \quad (2.25)$$

This result reflects that the dimer configurations are long-range ordered, if one of the weights exceeds the sum of the remaining two [56]. Fig. 2.5 illustrates the phase diagram.

Returning to spin ice, a magnetization plateau may exist on a pyrochlore lattice

in a magnetic field applied along [111], in which one of four spin is aligned with the field and the remaining spins form decoupled Kagomé layers. A one-to-one mapping to a full covering of hardcore dimers on a honeycomb lattice exists [55]. Upon slightly tilting the field, the three directions acquire different weights $z_i = e^{-\beta\epsilon_i}$ depending on the energies $\epsilon_i = \sum_{i \in \Delta} \mathbf{s}_i \cdot \mathbf{h}_\perp$ of the underlying spin configuration $\{s_i\}$ in the tilt field \mathbf{h}_\perp . As above, an ordered state is entered as soon as $z_0 \geq z_1 + z_2$ (or permutations). Within the ordered phase, the partition sum is given by (2.25) and no fluctuations occur.

In chapter 8 we study similar mappings to hardcore dimers that exist in the hexagonal water ice structure. There, a field direction can be found, for which the remaining degrees of freedom map one-to-one to dimers on a square lattice.

2.3 Emergent \mathbb{Z}_2 -Gauge Theory in the Kitaev Model

This section is devoted to the Kitaev model on a honeycomb lattice. The Kitaev model is an $SU(2)$ spin- $\frac{1}{2}$ model with strongly anisotropic Ising-like interactions giving rise to exchange frustration resulting. Already the classical Kitaev model with $O(3)$ Heisenberg spins features a classical spin liquid with an extensively degenerate ground state manifold [61, 62]. The ground state degeneracy bears some similarity to dimer coverings on the hexagonal lattice [61].

In this thesis, its quantum variant is studied as introduced by Kitaev in his seminal paper [16]. In the spin- $\frac{1}{2}$ Kitaev model, frustration and quantum fluctuations lead to quantum spin liquid phases with fractionalized excitations: the spin degrees of freedom separate into Majorana fermions and fluxes of an emergent \mathbb{Z}_2 gauge field. Upon either adding a magnetic field or making the interactions spatially anisotropic, the excitation spectrum of the Majorana fermions gaps out and topologically ordered phases are entered hosting anyons.

The structure of this section is as follows. First in section 2.3.1, the Kitaev model is introduced. As is outlined in 2.3.2, the Kitaev model exhibits an extensive number of conserved quantities: fluxes—or visons—of a static \mathbb{Z}_2 gauge field. Fixing the fluxes enables to solve the Kitaev model exactly, cf. 2.3.3, and reveals the excitation spectrum of the Majorana fermions, cf. 2.3.4. In his seminal paper, Kitaev studied how the magnetic field affects the Kitaev model using perturbation theory. Aspects of his work are summarized in 2.3.5 exposing a topologically ordered phase hosting non-abelian anyons. Properties of the topological phase and its excitations are discussed in section 2.3.6. Then, in section 2.3.7 the focus shifts towards probing the Kitaev spin liquid by discussing its dynamical spin-structure factor. As will be explained in 2.3.8, the Kitaev exchange can be mediated via spin orbit coupling and may play a role in magnetic compounds including Na_2IrO_3 , Li_2IrO_3 , and $\alpha\text{-RuCl}_3$.

2.3.1 Kitaev model

The Hamiltonian of the Kitaev model is defined as [16]

$$H = K_x \sum_{\langle i,j \rangle_x} \hat{S}_i^x \hat{S}_j^x + K_y \sum_{\langle i,j \rangle_y} \hat{S}_i^y \hat{S}_j^y + K_z \sum_{\langle i,j \rangle_z} \hat{S}_i^z \hat{S}_j^z, \quad (2.26)$$

where $\hat{S}_i^\gamma = \frac{1}{2} \hat{\sigma}_i^\gamma$ are spin operators defined via Pauli operators $\hat{\sigma}$. The \hat{S}_i^γ act on spin- $\frac{1}{2}$ degrees of freedoms at the sites i of the honeycomb lattice. On the honeycomb lattice, parallel links or bonds with one of three different orientations are labeled $\gamma = \{x, y, z\}$, see also Fig. 2.6(a). Two nearest-neighbor spins $\langle i, j \rangle_\gamma$ adjacent to a bond with label γ are coupled by an Ising exchange $S_i^\gamma S_j^\gamma$. With this particular structure, the exchange interactions cannot all be simultaneously minimized in energy. This *frustration* stems

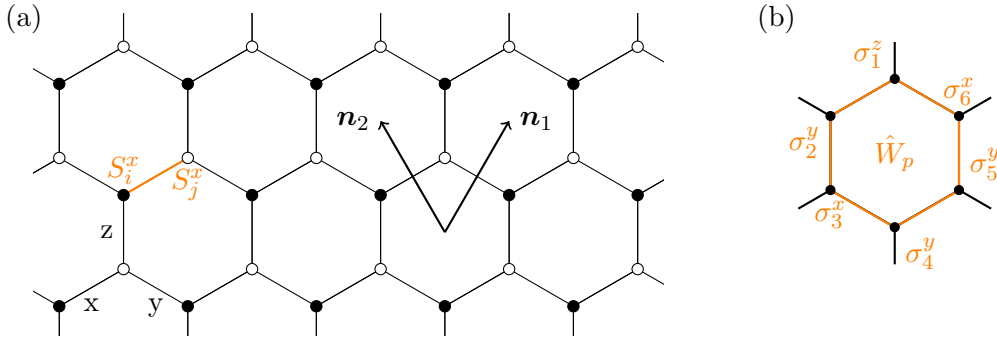


Figure 2.6: (a) Honeycomb lattice with lattice vectors \mathbf{n}_1 and \mathbf{n}_2 . The bonds are labeled with $\gamma = \{x, y, z\}$. A single Kitaev exchange term $S_i^x S_j^x$ is highlighted in orange. The filled black and white nodes depict the two sublattices. (b) Plaquette operator \hat{W}_p with eigenvalues $w_p = \pm 1$ for a single hexagon.

solely from the exchange and is therefore titled *exchange frustration*.

Generalizations of the Kitaev model to other lattices exist, like the triangular [63, 64], the decorated triangle-honeycomb [65], and to three-dimensional lattices [66]. In the remainder of this thesis, whenever the Kitaev model is stated, it is meant to be placed on the honeycomb lattice. We continue now with examining the properties of the Kitaev model.

2.3.2 Static \mathbb{Z}_2 Fluxes

The Kitaev model contains an extensive set of conserved quantities, static \mathbb{Z}_2 -fluxes, that are obtained via the following plaquette operator \hat{W}_p . Consider a loop denoted with \mathcal{P} , then \hat{W}_p is defined as [16]

$$\hat{W}_p = \prod_{i \in \mathcal{P}} \sigma_i^{\gamma_{\mathcal{P}}(i)}, \quad (2.27)$$

where σ^γ are the Pauli operators and $\gamma_{\mathcal{P}}(i)$ selects the label of the bond at site i , that is not part of the loop. On the honeycomb lattice, the smallest loop winds around a hexagonal plaquette. Such an operator \hat{W}_p winding around a plaquette with sites $(1, 2, 3, 4, 5, 6)$, thus $\hat{W}_p = \sigma_1^z \sigma_2^y \sigma_3^x \sigma_4^z \sigma_5^y \sigma_6^x$, is illustrated in Fig. 2.6(b). The \hat{W}_p for all possible loops around single plaquettes commute with each other and with each of the $S_i^\gamma S_j^\gamma$ terms of the Hamiltonian, Eq. (2.26). Its corresponding eigenvalues are $w_p = \pm 1$ defined via $\hat{W}_p |\psi\rangle = w_p |\psi\rangle$ with $|\psi\rangle$ being the eigenstates of the Kitaev model. Larger, contractible loops can simply be composed as a product of \hat{W}_p 's for each plaquette within the loop its eigenvalue is the product of eigenvalues w_p 's of the plaquettes.

As *each* of the \hat{W}_p commutes with the Hamiltonian, they define a set of quantum numbers $\{\forall j : w_{p_j}\}$ separating the full Hilbert space \mathcal{H} into disjunct subsets $\mathcal{H}_{\{w_p\}}$.

By fixing all $w_{\mathcal{P}}$, the Kitaev model can be solved exactly, cf. 2.3.3.

As a remark, non-contractible loops exist depending on the genus of the surface on which the Kitaev model is placed. Here, we are mainly concerned with cylinder and torus geometries due to the numerical method employed later. Likewise, an operator $\hat{W}_{\mathcal{L}}$ for a non-contractable loop \mathcal{L} commutes with the Hamiltonian and separates the full Hilbert space into two subspaces with corresponding eigenvalues $w_{\mathcal{L}} = \pm 1$. $\hat{W}_{\mathcal{L}}$ is essentially equivalent to a Wilson loop, which may differentiate different degenerate ground states of a topologically ordered phase. These loops will be of particular interest in chapter 6 where a topologically ordered phase is studied, but is also of some relevance in chapters 4 and 5.

The fluxes are, as will be clarified below, the physical excitations of a \mathbb{Z}_2 gauge field: fluxes can only be created pairwise by applying a single σ_i^γ operator. Such a creation of a pair of fluxes costs a finite amount of energy. Thence, fluxes are gapped excitations. Furthermore, the properties on a geometry with genus larger than one are not trivial in the sense, that topologically degenerate ground state exist. Let us create a pair of fluxes, move one of the fluxes along either circumference of a torus, and annihilate the two fluxes again. In doing so, we end up in exactly the same local configuration $\{w_{\mathcal{P}}\}$, but the flux of the non-contractible loop changed its sign. This construction leads to a 2^g degeneracy of the \mathbb{Z}_2 flux configuration on a surface with genus g . On a torus the degeneracy is fourfold with four topological sectors.

Note, that at this stage the energy cost of a flux-pair is not clearly defined, but will become so in the construction given below. The construction also elucidates the resemblance to a \mathbb{Z}_2 -gauge theory.

2.3.3 Exact solution via Majorana operators

In the original solution [16], the Hamiltonian in Eq. (2.26) was solved by replacing the spin- $\frac{1}{2}$ with Majorana degrees of freedom. An alternative solution utilizes a Jordan-Wigner transformation [67]. However, only the former approach is summarized below.

Let us recall some properties of Majorana fermions. Given a complex fermion with creation and annihilation operators a^\dagger and a , it can be recast into a pair of Majorana fermions γ_1 and γ_2 by

$$\gamma_1 = a + a^\dagger \quad \gamma_2 = i(a - a^\dagger) . \quad (2.28)$$

They have the property that the operator γ_i is its own hermitian conjugate, $\gamma_i^\dagger = \gamma_i$. Furthermore, the γ_i satisfy the anticommutator relation

$$\gamma_i \gamma_j + \gamma_j \gamma_i = 2\delta_{ij} ,$$

and thus $c_i^2 = 1$ and $c_i c_j = -c_j c_i$ if $i \neq j$.

Upon applying the following mapping of spin- to Majorana operators, a single spin

gets replaced by four Majorana fermions. Let these four Majorana operators at site j be denoted as b_j^x, b_j^y, b_j^z, c_j , then the mapping is defined as

$$2S_j^x \mapsto ib_j^x c_j \quad 2S_j^y \mapsto ib_j^y c_j \quad 2S_j^z \mapsto ib_j^z c_j . \quad (2.29)$$

Such a mapping enlarges the Hilbert space from $\dim(\mathcal{H}) = 2^N$ to $\dim(\tilde{\mathcal{H}}) = 4^N$. In particular, the local Hilbert space of the spin model is two, whereas in the Majorana representation it is four. Note that the physical subspace is given by all $|\phi\rangle$ that satisfy

$$\forall j : D_j |\phi\rangle = |\phi\rangle \quad \text{where} \quad D_j = b_j^x b_j^y b_j^z c_j . \quad (2.30)$$

This can be recognized by noting that the Pauli operators satisfy $\sigma_j^x \sigma_j^y \sigma_j^z = i\mathbb{1}$. Upon applying the mapping, $\sigma_j^x \sigma_j^y \sigma_j^z$ becomes $(ib^x c)(ib^y c)(ib^z c) = ib^x b^y b^z c$. The latter has eigenvalues $\pm i$. Thence, by projecting on states $|\psi\rangle$ that have eigenvalues $\forall j : D_j = +1$, the original Pauli matrix identity is restored and the physical subspace is selected.

Applying mapping to Majorana fermion operators to the original Hamiltonian, Eq. (2.26), yields [16]

$$\tilde{H} = - \sum_{\langle j,k \rangle_\gamma} \frac{K_\gamma}{4} (ib_j^\gamma b_k^\gamma)(ic_j c_k) , \quad (2.31)$$

where the sum runs over all nearest neighbor pairs $\langle i, j \rangle$, and $\gamma = \{x, y, z\}$ is the label of the bond connecting both sites.

Similar to the conserved fluxes $w_{\mathcal{P}}$ in the spin Hamiltonian, the Hamiltonian in (2.31) has a set of conserved quantities appearing as bond variables $\hat{u}_{jk} = ib_j^\gamma b_k^\gamma$ with eigenvalues $u_{jk} = \pm 1$. By fixing all u_{jk} , which fixes all $w_{\mathcal{P}}$, a Hamiltonian quadratic Majorana fermion operators remains. Eq. (2.31) simplifies to [16]

$$\tilde{H} = -\frac{i}{4} \sum_{j,k} A_{jk} c_j c_k , \quad (2.32)$$

where the matrix A_{jk} is defined as

$$A_{jk} = \begin{cases} \frac{K_\gamma}{2} u_{jk} & \text{if } j, k \text{ along } \gamma \\ 0 & \text{otherwise} \end{cases} . \quad (2.33)$$

A_{jk} is real-valued and antisymmetric. The commutation relation of the Majorana fermions $c_j c_k = -c_k c_j$ imply $\hat{u}_{jk} = -\hat{u}_{kj}$, and consequently $u_{jk} = -u_{kj}$. The antisymmetric A_{jk} together with the imaginary i as a prefactor render the Hamiltonian hermitian.

The flux variables of the spin Hamiltonian are covered by the u_{jk} via

$$w_{\mathcal{P}} = \prod_{\langle jk \rangle_{AB} \in \mathcal{P}} u_{jk} ,$$

where the convention is used that j belongs to sublattice A and k to B .

The \mathbb{Z}_2 gauge theory is more evident now and its terminology can be introduced. All the configurations $\{u_{kl}\}$ that produce the same flux configurations $\{w_{\mathcal{P}}\}$ belong to the same gauge equivalence class. A map between two gauge equivalent configurations is called a gauge symmetry or gauge transformation. In case of the Kitaev model, the previously introduced flux operator $\hat{W}_{\mathcal{L}} = \prod_{i \in \mathcal{L}} \sigma_i^{\gamma_i}$ along arbitrary loops provides such a gauge transformation. A single σ_i^{γ} changes the sign of u_{ik} (i, k connected by γ). By proceeding along a loop, $0 \bmod 2$ bonds per plaquette get flipped leaving their $w_{\mathcal{P}}$ invariant but changing one configuration $\{u_{kl}\}$ to a gauge-equivalent one $\{\tilde{u}_{kl}\}$.

Upon flipping a single u_{kl} , two fluxes adjacent to the bond (k, l) are created. The energy to create such a pair (locally) is now given by the difference in ground state energy of the quadratic Majorana fermion Hamiltonian containing the two fluxes and the flux-free ground state energy.

This \mathbb{Z}_2 gauge symmetry has been introduced by the Majorana representation and is thus artificial. Nonetheless, the \mathbb{Z}_2 -fluxes are physical and its properties captured correctly. In order to return to the spin representation, one needs to average over equivalent gauge field configurations $\{u_{jk}\}$ given they belong to the physical subspace.

2.3.4 The Spectrum of the Fermion Problem

Now, the quadratic Hamiltonian of the matter fermions remains to be solved. The ground state will be in the flux-free sector [68], in particular $\forall \mathcal{P} : w_{\mathcal{P}} = +1$. One choice to satisfy the flux-free condition is to set $u_{jk} = +1$, with an orientation such that site j belongs to sublattice A and k to sublattice B . With such a choice, Eq. 2.32 is solved by a Fourier transform [16]

$$H_{\text{iso}} = \frac{1}{2} \sum_{\mathbf{k}, \alpha, \beta} \tilde{A}(\mathbf{k}) c_{\alpha, -\mathbf{k}} c_{\beta, \mathbf{k}} \quad \text{with} \quad i\tilde{A}(\mathbf{k}) = \begin{pmatrix} 0 & if(\mathbf{k}) \\ -if(\mathbf{k})^* & 0 \end{pmatrix}, \quad (2.34)$$

where α and β denote the sublattice and $f(\mathbf{k})$ is a complex valued function

$$f(\mathbf{k}) = \frac{1}{2} \left(K_x e^{i(\mathbf{q} \cdot \mathbf{n}_1)} + K_y e^{i(\mathbf{q} \cdot \mathbf{n}_2)} + K_z \right). \quad (2.35)$$

Here, $\mathbf{n}_1 = (-1/2, \sqrt{3}/2)$ and $\mathbf{n}_2 = (1/2, \sqrt{3}/2)$ are the lattice vectors of the honeycomb lattice as depicted in Fig. 2.6(a). Consequently, the energy spectrum is given as $E(\mathbf{k}) = \pm |f(\mathbf{k})|$. The spectrum is gapless if $f(\mathbf{k}) = 0$, which occurs if the K_{γ} are chosen such

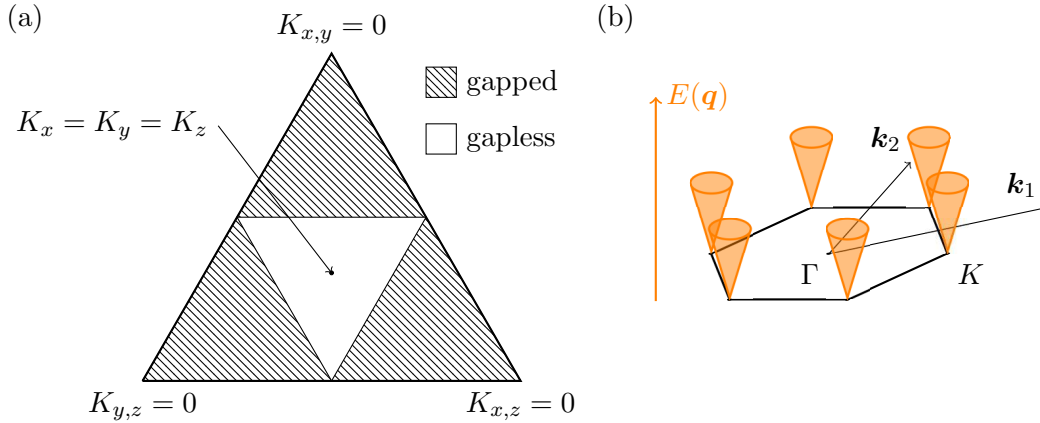


Figure 2.7: (a) Phase diagram of the Kitaev model upon varying K_x , K_y , and K_z . The isotropic limit is at the center, the corners represent the anisotropic limits $K_\gamma \ll K_\alpha + K_\beta$. (b) First Brillouin zone with the reciprocal lattice vectors \mathbf{k}_1 and \mathbf{k}_2 . In the isotropic limit $K_\gamma = K$, the (Majorana) Dirac cones are situated at the K high-symmetry point and have a linear dispersion.

that for any permutation $(\alpha, \beta, \gamma) = P(x, y, z)$

$$|K_\alpha| \leq |K_\beta| + |K_\gamma|. \quad (2.36)$$

A gap opens as soon as one of the K_γ exceeds the sum of the remaining two. The corresponding phase diagram is illustrated in Fig. 2.7(a).

Returning to the gapless phase, the spectrum has a linear dispersion $E(\mathbf{k}_0 + \delta\mathbf{k}) = \epsilon|\delta\mathbf{k}|$ near its gapless nodes at \mathbf{k}_0 . Two such Majorana cones exist, one each at \mathbf{k}_0 and $-\mathbf{k}_0$. At isotropic couplings $K_\gamma = K$, the gapless nodes are situated at the K and $K' = -K$ high-symmetry points at the corners of the first Brillouin zone, cf. Fig. 2.7(b). Hence, the spectrum resembles a Majorana variant of the Dirac cones, e.g., as occurring in graphene [69, 70]. Upon varying the K_γ , the gapless nodes move in reciprocal space. At the transition to the gapped phase, both gapless nodes join and gap out when the anisotropy is increased further.

In the strongly isotropic case, e.g., $|K^x| \gg |K^y| + |K^z|$, the toric code model [21] is recovered. The toric code, similarly a \mathbb{Z}_2 -gauge theory, is known to be topologically ordered and exhibits abelian anyons.

Now, that we obtained the spectrum in terms of Majorana fermions hopping in a \mathbb{Z}_2 gauge field background, let us return to the original Hamiltonian, Eq. (2.26), in terms of spin- $\frac{1}{2}$ degrees of freedom. First, we need to obtain a physical state, which is done by averaging over all gauge-equivalent states in the physical subspace. Given a ground state $|\tilde{\phi}_u\rangle$ of \tilde{H} , cf. Eq. (2.32), with a choice of $\{u_{kl}\}$, such that the flux-free condition

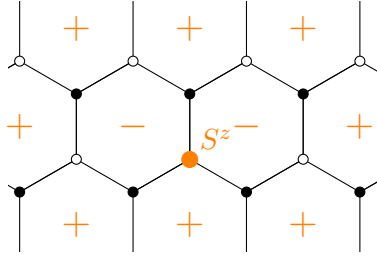


Figure 2.8: Applying a spin operator like S^z changes the flux configuration.

is fulfilled, then [16]

$$|\phi\rangle = \prod_i \frac{1 + D_i}{2} |\tilde{\phi}_u\rangle,$$

performs such an averaging and projects onto the physical subspace.

Due to the fluxes separating the Hilbert space, any operator that changes the flux configuration has a vanishing ground state expectation value. The Majorana representation demonstrates, that applying a single spin operator, e.g., $2S_i^z = ib_i^z c_i$ introduces a Majorana fermion and a flux-pair adjacent to the z -bond (cf. Fig. 2.8). Consequently, the ground state has no magnetic moment. Furthermore, the spin-spin correlators are strictly nearest neighbor

$$\langle \psi | S_i^\alpha S_j^\beta | \psi \rangle = \begin{cases} \frac{1}{4} \delta_{\alpha\beta} & \text{if } i = j \\ C \delta_{\alpha\beta} & \text{if } i, j \text{ connected along bond } \alpha \\ 0 & \text{otherwise} \end{cases}, \quad (2.37)$$

as the second spin operator S_j^β has to annihilate the flux-pair again in order to restore the original flux-free configuration. Here, C is a constant which is $C \approx 0.131$ for isotropic $K_\gamma = K$ and in the thermodynamic limit. Thus, magnetic long-range order is suppressed in the ground state of the Kitaev model, yet the gapless Majorana spectrum implies a strongly correlated ground state with diverging correlation length⁷ ξ . The ground state of the Kitaev model is a *quantum spin liquid*. The spins do not break any symmetry spontaneously nor do they exhibit long-range order.

2.3.5 The Kitaev Model in a Magnetic Field: Perturbation Theory

Let us now restrict to the isotropic Kitaev model and study how a magnetic field affects its ground state. Generally, the magnetic field breaks time-reversal symmetry and the gapless spectrum of the matter fermions is expected to open.

Based on a perturbative treatment, Kitaev [16] identified two third order terms $S_i^x S_j^y S_k^z$ as the first relevant terms breaking time-reversal and leaving the flux sector

⁷With respect to some correlations other than spin-spin.

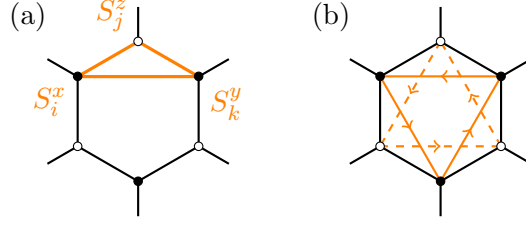


Figure 2.9: (a) A single exemplarily shown three-spin term $S_i^x S_j^z S_k^y$ of H_{K_3} defined in Eq. (2.38). (b) All symmetric variants of the three-spin term on a single plaquette with the orientation employed.

unchanged. One of these terms leads to a four-fermion exchange and breaks integrability of the Kitaev model. It has been argued by Kitaev to be irrelevant to the Majorana fermion spectrum.

The second term couples three neighboring spins in a way, that is illustrated in Fig. 2.9. Including a sum over all symmetric variants of the three-spin term, the Hamiltonian reads

$$H_{K_3} = \sum_{\langle i,j \rangle_\gamma} K_\gamma S_i^\gamma S_j^\gamma + K_3 \sum_{\langle\langle i,j,k \rangle\rangle} S_i^x S_j^y S_k^z, \quad (2.38)$$

which in the remainder is considered as the *extended* Kitaev model. In Eq. (2.38), $\langle\langle \cdot \rangle\rangle$ denotes an ordered tuple (i, j, k) of neighboring sites such that the S^x , S^y , and S^z at the outer two sites coincide with the label of the bond adjacent to the central site. The magnitude of $K_3 \propto h_x h_y h_z / K^2$ depends on the direction of the magnetic field $\mathbf{h} = (h_x, h_y, h_z)^T$ [16]. Hence, this term relies on a magnetic field with non-zero components along all three components, or is not relevant otherwise.

H_{K_3} remains exactly solvable in the same way as the bare Kitaev model is. The flux operators $W_{\mathcal{P}}$ commute with H_{K_3} and its eigenvalues $w_{\mathcal{P}} \pm 1$ serve as quantum numbers separating the Hilbert space. Following the same construction via Majorana operators, a Hamiltonian quadratic in the matter fermions c remains. This Hamiltonian is of similar structure as in Eq. 2.32, yet A_{jk} obtains additional next nearest neighbor terms

$$A_{jk} = \begin{cases} \frac{K_\gamma}{2} u_{jk} & \text{if } j, k \text{ along } \gamma \\ \frac{K_3}{4} u_{jl} u_{kl} & \text{if } j, k \text{ connected via } l \\ 0 & \text{otherwise} \end{cases}. \quad (2.39)$$

Here, we still use the orientation convention for u_{jk} with $j \in A$ and $k \in B$ sublattice. Similarly, the ground state lies in the flux free sector [16, 68] and fixing the u_{jk}

accordingly leads to the spectrum [16]

$$H_{\text{iso}} = \frac{1}{2} \sum_{\mathbf{k}, \alpha, \beta} \tilde{i}A(\mathbf{k})c_{\alpha, -\mathbf{k}}c_{\beta, \mathbf{k}} \quad \text{with} \quad i\tilde{A}(\mathbf{k}) = \begin{pmatrix} \Delta(\mathbf{k}) & if(\mathbf{k}) \\ -if(\mathbf{k})^* & -\Delta(\mathbf{k}) \end{pmatrix}, \quad (2.40)$$

where $\Delta(\mathbf{k})$ is a trigonometric function and $f()$ is defined as before, cf. Eq. (2.35). The energy spectrum gets

$$E(q) = \pm \sqrt{|f(\mathbf{k})|^2 + \Delta(\mathbf{k})^2}. \quad (2.41)$$

Most importantly, $\Delta(\mathbf{k}) \propto K_3$ such that a gap in the Majorana fermion spectrum opens linearly with K_3 .

The fermionic bands are topologically non-trivial by featuring Chern numbers ± 1 and thus implying the existence of gapless edge modes. Thus, the extended Kitaev model with a finite K_3 enters a topologically ordered phase, and, as we will see in the next section, hosts non-abelian anyons. Note that the structure in Eq. (2.40) is similar to that of a $p + ip$ superconductor, see for example the review [71]. Thence it shares the same physical properties.

A remark is on order regarding the Kitaev model with a magnetic field. The three-spin term may resemble the effect on the matter fermion spectrum upon applying a field, but does not account for fluxes. In particular, the treatment above relies on the fact that the three-spin term does not change the flux configuration and, consequently, the fluxes are static. However, a Zeeman coupling to a magnetic field $-\mathbf{h} \sum_i \mathbf{S}_i$ creates (or annihilates) flux-pairs. In case that a flux already exist, applying a S^γ moves this flux perpendicular to the bond with label γ . Thence, a magnetic field enables the fluxes to acquire a finite hopping amplitude and the fluxes are expected to have dispersion. How a magnetic field affects the Kitaev model beyond the integrable points is studied numerically and discussed in detail in chapter 6.

2.3.6 Topological Order and Anyonic Excitations

A quantum spin liquid in two dimensions is intimately connected to topological order and anyonic excitations. A phase is defined to be topological ordered if it is a gapped state of matter, that exhibits a degeneracy of the ground state depending on the genus of the surface the system is placed on [20, 72]. The degeneracy is a consequence of the existence of anyonic quasiparticles. Imagine a pair of quasiparticles is created locally, one particle is wind along a non-contractable loop, e.g., along the circumference of a torus, until the pair is annihilated again. Such a movement changes the initial state to a different state within the set of degenerate ground states, but leaves the local observables invariant. If the circumference is finite, the degeneracy may be slightly lifted, yet as long as any local excitation has a larger energy than the splitting of the degeneracy, the above description is still valid [73].

Topological order cannot be detected by any local measurement. However, the entanglement entropy, a measure of how strongly entangled two adjunct subsystems are, provides a way of determining topological order. The entanglement entropy is defined as the von-Neumann entropy

$$S_E = \text{Tr}(\rho_A \log \rho_A)$$

of the reduced density matrix $\rho_A = \text{Tr}_B \rho$ obtained by partially tracing the density matrix ρ of the full system. The entanglement entropy of a ground state of a gapped system satisfies an area law: The entanglement entropy grows with the length of the boundary between the two subsystem A and B . In a topologically ordered phase, the area law acquires a correction γ , which is called *Topological Entanglement Entropy* [74, 75].

A ground state of the (extended) Kitaev model has the property, that its entanglement entropy of a bipartition has two separate contributions [76]

$$S_E = S_F + S_G ,$$

where S_F originates from the matter fermions c_i and S_G from the gauge field $\{u_{kl}\}$. Both contributions can be computed exactly [76, 77] predicting a non-zero topological entanglement entropy of $\gamma = \log 2$ for two gapped phases of the extended Kitaev model. Thus, both gapped phases are topologically ordered [16]. Namely, the gapped phase existing for sufficiently anisotropic Kitaev exchange is adiabatically connected to the Toric Code [21] and exhibits besides the vacuum 1, an m , an e , and a composite $\epsilon = e \times m$ particle with abelian exchange statistics. The gapped phase appearing for (nearly) isotropic Kitaev exchange and finite K_3 hosts instead non-abelian anyons, composite quasiparticles of a Majorana fermion ϵ bound to a flux σ . The σ is also referred to as a vortex in the context of $p + ip$ superconductors. In chapter 6, the non-abelian topological phase is discussed in more detail. In particular, the topological entanglement entropy of each quasiparticle is extracted numerically, see also 3.1.3 for the methodology.

2.3.7 Dynamical Spin-Structure Factor

We have seen so far that the (extended) Kitaev model exhibits fractionalization of spin- $\frac{1}{2}$ degrees of freedom into fluxes and Majorana fermions of which the latter may be gapless depending on the particular set of parameters. Such fractionalization is most evident in dynamical probes. The dynamical spin-structure factor is of particular interest as it connects directly to inelastic neutron scattering experiments.

The dynamical spin-structure factor is defined as the spatio temporal Fourier trans-

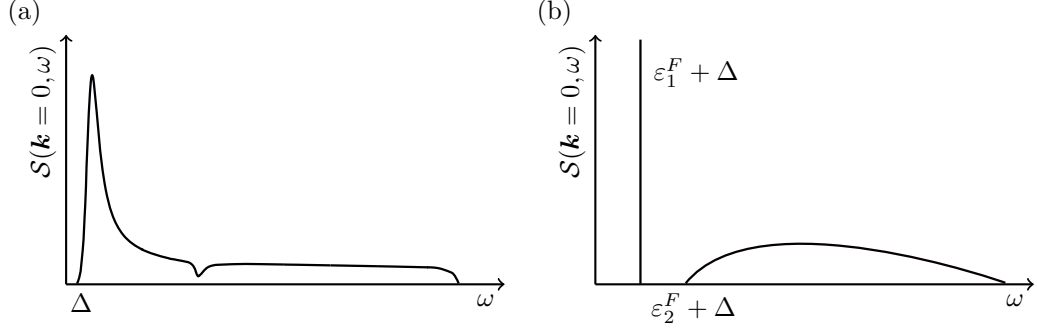


Figure 2.10: Schematic plots of the dynamical spin-structure factor $\mathcal{S}(\mathbf{k} = 0, \omega)$ as represented in Ref. [78]: (a) for the isotropic Kitaev model, $K_\gamma = K$, and (b) the isotropic Kitaev model with finite three-spin interaction $K_3 > 0$ as arises in a perturbation theory of a magnetic field along the [111] axis.

form

$$\mathcal{S}^{\alpha\beta}(\mathbf{k}, \omega) = \frac{1}{2\pi} \sum_{ij} \int_{-\infty}^{\infty} e^{i\omega t - i\mathbf{k} \cdot (\mathbf{r}_j - \mathbf{r}_i)} C_{ij}^{\alpha\beta}(t) dt \quad (2.42)$$

of the dynamical spin-spin correlation

$$C_{ij}^{\alpha\beta}(t) = \langle \psi_0 | S_i^\alpha e^{-iHt} S_j^\beta | \psi_0 \rangle, \quad (2.43)$$

where $\alpha, \beta = \{x, y, z\}$ are the spin components and $|\psi_0\rangle$ the ground state, zero temperature, wave function. Rewriting $\mathcal{S}(\mathbf{k}, \omega)$ in terms of eigenstates $|n\rangle$, the Lehmann spectral representation

$$\mathcal{S}^{\gamma\gamma}(\mathbf{k}, \omega) \propto \sum_n |\langle n | S_{\mathbf{k}}^\gamma | 0 \rangle|^2 \delta(\omega_n - \omega) \quad (2.44)$$

reveals that the dynamical spin-structure factor contains information about the excitation spectrum. Here, w_n are the energy eigenvalues corresponding to $|n\rangle$. Thus, (2.44) sums all eigenenergies weighted by an amplitude stemming from the overlap $\langle n | S_{\mathbf{k}}^\gamma | 0 \rangle$. Fractionalization leads to a continuum in $\mathcal{S}(\mathbf{k}, \omega)$ due to exciting multiple (at least two) quasiparticles with fractional statistics. The energy and momentum transfer splits across the excited quasiparticles allowing for a continuum of scattering channels.

Knolle et al. [22, 78, 79] provide an exact calculation of $\mathcal{S}^{\gamma\gamma}(\mathbf{k}, \omega)$ for all the phases of the extended Kitaev model. The basic ingredient comes from the separability of fluxes and Majorana fermions. Applying a spin operator creates a pair of static fluxes and a Majorana fermion. The static fluxes change locally the potential landscape in which the Majorana moves. Thence, the dynamical spin-spin correlations, Eq. (2.43), can be written as [22]

$$C_{ij}^{\alpha\beta}(t) = -i \langle M_0 | e^{iH_0 t} c_i e^{-i(H_0 + V_{\langle ij \rangle \alpha}) t} c_j | M_0 \rangle \delta_{\alpha\beta} \delta_{\langle ij \rangle \alpha}, \quad (2.45)$$

already taking into account that the initially created pair of fluxes has to be annihilated with the second spin operator, which results in the conditions $\delta_{\alpha\beta}\delta_{\langle ij\rangle\alpha}$. Here, H_0 is the Hamiltonian acting on the Majorana fermion subsystem given there are no fluxes and $|M_0\rangle$ is its ground state. Whereas $H_0 - V_\alpha$ is the Hamiltonian given a flux-pair adjacent to bond $\langle i, j\rangle_\alpha$. In this view, the problem of computing $\mathcal{S}^{\gamma\gamma}(\mathbf{k}, \omega)$ is analogous to a quantum quench problem. Furthermore, the dynamic spin-spin correlator remains strictly zero beyond nearest neighbors for all times similar to the zero-time spin-spin correlator in Eq. 2.37.

In the isotropic case of the Kitaev model, cf. Figures 2.10(a) for ferromagnetic Kitaev coupling, the Kitaev model exhibits a broad continuum with a lower edge at the two-flux gap, Δ , corresponding to the two fluxes created by applying a single spin operator. The upper edge of the continuum is determined by the upper edge in the density of states. Due to $C_{ij}^{\alpha\beta}(t)$ being strictly zero beyond nearest neighbor, $\mathcal{S}(\mathbf{k}, \omega)$ is broad and rather featureless with respect to \mathbf{k} . The two different signs in the Kitaev model, lead to either ferromagnetic or antiferromagnetic nearest neighbor spin-spin correlation. For the latter, most of the spectral weight shifts from the Γ high-symmetry point ($\mathbf{k} = 0$) towards the Γ' point ($\mathbf{k} = \pm\mathbf{k}_{1,2,1+2}$).

Upon applying K_3 , cf. Fig. 2.10, the fermionic spectrum gaps out lifting also the lower edge of the continuum to an energy given by the sum of a Majorana and a flux pair, $\varepsilon_2^F + \Delta$. A sharp in-gap mode exists at $\varepsilon_1^F + \Delta$ corresponding to a composite of a single Majorana bound to a flux-pair. This bound state does not exhibit dispersion, since the flux pair is localized.

2.3.8 Kitaev Materials

The Kitaev exchange may be realised in compounds with strong spin-orbit coupling as noted by Jackeli and Khaliullin [80]. Spin-orbit coupling entangles spin and orbital degrees of freedom and an effective interaction of spins is mediated via the electronic interaction between neighboring orbitals.

In particular for the iridates $A_2\text{IrO}_3$ ($A=\text{Na, Li}$) and for the ruthenate $\alpha\text{-RuCl}_3$, the Na^{3+} and Ru^{3+} are placed in the center of octahedra formed by oxygen or chloride ions. The octahedra are arranged on a honeycomb lattice. See Fig. 2.11(a) for an illustration. Let us focus on $\alpha\text{-RuCl}_3$ for the description of the realisation of the Kitaev exchange.⁸ The spin exchange is mediated by the electronic orbitals, in particular the d-orbitals of ruthenium and the p-orbitals of chloride. Two symmetric exchange paths via the chloride exist, the left and the right path in Fig. 2.11(b). Destructive interference between both paths suppresses the spin exchange. The next higher eigenstates of the orbital multiplet become dominant. Now, different edges of the octahedra are

⁸The explanation for the iridates is similar. Just replace oxygen by chloride and ruthenium by sodium or lithium.

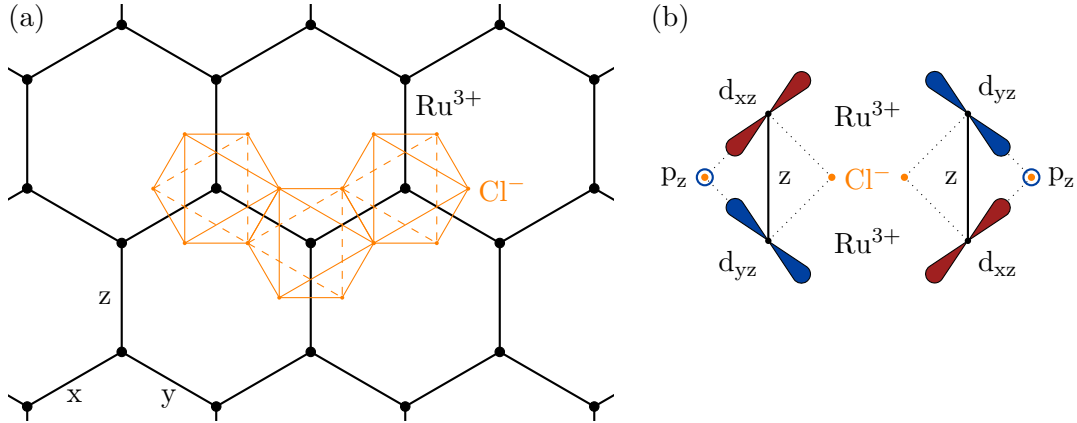


Figure 2.11: Anisotropic spin exchange interaction mediated by spin-orbit coupling. (a) Sketch of the structure of α - RuCl_3 : Ru^{3+} -ions form a hexagonal lattice (black) and the Cl^- form octahedral structures (orange) around the Ru^{3+} -ions. (b) Two interaction paths between electronic orbitals two neighboring Ru^{3+} -ions exist via a Cl^- -ion [80]. A similar structure applies to the iridates A_2IrO_3 .

shared with neighbors along different spatial directions and thus leaving to generally anisotropic coupling including the above discussed the Kitaev model with anisotropic Ising exchange.

However, additional couplings are allowed by symmetry [81, 82]. The following symmetries exist on a single bond: inversion, two-fold rotation around the bond, and the composition of both resulting in a mirror plane that is perpendicular to the bond. The point group at the center of the hexagon is D_3^d , generated by the S_6 rotoreflection (note that S_6^6 is the inversion) and the mirror plane.

Considering an x -bond and the sites 1, 2 adjacent to it, the inversion at the center of the bond exchanges the two sites without affecting the spin components, $S_1^\alpha \rightarrow S_2^\alpha$. The two-fold rotation does only act on the spin components $S_i^x \rightarrow -S_i^x$, $S_i^y \rightarrow -S_i^y$, and $S_i^z \rightarrow -S_i^z$ without exchanging the sites⁹

In total, the following invariants exist along the $\gamma = \{x, y, z\}$ -bond

$$\begin{aligned}
 & S_1^\gamma S_2^\gamma \\
 & S_1^\alpha S_2^\alpha + S_1^\beta S_2^\beta \\
 & S_1^\alpha S_2^\beta + S_1^\beta S_2^\alpha \\
 & S_1^\gamma S_2^\alpha + S_1^\alpha S_2^\gamma + S_1^\gamma S_2^\beta + S_1^\beta S_2^\gamma,
 \end{aligned}$$

where $(\alpha, \beta, \gamma) = \mathcal{P}(x, y, z)$ are permutations of (x, y, z) , such that $\beta, \gamma = \{x, y, z\}$ are distinct labels $\beta \neq \gamma$ and distinct from $\beta, \gamma \neq \alpha$. One may arrive at the following effec-

⁹The S^α component of the spin is perpendicular to the $\alpha = \{x, y, z\}$ bond and, with the constraint that the components form an orthogonal basis, there are eight possible choices of axis convention.

tive Hamiltonian with corresponding pre-factors (only incorporating nearest neighbor interactions)

$$\begin{aligned}
 H = & \sum_{\langle i,j \rangle_\gamma} 2K_\gamma S_i^\gamma S_j^\gamma + \sum_{\langle i,j \rangle} J_{i,j} \mathbf{S}_i \cdot \mathbf{S}_j \\
 & + \sum_{\langle i,j \rangle_\gamma, \alpha \neq \beta \neq \gamma} \Gamma_\gamma \left(S_i^\alpha S_j^\beta + S_i^\beta S_j^\alpha \right) \\
 & + \sum_{\langle i,j \rangle_\gamma, \alpha \neq \beta \neq \gamma} \Gamma'_\gamma \left(S_i^\gamma S_j^\alpha + S_i^\alpha S_j^\gamma + S_i^\gamma S_j^\beta + S_i^\beta S_j^\gamma \right) \quad (2.46)
 \end{aligned}$$

where the first term is the Kitaev exchange, the second term is the isotropic Heisenberg exchange, and the third and fourth terms are the symmetric off-diagonal exchanges Γ and Γ' .

An extensive literature on the ground state phase diagram is available for the Kitaev-Heisenberg model [83–86] and on the JKT -model [82]. In this thesis, the dynamical properties of the Kitaev-Heisenberg model are studied in chapter 4. Signatures of an extended quantum spin liquid phase in the Kitaev- Γ model are discussed in chapter 5. Exchanges between further nearest neighbors will also occur, and may be relevant for stabilizing ordered phases, but are not studied here.

Metal-Organic frameworks have been discussed as a further route to realizing Kitaev interactions [87]. Here, RuO_6 octahedra form a hexagonal lattice and organic ligands connect the edges of neighboring octahedra. Direct exchange interaction is suppressed and the same Jackeli-Khaliullin mechanism as above applies.

Chapter 3

Methods

Within this chapter, the main tools and methods used to study the ground state and the dynamics of strongly correlated and frustrated systems in one- or two-dimensions will be presented. The first section introduces *matrix product states* (MPS) to store a quantum mechanical wave function efficiently and extract quantum mechanical properties like entanglement. Within the concept of matrix product states, *density matrix renormalisation group* becomes an iterative variational method for obtaining the ground state by optimising with respect to the energy. Ground states of a system with a *gapped* spectrum can principally be represented exactly. However, those of a system with a *gapless* spectrum are always an approximation in the sense that an MPS induces an effective gap depending on its dimensions. Nevertheless, increasing the dimensions of an MPS increases its correlation length and entanglement entropy following a simple law, the *finite- χ scaling* which becomes particularly useful in combination with *infinite matrix product states* (iMPS).

Section 3.2 presents the concept of a *transfer matrix* applied to an iMPS. A transfer matrix is easily constructed from an iMPS and contains all possible correlations within the wave function. Using a mapping of the complex eigenvalues of the transfer matrix, the correspondence between correlation length and excitation gap is extended to the excitation spectrum in reciprocal space. The transfer matrix spectrum of the anisotropic XY-Heisenberg chain will illustrate this correspondence. An additional comparison to the two-dimensional Kitaev model is given at the time the TM spectrum is employed to study coherent excitations within the Kitaev- Γ model, see chapter 5.

In order to connect to dynamical probes used in experiments, section 3.3 gives an introduction on how to obtain the dynamical structure factors using a *matrix product operator* based time-evolution. Matrix product operators are a natural extension of the concept of matrix product states to operators. Using such a time-evolution allows to efficiently capture long-range exchange interactions occurring when two-dimensional system are studied using MPS.

3.1 Matrix Product States

Generally, an arbitrary wave function can be represented in terms of local degrees of freedom as

$$|\psi\rangle = \sum_{(j_0, j_1, \dots, j_N)} \Psi_{j_0, j_1, \dots, j_N} |j_0\rangle |j_1\rangle \dots |j_N\rangle, \quad (3.1)$$

where

$$|j_0\rangle |j_1\rangle \dots |j_N\rangle = |j_0\rangle \otimes |j_1\rangle \otimes \dots |j_N\rangle \quad (3.2)$$

form a basis of the full Hilbert space \mathcal{H} by direct products of local Hilbert spaces and their basis. Let d denote the dimension of local Hilbert space, then the dimension of the full Hilbert space is d^N . $\Psi_{j_0, j_1, \dots, j_N}$ is a coefficient matrix of the same dimension. Thus, $\Psi_{j_0, j_1, \dots, j_N}$ is growing exponentially with system size and the limits are reached quickly of what can be calculated numerically and stored on a modern computational cluster. This motivates to represent wave functions more efficiently by neglecting *not relevant* degrees of freedom, delaying the discussion of what *not relevant* may mean for now. A renowned approach is to rewrite the coefficient matrix $\Psi_{j_0, j_1, \dots, j_N}$ into a product of matrices, with a single matrix for each local degree of freedom

$$|\psi\rangle = A_0 A_1 A_2 \dots A_N, \quad (3.3)$$

where the A_i are rank-3 tensors, such that

$$[A_{(i)}]_{a_{i-1} a_i} = \sum_{j_i} [A_{(i)}]_{a_{i-1} a_i}^{j_i} |j_i\rangle. \quad (3.4)$$

Here, the matrix products are carried out over the indices a_i that are named auxiliary bonds. Such a state is called a *matrix product state* (MPS). A graphical representation of an MPS is given in figure 3.1. An MPS is not *a priori* an approximation, but becomes one once the dimension of each matrix is limited to the *bond dimension* χ . Now, the dimension reduced to order $\mathcal{O}(N\chi^2)$, but the question remains: *How to decide what 'not relevant' states are?*

To answer this, we will first convert a generic wave function, Eq. (3.1), to an MPS, Eq. (3.3). This is done by a *Schmidt decomposition*, a variant of the singular value decomposition, but in the context of separating Hilbert spaces.

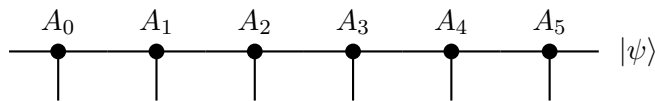


Figure 3.1: Graphical representation of a matrix product state.

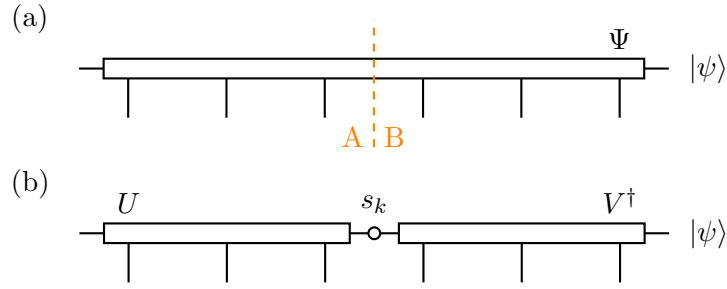


Figure 3.2: Graphical representation of a Schmidt decomposition of \mathcal{H} into two subspaces \mathcal{H}_A and \mathcal{H}_B with Schmidt values s_k .

3.1.1 Schmidt Decomposition

Let us consider a separation of \mathcal{H} into two subspaces \mathcal{H}_A and \mathcal{H}_B with dimension N_A and N_B , and with an orthonormal basis set $\{|j\rangle_A\}$ and $\{|j\rangle_B\}$, then Eq. (3.1) reads

$$|\psi\rangle = \sum_{\substack{1 \leq i \leq N_A \\ 1 \leq j \leq N_B}} \Psi_{i,j} |i\rangle_A \otimes |j\rangle_B . \quad (3.5)$$

Following a singular value decomposition of $\Psi_{i,j}$, we obtain

$$\Psi = USV^\dagger , \quad (3.6)$$

where U and V are unitary matrices of dimension $N_A \times N_A$ or $N_B \times N_B$, † denotes the complex transpose, and S is a rectangular matrix $N_A \times N_B$. The square part of $S_{i,j}$, that is for $i, j \leq \min(N_A, N_B)$, forms a diagonal matrix with *singular values* s_i , which are real and nonnegative. The remainder of S is identical zero. By absorbing U and V^\dagger into the basis $|i\rangle_A \otimes |j\rangle_B$, Eq. (3.5) changes to

$$|\psi\rangle = \sum_{1 \leq k \leq \min(N_A, N_B)} s_k |s_k\rangle_A \otimes |s_k\rangle_B , \quad (3.7)$$

where $|s_k\rangle_A \otimes |s_k\rangle_B$ forms an orthonormal basis called the Schmidt basis. Figure 3.2 provides a graphical representation of a single Schmidt decomposition. In the following, we return to the local basis $|j_0\rangle \cdots |j_N\rangle$. One arrives at the MPS representation through subsequent iteration of the Schmidt decomposition from left to right or vice versa on all local degrees of freedom

$$|\psi\rangle = \Gamma_0 s_0 \Gamma_1 \cdots \Gamma_{N-1} s_{N-1} \Gamma_N \quad (3.8)$$

which is represented graphically in Fig. 3.3. Here, $\Gamma_{(i)}$ is a similar mathematical object as $A_{(i)}$ defined in equation (3.4), and $s_{(i)}$ are real valued vectors of length χ_i containing

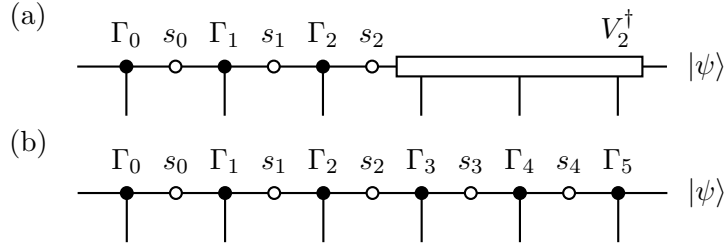


Figure 3.3: Graphical representation of an iterative Schmidt decomposition running over subsequent sites from left to right to obtain an MPS.

the Schmidt values.

Note, that the representation in Eq. (3.8) is linked to previous Eqs. (3.5) and (3.6) when considering a single Schmidt decomposition and obtaining the unitary matrices U and V . Let us consider a decomposition at site k , then

$$U_k = \Gamma_0 s_0 \Gamma_1 \cdots s_{k-1} \Gamma_k, \quad (3.9)$$

and

$$(V_k)^\dagger = \Gamma_{k+1} s_{k+1} \Gamma_{k+2} \cdots s_{N-1} \Gamma_N. \quad (3.10)$$

The fact that U_k and V_k are unitary implies that an MPS is left- and right-normalised, which reads as follows

$$U_k U_k^\dagger = \mathbb{1} \quad V_k^\dagger V_k = \mathbb{1}, \quad (3.11)$$

where $\mathbb{1}$ denotes the identity matrix.

Now we can return to the question about what *'not relevant'* states are and how to choose a suitable approximation of a general wave function. Generally, the Schmidt values (or singular values) are non-negative real numbers. If a Schmidt value is large, this state of the Schmidt basis has large weight in the wave function, whereas a small Schmidt value implies that the corresponding state has a low weight and is less relevant. If a Schmidt value is zero, it does not contribute at all and can be neglected in any case. Thence, the Schmidt values provide a criteria to truncate an MPS, i.e., by saying that all Schmidt states with its Schmidt values being below a certain threshold are neglected. For practical purposes, one also provides an upper threshold for the bond dimension. Then the Schmidt values of the truncated states give a first estimate of the accuracy of the MPS.

When discussing the Schmidt values and their distribution, one has to differ between the possible physical origin of the wave function. Having a ground state wave function of a system with a gapped spectrum, then the Schmidt values decay quickly with at most an exponential scaling. Whereas for a system with gapless spectrum, its ground

state wave function exhibits a distribution of Schmidt values decaying algebraically, that is following a power law. In the first case, an MPS representation with sufficiently large bond dimension is generally a good approximation of the exact wave function. For some theoretical models, like the Affleck-Kennedy-Lieb-Tasaki model [88], exact low-dimensional MPS representations of the ground state exist, not counting those models, that exhibit a simple product state as a ground state, e.g., the Ising model.

For gapless systems, however, the MPS representation is always an approximation. Long range correlations of an MPS always decay exponentially similar to how correlations decay in a gapped ground state. The MPS representation induces a gap due to truncating. Upon increasing its bond dimension, the accuracy of the MPS improves and the length enhances over which correlations are represented correctly. The correlation length increases accordingly enabling a scaling approach for gapless ground states, which is discussed in section 3.1.3.

In order to investigate gapless systems, one needs a way of approaching system sizes in the thermodynamic limit. Infinite matrix product states (iMPS) provide an elegant way to achieve this. They will be introduced now.

3.1.2 Infinite Matrix Product States

The concept of matrix product states can be extended to infinite boundary conditions in a natural way by exploiting translational invariance and using left- and right-normalisation.

Without loss of generality, let us assume a two-site unit cell. Then, the *infinite* sequence of matrix products

$$\cdots \Gamma_{i-1s_{i-1}} \Gamma_{is_i} \Gamma_{i+1s_{i+1}} \Gamma_{i+2s_{i+2}} \cdots$$

becomes a periodic sequence

$$\cdots \Gamma_{B^s B} \Gamma_{A^s A} \Gamma_{B^s B} \Gamma_{A^s A} \cdots$$

corresponding to sublattices A and B . The part before and after the unit cell are contracted to a left and a right *environment*. Physically one is interested in computing overlaps $\langle \psi | \hat{O} | \psi \rangle$, where \hat{O} can be any *local* operator. An operator is considered to be local if its support is finite, e.g., if only nearest neighbor term are present. Then, when computing an overlap, parts left and right of the support simplify to unity and only at the support a contraction of the tensor network is needed.

The assumption of translational invariance allows to construct a *transfer matrix*, that inherits all possible correlations. This transfer matrix will be introduced in detail in section 3.2.

3.1.3 Entanglement

Returning to a single bipartition of the Hilbert space into two subsystems A and B , the Schmidt decomposition, Eq. (3.7), allows an efficient computation of the *entanglement entropy* S_E .

Let $\rho = |\psi\rangle\langle\psi|$ be the density matrix of the full system and ρ_A or ρ_B may denote the reduced density matrices obtained by a partial trace

$$\rho_A = \text{Tr}_B |\psi\rangle\langle\psi| \quad \rho_B = \text{Tr}_A |\psi\rangle\langle\psi| . \quad (3.12)$$

Here, Tr_A denotes the partial trace over subsystem A . Then, the entanglement entropy S_E is defined as the *von-Neumann* entropy of the reduced density matrix

$$S_E = \text{Tr} \rho_A \log \rho_A = \text{Tr} \rho_B \log \rho_B . \quad (3.13)$$

In an MPS, this bipartition is done by construction. Using Eq. (3.7) and taking the partial trace over B , the reduced density matrix gets

$$\rho_A = \sum_k s_k^2 |s_k\rangle_A \langle s_k| . \quad (3.14)$$

Through combining Eqs. (3.13) and (3.14), the entanglement entropy can be simply read off a given MPS as

$$S_E = \sum_k s_k^2 \log s_k^2 , \quad (3.15)$$

where s_k are the Schmidt values related to the bond cut by the bipartitioning.

Area Law of Entanglement

The physical reason of why the MPS representation turns out to be very beneficial when studying ground states of many-body systems lies in the *area-law* scaling of entanglement. For a review see [89].

The area law states that the entanglement entropy of a bipartition of the full Hilbert space \mathcal{H} into two distinct subspaces A and B , such that $\mathcal{H} = \mathcal{H}_A \otimes \mathcal{H}_B$, grows with the area of the boundary L as

$$S_E = \alpha L - \gamma + \dots , \quad (3.16)$$

where α is a non-universal constant and γ is a correction occurring in topological ordered systems as will be discussed separately in the next subsection. This scaling is strictly true for ground states of gapped systems with local Hamiltonians. Otherwise, e.g., for critical systems, corrections of order $\log N$ occur [90], where N is the system size.

To put emphasize on how peculiar such an area law is, let us consider an arbitrary

state at an energy sufficiently above the ground state. The entanglement of such a state would generally scale with the volume of the systems, $S_E \propto V$. Thus, ground state wave functions are located in a tiny subset of the full Hilbert space, a subset that satisfies an area law of entanglement. It is this dimensional reduction, which makes the concept of MPS and DMRG so successful, since, by construction, an MPS representation restricts to this subset of area-law states.

Topological Entanglement Entropy

As already hinted at, the area law possesses a correction, if the system exhibits topological order [20, 72]. Topological order is a zero-temperature phase of matter that cannot be classified by a Landau order parameter. It manifest itself in a ground state degeneracy depending on the genus of the surface and hosts anyonic excitations. One of the models in this context is the Kitaev model, which exhibits two different topologically ordered phases. One of them occurs, when a magnetic field is applied and will be discussed in detail in chapter 6.

The correction γ in equation (3.16) is referred to as the *topological entanglement entropy* (TEE) [74, 75]. If it is non-zero, the TEE signals a topologically ordered phase. The TEE is connected to the total quantum dimension

$$\mathcal{D} = \log \sqrt{\sum_a d_a^2}, \quad (3.17)$$

where the sum runs over all the superselection sectors, the (almost) degenerate ground state, which are associated with quasiparticles. d_a denotes the quantum dimension of each quasiparticle. The quantum dimension of abelian anyons is $d_a = 1$, whereas for non-abelian anyons d_a is generally larger than one [71]. As a consequence, γ depends on the quasiparticle sector [74]

$$\gamma_a = \log \frac{\mathcal{D}}{d_a}, \quad (3.18)$$

if the bipartition is along a non-contractable loop [91].

One approach of extracting the TEE is, to do a finite size scaling of the entanglement entropy [92]. E.g., if a cylindrical geometry is used, the circumference L_{circ} can be varied resulting in a L_{circ} -dependent $S_E(L_{\text{circ}})$. Upon utilizing linear regression, γ is obtained by identifying it with the offset.

Finite-Entanglement Scaling

An MPS cannot capture algebraic correlations typical for a ground state wave function of systems with gapless spectrum, or critical systems, respectively. However, increasing the bond dimension gives an increasingly accurate approximation of the wave func-

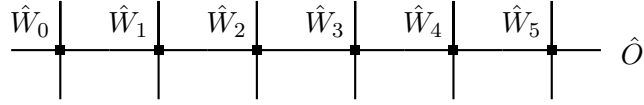


Figure 3.4: Graphical representation of a matrix product operator.

tion. Calabrese and Cardy [90] have shown that the entanglement entropy S_E scales logarithmically with the correlation length ξ . In the MPS formalism, this is known as *Finite-Entanglement Scaling* providing a scaling law of the entanglement entropy S_E and the correlation length ξ as

$$S_{E,\chi} = \frac{c}{6} \log \xi_\chi + \text{const.} , \quad (3.19)$$

where χ is the bond dimension of the MPS and c is the *chiral central charge* [93, 94]. Thus, by varying χ and measuring S_E and ξ the central charge, a universal property of a critical or gapless system, can be obtained even though the MPS itself remains an approximation to the ground state (as long as χ is finite).

3.1.4 Matrix Product Operators

Before the DMRG algorithm can be explained, an efficient description for the Hamiltonian is needed. However, the following description does not just apply to a Hamiltonian, but to any (sufficiently local) operator, e.g., for the unitary time evolution discussed later. Given an operator \hat{O} , it can be brought in a product of matrices with a matrix for each local degree of freedom similar to an MPS

$$\hat{O} = \prod_{i=1}^N \hat{W}_i . \quad (3.20)$$

where \hat{W}_i is the operator acting on the local Hilbert space spanned by $\{|p_i\rangle\}$ at site i :

$$[\hat{W}_{(i)}]_{a_{i-1}, a_i} = \sum_{p_i, p'_i} [W_{(i)}]_{a_{i-1}, a_i}^{p_i, p'_i} |p_i\rangle \langle p'_i| . \quad (3.21)$$

Here, a_i denote the auxiliary bonds over which the matrix product in (3.20) is carried out, and p_i are the physical bonds connecting to the local, physical degrees of freedom. Any operator can be rewritten in MPO form by using a variant of the Schmidt decomposition described in section 3.1.

Let us turn to the structure of an Hamiltonian, which shall be composed as sum of local operators. Then the Hamiltonian can be decomposed at an arbitrary bond $(i, i+1)$ into a part $\hat{H}_{i,L}$ that purely acts on sites left of of the bond, a part $\hat{H}_{i,R}$ acting

only on sites right of the bond, and an interacting part $h_{L_i} \otimes h_{R_i}$

$$H = H_{L_i} \otimes \mathbb{1}_{R_i} + \mathbb{1}_{L_i} \otimes H_{R_i} + \sum_{a_i=1}^N h_{L_i, a_i} \otimes h_{R_i, a_i}, \quad (3.22)$$

where the sum runs over all N_i interactions a_i crossing that bond. The decomposition of a Hamiltonian into MPO form can be conveniently recast into a recursion relation

$$\begin{pmatrix} H_{R_{i-1}} \\ h_{R_{i-1}, a_{i-1}} \\ \mathbb{1}_{R_{i-1}} \end{pmatrix} = \begin{pmatrix} \hat{\mathbb{1}} & \hat{C} & \hat{D} \\ 0 & \hat{A} & \hat{B} \\ 0 & 0 & \hat{\mathbb{1}} \end{pmatrix}_{(i)} \otimes \begin{pmatrix} H_{R_i} \\ h_{R_i, a_i} \\ \mathbb{1}_{R_i} \end{pmatrix}, \quad (3.23)$$

revealing the structure of the local \hat{W}_i of a Hamiltonian. Here, the operators $\hat{A}_{(i)}$, $\hat{B}_{(i)}$, $\hat{C}_{(i)}$, $\hat{D}_{(i)}$, and the identity $\hat{\mathbb{1}}$ act on the local degrees of freedom at site i . The identity $\hat{\mathbb{1}}$ and the on-site operator \hat{D} are of dimension $(1, 1, d, d)$, where d is the dimension of the local Hilbert space. $\hat{A}_{(i)}$ is of dimension (N_{i-1}, N_i, d, d) . $\hat{C}_{(i)}$ and $\hat{B}_{(i)}$ are of dimension $(1, N_i, d, d)$ and $(N_{i-1}, 1, d, d)$, respectively.

In order to illustrate the function of each of these operators, let us assume a two-site interaction $S_i^x S_{i+n}^x$. Then $\hat{C}_{(i)}$ contains S^x , the operators $\hat{A}_{(i+1)}, \dots, \hat{A}_{(i+n-1)}$ contain an identity operator carrying S_i^x over to the matrix at site $i+n$, where $\hat{B}_{(i+n)}$ contains the second S^x . Thus, upon conducting the matrix product, a term

$$S_i^x \otimes \mathbb{1}_{i+1} \otimes \dots \otimes \mathbb{1}_{i+n-1} \otimes S_{i+n}^x \quad (3.24)$$

adds to the Hamiltonian.

As a remark, the Hamiltonian and also the time-evolution operator, to be discussed later in section 3.3, have an illustrative representation as a finite state machine [95, 96].

3.1.5 Density Matrix Renormalisation Group

Density matrix renormalisation group (DMRG) is an iterative, variational method to optimise the wave function with respect to the energy. Within the MPS framework, DMRG sweeps through the matrices of an MPS and updates them by an optimised one. Here, the modern DMRG description based on the MPS framework is presented. Furthermore, only the basic ideas are provided, more technical details can be found in extensive reviews, e.g., by Schollwöck [97, 98], and in numerous freely available lecture notes.

The goal is to find the ground state and its energy of an Hamiltonian, that is one wants to solve the static Schrödinger equation

$$H|\psi\rangle = E|\psi\rangle \quad (3.25)$$

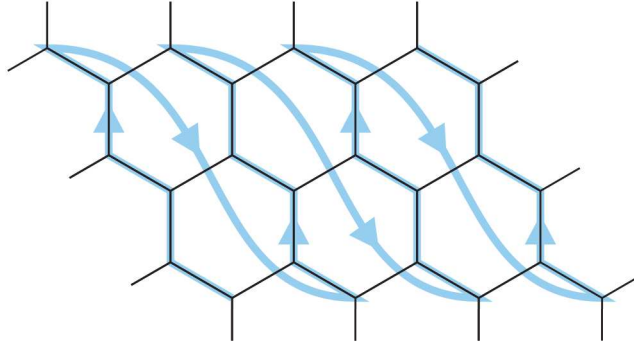


Figure 3.5: Illustration of winding the one-dimensional MPS structure around a cylinder. This allows for mapping cylindrical geometries to a chain, but at the cost of introducing longer ranged interactions.

for the lowest eigenvalue and related eigenvector. This is usually a hard problem due to the exponential scaling of the Hilbert space the eigenvector belongs to. Using MPS, this Hilbert space is reduced drastically and additionally a reduced, local eigenvalue problem will be solved instead. The DMRG update contains the following steps.

1. Make an initial guess for $|\psi\rangle$ represented as an MPS.
2. Sweep from left to right performing DMRG updates on each site (*two-site update*):
 - (a) Combine two sides together: $\Theta_i = \Gamma_i s_i \Gamma_{i+1}$
 - (b) Solve the (local) eigenvalue problem: $H\Theta'_i = E\Theta'_i$ keeping all other matrices constant. Here, an eigensolver that only provides the lowest eigenvalue and its vector is sufficient, e.g., Lanczos method.
 - (c) Perform a Schmidt decomposition: $\Theta' \rightarrow \Gamma'_i s'_i \Gamma'_{i+1}$
 - (d) Move to the next side: $i \rightarrow i + 1$
3. Sweep from right to left performing similar DMRG updates as above.
4. Repeat left- and right sweeps until convergence.

Other DMRG variants exist, where the two-site update has been exchanged for one-site update or multiple-site updates. The former has the advantage of reducing the dimensions of the local eigenvalue problem, but may be more likely to get stuck in local minima. In contrast, the multiple-site update reduces the likelihood of being stuck in a local minimum and needs generally less DMRG sweeps at an increased cost per DMRG update.

3.1.6 Extension to Two-Dimensional Lattices

An MPS has a linear structure naturally suitable for one-dimensional systems. In this thesis, the MPS framework is applied to two-dimensional systems, even though two-dimensional generalisations like *Projected Entangled Pair States* [99] have been developed. However, MPS provide a well controlled framework.

We utilize the MPS structure for two-dimensional systems by wrapping the lattice on a cylinder and winding a chain around the cylinder. See figure 3.5 for an illustration. The two-dimensional system is effectively reduced to a one-dimensional one and MPS based methods can be used. This happens at the cost of introducing long-ranged interaction, which consequently limit the circumference of the cylinder that can be reached as the necessary bond dimension grows exponentially with the circumference. The latter follows from the linear growth of the entanglement entropy S_E with the circumference, cf. Sec. 3.1.3, and the bond dimension χ needed to encode a state with entropy S_E increases exponentially, such that

$$\chi \propto e^{S_E} \propto e^{L_{\text{circ}}} . \quad (3.26)$$

Nonetheless, circumferences of the order of ten sites may be reached even in highly entangled states of, e.g., quantum spin liquid phases.

By using the infinite variant iMPS, the dimension along the cylinder axis is in the thermodynamic limit, whereas the second dimension along the circumference is finite. Due to the latter, the momentum is discretized along one reciprocal lattice vector and continuous along the second. Thence, the accessible momenta are placed along lines in reciprocal space. Specific details about the cylinder geometries, their unit-cell and their lines of allowed momenta are given in the corresponding chapter.

3.2 Transfer Matrix Spectrum

The transfer matrix (TM) of a wave function encoded as an infinite matrix product state (iMPS) contains full information about the static correlations [100]. Intuitively, the TM translates the iMPS by a lattice vector along the chain or the cylinder in two dimensions. For Hamiltonians with only local interactions, the static correlations are related to the spectral gap [101], e.g. $\xi \sim 1/\Delta$ for $z = 1$. This statement has been extended by Zauner et al. [100] to also include momentum, such that the length scale of the decay of static correlations with a momentum \mathbf{k} gives an upper bound on the spectral gap $\epsilon(\tilde{\mathbf{k}})$ at a momentum $\tilde{\mathbf{k}}$ in the vicinity of \mathbf{k} . Hence, the TM spectrum, a ground state property, provides information about the position of the minimal energy excitation within the reciprocal space. A connection between the TM eigenvalues and the exact excitation energies can only be made knowing the Lieb-Robinson velocity

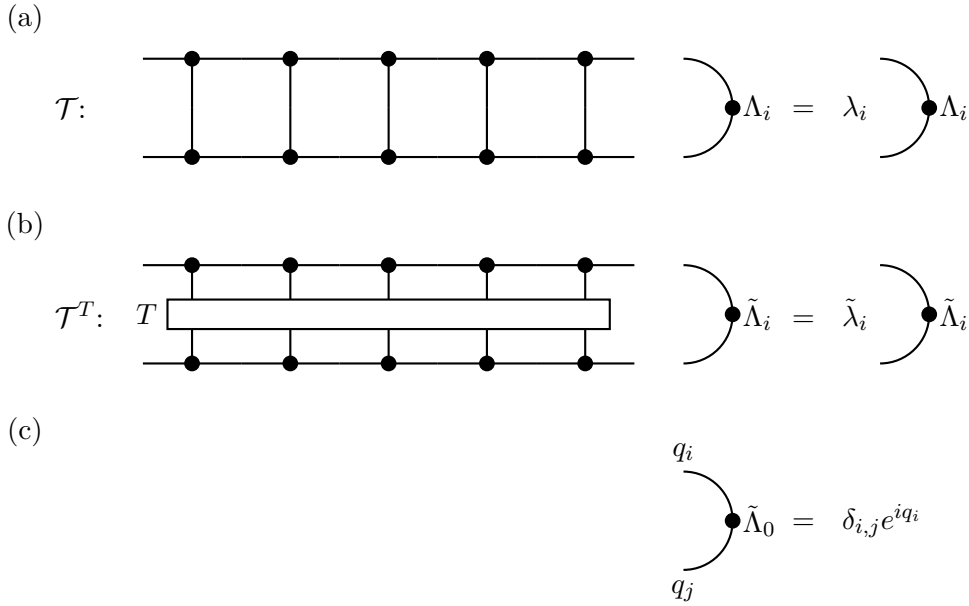


Figure 3.6: Schematic representation of (a) the regular and (b) the mixed transfer matrix \mathcal{T} with translation T applied along the circumference. (c) Dominant eigenvector $\tilde{\Lambda}_0$ of \mathcal{T}^T determines the q quantum numbers associated with each bond leg.

[102], e.g., from dynamics. If the Lieb-Robinson velocity is not known, the quasi-energies $E_i = -\log \lambda_i$, where λ_i are the eigenvalues of the TM, are *only* given up to an overall energy scale of the Hamiltonian.

On the cylinder geometry and if the symmetry upon translation along the cylinder's circumference is not broken, the transverse momentum k_y is a good quantum number. Then, for each k_y independently a set of λ_i exists with a longitudinal momentum $k_x = \arg \lambda_i$ corresponding to the momentum of minimal energy excitation.

The interested reader will find a rigorous and detailed explanation as well as more examples in Zauner et al. [100]. Here, the emphasis lies on the technical implementation in the context of iMPS and particularly in the context of two-dimensional models. One examples, the anisotropic XY-Heisenberg chain, is provided to illustrate the correspondence between TM spectrum and the excitation spectrum. The TM spectrum of the exactly solvable Kitaev model on a honeycomb lattice is provided and discussed in chapter 5.

3.2.1 Implementation

We turn now to the technical realization of obtaining the momentum resolved TM spectrum. Let λ_i be the eigenvalues of the transfer matrix with the ordering $|\lambda_0| > |\lambda_1| \geq |\lambda_2| \geq \dots$. By definition the dominant eigenvalue is $|\lambda_0| = 1$. Generally, λ_i

are complex and can be decomposed as $\lambda_i = |\lambda_i|e^{i\eta}$. The angle η is connected to the momentum k_x along the chain or cylinder. Exploiting the rotational invariance of the Hamiltonian on the cylinder geometry yields the transverse momentum k_y as will be explained now. In the following, the iMPS shall be in *canonical form*[103]. A translation with a lattice vector along the circumference keeps the Hamiltonian invariant and as such k_y can be treated as a regular quantum number. We extract k_y by computing the dominant eigenvector $\tilde{\Lambda}_0$ of the *mixed* transfer matrix constructed out of the ground state iMPS and a iMPS with the translation applied, see also Fig. 3.6(b). We like to remark, that the translation along the circumference is simply given by a permutation of sites within a ring. If the iMPS is sufficiently converged and the applied translation is indeed a symmetry, then the dominant eigenvalue $\tilde{\lambda}_0$ of the *mixed* TM equals unity. Its eigenvector $\tilde{\Lambda}_0$ has a diagonal form with eigenvalues $|\tilde{\lambda}_i|e^{iq}$ and q being discretized in steps $2\pi/n$, where n is the number of unit cells around the cylinder. If Schmidt values are degenerate, the diagonal form becomes block diagonal with blocks for each set of degenerate Schmidt values. Each block can be diagonalized separately by a unitary transformation which is then applied to the non-translated iMPS. The momentum quantum number q_i are associated with the entries i along a bond leg in the same way as Schmidt values are. The TM connects states i and j with corresponding q_i and q_j , hence the transverse momentum is given by $k_{y,(i,j)} = q_j - q_i$. The k_y label of λ_i can be read off from its eigenvector Λ_i due to the fact, that Λ_i has only non-zero entries with the same change of the quantum number $q_i - q_j$.

3.2.2 Example: Anisotropic XY-Heisenberg Chain

In Fig. 3.7 we illustrate an exemplary TM spectrum for the anisotropic XY-Heisenberg chain with transverse field h and anisotropy γ :

$$H = -J \sum_i [(1 + \gamma)S_i^x S_{i+1}^x + (1 - \gamma)S_i^y S_{i+1}^y + hS_i^z] , \quad (3.27)$$

This model can be solved exactly [104–108] and its energy spectrum is known [108]. The plot compares the TM spectrum $E_i(k_i) = -\log \lambda_i$ (blue dots) with the analytical single- and multi-particle excitations (lines) for a choice of parameter, where the spectrum is gapped. The position $k_i = \arg(\lambda_i)$ of the minimal eigenvalues E_i coincide nicely with the minimum in the excitation bands with an even number of particles. Single particle excitations are not present in the *regular* TM of the anisotropic XY chain [100]. In comparison to the dynamical spin-structure factor discussed later, cf. Sec. 3.3.3, we observe that the TM spectrum includes also four and more particle excitations as long as an even number is excited. This can be explained by noting, that the TM is not defined with respect a specific operator. The eigenvalues of the TM spectrum correspond to *any* correlation, that is sufficiently relevant to be captured in the ground state MPS.

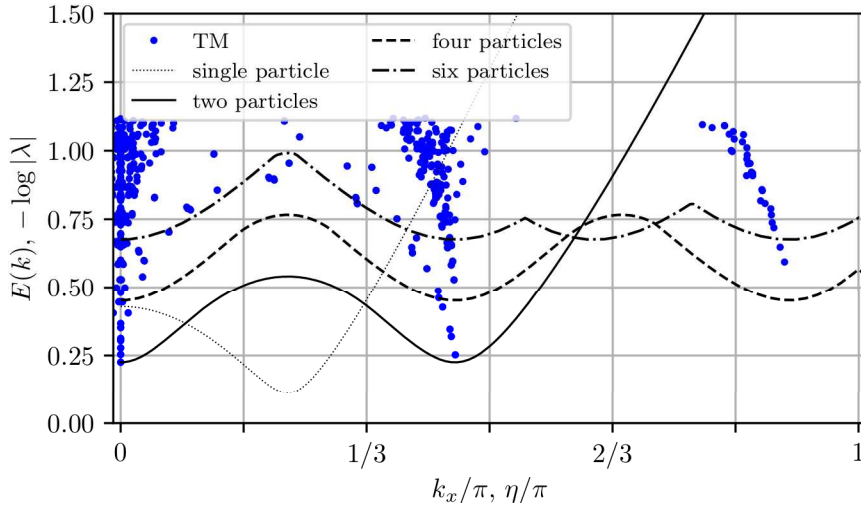


Figure 3.7: Quasi-energies $E(k) = -\log |\lambda_i|$ of the regular transfer matrix spectrum λ_i compared to analytical excitation energies for single- (thin dotted), two- (solid), four- (dashed), and six-particle excitations (dash-dotted) of the anisotropic XY-Heisenberg chain with transverse field. The parameters are: $\gamma = 0.1$, $h = 0.75$. The analytical results are scaled by a factor $a = 1.73$ in order to match the $\min(E_i)$ with $\min(E_{2p}(k))$, where $E_{2p}(k)$ is the lower edge of the two-particle excitation band.

3.3 Matrix Product Operator Based Time-Evolution

Dynamical probes provide insights into frustrated systems exhibiting spin liquid behaviour. The symmetry of a quantum spin liquid ground state may not be distinguishable from a paramagnet, yet its dynamics can be surprisingly rich including fractionalisation or emergent gauge fields. This motivates to study its dynamics.

3.3.1 Protocol for Time-Evolution

We are interested in the dynamical spin-structure factor $\mathcal{S}(\mathbf{k}, \omega)$ in particular, as introduced in Sec. 2.3.7. Here, the diagonal $\mathcal{S}(\mathbf{k}, \omega) = \sum_{\gamma=\{x,y,z\}} \mathcal{S}^{\gamma\gamma}(\mathbf{k}, \omega)$ is considered, where $\mathcal{S}^{\gamma\gamma}(\mathbf{k}, \omega)$ is the spatio-temporal Fourier transform of the dynamical correlations $C_{ab}^{\gamma\gamma}(t)$

$$\mathcal{S}^{\gamma\gamma}(\mathbf{k}, \omega) = N \int dt e^{i\omega t} \sum_{a,b} e^{i(\mathbf{r}_b - \mathbf{r}_a) \cdot \mathbf{k}} C_{ab}^{\gamma\gamma}(t), \quad (3.28)$$

where $\gamma = \{x, y, z\}$ is the spin component, r_a and r_b are the spatial positions of the spins, and diagonal elements \mathcal{S}^{xx} , \mathcal{S}^{yy} , and \mathcal{S}^{zz} are considered. N is determined by normalizing $\mathcal{S}^{\gamma\gamma}(\mathbf{k}, \omega)$ as $\int d\omega \int d\mathbf{k} \mathcal{S}^{\gamma\gamma}(\mathbf{k}, \omega) = \int d\mathbf{k}$.

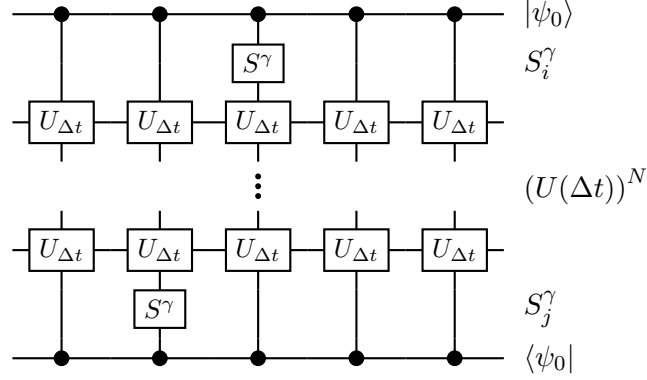


Figure 3.8: Graphical representation of $\langle\psi_0|S_j^\gamma U(t) S_i^\gamma|\psi_0\rangle$ using the tMPO scheme. $U(t)$ is discretized in time and constructed in matrix product operator form.

The dynamical spin-spin correlation $C_{ab}^{\gamma\gamma}(t)$ reads

$$\begin{aligned} C_{ab}^{\gamma\gamma}(t) &= \langle\psi_0|S_a^\gamma(t)S_b^\gamma(0)|\psi_0\rangle \\ &= \langle\psi_0|U(-t)S_a^\gamma U(t)S_b^\gamma|\psi_0\rangle \\ &= \langle\psi_0|S_a^\gamma U(t)S_b^\gamma|\psi_0\rangle, \end{aligned} \quad (3.29)$$

where the unitary time-evolution operator $U(t) = e^{-i(H-E_0)t}$ is modified by subtracting the ground state energy E_0 . Thus, the time-evolution $U(-t)$ acts trivially on the ground state $\langle\psi_0|U(-t) = \langle\psi_0|$.

Equation (3.29) provides a numerical protocol: (i) Obtain the ground state wave function $|\psi_0\rangle$ encoded as iMPS using DMRG and enlarge the iMPS unit cell along the cylindrical axis to make room for the excitation to spread spatially, (ii) apply spin operator S_i^γ at site i , (iii) time-evolve the MPS by $U(t)$, (iv) apply S_j^γ at j , and (v) compute the overlap. For an illustration of the protocol see Fig. 3.8.

The crucial part is to perform the real-time evolution. As we intend to study two-dimensional systems, which by mapping them back to chain introduce couplings beyond nearest neighbor, standard methods like *time-evolving block decimation* are inefficient if even applicable at all. Instead, Zaletel et al. [96] developed a method by representing the time-evolution operator $U(t)$ as a matrix product operators (MPO).

3.3.2 Represent the Time-Evolution Operator as MPO

To implement the numerical protocol, Fig. 3.8, an efficient time-evolution is needed. Zaletel et al. [96] introduce an MPO representation of the time-evolution operator

$$U(t) = e^{tH}, \quad (3.30)$$

assuming that a Hamiltonian H written in a compact MPO form, Eq. (3.23), is given. Let $H = \sum_i H_i$ be a sum of local terms, then Eq. (3.30) can be rewritten in a series expansion

$$U(t) = 1 + t \sum_i H_i + \frac{t^2}{2} \sum_{i,j} H_i H_j + \frac{t^3}{6} \sum_{i,j,k} H_i H_j H_k + \mathcal{O}(t^4) . \quad (3.31)$$

In order to proceed from here, approximations are necessary.

For a first MPO representation of Eq. (3.30), any product containing two or more overlapping H_i, H_j will be neglected. Then, Eq. (3.31) gets

$$U^I(t) = 1 + t \sum_i H_i + t^2 \sum_{i < j} H_i H_j + t^3 \sum_{i < j < k} H_i H_j H_k + \dots . \quad (3.32)$$

This is an approximation affecting the second and higher order terms, thus leading to an error of $\mathcal{O}(t^2)$. Note, that prefactors of $1/2$ or $1/6$ are absent due to a different counting of the terms. $U^I(t)$ allows for an exact MPO representation

$$\hat{W}_{(i)}^I(t) = \begin{pmatrix} \hat{1} + t\sqrt{\hat{D}} & \sqrt{t}\hat{C} \\ \sqrt{t}\hat{B} & \hat{A} \end{pmatrix}_{(i)} , \quad (3.33)$$

where $\hat{A}, \hat{B}, \hat{C}$, and \hat{D} are known from the MPO representation of the Hamiltonian, cf. Eq. 3.23. From the dimensions of those local operators, one obtains a bond dimension of $\chi = 1 + N_i$ for $\hat{W}_{(i)}^I$, which is reduced by one compared to the MPO representation of the Hamiltonian.

One can improve the approximation (3.32), by additionally considering terms which overlap by a single site. Then, the time-evolution operator reads

$$U^{II}(t) = 1 + t \sum_i H_i + \frac{t^2}{2} \sum_{\langle ij \rangle} H_i H_j + \frac{t^3}{6} \sum_{\langle ijk \rangle} H_i H_j H_k + \dots . \quad (3.34)$$

Here, $\langle ij \rangle$ denote such pairs of local terms H_i, H_j , that do not overlap at all or at a single site. Still, the approximation enters in the second and higher order terms and the error is of order $\mathcal{O}(t^2)$ per site, or $\mathcal{O}(Lt^2)$ in total. However, on-site terms are now captured correctly to all orders. Casting (3.34) into MPO form, needs further approximations, but of lower order $\mathcal{O}(Lt^3)$, and are thus not relevant. How to obtain \hat{W}^{II} is more complicated and is thus not captured here, but the reader finds more details in Ref. [96]. Applying $\hat{W}^{I/II}$ to a wave function encoded as MPS increases the bond dimension of the MPS to $\chi'_{\text{MPS},i} = \chi_{\text{MPO},i} \cdot \chi_{\text{MPS},i}$. To keep the time-evolved MPS compact, it has to be truncated after each time-steps either by Schmidt decomposition, or by variational methods [98].

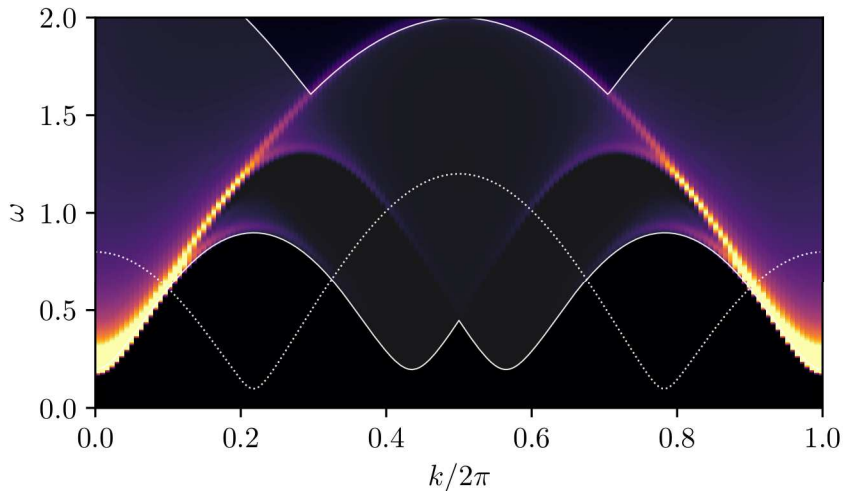


Figure 3.9: Dynamical spin-structure factor $\mathcal{S}^{yy}(k, \omega)$ for the anisotropic XY-Heisenberg chain with transverse field. The same parameter as for Fig. 3.7 are used: $\gamma = 0.1$, $h = 0.75$. Analytical results are added for the single particle excitations (dotted lines) and the two particle continuum (solid lines with white shading in between). Bright areas highlight large intensity.

A higher order approximation, let us say with errors of order $\mathcal{O}(Lt^p)$, can be obtained by a subsequent application of $W^{I/II}(t_i)$ with a particular sequence of times t_1, t_2, \dots, t_n , that is

$$W(t_1)W(t_2) \cdots W(t_n) = U(t) + \mathcal{O}(Lt^p) . \quad (3.35)$$

Comparing order by order of (3.35) up to the desired accuracy gives constraints on the time sequence. Ref. [96] provides a sequence for a second-order time stepper

$$W(t_1)W(t_2) = U(t) + \mathcal{O}(Lt^3) , \quad (3.36)$$

with two steps and times $t_1 = (1 + i)t/2$ and $t_2 = (1 - i)t/2$. As with any numerical time-integration method, improving to order of the error or the accuracy requires to increase the number steps in a sequence. In particular, going to order $\mathcal{O}(Lt^4)$ needs four steps, $\mathcal{O}(Lt^5)$ requires seven steps, etc \dots . To keep the MPS representation of the time-evolved wave function compact, it would be preferable to apply the truncation after each step. However, the truncation error imposed on the multi-step schemes is not included in the above method and may be checked separately.

3.3.3 Example: Anisotropic XY-Heisenberg Chain

As done for the transfer matrix spectra, cf. Sec. 3.2.2, an example is provided, which is based on the anisotropic XY-Heisenberg chain with transverse field

$$H = -J \sum_i [(1 + \gamma)S_i^x S_{i+1}^x + (1 - \gamma)S_i^y S_{i+1}^y + hS_i^z] . \quad (3.37)$$

In Fig. 3.9 the dynamical spin-structure factor $\mathcal{S}^{yy}(k, \omega)$ is presented using a set of parameters within the ferromagnetic phase (with ferromagnetic order along the x component). Applying an S^y operator flips a spin and creates two domain walls. Consequently, there is no spectral weight for a single quasiparticle (single domain wall). The energy induced by the spin-flip splits across the two domain walls and forms a continuum. The continuum reaches from the minimum of the sum of two single-particle bands $\varepsilon_2(k) = \min_{k=k_1+k_2}(\varepsilon_1(k_1) + \varepsilon_1(k_2))$ to the corresponding maximum. In the present model, a single spin flip does not induce more than two domain walls and multi-particle excitations beyond two particles are not captured by $\mathcal{S}^{yy}(k, \omega)$. This is to be seen in contrast to the transfer matrix spectrum, which does contain also multi-particle excitation beyond two quasi particles.

Chapter 4

Kitaev-Heisenberg Model

4.1 Introduction

The Kitaev-Heisenberg model has been introduced and discussed as a minimal model for several materials including Na_2IrO_3 , Li_2IrO_3 [85], and $\alpha\text{-RuCl}_3$ [109]. The pure Kitaev model is an exactly solvable spin-1/2 model harbouring quantum spin liquid ground states with anyonic excitations. The Heisenberg term, here only between nearest neighbors, can be thought of as being the simplest extension of the Kitaev model relevant to real materials. Questions about the stability of the quantum spin liquid phase arise, as well as possible experimental signatures within or when being proximate to it. First numerical studies of the ground state phase diagram of the Kitaev-Heisenberg model have shown an extended quantum spin liquid phase for small J and four symmetry broken phases for larger J [85].

The dynamical response functions of the pure Kitaev model are known exactly and reveal characteristic features [22, 110], such as a spectral gap in the dynamical spin structure factor due to a spin flip creating a gapless Majorana and also a gapped flux-pair excitation. This feature is perturbatively stable to small J [111], but the influence of J on high-energy features or, non-perturbatively at low energies, is unclear and of ongoing interest [112]. Furthermore, the possibility of high-energy features signifying to be proximate to a spin liquid is of recent interest [113, 114], such as for the currently much-studied $\alpha\text{-RuCl}_3$ [28, 109, 114–122], whose low-energy physics is consistent with spin waves on an ordered background, but whose broad high-energy features resemble those of the Kitaev quantum spin liquid (KSL). In particular, for intermediate energy scales there are star-like features [28] apparently arising from a combination of spin wave and quantum spin liquid (QSL) physics.

Here, a combination of the infinite density-matrix renormalization group method for obtaining the ground state and a matrix-product operator based time-evolution will be utilized as introduced in chapter 3. The latter enables to extract dynamical

response functions for generic two-dimensional spin systems in a non-perturbative way. With this, dynamics of exotic phases can be accessed that can occur in frustrated systems. Moreover, it is also very useful for regular ordered phases where one would conventionally use large- S approximations, which in some cases cannot qualitatively explain certain high energy features [28, 123].

This chapter is divided into the following sections. First, the ground state phase diagram is revisited and previously found phases are confirmed. The infinite cylinder geometry allows to numerically confirm that the gaplessness of the KSL remains throughout the entire phase when a small Heisenberg perturbation is applied. Secondly, the matrix product operator based time evolution algorithm [96] is utilized to obtain the dynamical spin-structure factor of different (non-soluble) phases of the Kitaev-Heisenberg model. Most notably, broad high energy continua are observed even in the ordered phases, which are moreover similar to the high energy features in the nearby spin liquid phase. This provides a concrete realisation of the concept of a proximate spin liquid, which was recently invoked in the context of neutron scattering experiments on α -RuCl₃.

4.2 Ground State Phase Diagram

The Hamiltonian of the *Kitaev-Heisenberg model* (KHM), as a part of Eq. (2.46), reads

$$H = \sum_{\langle i,j \rangle_\gamma} 2K_\gamma S_i^\gamma S_j^\gamma + J \sum_{\langle i,j \rangle} \mathbf{S}_i \cdot \mathbf{S}_j . \quad (4.1)$$

The first term is the pure Kitaev model exhibiting strongly anisotropic spin-exchange coupling [16]. Neighboring spins couple depending on the direction of their bond γ with $S^x S^x$, $S^y S^y$ or $S^z S^z$ (Fig. 4.1). This strongly anisotropic coupling leads to exchange frustration and harbours a quantum spin liquid ground state. See section 2.3 for more details. The second term in Eq. (4.1) is the $SU(2)$ -symmetric Heisenberg term. Here, the coupling J and K are varied using a trigonometric parametrization $J = \cos \alpha$ and $K = \sin \alpha$ with isotropic $K_\gamma = K$. For $\alpha = \pm \frac{\pi}{2}$, the pure Kitaev model in the gapless phase (B-phase) is recovered, which is stable under time-reversal symmetric perturbations [16].

The phase diagram of the KHM on a honeycomb lattice is mapped out by employing *infinite Density Matrix Renormalization Group* (iDMRG) as introduced in Sec. 3.1. The lattice is wrapped on an infinite cylinder with its unit cell and circumference L_{circ} chosen such that the corresponding momentum cuts contain the gapless Majorana modes of the Kitaev spin liquid. For the pure isotropic Kitaev model, there are gapless Majorana cones at K and K' on the corners of the first Brillouin zone, Fig. 4.1(b). The full KHM retains the C_6 symmetry of the Kitaev model on a honeycomb lattice implying that in

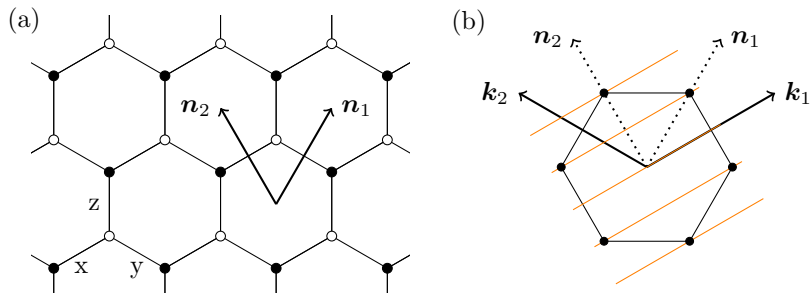


Figure 4.1: (a) x , y , and z edges of an honeycomb lattice, which correspond to Kitaev exchange couplings $S_i^\gamma S_j^\gamma$ with $\gamma = x, y, z$. (b) Allowed \mathbf{k} -vectors (orange lines) for an infinite long cylinder with circumference $L_{\text{circ}} = 6$ and periodic boundary condition along \mathbf{n}_2 . Black nodes picture the position of the gapless Majorana cones.

the two-dimensional limit these cones cannot shift. The iDMRG method determines the ground state of systems of size $L_x \times L_{\text{circ}}$ where L_{circ} is finite with up to 12 sites. L_x is defined along the cylinder's axis and by construction in the thermodynamic limit. An iDMRG cluster is repeated along L_x to mimic the thermodynamic limit. As such the cluster has to be sufficiently sized to fit relevant ordering patterns, e.g., in case of magnetic order, the iDMRG cluster size has to be an integer multiple of the magnetic unit cell both along the axis and the circumference of the cylinder.

The resulting phase diagram for $L_{\text{circ}} = 12$ is shown in Fig. 4.2, which agrees with previous studies [83–86, 124, 125]. For this L_{circ} , the system is compatible with the Klein-duality, that is a four-sublattice transformation mapping the zigzag to antiferromagnetic and the stripy to ferromagnetic order [83]. Plotted are the ground state energy and the entanglement or von-Neumann entropy

$$S = -\text{Tr} \rho^{\text{red}} \log \rho^{\text{red}} , \quad (4.2)$$

of the reduced density matrix ρ^{red} for a bipartitioning of the cylinder by cutting along a ring. Both the cusps in the energy density and the discontinuities of the entanglement entropy indicate first order transitions. A careful finite size scaling is difficult because of the large bond dimension needed and thus it is not possible to make definite statements about the order of the transitions in the limit $L_{\text{circ}} \rightarrow \infty$.

The symmetry broken phases can be identified by measuring the local magnetic moment: (i) a Néel phase extending around the pure antiferromagnetic (AF) Heisenberg point, $-0.185 < \alpha/\pi < 0.487$, (ii) a zigzag phase ranging from $0.513 < \alpha/\pi < 0.894$, (iii) a ferromagnetic (FM) phase ranging from $0.894 < \alpha/\pi < 1.427$ around the pure FM Heisenberg point, and (iv) a phase with stripy order from $1.559 < \alpha/\pi < 1.815$. The FM and its dual phase with stripy order are characterised by an almost saturated staggered magnetisation, cf. Fig. 4.3. Quantum fluctuations are absent at $\alpha = \pi$ and

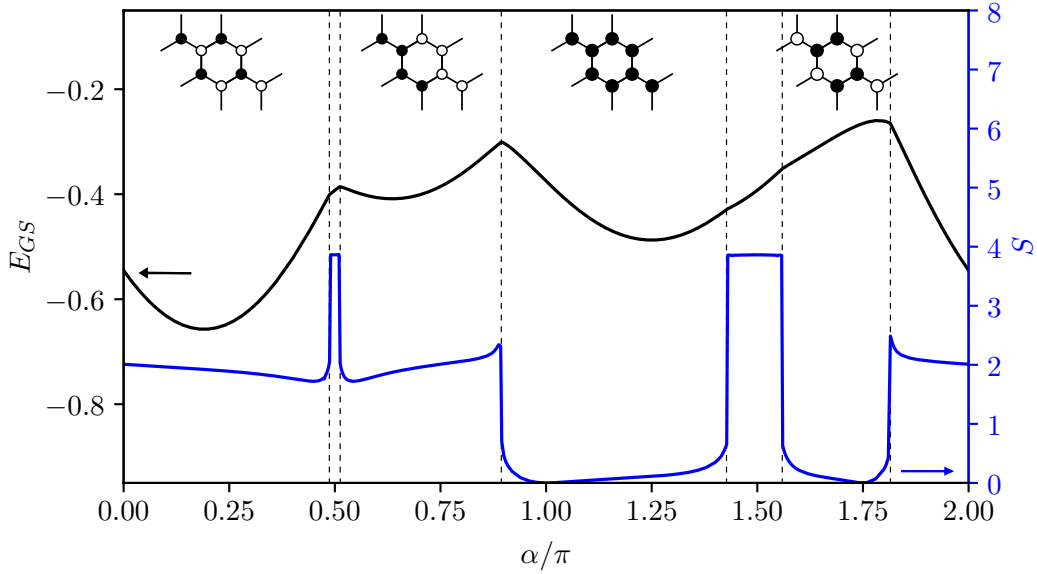


Figure 4.2: Phase diagram for an infinite cylinder with circumference $L_{\text{circ}} = 12$ obtained using *i*DMRG. The black line corresponds to the ground state energy density and the blue line to the entanglement entropy for a bipartition of the cylinder into a left and right half. The insets illustrate the ordering pattern of the magnetic phases. Two spin liquid phases exist around the pure Kitaev model ($\alpha = 0.5\pi$ and 1.5π). Dashed lines illustrate the phase boundaries. A bond dimension of $\chi = 1200$ states per site is used.

1.75π and remain small in the full range of the corresponding phases.

Note that due to the mapping of the two-dimensional lattice onto a chain, Mermin-Wagner-Coleman [126] applies at the pure AF-Heisenberg point and suppresses long range Néel order. In fact it is replaced by a gapped symmetry-preserving state, which extends over a finite region in parameter space [127, SM]. Because of the bond dimension $\chi = 1200$ not being large enough to capture the symmetry-preserving state for cylinders with $L_{\text{circ}} = 12$, the expected ordered phases are observed with a finite, but presumably reduced, staggered magnetisation, cf. Fig. 4.3.

The two *Kitaev spin liquid* phases between Néel and zigzag as well as between FM and stripy are characterised by the conserved fluxes $\langle W_p \rangle \approx 1$. Furthermore, the KSL are gapless, as expected for the B-phase. In order to observe the gapless sector, one has to note that the KSL exhibits two sectors on the cylinder determined by a *Wilson loop* encircling the cylinder. Similar to the plaquette operators $W_p = \prod_{j \in \mathcal{P}} \sigma_j^{\gamma_j}$, let us define a loop operator around the cylinder as

$$W_l = \prod_{j \in \text{loop}} \sigma_j^{\gamma_j}, \quad (4.3)$$

where $\gamma_i = \{x, y, z\}$ corresponds to the bond at site i that is not part of the loop.

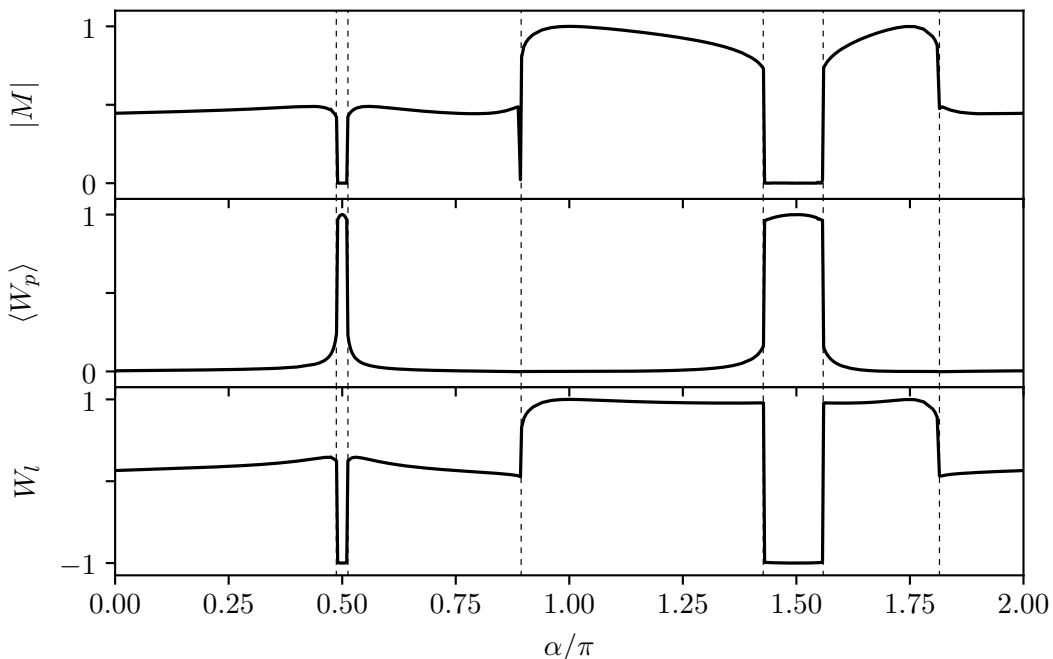


Figure 4.3: Several observables complementing the phase diagram in Fig. 4.2: staggered magnetisation $|M|$ normalised to 1 (top), average of plaquette fluxes $\langle W_p \rangle$ (mid), and the cylinder flux W_l corresponding to a loop around the cylinder (bottom). Dashed lines illustrate the phase boundaries.

Following Sec. 2.3.2, W_l can be expressed in terms of \mathbb{Z}_2 gauge field variables u_{jk} [16]

$$\tilde{W}_l = \prod_{(j,k) \in \text{loop}} u_{jk} . \quad (4.4)$$

For here chosen lattice periodicity, cf. Fig. 4.1, both loop operators are related by a minus sign. Thus, $W_l \rightarrow +1$ (periodic boundary condition of the fermions) translates to $W_l \rightarrow -1$, which corresponds to the gapless sector assuming a cylinder geometry is used such that cuts in reciprocal space go through the nodes of the Majorana cones. The second sector (antiperiodic boundary condition of the fermions) is always gapped and has a lower ground state energy than the gapless sector. Thus, the gapless state is a metastable state.

Regarding the computation of the ground state, iDMRG is initialized with a state $|\psi\rangle$ that has $\langle \psi | W_l | \psi \rangle = \pm 1$ depending on the desired sector. Table 4.1 contains the phase transitions for the gapped and the gapless sector and compares it to results using *exact diagonalization* (ED) [112] and *infinite Projected Entangled Pair States* (iPEPS) [86]. As the gapped sector with a non-zero flux through the cylinder has a lower energy, its stability is enhanced and the stability of the KSL phase is overestimated. This effect is more pronounced for a small circumference $L_2 = 6$ because of the energy

Table 4.1: Transition points in α/π for different circumferences and sectors compared to exact diagonalization (ED)[112] and infinite Projected Entangled Pair States (iPEPS)[86].

	ED	iPEPS	DMRG			
			$L_2 = 6$		$L_2 = 12$	
			gapped	gapless	gapped	gapless
AF/KSL	0.488	0.487	0.484	0.494	0.485	0.487
KSL/ZZ	0.510	0.513	0.523	0.513	0.514	0.512
FM/KSL	1.399	1.432	1.405	1.44	1.421	1.428
KSL/ST	1.577	1.557	1.573	1.548	1.562	1.558

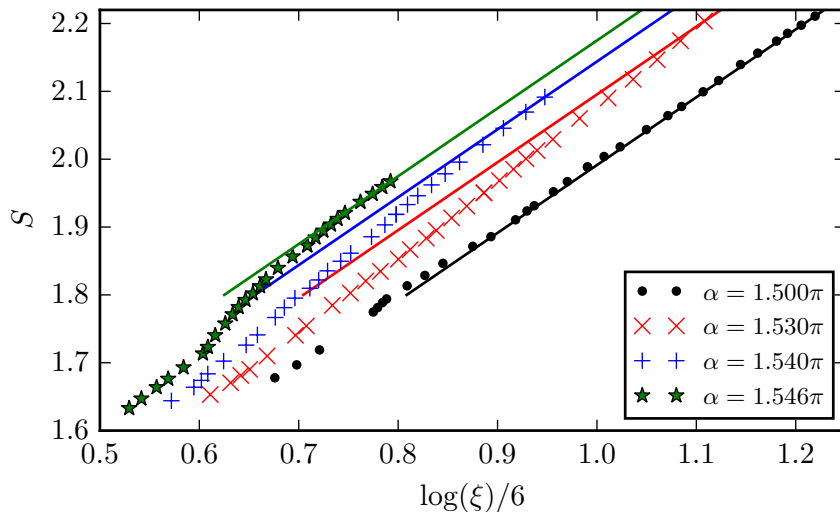


Figure 4.4: Entanglement entropy S of a bipartition of the cylinder vs the logarithm of correlation length ξ for different bond dimensions up to $\chi = 1024$ and a narrow cylinder with $L_2 = 6$ sites circumference. The lines correspond to a central charge of $c = 1$.

splitting depending inversely on the circumference. With this in mind, it is notable how well the phase boundaries obtained using iDMRG agree with those from the iPEPS simulations, which are by construction working in the two dimensional limit.

Further on, employing a finite entanglement scaling approach [90, 93, 94] in the gapless sector confirms the expected chiral central charge $c = 1$ for both KSLs. Fig. 4.4 shows S and $\log \xi$ for various χ of up to 1024. The lines serve as a guide to the eye corresponding to a slope with $c = 1$. The numerical data for the KSL at $\alpha = 3/2\pi$ agrees well with the scaling. This reflects the fact, that the KSL can be mapped to a free fermion problem with two Majorana cones in the first Brillouin zone, each contributing $1/2$ to the central charge. The gapless nature persists within the whole KSL phase with small Heisenberg interaction.

4.3 Dynamical Spin Structure Factor

Starting from a ground state $|\psi_0\rangle$ obtained using iDMRG and encoded as a matrix-product state (MPS), the dynamical spin-structure factor $\mathcal{S}(\mathbf{k}, \omega)$, Eq. (2.42), is obtained by a spatio-temporal Fourier transform of the dynamical correlation function

$$C_{ij}^{\gamma\gamma}(t) = \langle \psi_0 | S_i^\gamma(t) S_j^\gamma(0) | \psi_0 \rangle , \quad (4.5)$$

where $\gamma = \{x, y, z\}$ and S_i^γ is the spin component at site i .

The real-time correlations $C_{ij}^{\gamma\gamma}(t)$ are computed using the matrix-product operator based time evolution method (tMPO) [96] described in Sec. 3.3. In contrast to standard methods like time-evolving block decimation, tMPO allows to efficiently handle the long-range interactions stemming from unraveling the cylinder to a one-dimensional system. Applying a local excitation, like $S_i^\gamma(0)$, breaks the translational invariance used to encode the infinite wave function. Thus, the ground state MPS is modified in that the unit cell size is enlarged and the infinite boundaries are pushed further out. This provides room for the excitation to spread (which in case of a gapped system happens in a light cone fashion) and provides an upper limit for the time-evolution, as we can only expect the time-evolution to represent the physics of an infinite system as long as the excitation does not hit the boundary. This follows the general strategy laid out in Refs. [128–130]. The entanglement will not only spread but also grow locally. However, this entanglement growth and the resulting growth of the required number of states is expected to be slow as the ground state gets only perturbed locally. Thus, long times can be reached even in the cylinder geometry. The data is processed further to avoid oscillations due to the finite-time window. Firstly, the real-time data is extended in time using linear predictive coding. Secondly, the extended real-time data is multiplied with a Gaussian ($\sigma_t \approx 0.43T$) to suppress long time oscillations. This corresponds to a broadening in ω -space ($\sigma_\omega \approx \frac{2.3}{T}$). Linear predictive coding is used to allow room for the tail of the Gaussian, but σ_t is chosen such that only a small fraction of the spectral weight contributes from the predicted part [131]. If not stated otherwise, results for the diagonal $\mathcal{S}(\mathbf{k}, \omega) = \sum_\gamma \mathcal{S}^{\gamma\gamma}(\mathbf{k}, \omega)$ are presented. The results of the numerical time-evolution presented for the KHM are obtained by Ruben Verresen, a collaborator on the joint publication [127]. The main aspects are summarized below.

Figure 4.5 shows $\mathcal{S}(\mathbf{k}, \omega)$ in different phases of the KHM along the central cut $k_2 = 0$ including the Γ and M high-symmetry points. All plots have an intrinsic broadening $\sigma_\omega \approx 0.06$ caused by the above mentioned Gaussian envelope. The first panel, Fig. 4.5(a), for $\alpha = 1.1/\pi$ within the ferromagnetic phase features a well resolved magnon mode in agreement with linear spin-wave theory (LSWT). Note, that LSWT is not able to capture the small gap $\Delta \approx 0.05|J|$ at Γ , which is caused by the Kitaev coupling $2K = 0.65J$.

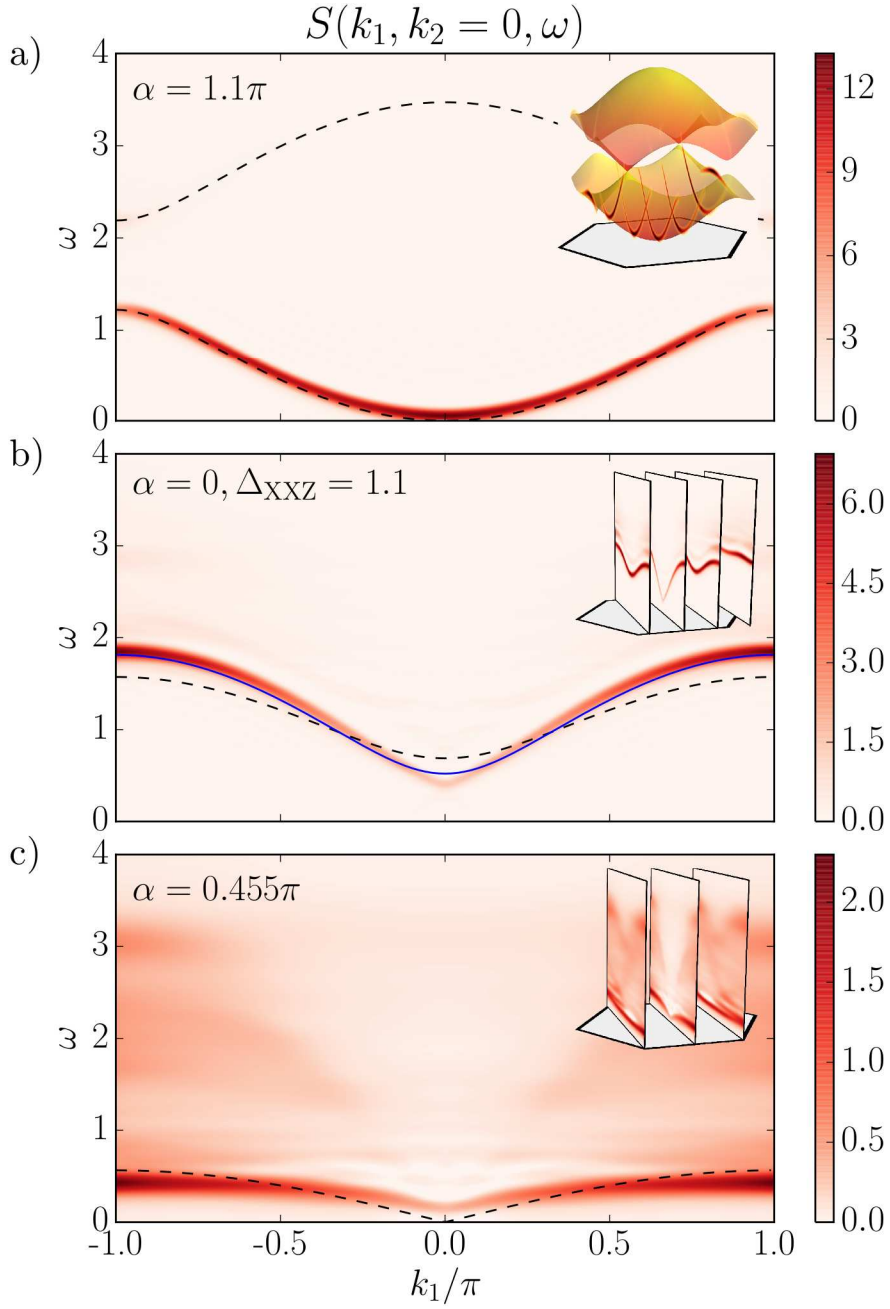


Figure 4.5: $S(\mathbf{k}, \omega)$ for cuts $\mathbf{k} = (k_x, 0)$ in different phases of the KHM with a ω -resolution $\sigma_\omega \approx 0.06$. Dashed lines show results from LSWT. Insets show the data for all allowed cuts. (a) FM phase for a cylinder with $L_2 = 12$. (b) Antiferromagnet with small spin anisotropy without Kitaev term ($L_2 = 8$). The solid blue line shows next order spin wave calculations [132]. (c) AF phase in proximity of the KSL ($L_2 = 6$).

For the second panel, Fig. 4.5(b), a small XXZ anisotropy $\Delta_{\text{XXZ}} = 1.1$ is added to the pure AF Heisenberg coupling $\alpha = 0$ to induce a small gap and stabilize the Néel ordering¹. The tMPO result features significant deviations from LSWT. However, second order spin wave theory for the XXZ-model [132] improves. Moreover, the spectral weight in the spin wave is reduced, indicating higher-order magnon contributions becoming more important. The third panel, Fig. 4.5(c), shows $\mathcal{S}(\mathbf{k}, \omega)$ for $\alpha = 0.455\pi$ still within the Néel phase but closer to the quantum spin-liquid phase and without the XXZ anisotropy. Here, the magnon band flattens and attains a broader line shape. Lots of the spectral weight shift from the magnon band to higher energies. LSWT describes a flattening of the magnon band. The high-energy continuum is generically not accounted for, as is a possible repulsion of the magnon band due to the nearby continuum. As in the FM phase at $\alpha/\pi = 1.1$, the Kitaev coupling induces a gap not captured within LSWT.

Higher order spin-wave theory may help to gain insight, but has not been applied so far.

Let us turn now to a discussion about the dynamics of the zigzag phase. The zigzag ordering is observed in $\alpha\text{-RuCl}_3$ [28, 114, 115]. To allow a phenomenological comparison between experiment and the dynamical spin-structure factor obtained with tMPO, the presentation in Fig. 4.6 is changed to constant energy cuts. One representative cut each for low, intermediate, and high energy. The top row shows the exact results for the two-dimensional quantum spin-liquid phase in the Kitaev limit $\alpha = 0.5\pi$. Subsequent rows show the tMPO result for increasing $\alpha/\pi = \{0.55, 0.7, 0.8\}$. Here, the circumference is increased to $L_{\text{circ}} = 12$ to obtain more cuts in reciprocal space. This, however, requires to shorten the time cut-off to $T = 10$ and leads to an intrinsic broadening in frequency of $\sigma_\omega \approx 0.23$. The latter recovers to some extent the integration over energy applied to the scattering data. Data for smaller circumferences, but longer times, is presented in the supplemental material of Ref. [127]. For the tMPO data, an averaging over all three ordering directions is taken.

At low-energies, the Kitaev quantum spin liquid (KSL) exhibits broad features with vanishing weight at the central Γ -point and large spectral weight at Γ' (edges of the second Brillouin zone), reflecting the antiferromagnetic nearest neighbor spin-spin correlations. During the time-evolution, the spin-spin correlations remain strictly zero beyond nearest neighbor causing the broad continuum in \mathbf{k} -space. Moving to the zigzag phase, the onset of spin-wave bands appears at the M -points. For $\alpha = 0.55\pi$, the intensities at the M -points are different due to finite-size effects on the cylinder geometry breaking the C_6 -symmetry of the Kitaev-Heisenberg model. At intermediate

¹The small XXZ anisotropy is necessary to gap the magnons and allow long-range order. The pure Heisenberg AFM does not have a long-range ordered ground state on the cylinder geometry due to a gapless Higgs mode and Mermin-Wagner-Coleman [126] applying.

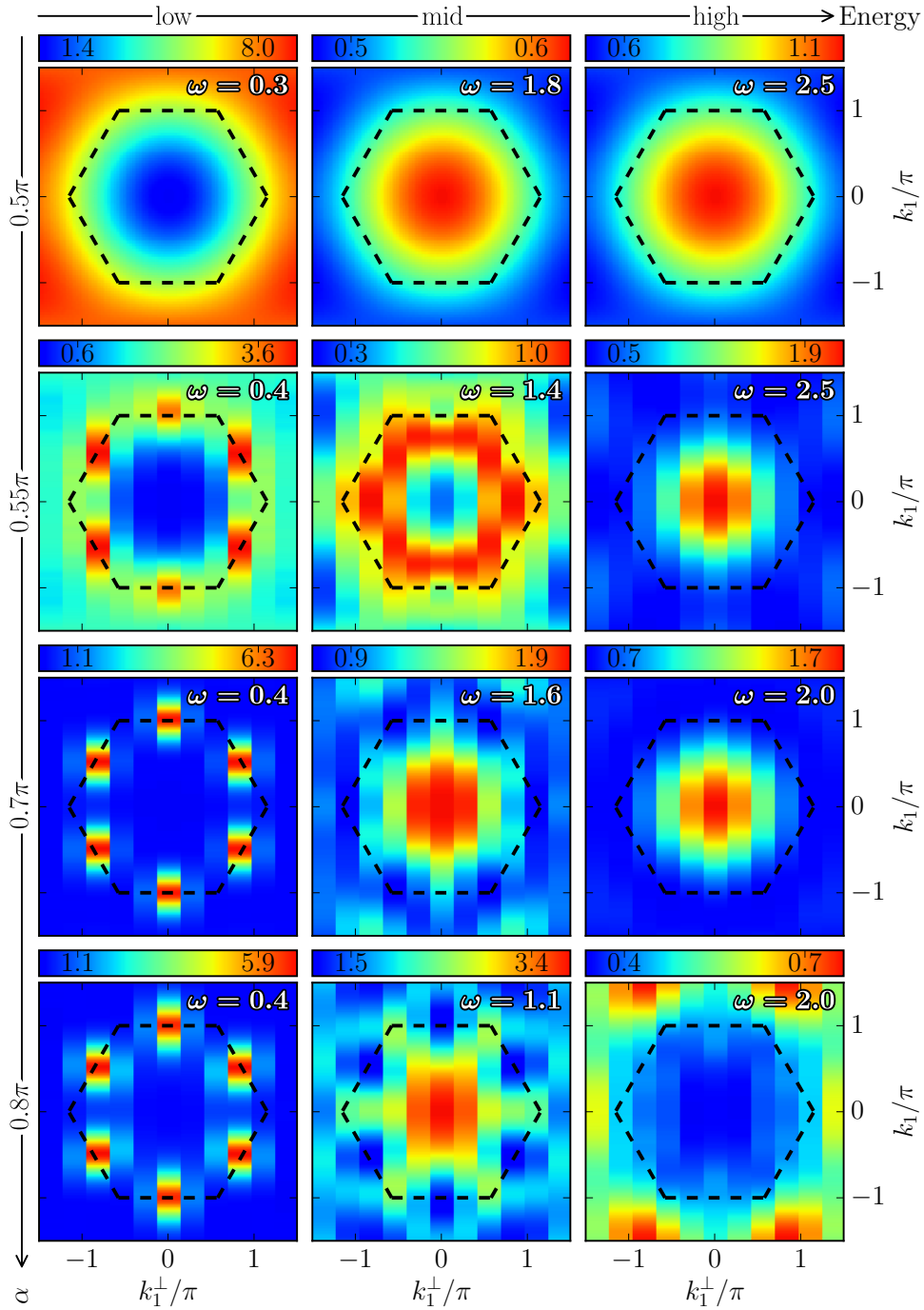


Figure 4.6: $\mathcal{S}(\mathbf{k}, \omega)$ at three different energies for four models: KSL at $\alpha = 0.5\pi$ (analytic result, 2D), and zigzag order at $\alpha = 0.55\pi, 0.7\pi, 0.8\pi$ with $L_2 = 12$. Figure is taken from [127].

and high energies, the KSL has generally less spectral weight, but with a maximum at Γ forming a broad circular feature. It appears, that this broad circular feature carries over to the zigzag phase with declining energy and spectral weight as α is tuned away from the KSL phase. It is this persistence of the broad high energy features characteristic of the KSL phase across the transition into the zigzag phase, which is the essence of the idea of a proximate spin liquid. This concept was recently invoked for the putative Kitaev-compound α -RuCl₃ [28, 85, 109, 114]. However, its specific microscopic Hamiltonian likely contains important terms beyond the KHM studied in this chapter [116, 133–135], e.g., among others the symmetric-antisymmetric Γ exchange studied in chapter 5.

A direct comparison of the tMPO data at $\alpha = 0.7\pi$ with experimental data for α -RuCl₃ [28], in particular Fig. 2 and Fig. 3 therein, reveals some phenomenological similarities: at high energies both exhibit characteristic broad feature at Γ that deforms to a star-like shape with prongs at the M -points presumably due to overlapping with the diffuse remnants of the spin waves. The onset of the spin wave dispersion is clearly visible as high-intensity dot around M . However, α -RuCl₃ also features low energy spectral weight at Γ not present in the spectrum of the KHM. This feature may be caused by two-magnon processes that are allowed if a significant Γ -exchange and ferromagnetic K is considered, but such two-magnon processes would be suppressed for antiferromagnetic K [135].

4.4 Conclusion

In this chapter, the phase diagram of the Kitaev-Heisenberg model has been revisited using the (quasi-)two-dimensional iDMRG method. The transition points from the ordered phases into the Kitaev spin liquid are slightly renormalized in comparison to exact diagonalization which is known to be prone to finite-size effects. Utilizing a cylindrical geometry with one dimension being infinite enables to verify the gapless nature of the Kitaev spin liquid: the finite- χ scaling of the MPS is consistent with a central charge of $c = 1$.

A new method for obtaining the dynamical properties of generic lattice spin model in (quasi-)two dimensions has been applied. An extended continuum in the ordered phases close to the Kitaev spin liquid is observed that possesses high-energy features similar in appearance within reciprocal space to those of the Kitaev spin liquid. These features are beyond spin-wave theory and, thus, provide a concrete of the concept of a proximate spin liquid. The spectrum of the zigzag phase bears some resemblance with the neutron scattering data for α -RuCl₃ at high energies. However, at low energies α -RuCl₃ exhibits spectral weight at the Γ high-symmetry point, which is not observed in the Kitaev-Heisenberg model.

Chapter 5

Kitaev-Gamma Model

5.1 Introduction

Despite first studies [83, 114] suggesting the Kitaev-Heisenberg model, see chapter 4, as a minimal approach to describe experimental inelastic neutron scattering data of α -RuCl₃ [28, 114, 136], follow up *ab initio* computations indicate that the symmetric-anisotropic Γ -interaction may be even more dominant [137]. This dominance of K - and Γ -interactions is also pointed out in studies of multi-orbital Hubbard model [134]. Furthermore, metal-organic frameworks with Ru³⁺ or Os³⁺ ions are proposed as possible quantum spin liquid materials with significant K - Γ [87]. Using *exact-diagonalization* on finite size clusters Catuneanu et al. [138] suggest already that the K - Γ model may host quantum spin liquid phases in an extended region of the phase diagram. Such a method is prone to finite-size effects and, in fact, in the ED study they introduced a spatial anisotropy in the Kitaev interaction as an attempt to circumvent such finite size effects. Adding a small J_3 , third nearest neighbor Heisenberg, leads to a transition to the zig-zag ordered ground state that is observed experimentally for α -RuCl₃.

Classically, both the pure Kitaev and the pure Γ model are spin liquids with an extensive ground state degeneracy [61, 139]. Turning on quantum fluctuations results in a quantum spin liquid phase in the Kitaev limit [16], but a clear understanding is lacking in pure Γ limit.

In this chapter, the K - Γ model is studied using matrix product states (MPS) and the infinite density matrix renormalization group (iDMRG) method [23, 140, 141], as introduced in Sec. 3.1. Being a standard method for one-dimensional systems, it has been applied successfully in two dimensions by wrapping the lattice on a cylinder a winding a chain around the cylinder. This allows to use a non-perturbative technique to investigate frustrated or strongly correlated methods, but the cylinder geometry may cause finite-size effects which have to be examined carefully.

First, we focus on ground state properties like energy, entanglement entropy, flux-

average, magnetization, and static structure factor for the K - Γ model. An extended region in the phase diagram ranging from ferromagnetic Kitaev- to the antiferromagnetic Γ -interaction exhibits a quantum paramagnetic state. At the same time, the entanglement entropy remains comparably high as in the gapped sector of pure Kitaev limit. In comparison, the entanglement entropy of a magnetically ordered phase for antiferromagnetic Kitaev interaction is much lower, because it extends around a point dual to the ferromagnetic Heisenberg-limit [142].

Once the ground state wave function is obtained using iDMRG and encoded as an MPS, its *transfer matrix* (TM) is utilized to test for possibly coherent excitations. In a recent work Zauner et al. [100] proofed a mapping between the complex eigenvalues and low-energy excitation spectra as a function of momentum. Furthermore, exploiting the translation symmetry around the cylinder [143] enables to map out the low-energy excitation spectra along cuts in reciprocal space. The main finding is, that the lower edge of the excitation spectra moves coherently in momentum space in a well-defined fashion as a function of Γ/K . This may already suggest that these states are non-trivial and likely correspond to a quantum spin liquid. More so, the TM spectrum has an emergent symmetry in its momentum dependence, The same symmetries are found in the single- and two-particle spectra of a Majorana mean-field theory.

This chapter is organized as follows. The K - Γ model is defined in the next section 5.2 including the iDMRG results and its phase diagram. In section 5.3 the transfer matrix (TM) spectrum is introduced and discussed. A short summary of a Majorana based MFT is given in section 5.4 and compared to the TM spectrum. A discussion of the results follows in section 5.6

5.2 Ground State Phase Diagram

The K - Γ model is a part of the general Hamiltonian under consideration of the symmetries relevant to the Kitaev compounds, cf. Sec. 2.3.8. The Hamiltonian of the K - Γ model is given by

$$\begin{aligned}
 H = & \sum_{\langle ij \rangle \in x} K_x S_i^x S_j^x + \Gamma_x (S_i^y S_j^z + S_i^z S_j^y) \\
 & + \sum_{\langle ij \rangle \in y} K_y S_i^y S_j^y + \Gamma_y (S_i^x S_j^z + S_i^z S_j^x) \\
 & + \sum_{\langle ij \rangle \in z} K_z S_i^z S_j^z + \Gamma_z (S_i^x S_j^y + S_i^y S_j^x), \tag{5.1}
 \end{aligned}$$

where S_i^α are spin-1/2 operators at site i of a honeycomb lattice. Unless otherwise noted, the isotropic case is considered, $K_\gamma = K, \Gamma_\gamma = \Gamma$. Throughout the following, K and Γ are parameterized using a trigonometric parametrizations such that $K = -\cos \phi$

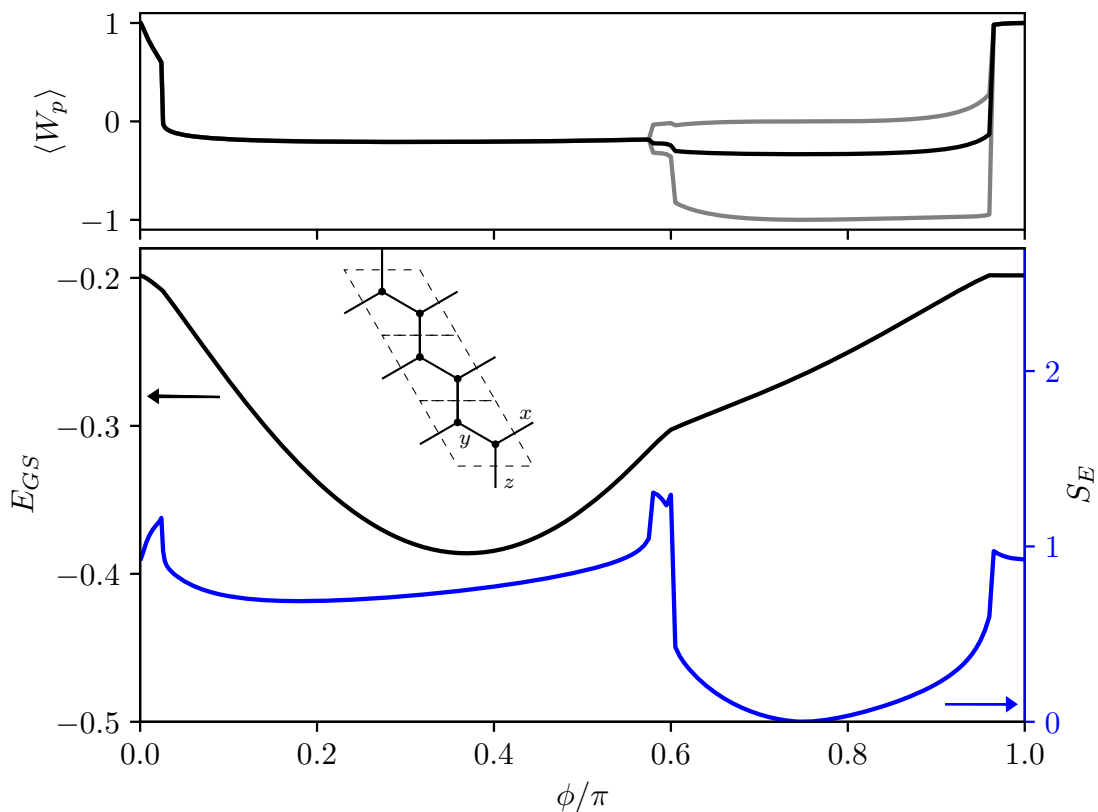


Figure 5.1: Top: Plaquette-flux average $\langle W_p \rangle$, see main text for more details. The lines in gray are the minimal and maximal values of W_p . Bottom: Ground state energy density, E_{GS} , of the K - Γ model, and the corresponding entanglement entropy, S_E , for a bipartition of the cylinder determined using iDMRG for cylinders with circumference $L_{\text{circ}} = 6$. Cusps in E_{GS} are indications of first order phase transitions. The inset illustrates the unit cell used for iDMRG.

and $\Gamma = \sin \phi$. The iDMRG method with bond dimensions of up to $\chi = 400$ is used to obtain the ground state of this model on a narrow infinite cylinder with a three unit cell circumference ($L_{\text{circ}} = 6$). Figure 5.1 shows the ground state energy density, E_{GS} , as a function of the parameter $0 < \phi < \pi$. Starting from the ferromagnetic Kitaev limit, $\phi = 0$, E_{GS} evolves smoothly through the Γ limit, $\phi = \pi/2$. A discontinuity appears at $\phi \approx 0.6\pi$ and again slightly before the anti-ferromagnetic Kitaev limit, $\phi = \pi$. The two discontinuities are associated with a transition into, and out of, a magnetically ordered vortex state, which becomes an exact product state for $\phi = 3\pi/4$. This is evident in a plot of the entanglement entropy, S_E , also in Fig. 5.1, showing a vanishing S_E at this point. Notice that the entanglement entropy remains of comparable magnitude as that of the Kitaev limit in the entire region of $0 < \phi < 0.6\pi$. The plaquette flux around a hexagon $W_p = \prod_{i \in \mathcal{P}} \sigma_i^{\gamma(i)}$, where $\gamma(i)$ is the label of the bond at site i that is not part of the loop, commutes with the bare Kitaev Hamiltonian, $\phi = \{0, \pi\}$, and splits the Hilbert space into subspaces. In that limit, the ground state is in the flux-free sector,

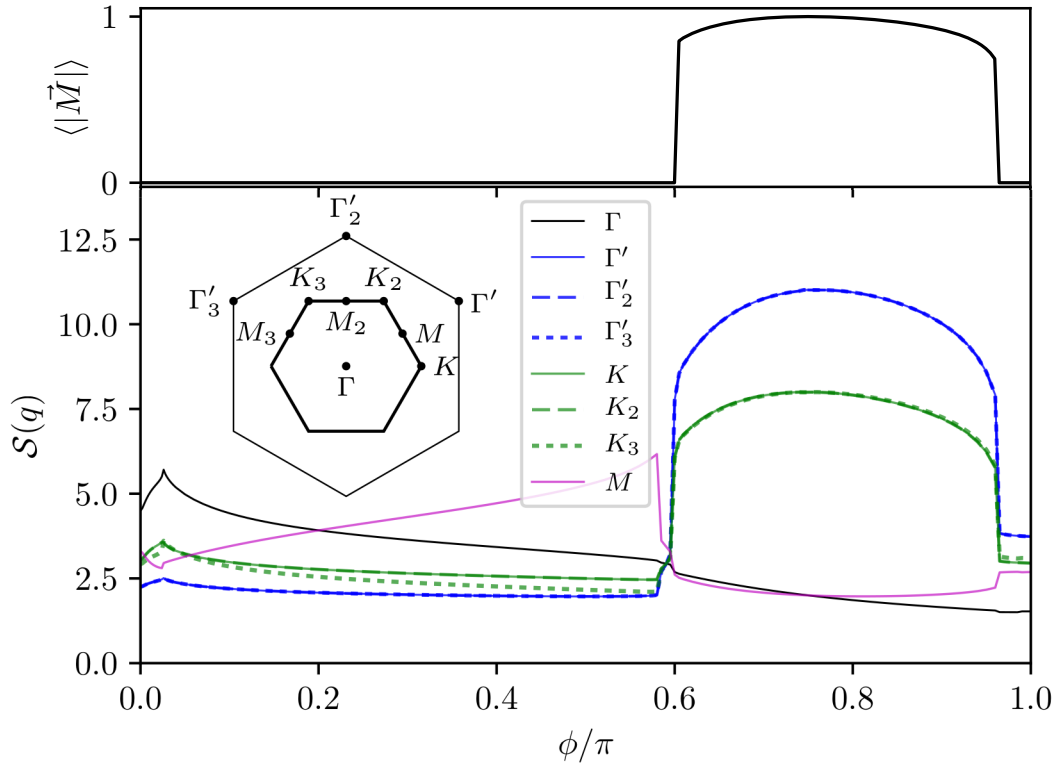


Figure 5.2: Staggered magnetization (top) and static spin-structure factor (bottom), calculated using iDMRG. Inset: Brillouin zone with labeled positions of symmetry points.

$\langle W_p \rangle = +1$. The average plaquette flux declines quickly and drops at $\phi/\pi = 0.025$, at the same point where S_E has a cusp. Beyond that W_p stays almost constant with slight cusps where the magnetically ordered state is entered, and a kink back to $W_p = +1$ signaling the transition to the KSL at $\phi/\pi = 0.96$. Within the magnetically ordered state, W_p is not translationally invariant. One out of the three sublattices formed by the hexagons has $W_p = -1$. Thus, the selected magnetically ordered ground state is related to the classical ground state manifold discussed for the pure Γ -model [139]. Consequently, iDMRG shows a finite staggered magnetization in $0.6\pi < \phi < 0.96\pi$, as well as an enhanced spin-structure factor, Fig. 5.2, all consistent with a magnetically ordered phase illustrated in Fig. 5.3. This phase extends around a point, $\phi/\pi = 0.75$, with hidden $SU(2)$ -symmetry [142]: a six-sublattice transformation maps the Kitaev- and Γ -interaction to the ferromagnetic Heisenberg model, whose ground state is a simple product state with a global $SU(2)$ -symmetry. Being a product state, the entanglement entropy is strictly zero. Applying the sublattice transformation breaks the global $SU(2)$ symmetry and leads to a plethora of seemingly different ground states including Néel or the coplanar 120° state discussed in [142]. However, on the K - Γ axis a different order is selected, where the spins are pairwise antiparallel and the pair alternately aligned

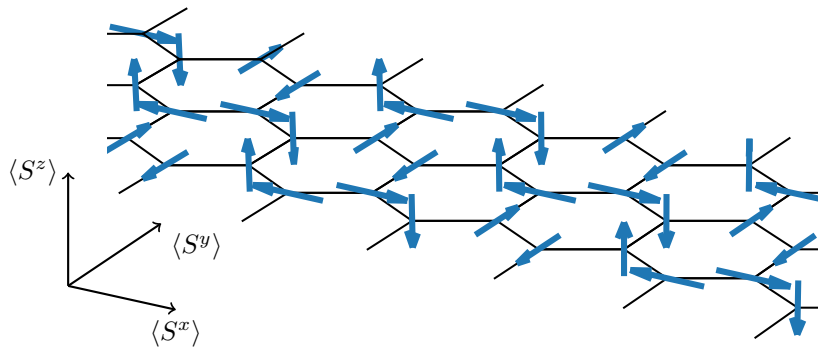


Figure 5.3: Illustration of the spatial magnetisation within the magnetically ordered phase. The spins are aligned along the cubic axis.

along the x -, y -, or z -direction.

The subsequent sections address the question of the nature of the ground state outside of the magnetically ordered state. The large entanglement and lack of magnetic order suggest that the ground state in this region is occupied by quantum spin liquid phases. However, a small discontinuity at $\phi \approx 0.025\pi$ in both the entanglement entropy and the spin-structure factor as well as the vanishing Kitaev-fluxes raise the question whether there exists a subtle transition between different kinds of spin liquid phases. To address this issue, and to gain insight into the low-energy physics of the K - Γ model as ϕ is tuned from the Kitaev to Γ limits, a detailed examination of the transfer matrix spectrum follows.

5.3 Transfer Matrix Spectrum

The *transfer matrix* is constructed from an infinite MPS, which encodes the ground state being obtained using iDMRG. As introduced in section 3.2, the eigenvalues λ_i of the transfer matrix are complex in nature, $\lambda_i = e^{-\epsilon_i + i\eta_i}$. Its argument $\arg \lambda$ is identified with the longitudinal momentum along the cylinder axis, $k_{x,i} \sim \eta_i = \arg \lambda_i$. The transverse momentum k_y follows from the translational invariance along the circumference and is discretized, $k_y = 2\pi n/L_{\text{circ}}$, depending on the circumference L_{circ} . Here, a cylinder with $L_{\text{circ}} = 3$ is used, thus transverse momenta $k_y = 0, \pm 2\pi/3$ are available. Zauner et al. [100] have been demonstrating the correspondence between the complex eigenvalues of the transfer matrix and the excitation spectrum, $E(k) \sim E(k_x, k_y)$, with the above momenta and the energy identified via $E_i \sim \epsilon_i = -\ln |\lambda_i|$.

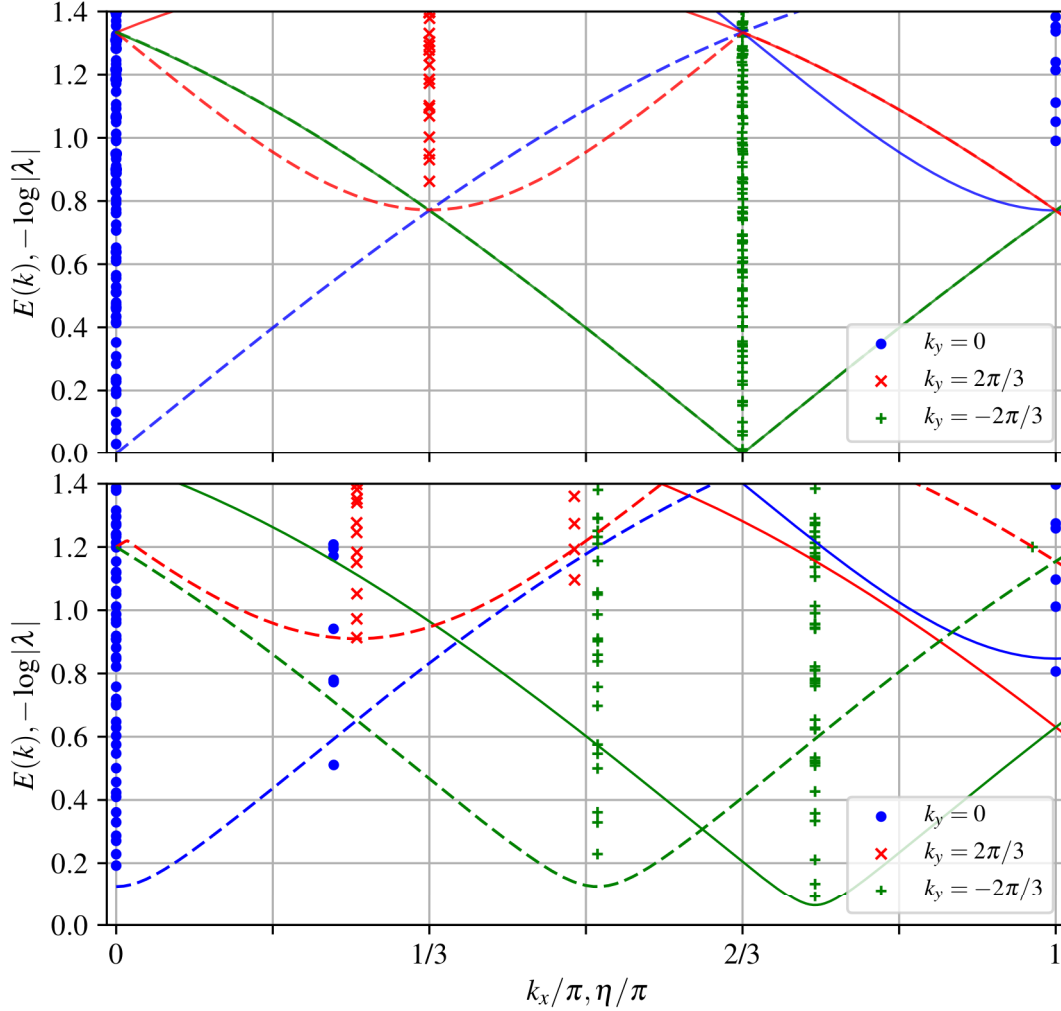


Figure 5.4: Quasi-energies $E(k) - \log |\lambda|$ with each point corresponding to a single eigenvalue λ , where $\lambda = |\lambda|e^{i\eta}$ and η is identified with the momentum k_x along the cylinder. k_y denotes the transverse momentum obtained as a quantum number with respect to translation along the cylinder. Top: isotropic Kitaev model with $K_x = -1$, $K_y = -1$, and $K_z = -1$, Bottom: anisotropic Kitaev model with $K_x = -1$, $K_y = -1.2$, and $K_z = -0.9$. Lines display the analytic results of the single-particle (solid) and two-particles (dashed) lowest energy excitation [16] on the corresponding momentum cuts: $k_y = 0$ (blue), $k_y = 2\pi/3$ (red), and $k_y = -2\pi/3$ (green). The analytic results are scaled by a factor $a = 0.38$.

5.3.1 Kitaev Limit

Taking the limit $\phi \rightarrow 0$ of Eq. 5.1 one obtains the exactly solvable Kitaev model on a honeycomb lattice [16]. If the Kitaev couplings are isotropic $K_x = K_y = K_z$, the model exhibits gapless Dirac nodes at the K -points of the Brillouin zone. More specifically, there exist two (Majorana) Dirac nodes at K and $K' = -K$. In the TM spectrum plotted in Fig. 5.4(a), the gapless excitations become apparent as pillars of eigenvalues at $\mathbf{k} = (k_x, k_y) = (2\pi/3, -2\pi/3)$ (green) and similarly at $(-2\pi/3, 2\pi/3)$ (not shown). Two particle low-energy excitations occur at $K + K' = \Gamma = (0, 0)$ (blue), and at $K' + K' = K$ (green). The latter lies exactly on top of the gapless single particle excitations and cannot be distinguished. Once the Kitaev couplings, K_γ , are tuned away from isotropy, cf. Fig. 5.4(b), the Dirac node moves and odd-numbered particle excitations get separated in reciprocal-space from even-numbered. Here, the anisotropy is chosen such that the Dirac nodes leave the allowed momentum cuts of the cylinder, and a small gap is introduced. The agreement between the (k_x, k_y) of the TM eigenvalues and the minima of excitation bands are striking. Remarkably, the TM spectrum recovers single-, three-, etc. particle excitations as well as two-, four-, etc. particle excitations.

5.3.2 K - Γ Model

Moving away from the exactly solvable Kitaev limit, we now turn to analyze the transfer matrix spectrum of the K - Γ model, Fig. 5.5, which shows the transfer matrix spectrum, $E(k_x, k_y)$, for various values of ϕ . Similarly to the Kitaev limit, minima in the continuum of excitations are clearly identified at $\mathbf{k} = (0, 0)$, $(\pi/3, 2\pi/3)$, $(2\pi/3, -2\pi/3)$, and $(\pi, 0)$. All, however, are gapped. This can be understood in the context of Majorana fermions by noting that the cylindrical geometry breaks the symmetry between x bonds and y, z bonds, which in turn can lead, for $\Gamma > 0$, to anisotropic hopping amplitudes, and the gapping out of the fermions. To corroborate this point, Fig. 5.6 depicts the energy density per bond as a function of ϕ , displaying that indeed the symmetry between bonds is broken for $\phi > 0$.

Several additional minima appear for $\phi > 0$, with their momentum position moving as ϕ is increased. Strikingly, these additional minima seem to obey an underlying symmetry, i.e., a considerable number of eigenvalues obey $E(k_x, k_y) = E(k_x + 2\pi/3, k_y - 2\pi/3)$. For instance, the $\phi = 0.1\pi$ panel in Fig. 5.5 has a minimum near $(\pi/6, -2\pi/3)$ (green +), which has a symmetric counterpart near $(5\pi/6, 2\pi/3)$ (red x), i.e., shifted in momentum by $(2\pi/3, -2\pi/3)$. An additional counterpart is located near $(\pi/2, 0)$ (blue circle), which can be reached by inversion $\mathbf{k} \rightarrow -\mathbf{k}$, followed by the same shift in momentum. Interpreting the TM spectrum as being associated with two-particle excitations, the above symmetry suggests the existence of single-particle excitations

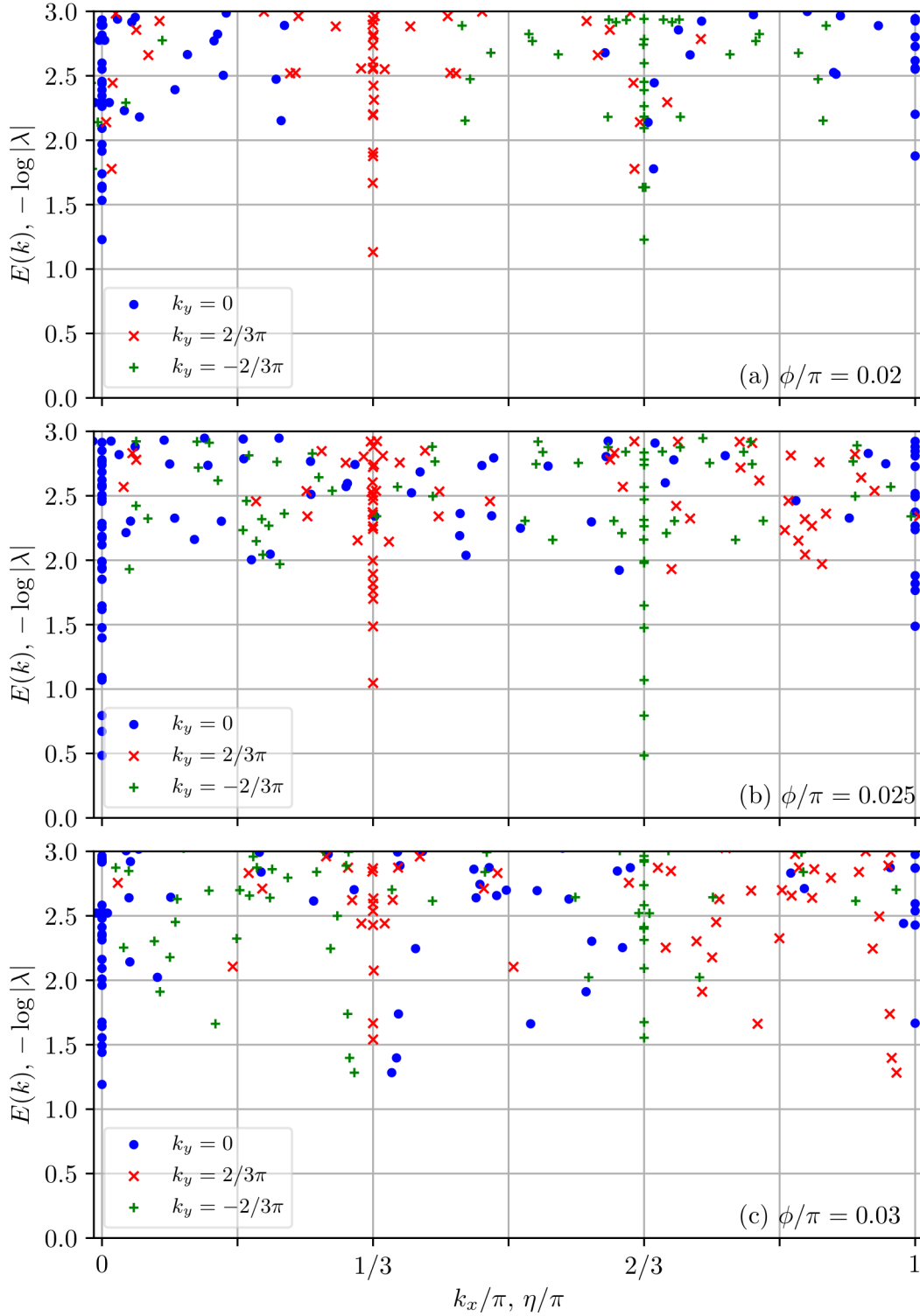


Figure 5.5: Quasi-energies $E(k) - \log|\lambda|$ with each point corresponding to a single eigenvalue λ , where $\lambda = |\lambda|e^{i\eta}$ and η is identified with the momentum k_x along the cylinder. k_y denotes the transverse momentum obtained as a quantum number with respect to translation along the cylinder. Shown are the transfer matrix spectra for (a) $\phi = 0.02\pi$, (b) $\phi = 0.025\pi$, and (c) $\phi = 0.03\pi$.

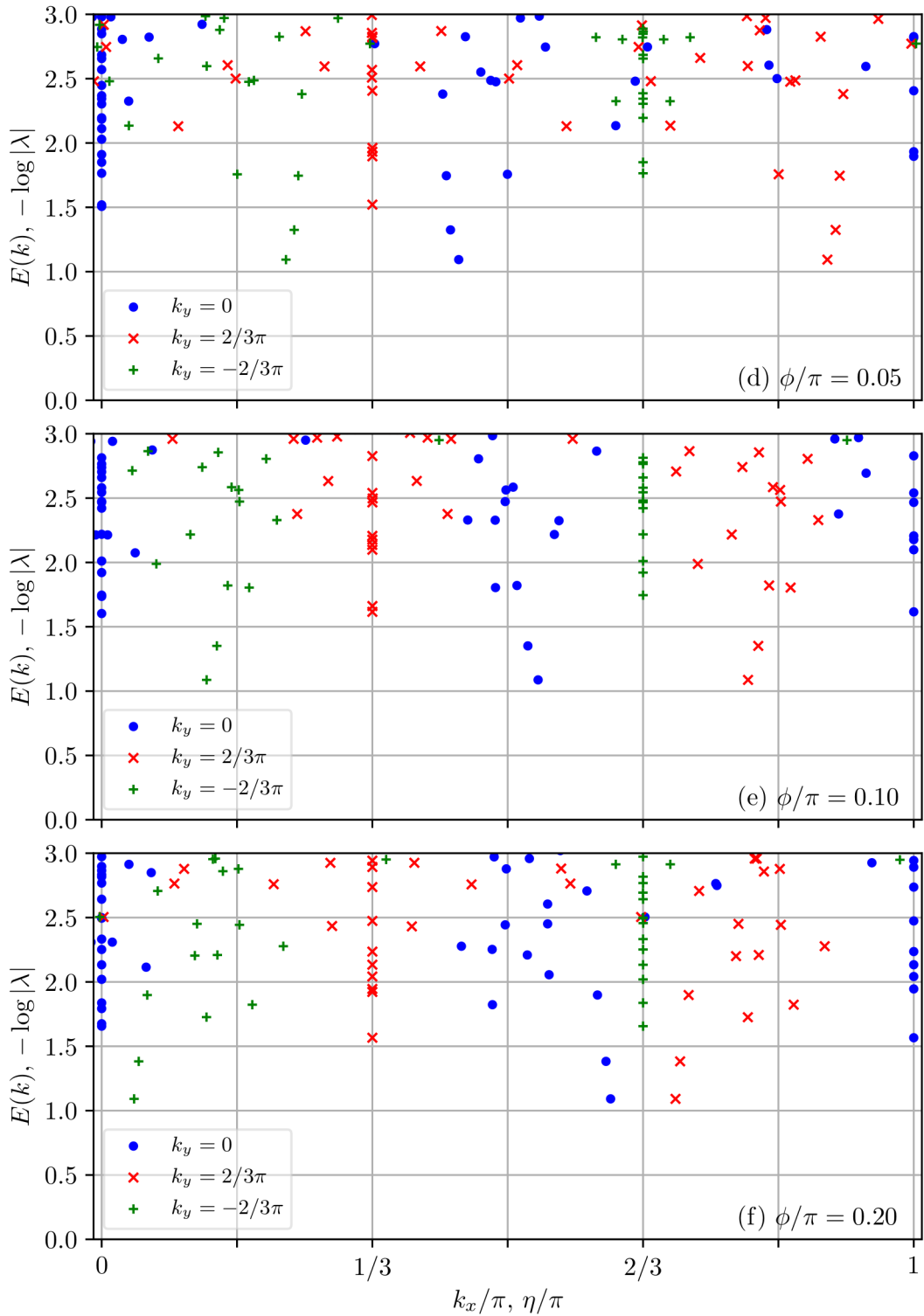


Figure 5.5 (Cont.): Transfer matrix spectra for (d) $\phi = 0.05\pi$, (e) $\phi = 0.10\pi$, and (f) $\phi = 0.20\pi$.

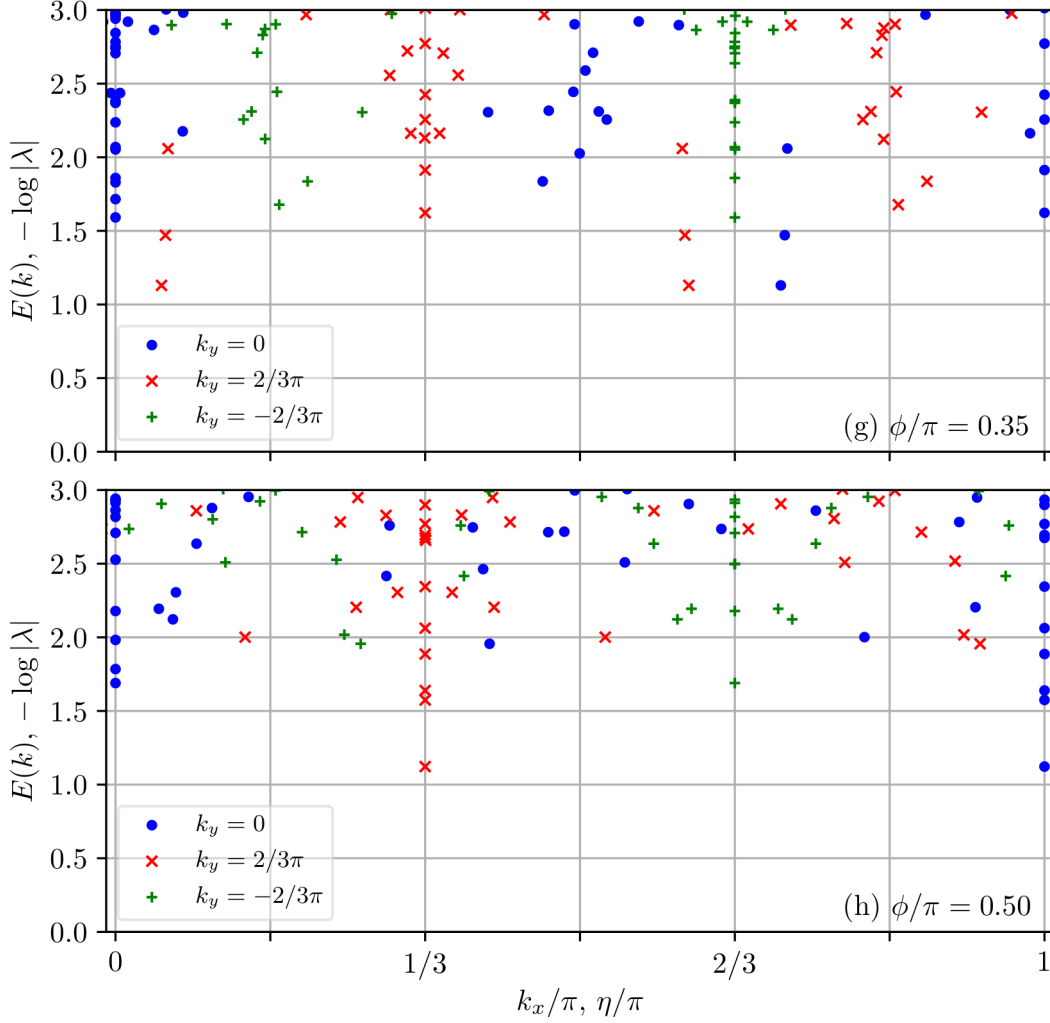


Figure 5.5 (Cont.): Transfer matrix spectra for (g) $\phi = 0.35\pi$, and (h) $\phi = 0.50\pi$.

which, in addition to inversion symmetry $\varepsilon(-\mathbf{k}) = \varepsilon(\mathbf{k})$, obey also $\varepsilon(\mathbf{k}) = \varepsilon(\mathbf{k} \pm \mathbf{K})$, where $\pm \mathbf{K}$ are the momenta at the Brillouin zone corners, K and K' , respectively. Figure 5.7 shows the positions of the soft two-particle excitations, for $\phi = 0.03\pi$ and $\phi = 0.2\pi$, further demonstrating the above symmetry.

In summary, the features of the TM spectrum strongly indicate that the paramagnetic phase of the K - Γ model harbours coherent excitations commonly associated with quantum spin liquids. However, it is difficult to determine the nature of this spin liquid phase, based on the iDMRG data alone. On the one hand, the TM features suggest that in the region $0 < \phi < 0.6\pi$ the K - Γ model harbours Majorana fermion excitations, sharing basic properties with the ground state of the ferromagnetic Kitaev model. On the other hand, the apparent transition at $\phi = 0.025\pi$ may indicate that there are two distinct spin liquid phases with a sharp transition between them. In the next section a mean-field approximation is summarized and its results used to shed

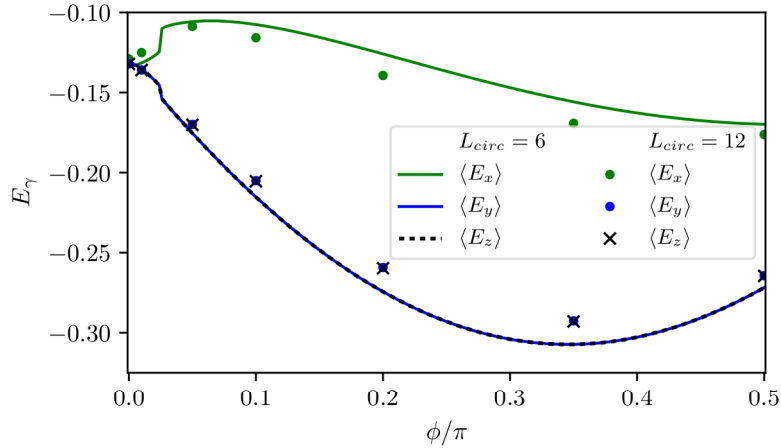


Figure 5.6: Energy density per bond, as obtained using iDMRG, for systems with a three ($L = 6$) and six ($L = 12$) unit cell circumference.

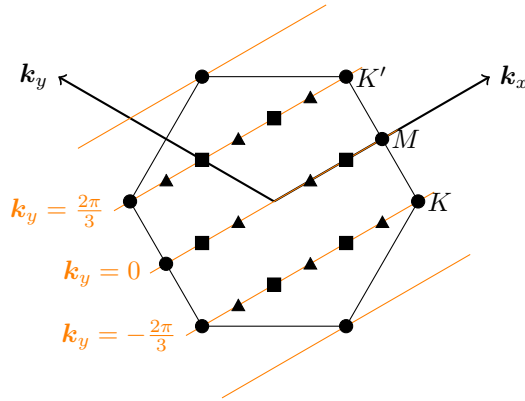


Figure 5.7: Brillouin zone with lines of accessible momenta. The black circles denote the leading soft modes at the K , K' , and M high-symmetry points. The TM spectra exhibits additional soft modes, that are illustrated by the solid polygons for: $\phi/\pi = 0.03$ (triangles), and $\phi/\pi = 0.2$ (squares). The soft modes shift continuously in reciprocal space as ϕ is varied within the paramagnetic regime.

light on the transfer matrix spectra.

5.4 Majorana Mean Field Theory

The following derivation has been carried out by a coauthor of the joint publications, Ref. [144]. It is only sketched here to provide a discussion in the context of the transfer matrix spectra.

The motivation is to derive a fermionic mean-field theory which closely resembles the exact solution of the Kitaev model. Therefore, following Kitaev [16] (cf. Sec. 2.3.3), the spin operators in the Hamiltonian 5.1 get replaced by products of Majorana fermion

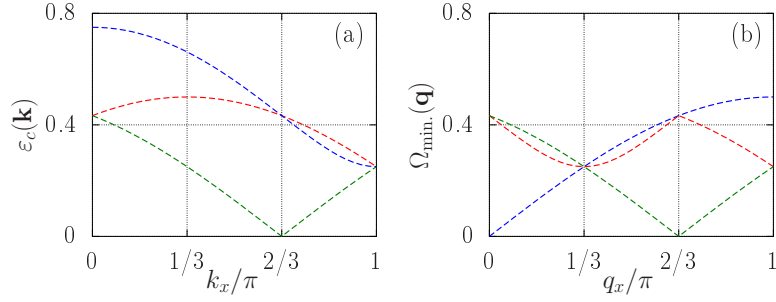


Figure 5.8: (a) Single Majorana fermion spectrum $\varepsilon_c(\mathbf{k})$ for the isotropic Kitaev model, $K_x = K_y = K_z = -1$, on a cylinder with a three unit cell circumference. (b) Corresponding minimum energy for two-particle excitations, $\Omega_{\min.}(\mathbf{q})$.

operators, $2S_i^\alpha \rightarrow ib_i^\alpha c_i$,

$$\tilde{H} = - \sum_{\langle ij \rangle \alpha \beta} K_{ij}^{\alpha \beta} ib_i^\alpha b_j^\beta ic_i c_j, \quad (5.2)$$

where for $\langle ij \rangle$ a z -type bond,

$$K_{ij}^{\alpha \beta} = \frac{1}{4} \begin{cases} K & \alpha = \beta = z \\ \Gamma & \alpha \neq \beta \neq z \\ 0 & \text{otherwise} \end{cases}. \quad (5.3)$$

Similar definitions follow for x and y -type bonds. Here, the Majorana fermion operators are normalized such that $\{b_i^\alpha, b_j^\beta\} = 2\delta_{ij}\delta_{\alpha\beta}$ and $\{c_i, c_j\} = 2\delta_{ij}$. The physical Hilbert space of the spin Hamiltonian H is then obtained by projecting the Majorana Hamiltonian \tilde{H} onto the subspace of states $|\Psi\rangle$ which obey $D_i |\Psi\rangle \equiv b_i^x b_i^y b_i^z c_i |\Psi\rangle = |\Psi\rangle$. Within a mean-field approach, we can approximate \tilde{H} with

$$H_{MF} = - \sum_{\langle ij \rangle \alpha \beta} B_{ij} K_{ij}^{\alpha \beta} ib_i^\alpha b_j^\beta - \sum_{\langle ij \rangle} A_{ij} ic_i c_j + \sum_{\langle ij \rangle} A_{ij} B_{ij}, \quad (5.4)$$

where the fields A_{ij} and B_{ij} obey the mean-field self-consistency equations on each bond,

$$A_{ij} = \sum_{\alpha \beta} K_{ij}^{\alpha \beta} \langle ib_i^\alpha b_j^\beta \rangle_B, \quad (5.5)$$

$$B_{ij} = \langle ic_i c_j \rangle_A. \quad (5.6)$$

Given the ground state $|\Psi_0\rangle_{MF}$ of H_{MF} , it is possible to construct an approximate ground state for H by projection onto the physical Hilbert space, $|\Psi_0\rangle \approx \prod_i (1 + D_i)/2 |\Psi_0\rangle_{MF}$.

It is straightforward to obtain a uniform, Z_2 -flux-free, solution of Equations (5.5)

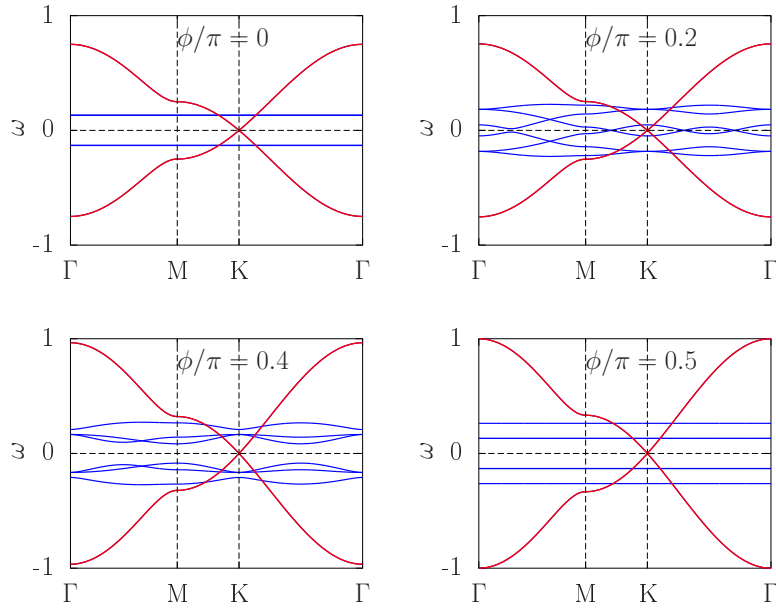


Figure 5.9: Band structure of c (red) and b (blue) Majorana fermions, plotted along high symmetry lines of the Brillouin zone, for several values of ϕ in the two dimensional thermodynamic limit. The flat bands for $\phi = 0$ are three-fold degenerate; for $\phi/\pi = 0.5$, the lower energy flat bands are two-fold degenerate. When $\phi/\pi \sim 0.2$, there is a finite density of zero energy b fermion states, around the K (and Γ) points in the Brillouin zone. At $\phi/\pi = 0.4$ the b fermion bands are still dispersive, but gapped.

and (5.6), in the two-dimensional thermodynamic limit. In the following we use the convention that in A_{ij}, B_{ij} etc., the subscript i indicates a site on the odd sublattice and j a site on the even sublattice. Assuming that $A_{ij} \equiv A$ on all bonds, we obtain $B_{ij} \equiv B = 0.5248$, which is independent of A . Similarly, A is independent of B , but it does depend on the ratio K/Γ . The mean-field ground state energy per bond is given by $E_{MF} = -AB$. By solving H_{MF} , it is possible to obtain the Majorana fermion spectrum, shown in Fig. 5.9 along high symmetry lines in the Brillouin zone, for several values of ϕ . In the Kitaev limit, $\phi = 0$, one finds a single dispersing c -fermion band, with Dirac nodes at the K points of the Brillouin zone, and whose band width is set by $A = K$. Three flat bands describe the b -fermions, which are localized on the bonds. For $\phi = \pi/2$, one obtains a similarly dispersing c -fermion band, with band width $A = 4\Gamma/3$, and three flat bands which describe the b -fermions localized on the hexagons. When both K and Γ are nonzero, the b -fermions are dispersive, and become gapless in the parameter range $0.15 < \phi/\pi < 0.25$.

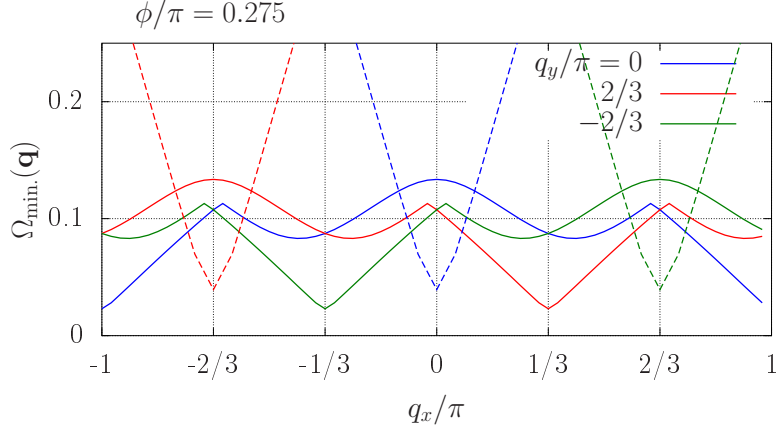


Figure 5.10: $b + c$ (solid) and $c + c$ (dashed) two-Majorana fermion spectrum plotted along the three momentum cuts allowed on a cylinder with a three unit cell circumference (see fig. 5.7)

5.5 Two-Majorana Spectrum, iDMRG vs. MFT

We have suggested that the TM spectrum can be associated with two-particle continua of fractionalized excitations, *some of which* obey a symmetry relation $E(k_x, k_y) = E(k_x + 2\pi/3, k_y - 2\pi/3)$. Interestingly, the Majorana mean-field Hamiltonian, Eq. (5.4), exhibits this symmetry for the b fermion spectrum, $\varepsilon_b(\mathbf{k}) = \varepsilon_b(\mathbf{k} \pm \mathbf{K})$ (see Sec. 5.5.1), inducing the same symmetry in the two-particle spectrum, $\Omega_{b+c}(\mathbf{q}, \mathbf{k}) = |\varepsilon(\mathbf{q} - \mathbf{k})| + |\varepsilon(\mathbf{k})|$, as well. We note that this symmetry, $\Omega_{b+c}(\mathbf{q} \pm \mathbf{K}, \mathbf{k}) = \Omega_{b+c}(\mathbf{q}, \mathbf{k})$, holds irrespectively of the properties of the c -fermion spectrum. In Sec. 5.5.1, we show that this is consistent with the iDMRG results, which exhibit this symmetry in the TM spectrum even when the K - Γ coupling are anisotropic such that the minima in the c spectrum move away from the K, K' points.

Thus, the form of H_{MF} may give a good description of the fractionalized excitations, as probed by iDMRG. However, due to the strongly interacting nature of the K - Γ model, the actual amplitudes A_{ij} and B_{ij} which should be used for such a description, as well as the value of ϕ itself, will most likely be very different from their values as determined by MFT. Nevertheless, we may still compare the MF spectra with the TM spectra, demonstrating the usefulness of H_{MF} . To do so let us study the same cylindrical geometry considered above using iDMRG. As in the iDMRG calculation where the cylindrical geometry breaks the symmetry between x and y, z bonds, here different amplitudes A_{ij}, B_{ij} for different bonds are chosen. Figure 5.10 contains a plot of the minimal energies required to excite two Majorana fermions, as given by

$$\Omega_{\min.}(\mathbf{q}) = \min_{\mathbf{k}} (|\varepsilon_{b,c}(\mathbf{q} - \mathbf{k})| + |\varepsilon_c(\mathbf{k})|), \quad (5.7)$$

where $\varepsilon_{b,c}(\mathbf{k})$ is the Majorana spectrum of H_{MF} . For finite anisotropy, $\varepsilon_{b,c}(\mathbf{k})$ opens a

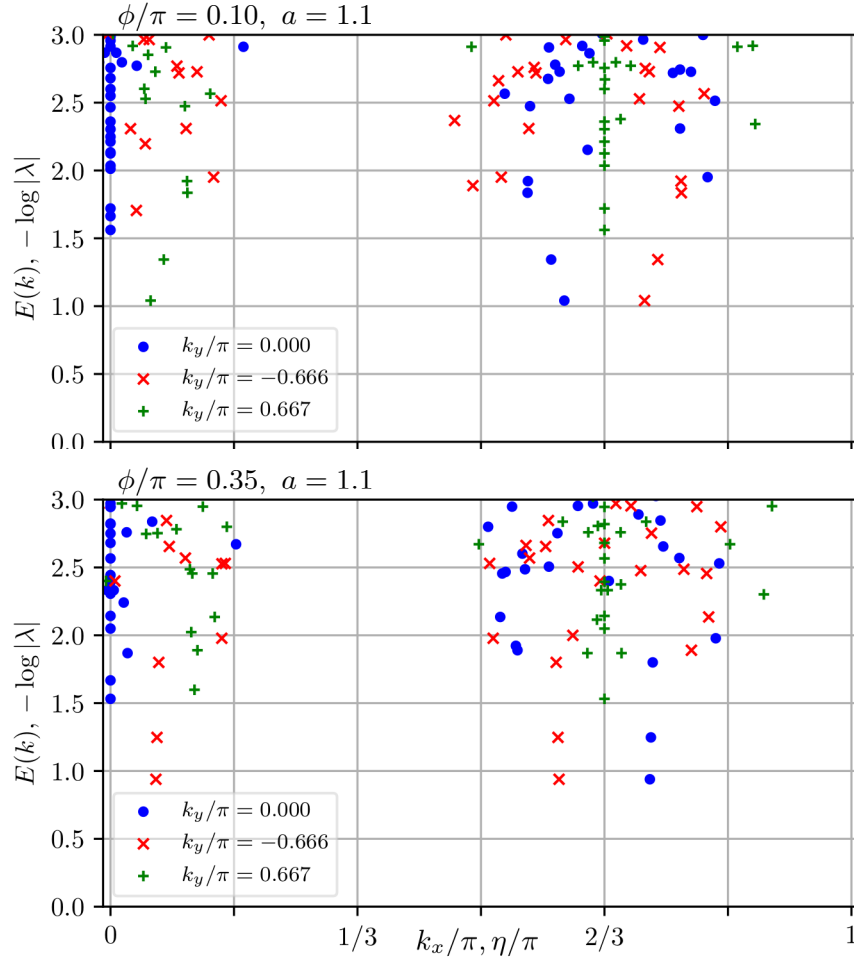


Figure 5.11: Quasi-energies $E(\mathbf{k})$ of the anisotropic K - Γ model for $\phi = 0.1$ (top) and $\phi = 0.35$ (bottom) with an anisotropy $a = 1.1$ according to Eq. 5.8.

gap at all allowed momenta, and consequently, also in $\Omega_{\min.}(\mathbf{q})$. Nevertheless, the K and K' points remain soft, as in the TM spectrum. Furthermore, additional soft modes appear at finite Γ in the $b + c$ spectrum, which obeys the symmetry $\Omega_{\min.}(\mathbf{q} \pm \mathbf{K}) = \Omega_{\min.}(\mathbf{q})$. For example, shifting the solid green curve ($q_y = -2\pi/3$) in Fig. 5.10 by $q_x = 2\pi/3$, yields the solid red curve ($q_y = 2\pi/3$). By demonstrating this symmetry, we may conclude that H_{MF} may give a good description of the low energy excitations of the K - Γ model, as seen in the TM spectrum.

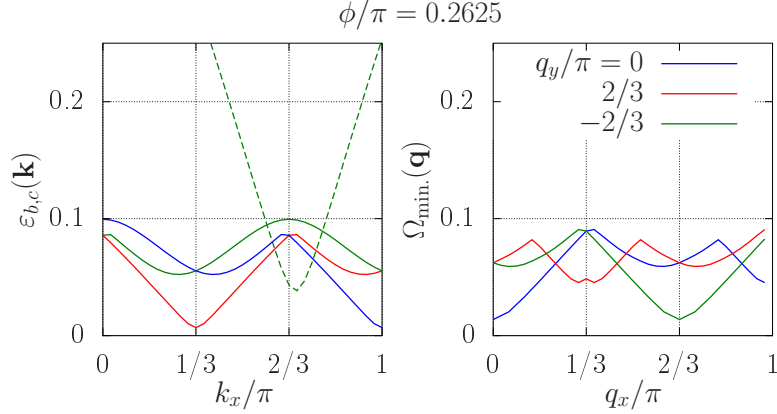


Figure 5.12: Left: $\varepsilon_c(\mathbf{k})$ (dashed) and $\varepsilon_b(\mathbf{k})$ (solid) for anisotropic mean-field amplitudes $A_x = 1, A_y = 1.1, A_z = 1.2$ and $B_x = 0.45, B_y = 0.5, B_z = 0.55$. Right: minimum energy for $b + c$ excitations. The spectra are plotted along the allowed momentum cuts, as in Fig. 5.7.

5.5.1 Anisotropic Coupling

Let us introduce an anisotropy by scaling the coupling parameter K_γ, Γ_γ by a factor a

$$\begin{aligned}
 (K_x, \Gamma_x) &\rightarrow (aK_x, a\Gamma_x) \\
 (K_y, \Gamma_y) &\rightarrow ((3/2 - a/2)K_y, (3/2 - a/2)\Gamma_y) \\
 (K_z, \Gamma_z) &\rightarrow ((3/2 - a/2)K_z, (3/2 - a/2)\Gamma_z) ,
 \end{aligned} \tag{5.8}$$

with respect to the x-bond. The anisotropy leads to a shift of the minimum in the c-fermion spectrum away from the K -point as is apparent in the MFT spectrum Fig. 5.12. The TM spectra, Fig. 5.11, do not display such a shift of the eigenvalues at the K -point (green +), neither for $\phi/\pi = 0.1$ nor for 0.35. Furthermore, the symmetry $\Omega_{\min.}(\mathbf{k} \pm \mathbf{K}) = \Omega_{\min.}(\mathbf{k})$ is unaffected by the anisotropy, which is consistent with the MFT prediction for the b and the $b + c$ fermion spectrum. In fact, the symmetry $\varepsilon_b(\mathbf{k} \pm \mathbf{K})$ emerges from the Majorana mean-field Hamiltonian, Eq. (5.4). As shown in Ref. [144, App. B], a unitary transformation exists, which takes $K(\mathbf{k} \pm \mathbf{K}) \rightarrow K(\mathbf{k})$. Therefore, the spectrum at the shifted momentum must be the same. As this symmetry holds irrespective of the details of the c fermion spectrum, it is therefore always induced in the $b + c$ spectrum as well. Figure 5.12 shows the single and two particle spectrum with fully anisotropic mean-field couplings. The minimum in the c fermions spectrum is clearly shifted away from the K point $(2\pi/3, -2\pi/3)$, while the $b + c$ spectrum exhibits the symmetry $\Omega_{\min.}(\mathbf{k} \pm \mathbf{K}) = \Omega_{\min.}(\mathbf{k})$.

5.6 Conclusion

In this chapter, a spin model with both the Kitaev (K) and symmetric-anisotropic (Γ) interactions on the honeycomb lattice was studied using iDMRG and Majorana mean-field theory. This model is strongly motivated by recent experiments on α -RuCl₃, where K and Γ are considered as the possibly dominant exchange interactions.

Numerical indication was presented for the existence of a quantum spin liquid for arbitrary ratio of Γ/K for ferro-type Kitaev interactions in iDMRG. In particular, the entanglement entropy remains high in this entire region while there is no sign of magnetic order in iDMRG computations. In contrast, we found a magnetically ordered state with very small entanglement entropy on the antiferro-type Kitaev side. Moreover, coherent two-dimensional multi-particle excitations exist as was demonstrated using the correspondence between transfer-matrix eigenvalues and the lower boundary of multi-particle excitation spectrum. The cylinder geometry in iDMRG induces an anisotropy in bond-dependent energy, which is expected to move the locations in momentum space of low energy excitations. This can indeed be seen in the transfer-matrix spectra. The existence of such two-dimensional coherence excitations without magnetic order is a very strong evidence of quantum spin liquid. Majorana mean-field theory was used to gain analytical insight in these numerical results. For example, we computed single and two-particle excitation spectra for the K - Γ model showed they exhibit an emergent symmetry in their momentum dependence, which is also found in the transfer matrix spectrum.

We may conclude that the scattering continuum seen in the neutron scattering experiment on α -RuCl₃ may come from a nearby quantum spin liquid supported by K - Γ interactions. In our numerical computations, the spin liquid phases at finite Γ/K show (to some extent) qualitatively the same behavior as the Kitaev spin liquid. However, a jump in the bond-dependent energy at a small value of Γ/K exists in iDMRG on a cylinder geometry, which causes a small kink in the entanglement entropy. This may be interpreted as a “meta-nematic” transition, where the bond-anisotropy (or broken 3-fold rotation symmetry) increases abruptly. Whether such a transition would survive in the two-dimensional limit is not clear at present. If it does survive, two possible scenarios could be considered. (i) The transfer matrix spectra on both sides of the transition share some qualitative features, suggesting that they are actually the same spin liquid phase, while the apparent transition may be interpreted as a Lifshitz transition on the Fermi surface topology of the underlying quasiparticles. As such it would be sensitive to the cylindrical geometry. (ii) Although the transfer matrix spectra may be described using Majorana fermions both before and after the transition, the underlying spin liquid ground states may be distinct. These questions will have to be addressed in future theoretical investigations. Further experimental data, e.g., in

external magnetic field, would provide additional clues for the validity of the assumption that the $K\text{-}\Gamma$ or $K\text{-}\Gamma\text{-}J_3$ is a good minimal model for $\alpha\text{-RuCl}_3$.

Chapter 6

Kitaev-Model in $[111]$ Magnetic Field

6.1 Introduction

On the theory side, significant insight into the physics of Quantum Spin Liquids (QSL) comes from the study of exactly solvable models. A prominent example is the Kitaev model on the honeycomb lattice [16], which exhibits a QSL phase featuring fractionalization of spin-1/2 degrees of freedom into fluxes and Majorana excitations as introduced in Sec. 2.3. The Kitaev interaction, a strongly anisotropic Ising exchange appears to be realized approximately in compounds with strong spin-orbit interaction [80, 145–148], such as the iridates Na_2IrO_3 , Li_2IrO_3 [85], and $\alpha\text{-RuCl}_3$ [109, 114, 149]. It may also be realized in metal-organic frameworks [87]. In such materials, additional interactions are important and typically lead to long-range magnetic order, nonetheless signatures of being in the proximity to the Kitaev QSL are discussed [28, 114, 133]. Recent attention has shifted to applying a magnetic field [133, 136, 144, 150–154], in particular experiments on the Kitaev compound $\alpha\text{-RuCl}_3$ (with an in-plane magnetic field) reveal a single transition into quantum paramagnetic phase with spin-excitation gap [115, 155–160].

In this chapter, the Kitaev model in a magnetic field along the $[111]$ axis is considered, such that the field couples to the spins in a symmetry-equivalent way and the field does not prefer any bond in particular. While the magnetic field breaks integrability, Kitaev has identified two three-spin exchange terms within perturbation theory, that break time-reversal symmetry and open a gap in the spectrum. One of the terms retains integrability and upon adding to the Kitaev model, leads to a topologically ordered phase hosting non-abelian anyons [16]. However, numerical simulations [84] reveal that the same topological phase occurs for small magnetic fields and ferromagnetic Kitaev coupling. The topological phase turns out to be more stable, by one order

of magnitude in the critical field strength, if an antiferromagnetic coupling is considered [161]. Remarkably, an additional regime, possibly gapless, between the low-field topological and the high-field polarized phase appears to exist [161].

The ground state phase diagram of the Kitaev model in a magnetic field along [111] is obtained utilizing large scale infinite density matrix renormalisation group (iDMRG) methods [23, 129, 140, 141] and simulate its dynamics using a matrix-product operator (MPO) based time-evolution [96].

The topologically ordered phase is characterized by its finite topological entanglement entropy (TEE) [74, 75]. By subtracting contributions of the Majorana fermions and the \mathbb{Z}_2 -gauge field from the numerically obtained entanglement entropy of a bipartition, one can extract a remainder which is identical to the TEE in the integrable case. In doing so, a clear signature of non-abelian anyonic quasiparticles in the topological phase is obtained. In a magnetic field, this remainder is still consistent with the existence of non-abelian anyons. Furthermore, the correlation length decreases with magnetic field in a way that is consistent with a cubic opening of the gap as found for the three-spin exchange [16]. However, the dynamical spin-structure factor in presence of a field behaves very differently compared to what is known for the three-spin exchange [78]. The magnetic field causes the flux degrees of freedom to become mobile. As a consequence the low-energy spectrum contains more structure and the gap in the dynamical spin-structure factor is reduced.

Approaching the intermediate regime from the polarized phase, the magnon modes reduce in frequency and simultaneously flatten. This resembles the phenomenology within linear spin wave theory (LSWT) [150, 162], but the transition is significantly renormalised to lower fields. Close to the transition, a broad continuum exists that, within our reachable resolution in frequency, reaches down to zero frequency and merges with the single magnon branches. At the transition, the appears to be (nearly) gapless in the entire reciprocal space.

The remainder of this chapter is structured as follows: In Sec. 6.2 the model consisting of Kitaev term, Zeeman coupling to a magnetic field along [111], and three-spin exchange is introduced. In Sec. 6.3, the ground state phase diagram is discussed for both signs of the Kitaev coupling. We then focus on the antiferromagnetic Kitaev coupling in Sec. 6.4 and study its dynamical signatures within the low-field topological as well as the high-field polarized phases. The latter phase exhibits topological magnons, that are addressed separately in the next chapter 7. A summary and discussion follows in Sec. 6.5.

6.2 Model

The Hamiltonian describing the Kitaev model in a magnetic field along [111] direction reads

$$H = \sum_{\langle i,j \rangle_\gamma} K_\gamma S_i^\gamma S_j^\gamma - h \sum_i (S_i^x + S_i^y + S_i^z) , \quad (6.1)$$

where the first term is the pure Kitaev model (cf. Sec. 2.3.1) exhibiting strongly anisotropic spin exchange coupling [16]. Neighboring spins couple depending on the direction of their bond γ with $S^x S^x$, $S^y S^y$ or $S^z S^z$. The second term is the Zeeman-coupling of the spins to a magnetic field applied in [111] direction. Note that, the factor of 2 in front of K_γ as in Eq. (2.46), cf. Sec. 2.3.8, is not added throughout this chapter.

In the zero field limit, the Kitaev model exhibits a quantum spin liquid ground state with fractionalized excitations [16]. Depending on K_γ , the spectrum of the fermions is either *gapped* (*A-phase*) or *gapless* (*B-phase*). Let the K_γ be sorted as $K_\alpha \geq K_\beta \geq K_\gamma$, then the gapless B-phase occurs if $|K_\alpha| \leq |K_\beta| + |K_\gamma|$ and the A-phase if $|K_\alpha| > |K_\beta| + |K_\gamma|$. In the remainder, we consider the isotropic case $K_\gamma = K = \pm 1$.

As introduced in Sec. 2.3.2, the full Hilbert space gets separated (in the $h = 0$ limit) by an extensive set of quantum numbers, so called fluxes, defined as $W_p = \prod_{i \in \mathcal{P}} \sigma_i^{\gamma(i)}$ with eigenvalues $w_p = \pm 1$. After fixing all the fluxes w_p , a free fermion problem remains to be solved. The ground state lies in the flux-free sector, that is $\forall i : W_{p,i} = +1$.

For later use, let me comment on placing the Kitaev model on a cylinder. A second flux operator of a non-contractable loop \mathcal{C} going around the cylinder can be defined: $W_l = \prod_{i \in \mathcal{C}} \sigma_i^{\gamma(i)}$. Similarly to W_p , W_l commutes with the Hamiltonian, has eigenvalues ± 1 , and separates the full Hilbert space in two subspaces. With respect to the free fermions, $W_l = -1$ (flux-free) corresponds to periodic and $+1$ to antiperiodic boundary conditions along the circumference of the cylinder. The ground state within each of the two sectors are separated in energy by ΔE , which depends on the circumference L_{circ} and vanishes in the limit $L_{\text{circ}} \rightarrow \infty$.

Applying a magnetic field h along [111], as in Eq. (6.1), breaks time-reversal symmetry and opens a gap in the fermionic spectrum. The lowest order terms breaking time-reversal and not changing the flux configuration are the three-spin exchanges $S_i^x S_j^y S_k^z$. Two such terms appear in a perturbation theory approach [16], see also Sec. 2.3.5. Here, only the three spin term is taken into account, that preserves integrability. The corresponding Hamiltonian reads

$$H_{K_3} = \sum_{\langle i,j \rangle_\gamma} K_\gamma S_i^\gamma S_j^\gamma + K_3 \sum_{\langle\langle i,j,k \rangle\rangle} S_i^x S_j^y S_k^z , \quad (6.2)$$

where $\langle\langle \cdot \rangle\rangle$ denotes an ordered tuple (i, j, k) of neighboring sites such that the S^x , S^y , and S^z at the outer two sites coincide with the label of the bond connecting to the

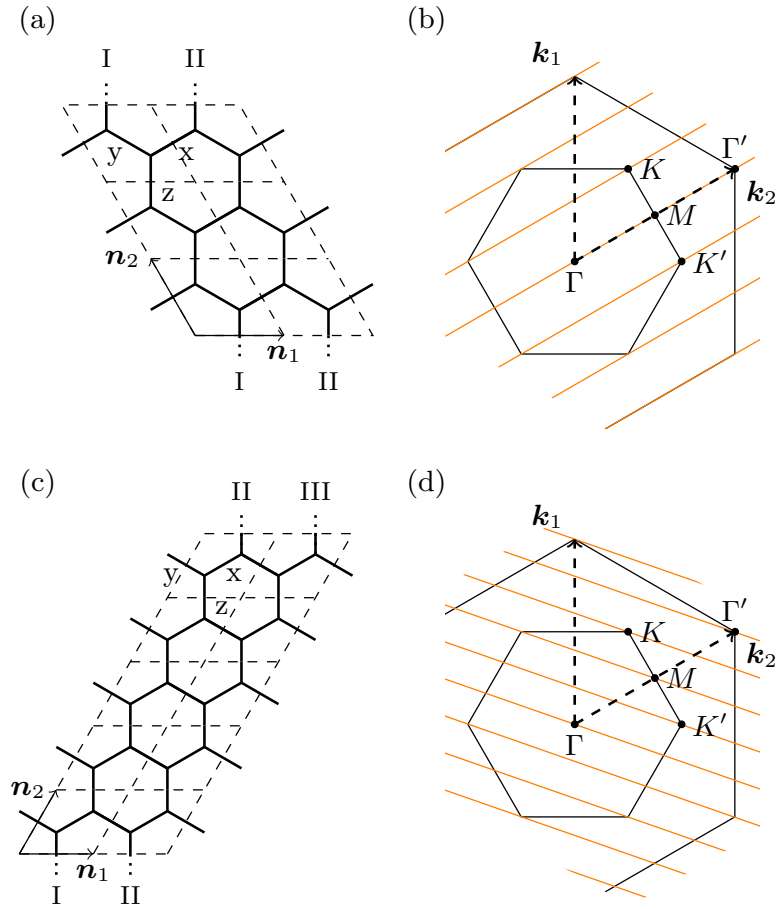


Figure 6.1: Geometries used for iDMRG and their corresponding accessible momenta (orange lines) in reciprocal space with respect to the first Brillouin zone (inner hexagon). The second Brillouin zone is shown partially. The roman numbers label links across the boundary. (a) rhombic geometry with three unit cells, $L_{\text{circ}} = 6$ sites, along the circumference and (b) its corresponding reciprocal space. (c,d) rhombic-2 geometry with five unit cells circumference, $L_{\text{circ}} = 10$ sites.

central site. The flux operators W_p and W_l still commute with H_{K_3} and separate the Hilbert space. The remaining fermionic Hamiltonian is quadratic with the corresponding bands having non-zero Chern number ± 1 and yielding composite excitations with anyonic exchange statistics [16].

6.3 Ground State Phases

The ground state is obtained using the *matrix product state* (MPS) based *infinite density matrix renormalisation group* (iDMRG) method [23, 129, 140, 141]. Being a standard technique for one-dimensional systems, it has been used in two dimensions by wrapping the lattice on a cylinder and mapping the cylinder to a chain with longer range interactions.

We employ a *rhombic-2* geometry with a circumference of $L_{\text{circ}} = 10$ sites and a *rhombic* geometry with $L_{\text{circ}} = 6$ as illustrated in Fig. 6.1. Both geometries capture the K -points in reciprocal space and hence are gapless for pure Kitaev-coupling ($h = 0$). A main advantage of the *rhombic-2* geometry is its translational invariance of the chain winding around the cylinder. While the mapping to a cylinder for the *rhombic* geometry requires an iDMRG unit cell of at least L_{circ} sites, a single fundamental unit cell with two sites is sufficient to simulate an infinite cylinder using the *rhombic-2* geometry. Different iDMRG cells have been used to test for possible breaking of translational symmetry and corresponding results will be presented when of relevance. Bond dimensions of up to $\chi = 1600$ are used for the computation of the phase diagram.

We confirm the existence of two phases and a single transition for ferromagnetic Kitaev coupling [84, 161] (FMK, $K < 0$), and of at least three phases for antiferromagnetic Kitaev coupling [161] (AFK, $K > 0$). For both, FMK and AFK, a topological phase at low field and a field-polarized phase at high field exist. Only for AFK, an intermediate, seemingly gapless, phase can be identified.

6.3.1 Topological Phase

For small h , the system forms a non-abelian topological phase [16]. Its stability upon applying h vastly differs depending on the sign of the Kitaev interaction. Employing a *rhombic-2* geometry with $L_{\text{circ}} = 10$, we find, in case of AFK, that this phase ranges up to $h_{c1,AF} \approx 0.22$, whereas for FMK it ranges only up to $h_{c,FM} \approx 0.014$. Both values are based on the peaks in the second derivative $-d^2E/dh^2$ of the energy with respect to the magnetic field. However, subtle features are present for AFK at slightly lower $h \approx 0.2$, which become less pronounced with larger bond dimension χ . In comparison to values reported earlier [84, 161] we find a nearly 30% lower value for the FMK transition $h_{c,FM}$. This is due to the fact that for rather small circumferences, the ground state energy within the topological phase is strongly sensitive to the boundary condition as has already been noted in Ref. [16]. The *rhombic-2* geometry we employ has the same twisted boundary condition as the $(L\mathbf{n}_1, L\mathbf{n}_2 + \mathbf{n}_1)$ geometry employed in [16], which is shown to converge better in energy when increasing L or L_{circ} , respectively. The transition field $h_{c,FM}$ may still decrease slightly upon further increasing L_{circ} and approaching the two-dimensional limit $L_{\text{circ}} \rightarrow \infty$.

For small h , the staggered magnetisation (not shown here) grows proportionally with h . The two sectors found on the cylindrical geometry and determined by $W_l = +1$ or $W_l = -1$ are distinguished by their behaviour of the entanglement entropy S_E and the correlation length ξ . The $W_l = +1$ sector is characterized by finite ξ and S_E due to being gapped by imposing antiperiodic boundary conditions on the Majorana fermions, see also the remark in Sec. 2.3.2. In contrast, the $W_l = -1$ sector has divergent ξ and S_E when $h = 0$, where it is gapless. In the latter, encoding the wave function as MPS

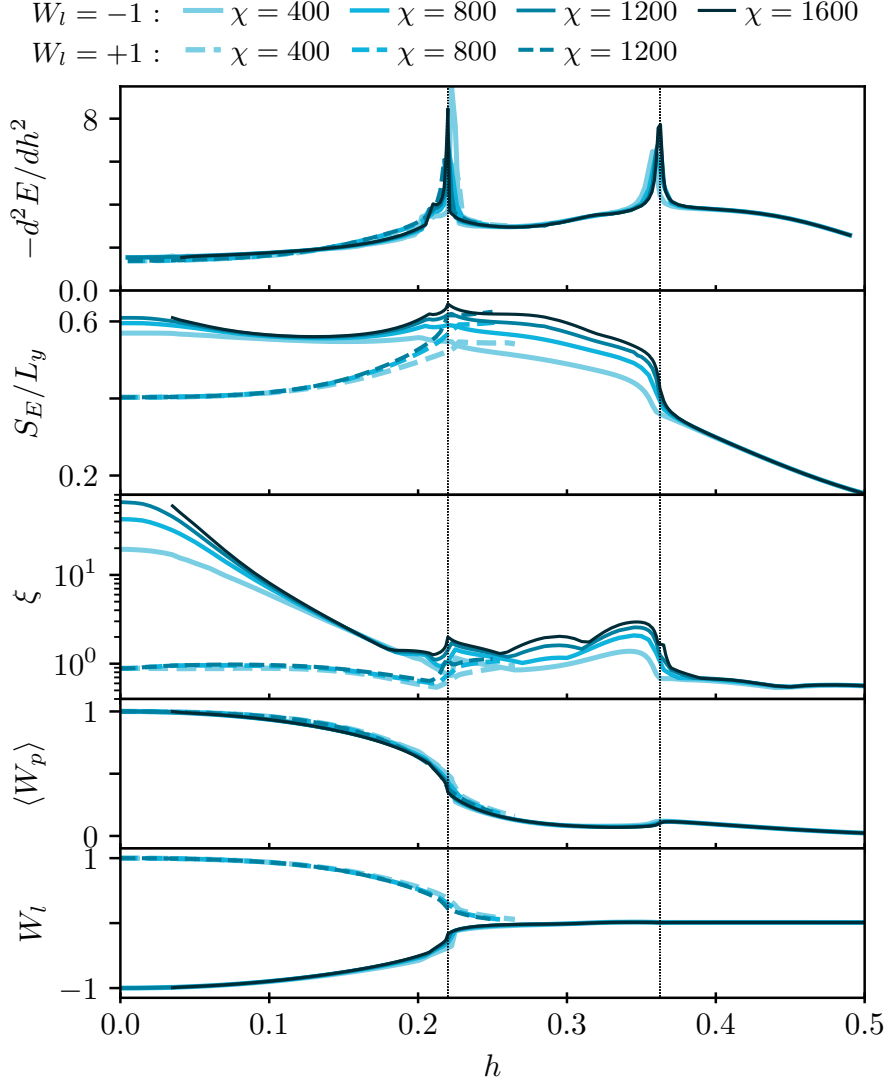


Figure 6.2: Several observables of the Kitaev model with antiferromagnetic coupling, $K > 0$, in a magnetic field along [111]. From top to bottom: Second derivative $-d^2E/dh^2$ of the energy with respect to the field h , entanglement entropy S_E of a bipartition of the cylinder divided by the number L_y of bonds cut, correlation length ξ , average of plaquette fluxes $\langle W_p \rangle$, and flux W_l of a non-contractible loop around the cylinder. At least three phases are observed: topological phase for $h < h_{c1,AF} \approx 0.22$, intermediate possibly gapless $h_{c1,AF} < h < h_{c2,AF} \approx 0.36$, and a subsequent field-polarised phase. Solid blue lines are for the $W_l = -1$ sector, dashed blue lines for $W_l = +1$, and its intensity encodes the bond dimension χ used, where dark blue refers to a large χ . Thin dashed black lines depict the phase transitions obtained from the peaks in $-d^2E/dh^2$.

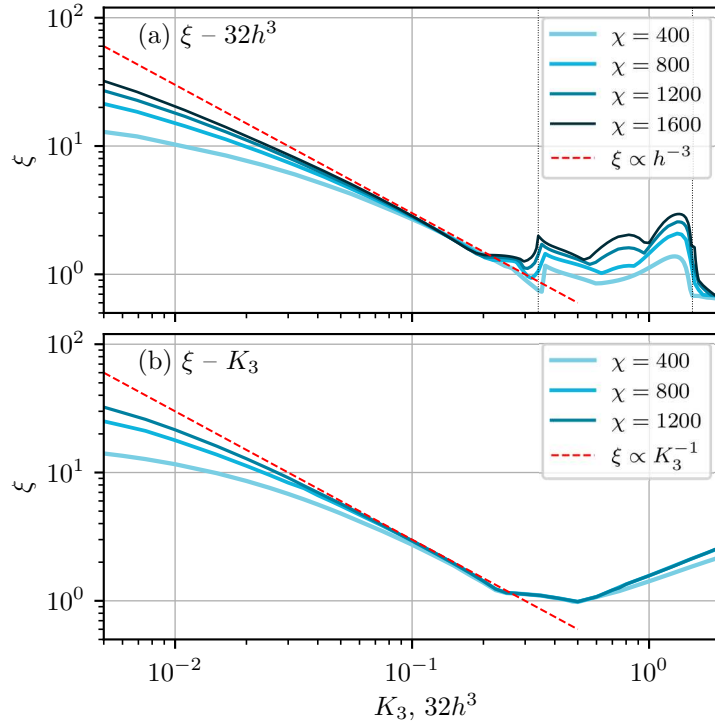


Figure 6.3: Comparison of correlation length ξ between (a) the rescaled magnetic field $h \rightarrow 8h^3$ and (b) the three-spin exchange K_3 . The solid red line is a guide-to-the-eye corresponding to a $1/K_3$ or $1/(32h^3)$ scaling. Within $0.05 < K_3, 32h^3 < 0.2$, that is where numerical convergence is achieved, the behaviour of ξ is consistent with a predicted opening of the gap as $\Delta E \propto h^3$ or as $\Delta E \propto K_3$, respectively.

with a finite χ induces an effective gap that limits ξ and S_E . In fact, the growth of ξ and S_E with increasing χ is connected via $S_{E,\chi} = c/6 \log \xi_\chi + \text{const}$ [90, 93], where c is the universal *central charge*. This has been named finite entanglement scaling and allows to confirm $c = 1$ (for $h = 0$, $W_l = -1$) as has been checked previously on a different cylinder geometry [127]. As a side remark, the notion of a central charge is applicable due to using a cylinder geometry and effectively mapping the model in question to a one-dimensional system.

In a magnetic field, $\langle W_p \rangle$ as well as the cylinder flux W_l begin to slowly deviate from ± 1 until they vanish close to the transition. The plaquette fluxes W_p , as defined in the integrable limit, are not conserved anymore for finite h as the application of a single S_i^z creates a flux each on the two plaquettes adjacent to bond γ at site i . However, an adiabatically connected operator \tilde{W}_l of W_l is expected to exist, such that $\tilde{W}_l \approx \pm 1$ [163]. Such a dressed Wilson loop \tilde{W}_l separates the two sectors found on the cylinder for any h within the topological phase.

Numerical convergence, that is ξ and S_E become χ -independent, is achieved for

$0.1 < h < 0.18$. In that range ξ reflects the physical excitation gap [101] via $\Delta E \propto 1/\xi$. Figure 6.3, where the x-axis has been rescaled $h \rightarrow 32h^3$, enables a direct comparison with the three-spin exchange K_3 in H_{K_3} . Both exhibit a very similar decrease of ξ with a $\xi \propto 1/x$ scaling, where x is either $32h^3$ or K_3 . ξ reaches a plateau at $x = 0.2$ with a low $\xi \approx 1$. If h is applied, a small χ -dependent dip and the phase transition into the intermediate regime follows, whereas for K_3 the plateau ranges up to $K_3 = 1$, from where ξ increases again¹. The entanglement entropy S_E reaches, in the case of a magnetic field, a plateau already at $32h^3 \approx 0.06$ ($h \approx 0.12$) beyond which it raises again until the transition field $h_{c1,AF}$ is reached. At all fields the entanglement remains larger than for the corresponding K_3 . A more detailed discussion about the entanglement in the context of topological excitations and topological entanglement entropy follows below. The $W_l = +1$ sector has χ -independent ξ and S_E up to $h \approx 0.18$. Before the transition ($0.18 < h < h_{c1,AF}$) both sectors exhibit a χ -dependents which suggests a closing of the gap at the transition and, thence, indicates that the transition might be continuous.

Let us now focus on the characterization of the topological order occurring at low magnetic fields h or when non-zero K_3 is considered. First, recall some facts about topologically ordered systems on an infinite cylinder [73, 164]. Generally, topological order leads to a ground state degeneracy with a number of degenerate states being equal to the number of emergent quasiparticle species. These ground states are conveniently represented as minimally entangled states (MES) [91, 164], say $|\psi_0^i\rangle$, where the superscript i denotes the particular quasiparticle. By utilizing iDMRG, such MES are selected naturally, and the obtained MPS corresponds to one of the quasiparticles [73, 92].

Upon cutting a cylinder into two semi-infinite halves, the entanglement entropy grows proportional with the circumference L_{circ} as [74]

$$S_E = \alpha L_{\text{circ}} - \gamma_i, \quad (6.3)$$

where γ_i denotes the topological entanglement entropy (TEE) [74, 75]. A non-zero TEE $\gamma_i = \log(\mathcal{D}/d_i)$ reveals topological order and is connected to the total quantum dimension \mathcal{D} , which itself is a sum of the quantum dimension d_i of each quasiparticle

$$\mathcal{D} = \sqrt{\sum_i d_i^2}. \quad (6.4)$$

The quantum dimension is related to the fusion vector space, which is spanned by all the different ways anyons can fuse to yield a trivial charge [71, 74]. The quantum dimension

¹For large $K_3 \gg 1$, the flux gap reduces and vanishes. The ground state is then not in a flux-free sector anymore.

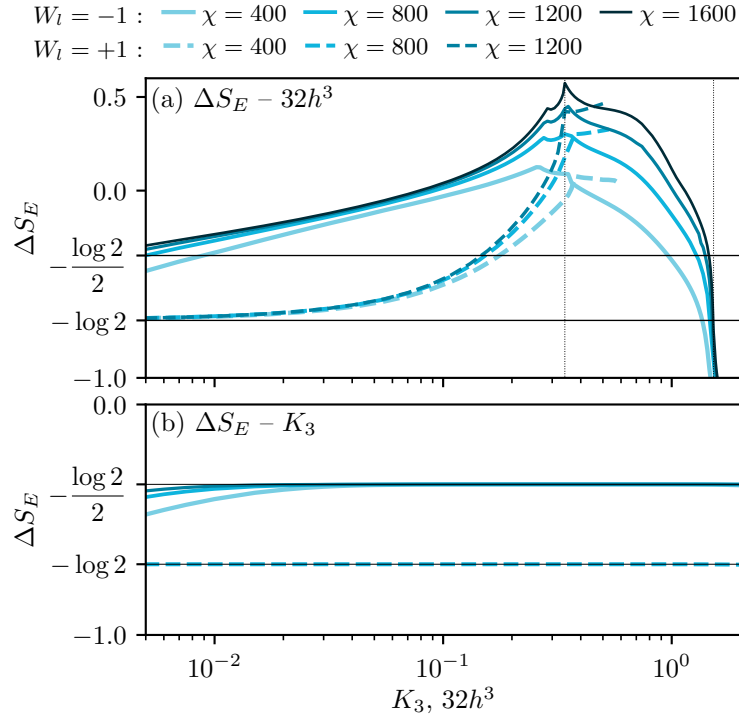


Figure 6.4: Remainder ΔS_E of the entanglement entropy of a bipartition of the cylinder after subtracting a fermionic and a gauge field contribution following Eq. (6.7). The magnetic field has been rescaled, $h \rightarrow 32h^3$, based on the behaviour of the correlation length in Fig. 6.3. The vertical dashed lines signal the transitions in a magnetic field. The horizontal lines correspond to $\log(\mathcal{D}/d_i)$ as discussed in the main text.

of abelian anyons is $d_i = 1$, whereas for non-abelian anyons d_i is generally larger than one [71]. The gapped phase of the Kitaev model upon applying K_3 is known to exhibit topological order hosting non-abelian Ising anyons [16]. The following quasiparticles exist: $\mathbb{1}$ (vacuum), ϵ (fermion), and σ (vortex), of which σ has a quantum dimension $d_\sigma = \sqrt{2}$ and the other two $d_{\mathbb{1}} = d_\epsilon = 1$. From (6.4) follows a total quantum dimension of $\mathcal{D} = 2$.

The Kitaev model has two separate contributions [76] to the entanglement entropy

$$S_E = S_G + S_F . \quad (6.5)$$

The first contribution, S_G , originates from the static \mathbb{Z}_2 -gauge field and is stated to be [76, 77]

$$S_G = \left(\frac{N_y}{2} - 1 \right) \log 2 , \quad (6.6)$$

where N_y is the number of unit cells along the circumference and equals the number of bonds cut by the bipartition, thus $N_y = L_{\text{circ}}/2$. The second contribution, S_F ,

describes the entanglement of the matter fermions [76]. By comparison with Eq. (6.3), the constant part in Eq. (6.6) reflects the aforementioned TEE, $\gamma_i = \log 2$.

Turning to the iDMRG results now, the entanglement entropy is readily available from the MPS representation of the ground state wave function. As will become clear later, the following quantity is considered

$$\Delta S_E = S_E - S_F - \frac{N_y}{2} \log 2 \approx \gamma_i, \quad (6.7)$$

where S_E is the entanglement entropy extracted numerically using iDMRG. S_F can be computed exactly via the eigenvectors of the fermion hopping matrix if H_{K_3} is considered [76, 165]. S_F is computed on a torus with one dimension equalling L_{circ} and the second dimension being much larger. Note that a bipartition of a torus leaves two cuts of length L_{circ} , whereas on the cylinder there is only one such cut. Thence, only half of \tilde{S}_F of a torus is considered in Eq. (6.7).

In the exactly solvable case of H_{K_3} , ΔS_E reproduces the TEE, such that $\Delta S_{E,K_3} = \gamma_i$ for all K_3 , except when iDMRG is not converged with respect to χ . From Fig. 6.4, we recover the following TEE

$$\gamma_i = \begin{cases} \log 2 & (W_l = +1), \\ \log \frac{2}{\sqrt{2}} & (W_l = -1), \end{cases} \quad (6.8)$$

which depends on the sector $W_l = \pm 1$. In the gapless limit of the $W_l = -1$ sector ($K_3 = 0$), S_F is divergent. Thus, at small K_3 the MPS improves with increasing χ similar to the behaviour of ξ discussed before. Nonetheless, from (6.8) a total quantum dimension of $\mathcal{D} = 2$ can simply be read off. The $W_l = -1$ sector contains a non-abelian anyon, a vortex σ , with quantum dimension $d_i = \sqrt{2}$. The ground state of the $W_l = +1$ sector is doubly degenerate with $d_i = 1$ for both states. Thus, the expected degeneracy is recovered.

Upon applying the magnetic field, the integrability of H_{K_3} in Eq. (6.2) is lost and the fermionic contribution S_F cannot be computed exactly. Based on the fact that we observe a similar opening of the gap in the fermionic spectrum for K_3 and h when the magnetic field is rescaled as $h \rightarrow 32h^3$, we assume that S_F as a function of the rescaled magnetic field $S_F(32h^3)$ is similar to $S_F(K_3)$ as a function of K_3 . This assumption is at least justified in the limit of small h . Figure 6.4(a) displays ΔS_E in a magnetic field, where it approaches the same values of γ_i for small h . At elevated fields, ΔS_E begins to deviate from $\gamma = \log 2$ or $\gamma_\sigma = \log \sqrt{2}$. ΔS_E increases monotonically until the transition into the intermediate phase is reached.

In a magnetic field, the separability of fluxes and fermions is lost and generically additional entanglement between fluxes and fermions is created. Such entanglement generates an additional contribution $S_{F \otimes G}$ to the entanglement entropy, which is not

accounted for in Eqs. (6.5) and (6.7). As this deviation occurs continuously, we like to argue that the topological phase in a low magnetic field is adiabatically connected to the topological phase of H_{K_3} at non-zero K_3 .

As a remark, the difference of ΔS_E between the $W_l = \pm 1$ sectors is not constant. This is due to the correlation length of the fermions being enhanced in the -1 sector, particularly near the gapless limit ($h = 0$), where it diverges. Thus, the fermions may build up entanglement with the fluxes in an increased area near the cut resulting in an enhanced $S_{F \otimes G}$.

In conclusion, we find numerical evidence for a total quantum dimension $\mathcal{D} = 2$ with non-abelian anyons having quantum dimension $d_i = \sqrt{2}$ in the exactly solvable model using the three-spin term. The results using the magnetic field, breaking integrability of the original model, are still consistent with the results above. However, a significant contribution to the entanglement entropy arises at increased magnetic fields.

6.3.2 Intermediate Regime

Only for AFK, an intermediate region exists ranging from $h_{c1,AF} < h < h_{c2,AF}$, where $h_{c1,AF} \approx 0.22$ (for *rhombic-2*, $L_{\text{circ}} = 10$) marks the transition from the topological phase and $h_{c2,AF} \approx 0.36$ the transition into the field-polarised phase.

The flux expectation values W_p and W_l approach zero continuously. Interestingly, the coexistence of both sectors found in the topological phase, $W_l|_{h=0} = \pm 1$, persists beyond the transition $h_{c1,AF}$. The peak in $-d^2 E/dh^2$ signaling this transition is independent of the particular sector.

The ground state within the intermediate regime requires to go to comparably large bond dimensions $\chi \approx 1000$. Using smaller χ , the ground state is very sensitive to the cylindrical geometry as well as the size of the iDMRG cell. However, based on a $1/\chi$ -extrapolation of the ground state energy, that is presented below, we find evidence for a translationally invariant ground state. In particular, when using a larger iDMRG cell, translational symmetry gets restored upon reaching a sufficiently large χ .

Finite size dependence

Let us focus on issues arising due to finite-size as well as finite bond dimension of the matrix product state (MPS). Figure 6.5 provides a comparison of the ground state energy E_{GS} for two different geometries, *rhombic* with $L_{\text{circ}} = 6$ or *rhombic-2* with $L_{\text{circ}} = 10$, as well as several different sizes of the iDMRG cluster at a magnetic field of $h = 0.275$. Similar checks are done at different h .

In case of *rhombic-2* with $L_{\text{circ}} = 10$ (green symbols), the smallest cluster is similar to a single fundamental unit cell with two sites (green circles), that is repeated along a chain winding around the cylinder. Next larger clusters are: four sites ($n = 2$

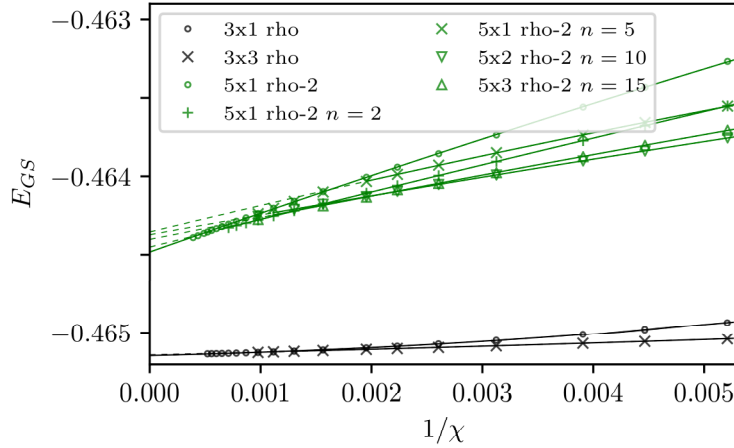


Figure 6.5: Comparison of the ground state energy E_{GS} vs. bond-dimension χ for different geometries and sizes of the iDMRG cluster at a single field strength of $h = 0.275$. For small χ , larger iDMRG cluster have a smaller E_{GS} . However, in the limit $1/\chi \rightarrow 0$, E_{GS} is of very similar value for all geometries used. In fact, large iDMRG cluster show a phase transition from an ordered ground state at small χ to a translational invariant ground state at large χ captured by the smallest iDMRG cluster.

fundamental unit cells, green 'x'), 10 sites ($n = 5$, green '+'), 20 sites ($n = 10$, green lower triangle), and 30 sites ($n = 15$, green upper triangle). When using small bond-dimensions $\chi < 500$, larger iDMRG clusters result in lower ground state energies E_{GS} . Upon increasing χ , the different energies approach each other until eventually a transition to the ground state of a smaller cluster occurs, e.g., at $\chi \geq 512$ the 10 site cluster ('x') has the same ground state properties as the fundamental unit cell (circles). Such a χ -transition is unphysical and a mere property of truncating the MPS.

In case of *rhombic* with $L_{\text{circ}} = 6$ (black symbols) in Fig. 6.5, the smallest iDMRG cluster is a single ring with three fundamental unit cell along the circumference ('3x1', black circles). Larger clusters of three repetitions along the cylinder ('3x3', black triangles) and six repetitions (not shown, but equivalent to '3x3') are checked. As above, a similar χ -transition at $\chi \approx 800$ is found, where for smaller χ the '3x3' has a lower E_{GS} , but transitions to the same state as '3x1' for larger χ .

In conclusion, the ground states for larger χ are not exhibiting any broken translational symmetry and may resemble the physical ground state. Thus, the use of iDMRG cell composed of a single fundamental unit cell is justified for computing the phase diagram shown in Fig. 6.2.

This motivates the use of the *rhombic-2* geometry with an iDMRG cell equivalent to a single fundamental unit cell, which on the one hand suppresses ground states with enlarged unit cells due to broken translational symmetry, but on the other hand saves computational resources better spent in reaching larger χ .

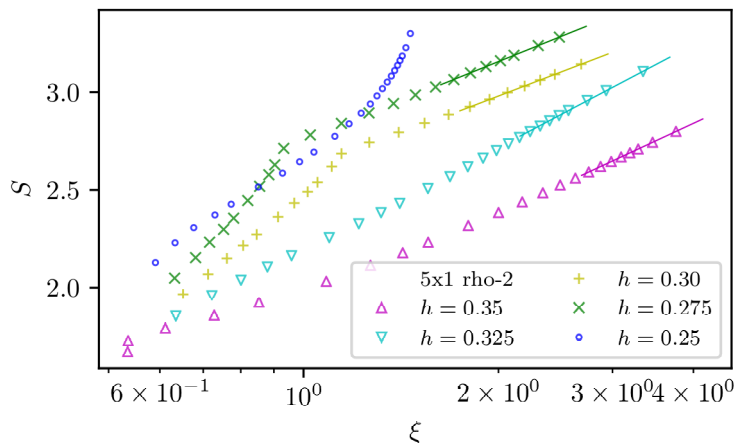


Figure 6.6: Entanglement entropy S of a bipartition of the cylinder over correlation length ξ for various bond dimension χ to check for possible finite- χ scaling. Data is shown for different magnetic field strength $h = 0.25, 0.275, 0.3, 0.325, 0.35$ across the intermediate regime. Lines are fits to the five points with largest ξ at each field.

Finite- χ scaling

Returning to its physical properties, the intermediate region exhibits a behaviour typical for a gapless phase. Both correlation length ξ and entanglement entropy S_E are not converged with respect to χ , where ξ increases slowly with χ , while S_E increases somewhat faster than in the gapless Kitaev limit. As we are studying effectively a one-dimensional system due to the cylindrical geometry, the finite- χ scaling [93] extracting a central charge may be applicable [166]. In that context, the behaviour of S_E and ξ indicate a larger central charge c , than found in the B-phase of the bare Kitaev model.

To get more specific, let us assume the MPS do reflect physical properties of the underlying phase and apply a finite- χ scaling. For $h = 0.275, 0.3, 0.325$, and 0.35 we obtain a $S_{E,\chi} = c/6 \log \xi_\chi + \text{const}$ scaling typical for a gapless phase [90, 93], see Fig. 6.6. Linear regression of the five points with largest χ reveal slopes corresponding to central charges of $c = 3.49$ at $h = 0.275$, $c = 3.31$ at $h = 0.30$, $c = 4.54$ at $h = 0.325$, and $c = 4.01$ for $h = 0.35$, all for *rhombic-2* with $L_{\text{circ}} = 10$. Not all of the c represent physical central charges. $h = 0.3$ has a very similar behaviour in terms of S_E vs. ξ , but a slightly smaller c , which may converge to 3.5 for larger χ . For $h = 0.25$, χ does not yet suffice to enter a linear $S_E \propto \log \xi$ regime. In summary, the finite- χ scaling does not reveal a conclusive c , and the extracted central charges are to be taken with care. In particular, the range of ξ over which linear regression is applied is rather limited.

Furthermore, the behaviour ξ for larger $\chi \geq 800$ suggests a separation of the intermediate region into three phases, of which the middle one grows in extent with larger χ . Given the large entanglement and the sensitivity to boundary conditions, our iDMRG results can only be suggestive for the nature of the ground state in the two-dimensional

limit.

6.3.3 Polarized Phase

A transition to the large- h field-polarized phase occurs at $h_{c2,AF} \approx 0.36$ (AFK), or $h_{c,FM} \approx 0.014$ (FMK), respectively. The polarized phase is gapped, which is signaled by the DMRG simulations by a finite correlation length ξ and finite entanglement entropy S_E . The entanglement S_E decreases with increasing field h and vanishes once the magnetic moments approach saturation, where the ground state is a simple product state. At the transition both, FMK and AFK, exhibit a longitudinal magnetic moment of $\approx 55\%$ of saturation along the [111] direction without any transverse component. The longitudinal moment grows with h reaching 90% saturation near $h \approx 0.6$ (AFK) and $h \approx 0.2$ (FMK). Large magnetic moments motivate perturbative methods like spin wave-theory [162]. In comparison to linear spin wave theory (LSWT) [150], the transition gets renormalized significantly from $h_{LSW,AF} = 1/\sqrt{3} \approx 0.58$ down to $h_{c2,AF}$. For FMK, LSWT predicts a transition at exactly zero [150], whereas in iDMRG it occurs at small, non-zero field.

6.4 Dynamical Spin-Structure Factor

The *dynamical spin-structure factor* $\mathcal{S}(\mathbf{k}, \omega)$ contains information about the excitation spectrum and is experimentally accessible via scattering experiments, in particular inelastic neutron scattering. $\mathcal{S}(\mathbf{k}, \omega)$, here considering the diagonal $\mathcal{S}(\mathbf{k}, \omega) = \sum_{\gamma=\{x,y,z\}} \mathcal{S}^{\gamma\gamma}(\mathbf{k}, \omega)$, is defined as the spatio-temporal Fourier transform of the dynamical correlations $C_{ab}^{\gamma\gamma}(t)$ that is computed numerically utilizing a matrix-product-operator based method outlined in Sec. 3.3.

On the technical side, we first compute the spatial Fourier transform of $C_{ab}^{\gamma\gamma}(t)$, extend the time-signal using linear predictive coding [131], and multiply with a gaussian to suppress ringing due to the finite-time window. The extension of the time-signal allows for much wider finite-time windows keeping a significant part of the simulated real-time dynamics. All spectra shown in the remainder have a broadening of $\sigma_\omega = 0.018$ due to multiplying the real-time data with a Gaussian of width $\sigma_t = 55.8$. The real-time data is obtained for times up to $T = 120$ on cylinders with *rhombic* geometry and $L_{\text{circ}} = 6$.

In the following, we discuss $\mathcal{S}(\mathbf{k}, \omega)$ within the topological phase and the polarized phase. Simulating the dynamics within the intermediate regime is left for future work as the necessary bond dimension for encoding the ground state is too large to achieve appreciably long times in the time-evolution.

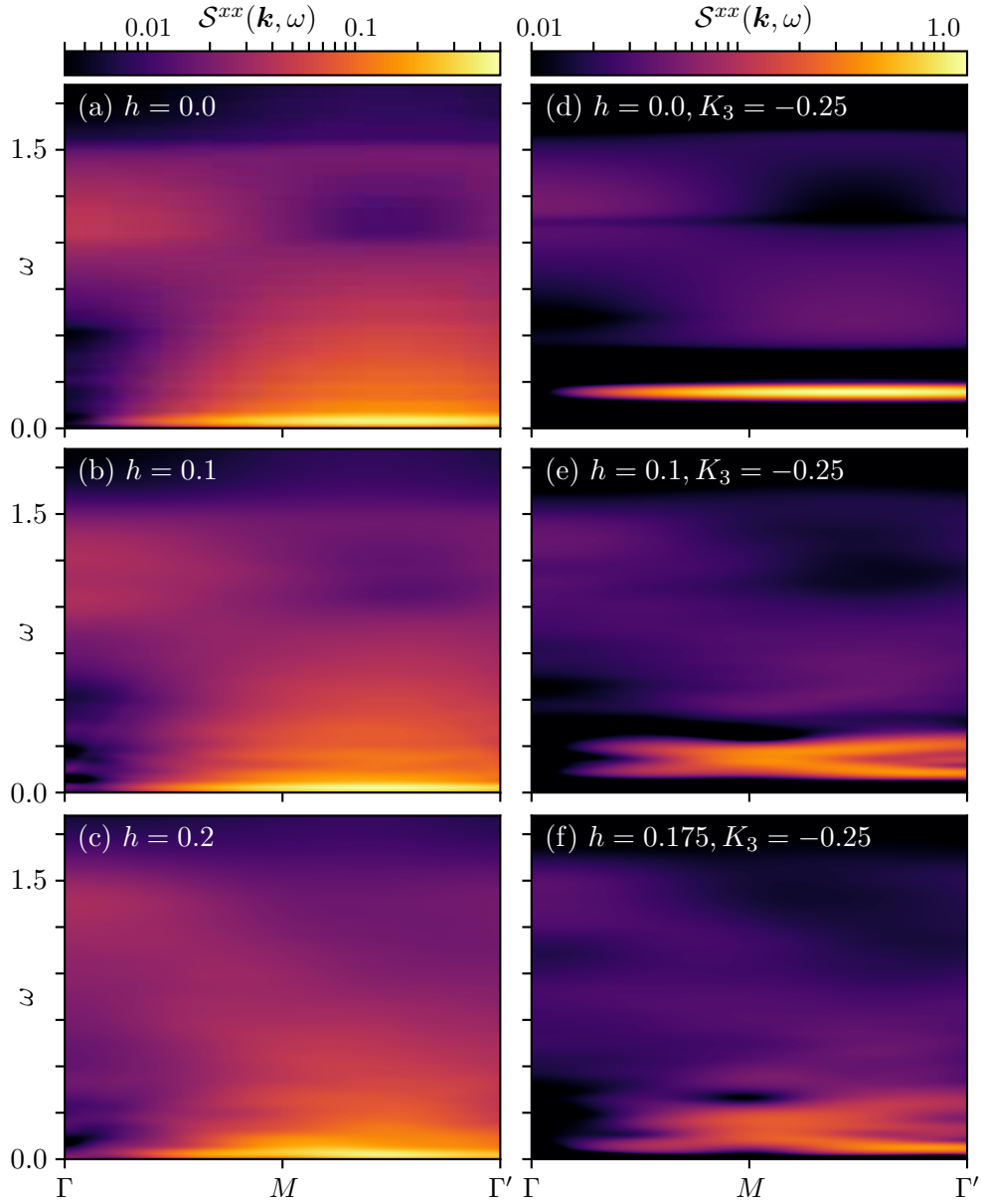


Figure 6.7: Dynamical spin-structure factor $\mathcal{S}^{xx}(k, \omega)$ along Γ - M - Γ' at: (a) $h = 0.0$, (b) $h = 0.1$, (c) $h = 0.20$, (d) $h = 0.0, K_3 = -0.25$, (e) $h = 0.10, K_3 = -0.25$, (f) $h = 0.175, K_3 = -0.25$ within the topological phase. (a)-(f) have a logarithmic color scale ranging over two decades.

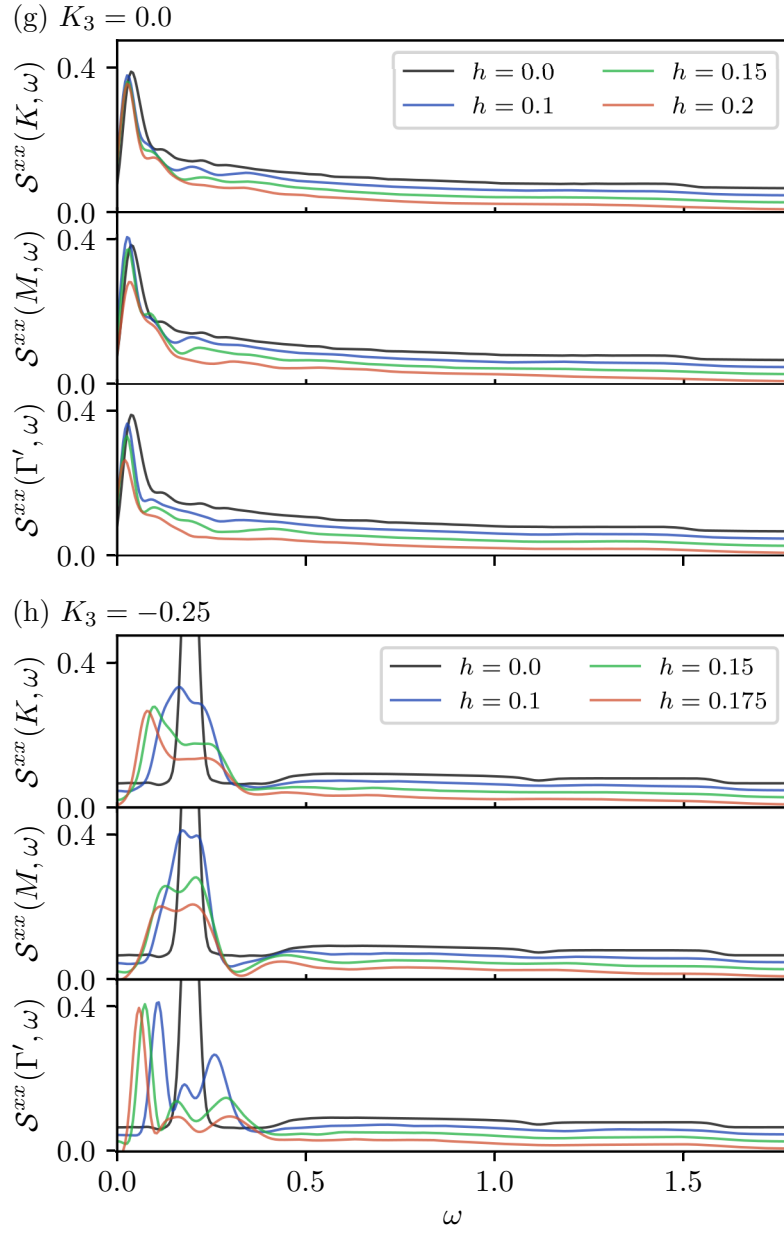


Figure 6.7 (Cont.): (g,h) $S^{xx}(k, \omega)$ at high-symmetry points Γ , K , M , and Γ' for different h and K_3 . An vertical offset is used for better visibility. In all plots, $S^{xx}(k, \omega)$ is normalized as given in the main text.

6.4.1 Topological Phase

Near $h = 0$, see Fig. 6.7(a), the numerically obtained $\mathcal{S}(\mathbf{k}, \omega)$ exhibits the features of the analytic solution [22, 78] with some adjustments due to the cylindrical geometry [127]. Firstly, this involves a low-energy peak at $\omega = 0.03$ of which its spectral weight is shifted towards Γ' due to the antiferromagnetic nearest-neighbor spin-spin correlation caused by the antiferromagnetic Kitaev exchange. When using a cylindrical geometry, an additional δ -peak with finite spectral weight occurs at the two-flux energy. This δ -peak, together with the finite-time evolution and subsequent broadening in frequency space, hides the two-flux gap. Nevertheless, the δ -peak position coincides with the two-flux gap², $\Delta_2 \approx 0.03$.

Secondly, a broad continuum exists, that is cut off near $\omega \approx 1.5$. Increasing h to 0.1 and 0.2, cf. Fig. 6.7(b) and (c), only leads to minor changes of the spectrum. Most notably, the low-energy peak develops a shoulder towards slightly elevated energies, and the cut-off at $\omega = 1.5$ is somewhat blurred out. Both features are more prominent in the line plots, Fig. 6.7(g). Any changes to the low-energy spectrum near or even below the two-flux gap are hidden in the energy resolution caused by the finite time-evolution.

In order to get a qualitative view on how the magnetic field affects the spectrum, let us investigate the effect of both, K_3 and h . For $K_3 = -0.25$ and $h = 0.0$, Fig. 6.7(d), the low-energy peak gets elevated to $\omega \approx 0.2$. This peak originates from a single fermion bound to a pair of fluxes [78] and its shift is caused by K_3 increasing the two-flux gap. The fermion continuum starts at $\omega \approx 0.4$, and the upper cut-off of the continuum remains near $\omega = 1.5$. Both edges are sharp. Note that, $K_3 = -0.25$ has a similar correlation length as $h = 0.2$ as discussed above in relation to Fig. 6.3. Yet, the corresponding spectra, Fig. 6.7(c) and Fig. 6.7(d), are qualitatively different in that for $h = 0.2$ the spectral weight is significantly closer to zero frequency with no observable gap within the achieved energy resolution.

Upon increasing h to 0.1, the low-energy peak splits into at least three peaks, two of them develop a dispersion. Due to the field, the fluxes acquire a finite hopping amplitude and become mobile. The fluxes are thence no longer required to lie on neighboring plaquettes, but instead may separate. Hence, the mode describing a fermion bound to the two-flux pair generally attains more structure [167]. Moreover, interaction between fluxes may induce further dispersion [168, 169]. At further elevated fields, cf. Fig. 6.7(f) at $h = 0.175$, somewhat before the phase transition into the intermediate regime³, the splitting increases with lots of the spectral weight shifting to the peak that is lowest in energy. The spectral gap reduces significantly with h and has its minimum at the Γ and Γ' high-symmetry points.

²The two-flux gap is shifted towards smaller frequencies for narrow cylinders.

³In analogy to the findings in [84], the additional K_3 term shifts the critical field. For $K_3 = -0.25$ the transition occurs at $h_{c1,AF} = 0.19$.

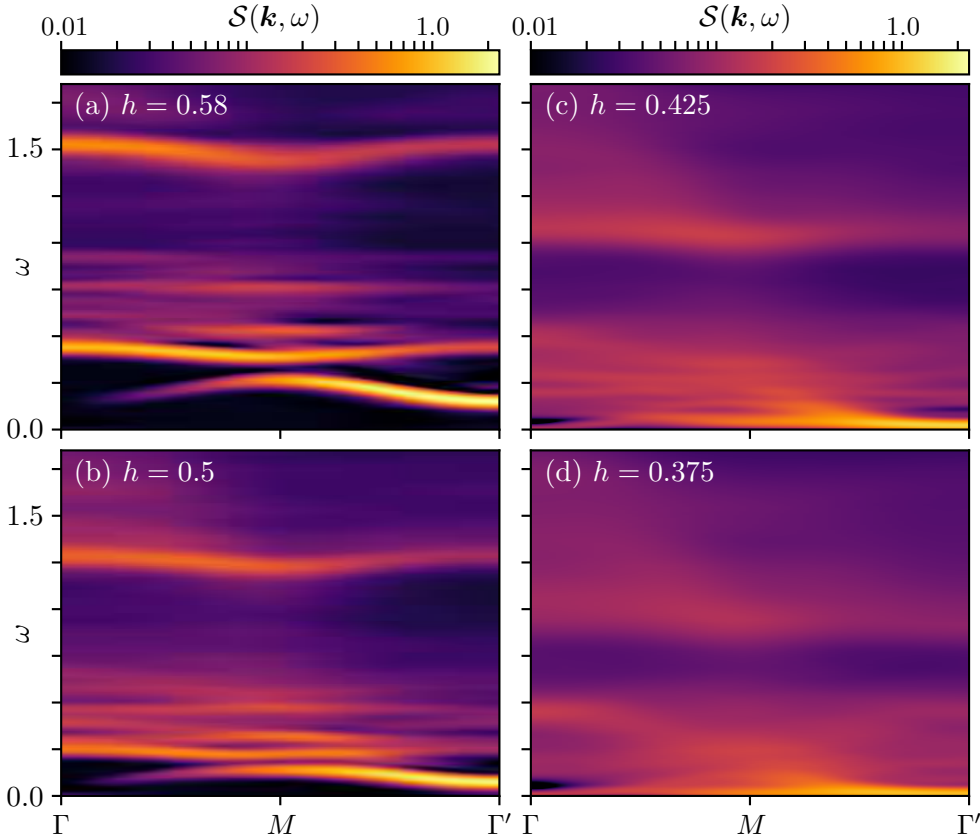


Figure 6.8: Dynamical spin-structure factor $\mathcal{S}(k, \omega)$ in the field-polarized phase along Γ - M - Γ' at: (a) $h = 0.58$, (b) $h = 0.5$, (c) $h = 0.425$, and (d) $h = 0.375$. In all plots, $\mathcal{S}(k, \omega)$ is normalized as given in the main text.

6.4.2 Polarized Phase

From linear spin-wave theory (LSWT) it is known that the magnons are topological. Their bands carry a ± 1 Chern number and chiral edge modes have been observed on a slab geometry [162, 170]. But LSWT is only applicable for fields above the classical critical field $h_{\text{clas}} = 1/\sqrt{3} \approx 0.58$. Here, we focus on the bulk excitation spectrum at fields between the numerically observed, $h_{c2,AF} \approx 0.36$, and the classical critical field. Results for larger fields are presented in Ref. [162] using the same method.

Beginning the discussion at the classical critical field $h = 0.58$ shown in Fig. 6.8(a), two magnon-bands are found with a minimum of $\omega \approx 0.15$ at the high-symmetry points Γ and Γ' . The two-magnon continuum has some overlap with the upper magnon band. With lowering the field, the magnon bands move down in energy and flatten in the sense that their bandwidth decreases. At $h = 0.5$, cf. Fig. 6.8(b), the continuum already overlaps with major parts of the upper magnon band. This opens decay channels, limiting its lifetime, and consequently broadening the mode.

Approaching the transition, cf. Fig. 6.8(d) at $h = 0.375$ and (c) at $h = 0.425$,

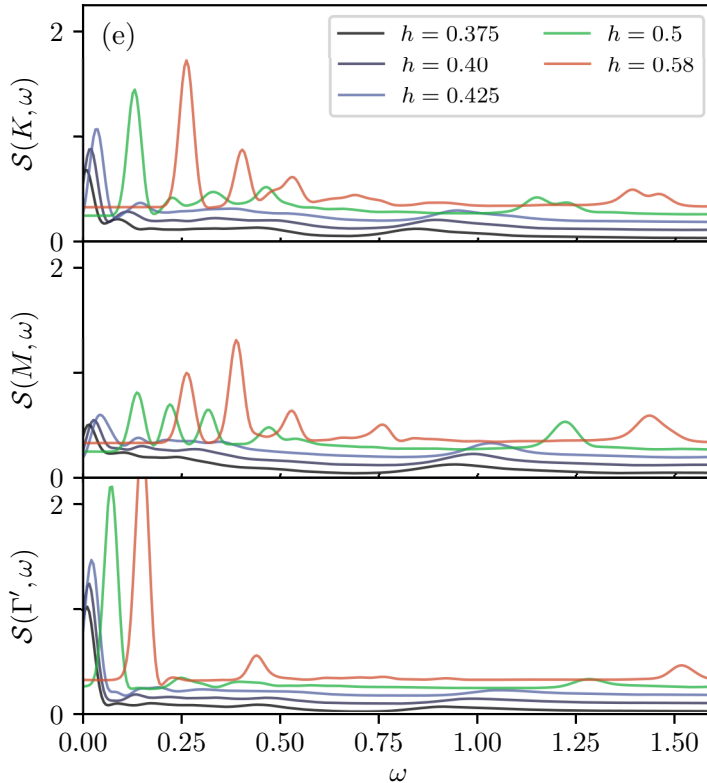


Figure 6.8 (Cont.): (e) $\mathcal{S}(k, \omega)$ at high-symmetry points K , M , and Γ' for different h . A vertical offset is used for better visibility.

$\mathcal{S}(\omega, \mathbf{k})$ shows a very broad continuum ranging down to almost zero energy, where also most of the spectral weight is observed. The upper magnon band is completely obscured by the multi-magnon continuum and lots of the spectral weight is distributed over a wide range in energy. The lower edge of the spectrum flattens towards the transition, which is even more evident in the line plots shown in Fig. 6.8(e). In particular at $h = 0.375$ the low-energy peaks shift down to almost zero energy simultaneously at the K , M , and Γ' high-symmetry points, with most of the spectral weight still appearing above the Γ' -point.

This reproduces to some extent the phenomenology of LSWT, namely that the lower magnon band flattens completely while decreasing to zero energy [150, 162], yet it occurs at lower fields than in LSWT. On the other hand, a clear remnant of the single magnon branch cannot be observed close to the transition as it overlaps and merges with the multi-magnon continuum. It may be possible that the single magnon branch is still dispersive, even though with a significantly reduced bandwidth.

A feature in the spectrum not mentioned so far, emerges at around $\omega \approx 1$ at magnetic fields near the transition. Initially this high-energy feature is very broad in energy, but sharpens and moves to higher energy upon increasing the field. At $h = 0.5$

($h = 0.58$) it appears around $\omega \approx 1.25$ ($\omega \approx 1.5$) and exhibits a slight dispersion. At even larger fields, beyond what is presented here, the high-energy feature moves up in energy with a linear dependence on the field and twice the slope compared to the single-magnon excitations. Furthermore, the high-energy feature is situated at the upper edge of the two magnon continuum. Its intensity first increases, but starts to decrease at higher fields. It would be interesting to investigate, if this may be due to the appearance of an anti-bound state [171] of two magnons experiencing a repulsive interaction on account of the antiferromagnetic Kitaev exchange interaction between two adjacent flipped spins.

6.5 Conclusion

We confirm the vastly different phenomenology between ferromagnetic and antiferromagnetic Kitaev interaction, if a magnetic field along [111] direction is applied. In case of ferromagnetic Kitaev coupling, only a single magnetic transition is observed, that separates a low- h topological phase from the large- h field-polarized phase. Whereas for antiferromagnetic Kitaev coupling, the topological phase is more stable and an intermediate regime exists, that is possibly gapless. The topological order of the low- h phase and its non-abelian anyonic excitations are verified by extracting the topological entanglement entropy. In addition to Ref. [84], the topological order obtained with a finite three-spin term or when applying a weak magnetic field is the same also for antiferromagnetic Kitaev coupling.

Upon applying the magnetic field, the spectral gap in the dynamical spin-structure factor remains within the frequency resolution and the overall spectrum exhibits only minor changes. However, the dynamical spin-structure factor is remarkably different when applying the three-spin term lifting the spectral gap, both due to the flux gap increasing and the fermions gapping out. When a combination of magnetic field and three-spin term is applied, we observe a drastic reduction of the spectral gap with increased field and more structure in the low-energy peak corresponding to a bound state of a flux pair and a fermion. This additional structure is due to the fluxes becoming mobile and the flux-pair may separate providing a richer energy manifold for that bound state. Upon approaching the intermediate regime, the spectral gap reduces with a minimum at the Γ' high-symmetry point. We can conclude, that even though the energy gap opens in a similar manner when either the magnetic field or three-spin term is varied, the dynamical spin-structure factor exhibits a remarkably different low-energy structure. Thus, additional terms in perturbation theory, other than the three-spin term preserving integrability, are relevant to describe the dynamical spin-structure factor in the topological phase.

When approaching the intermediate region from high-fields, we observe a strong

reduction in frequency with a simultaneous flattening of the lower magnon band. A broad continuum develops, that ranges down to the lowest frequencies and merges with the single magnon branch. It remains an open question, whether this flattening could be attributed to the collapse of the lower magnon branch, as observed within LSWT, or rather to multi-magnon excitations obscuring any dispersion of the very same magnon branch. Nonetheless, the flat gap closing as such is interesting in various aspects as it may indicate exotic spin states like a quantum spin liquid.

Chapter 7

Topological Magnons in Kitaev Magnets at High Fields

7.1 Introduction

One of the most important concepts in recent condensed matter physics is the notion of a topological band structure. Such band structures may carry nontrivial topological indices that protect certain features of the spectrum of a solid at its boundaries [172, 173]. Most famous examples include the quantum Hall effect, topological insulators, as well as Weyl and Dirac semimetals.

Similarly, magnon bands may as well carry nontrivial topological indices implying the existence of protected edge modes. In the past, some models have been proposed to exhibit such Chern bands [174–181], however, the robustness of the corresponding chiral edge modes against interactions remains to be demonstrated. In comparison to electronic topological insulators, their bosonic analogue, like the topological magnons discussed here, are more likely to possess interactions possibly resulting in a break down of the single particle picture. In the case of the kagome ferromagnet with Dzyaloshinskii-Moriya, it has been argued that magnon-magnon interactions broaden the bulk bands on a scale comparable to the bulk gap so that the band topology cannot be understood in terms of single magnons [182]. The question remains open whether any model can be found in which the prediction of chiral edge modes in a magnonic band structure survives in the strong coupling limit.

The purpose of this chapter is to expose the possibility of Kitaev materials to exhibit topological magnons, if a strong magnetic field along [111] is applied. In the context of bare Kitaev interactions, this chapter links directly to chapter 6 and the high-field paramagnetic state discussed therein. However, topological magnons exist also in the general Kitaev model including Heisenberg, and symmetric off-diagonal Γ and Γ' , cf. Eq. (2.46), and thus may be observable in compounds like Na_2IrO_3 , Li_2IrO_3 ,

and α -RuCl₃. In particular, number non-conserving terms open a gap in the spectrum allowing for non-trivial Chern numbers. By tuning the field, a separation of energy scales is achieved such that multi-magnon excitations do not overlap with the in-gap edge mode. Consequently, no low-energy scattering channels into the continuum exist and the lifetime of single magnons is not limited.

This chapter is structured as follows. First, cf. Sec. 7.2, the linear spin-wave theory for the Kitaev-Heisenberg model in a strong magnetic field along the [111] axis is introduced. The Berry curvature of the magnon bands reveals the non-trivial Chern numbers. In Sec. 7.3, the effect of magnon-magnon interactions is studied within the dynamical structure factor obtained using higher-order spin-wave theory and infinite density matrix renormalization group (iDMRG) method applied on the bulk. Subsequently, cf. Sec. 7.4, chiral edge modes as a signature of the topological magnon band structure are observed on a slab geometry using DMRG and a matrix product operator based time-evolution, see Ch. 3. The extension to the more general $JKTI'$ model is captured in Sec. 7.5.

7.2 Linear Spin Wave Theory and the Non-Trivial Chern Number

In the high-field limit $h \rightarrow \infty$, the magnetic moments saturate along the field direction. This polarized yet paramagnetic ground state may be used as a starting point of a spin-wave theory. Using the Holstein-Primakoff ansatz [183] the spin operators S^γ get replaced by bosonic construction and annihilation operators $\zeta_{\mathbf{k}} = (a_{\mathbf{k}}, b_{\mathbf{k}}, a_{-\mathbf{k}}^\dagger, b_{-\mathbf{k}}^\dagger)^T$, with a pair each for the two sites within the unit cell. Note that, the Ansatz is applied to the rotated frame, such that \tilde{S}^z acts along the [111] direction.

LSWT for the Kitaev-Heisenberg Model at High Fields

To lowest order in $1/S$, the linear spin-wave Hamiltonian contains only quadratic terms in a, b and after performing a Fourier transform it has the general structure

$$H_{LSW} = \frac{1}{2} \sum_{\mathbf{k} \in BZ} \zeta_{\mathbf{k}}^\dagger \cdot M_{LSW}(\mathbf{k}) \cdot \zeta_{\mathbf{k}}, \quad (7.1)$$

where M is a 4×4 matrix. For the Kitaev-Heisenberg model, cf. Ch. 4, with a Zeeman-coupling of the spins to a magnetic field along the [111] axis,

$$H_{KH} = \sum_{\langle i,j \rangle_\gamma} 2K_\gamma S_i^\gamma S_j^\gamma + \sum_{\langle i,j \rangle} J_{ij} \mathbf{S}_i \cdot \mathbf{S}_j - h \sum_i (S_i^x + S_i^y + S_i^z), \quad (7.2)$$

M is given as [150]

$$M_{LSW} = \begin{pmatrix} A(\mathbf{k}) & B(\mathbf{k}) \\ B^\dagger(\mathbf{k}) & A^T(-\mathbf{k}) \end{pmatrix}, \quad (7.3)$$

with

$$A(\mathbf{k}) = \sqrt{3}h \begin{pmatrix} 1 & 0 \\ 0 & 1 \end{pmatrix} + (3J + 2K)S \begin{pmatrix} -1 & \gamma_{0,\mathbf{k}}^* \\ \gamma_{0,\mathbf{k}} & -1 \end{pmatrix} \quad (7.4)$$

$$B(\mathbf{k}) = 2KS \begin{pmatrix} 0 & \gamma_{1,\mathbf{k}}^* \\ \gamma_{2,\mathbf{k}} & 0 \end{pmatrix}. \quad (7.5)$$

Here, a spin- $\frac{1}{2}$ system is considered and thus $S = 1/2$. The $\gamma_{i,\mathbf{k}}$ are introduced for convenience

$$\begin{aligned} \gamma_{0,\mathbf{k}} &= \frac{1}{3} \left(e^{-i\mathbf{k}\cdot\boldsymbol{\delta}_x} + e^{-i\mathbf{k}\cdot\boldsymbol{\delta}_y} + e^{-i\mathbf{k}\cdot\boldsymbol{\delta}_z} \right) \\ \gamma_{1,\mathbf{k}} &= \frac{1}{3} \left(e^{-i\mathbf{k}\cdot\boldsymbol{\delta}_x - 2\pi i/3} + e^{-i\mathbf{k}\cdot\boldsymbol{\delta}_y + 2\pi i/3} + e^{-i\mathbf{k}\cdot\boldsymbol{\delta}_z} \right) \\ \gamma_{2,\mathbf{k}} &= \frac{1}{3} \left(e^{-i\mathbf{k}\cdot\boldsymbol{\delta}_x + 2\pi i/3} + e^{-i\mathbf{k}\cdot\boldsymbol{\delta}_y - 2\pi i/3} + e^{-i\mathbf{k}\cdot\boldsymbol{\delta}_z} \right). \end{aligned} \quad (7.6)$$

The $\boldsymbol{\delta}_{x,y,z}$ denote the lattice vectors with the choice [162]: $\boldsymbol{\delta}_x = (0, 1)$, $\boldsymbol{\delta}_y = (-\sqrt{3}/2, -1/2)$, and $\boldsymbol{\delta}_z = (\sqrt{3}/2, -1/2)$. Equation (7.1) can be diagonalized by a Bogoliubov transform, i.e. as in Ref. [184].

Figure 7.1 summarizes the findings within LSWT. Following the convention in Ch. 4, a trigonometric parametrization $K = \sin \alpha$, $J = \cos \alpha$ is used. The critical field is identified from the closing of the gap to the lower magnon band. Depending on α the critical field varies: it is zero above the ferromagnetic phase, and increases towards the antiferromagnetic phase, in which it the critical field reaches a maximum. The gap in between the magnon modes vanishes if $K = 0$ (bare Heisenberg exchange) or $3J + 2K = 0$. For all other α , this in-between gap is either minimal at the K point, the M point, or at both K and M in the vicinity of bare Kitaev coupling. See Fig. 7.1(b). Note that within LSWT the critical field at the ferromagnetic Kitaev exchange (FMK) is zero, whereas for the antiferromagnetic exchange (AFK) it is finite, $h = 2/\sqrt{3} \approx 1.15$. In comparison to the findings in Ch. 6, the critical field is slightly lifted for FMK, $h_{c,\text{FM}} = 0.028$, and significantly reduced for AFK when utilizing iDMRG, $h_{c,\text{AF}} = 0.72$. This rescaling is likely affecting a broader range around $\alpha = \pi/2$. In a classical treatment [150], numerous long-range ordered phases are observed within the shaded area below the critical field.

To gain more insight about the magnons, let us apply a Schrieffer-Wolf transformation [185], that perturbatively diagonalizes the Hamiltonian by a unitary transforma-

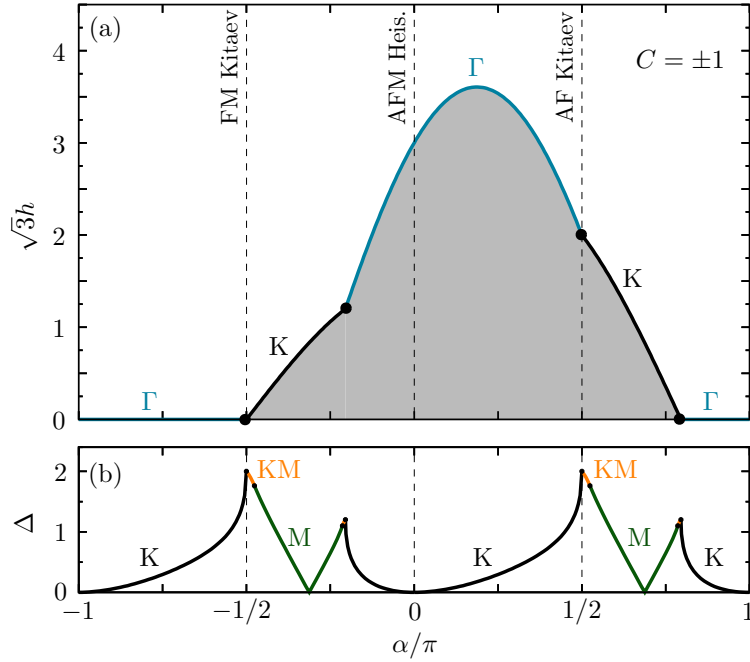


Figure 7.1: (a) Phase boundary between the high-field paramagnetic phase and the low field phases (shaded area) as obtained from linear spin-wave theory. The entire paramagnetic phase has topological magnons with Chern number $C = \pm 1$ with the exception of $K = 0$ and $3J + 2K = 0$, see below. The gap closing of the lower magnon branch occurs either at the K (black line) or the Γ (blue line) high-symmetry point, except above the pure Kitaev points, where the lower magnon band becomes flat and condenses in the entire reciprocal space. Possible semi-classical phases [150] or effects due to interaction, cf. Ch. 6, are not captured in this plot. (b) Magnitude and position of the minimal gap in between both magnon modes at the critical field. The in-between gap vanishes if $K = 0$ or $3J + 2K = 0$. At these two points, the Berry curvature is not well defined. This figure is based on Fig. 1 of Ref. [162].

tion,

$$H_{eff} = e^{-W} H_{LSW} e^W,$$

such that the number non-conserving terms, terms of the form $a_{\mathbf{k}} a_{\mathbf{k}}$ or $a_{\mathbf{k}}^\dagger a_{\mathbf{k}}^\dagger$, get eliminated to lowest order. The corresponding matrix W is

$$W(\mathbf{k}) = \frac{1}{2\sqrt{3}h} \begin{pmatrix} 0 & B(\mathbf{k}) \\ -B^\dagger(\mathbf{k}) & 0 \end{pmatrix}. \quad (7.7)$$

Here, we include terms up to second order in the transformation,

$$H_{eff} \approx H + [W, H] + \frac{1}{2} [W, [W, H]] + \dots \quad (7.8)$$

The effective Hamiltonian, still of the same structure as in Eq. (7.1), gets

$$A_{eff}(\mathbf{k}) = A(\mathbf{k}) - \frac{2K^2S^2}{\sqrt{3}h} \begin{pmatrix} \gamma_{1,\mathbf{k}}^* \gamma_{1,\mathbf{k}} & 0 \\ 0 & \gamma_{2,\mathbf{k}}^* \gamma_{2,\mathbf{k}} \end{pmatrix} \quad (7.9)$$

$$B_{eff}(\mathbf{k}) = -\frac{K(3J+2K)S^2}{\sqrt{3}h} \begin{pmatrix} \gamma_{0,\mathbf{k}} \gamma_{1,\mathbf{k}}^* + \gamma_{0,\mathbf{k}}^* \gamma_{2,\mathbf{k}} & -2\gamma_{1,\mathbf{k}}^* \\ -2\gamma_{2,\mathbf{k}} & \gamma_{0,\mathbf{k}} \gamma_{1,\mathbf{k}}^* + \gamma_{0,\mathbf{k}}^* \gamma_{2,\mathbf{k}} \end{pmatrix}. \quad (7.10)$$

Since the energies of the magnon excitations are similar for the 4×4 and the 2×2 matrix A_{eff} , it is sufficient to diagonalize A_{eff} . First, note that A_{eff} can be rewritten as

$$A_{eff}(\mathbf{k}) = d_0(\mathbf{k})\mathbb{1} + \frac{1}{2}\mathbf{d}(\mathbf{k}) \cdot \boldsymbol{\sigma}, \quad (7.11)$$

where $\boldsymbol{\sigma} = (\sigma^x, \sigma^y, \sigma^z)$ is a vector of Pauli matrices. The scalar $d_0(\mathbf{k})$ and the vector $\mathbf{d}(\mathbf{k})$ read as

$$d_0(\mathbf{k}) = \sqrt{3}h - (3J + 2K)S - \frac{K^2S^2}{\sqrt{3}h} (\gamma_{1,\mathbf{k}}^* \gamma_{1,\mathbf{k}} + \gamma_{2,\mathbf{k}}^* \gamma_{2,\mathbf{k}}) \quad (7.12)$$

$$\mathbf{d}(\mathbf{k}) = \begin{pmatrix} (3J + 2K)S(\gamma_{0,\mathbf{k}}^* + \gamma_{0,\mathbf{k}}) \\ i(3J + 2K)S(\gamma_{0,\mathbf{k}}^* - \gamma_{0,\mathbf{k}}) \\ -\frac{2K^2S^2}{\sqrt{3}h} (\gamma_{1,\mathbf{k}}^* \gamma_{1,\mathbf{k}} - \gamma_{2,\mathbf{k}}^* \gamma_{2,\mathbf{k}}) \end{pmatrix}. \quad (7.13)$$

The terms with the coefficient of $\propto \frac{K^2}{h}$ in $d_0(\mathbf{k})$ and $\mathbf{d}(\mathbf{k})$ reveal the topological property of the magnon bands: transformed back to real-space they generate a second-nearest neighbor term as would occur from a Dzyaloshinskii-Moriya term [162], which is known to result in Chern bands for the magnons [177]. Let us continue with the eigenvalues of A_{eff} . Given A_{eff} is of the form (7.11), the eigenvalues are

$$\omega_{\pm} = d_0(\mathbf{k}) \pm \frac{1}{2}|\mathbf{d}(\mathbf{k})|, \quad (7.14)$$

where $d(\mathbf{k}) = |\mathbf{d}(\mathbf{k})|$. Here, two magnon branches exist with a spacing $d(\mathbf{k})$ between the two bands. The two bands touch, that is $d(\mathbf{k}) = 0$, only if $K = 0$ or $3J + 2K = 0$, which are the points of pure Heisenberg coupling and points in the corresponding dual phases¹. Note that the Schrieffer-Wolf transformation is not exactly resembling the LSWT result: the Schrieffer-Wolf transformation is essentially a perturbation theory at high field and results in an expansion in terms of $1/h$. The magnon modes are only expected to be similar to LSWT for larger fields, but not close to the critical field.

¹The couplings J, K for which $3J + 2K = 0$ are not related to the hidden $SU(2)$ point given by a sublattice transform [85, 142], since the field would also be changed by the transformation.

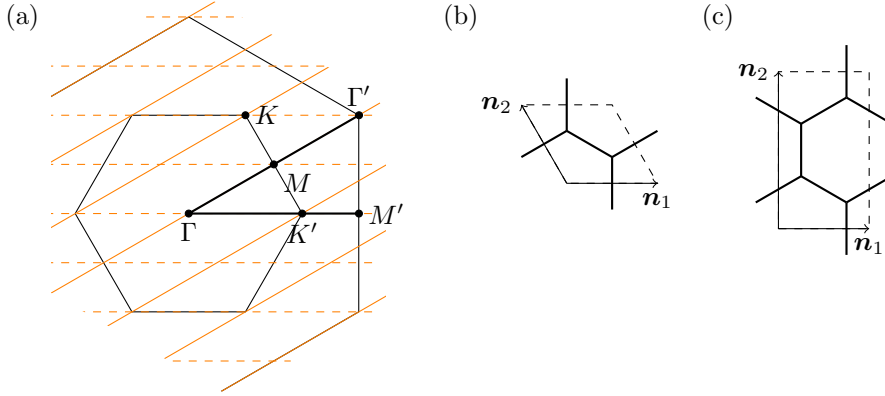


Figure 7.2: (a) Brillouin zone and the path along which $\mathcal{S}(\mathbf{k}, \omega)$ is plotted (solid black line). (b) The rhombic unit cell results in diagonal cuts (solid orange lines) and is used for the $\Gamma'-M-\Gamma$ segment, whereas (c) the rectangular unit cell results in horizontal cuts (orange dashed lines) and is used for the $\Gamma-K-M'$ segment.

Berry Phase and Chern Number

From $\mathbf{d}(\mathbf{k})$ defined in Eq. (7.13) one obtains the Berry flux, which for a two-dimensional system is defined as [172, 186]

$$F_{\pm}^{xy}(\mathbf{k}) = \pm \frac{i}{2} \hat{\mathbf{d}}(\mathbf{k}) \left(\frac{\partial \hat{\mathbf{d}}(\mathbf{k})}{\partial k_y} \times \frac{\partial \hat{\mathbf{d}}(\mathbf{k})}{\partial k_x} \right), \quad (7.15)$$

where $\hat{\mathbf{d}} = \mathbf{d}(\mathbf{k})/d(\mathbf{k})$ is a unit vector. Given a Berry flux F_{\pm}^{xy} of the two band denoted by \pm , its Chern number C_{\pm} is defined by integrating the Berry flux over the first Brillouin zone

$$C_{\pm} = \frac{1}{2\pi i} \int_{\text{BZ}} dk_x dk_y F_{\pm}^{xy} = \pm N_s, \quad (7.16)$$

where N_s is generally an integer. In the case of the Kitaev-Heisenberg model $C_{\pm} = \pm 1$ for all J and K except when the two magnon branches are not separated by a finite gap, which occurs for $K = 0$ and $3J + 2K = 0$. In conclusion, almost the entire high-field paramagnetic phase, cf. Fig. 7.1, exhibits topological non-trivial magnon bands implying edge modes.

7.3 Include Magnon-Magnon Interactions: Comparison with DMRG

One might ask how robust the signatures of the topological bands are, considering that a non-interactive theory is applied. To provide a test, we will now compare the LSWT results with numerical, non-perturbative, methods. Two such methods are used: exact diagonalisation (ED) on an hexagonal 24 site cluster preserving the symmetry of the

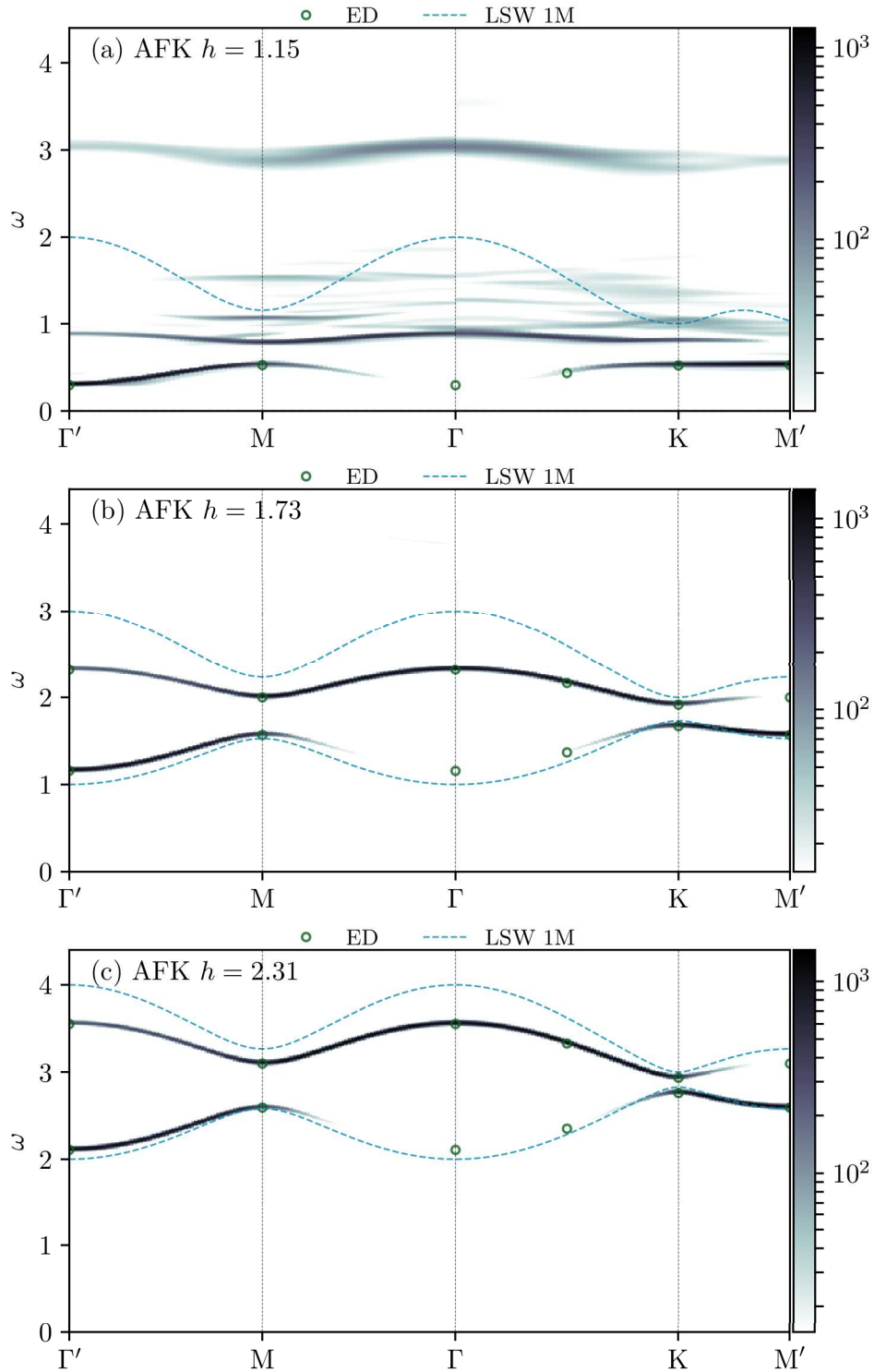


Figure 7.3: Bulk dynamical spin-structure factor $\mathcal{S}(\mathbf{k}, \omega)$ for antiferromagnetic Kitaev coupling at the magnetic fields (a) $h = 1.15$, (b) $h = 1.73$, and (c) $h = 2.31$. The two magnon modes obtained using linear spin wave theory (cyan dashed lines), and the eigenvalues obtained using exact diagonalisation on an hexagonal 24 site cluster (green circles) are plotted on top.

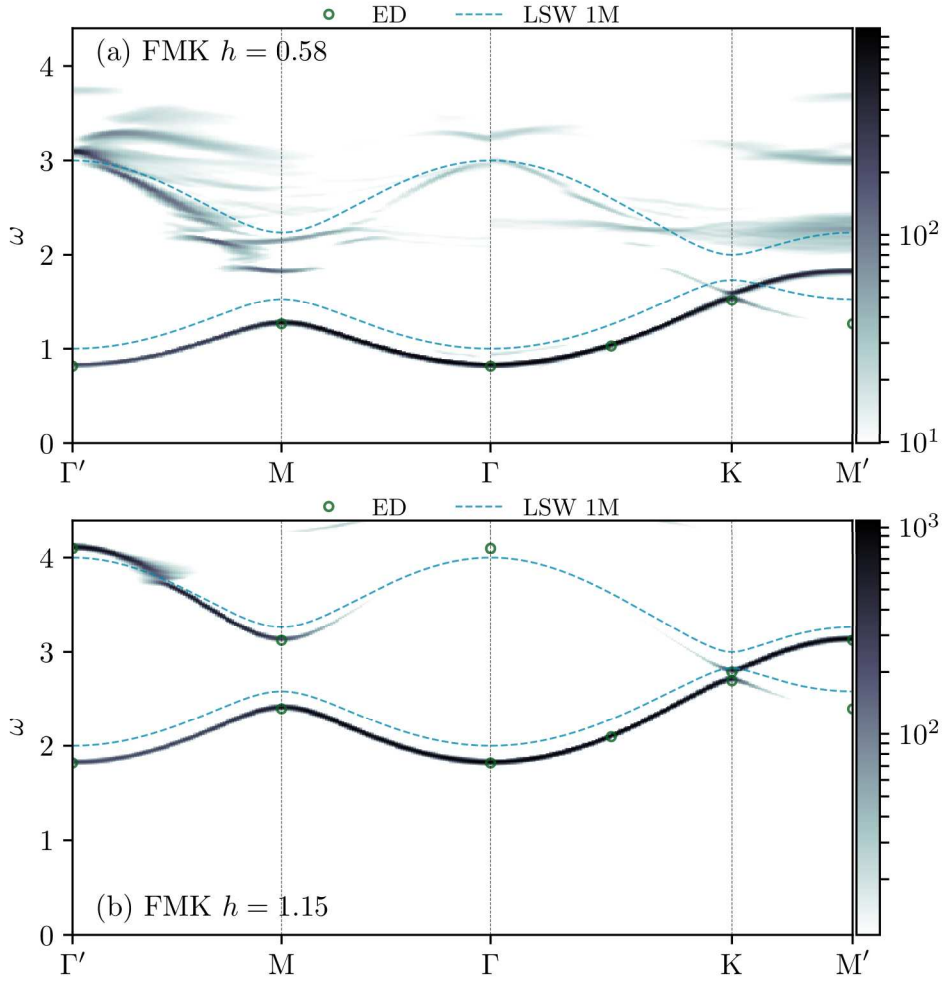


Figure 7.4: Same as Fig. 7.3, but for ferromagnetic Kitaev coupling at the magnetic fields (a) $h = 0.58$, and (b) $h = 1.15$. Note that within LSWT, identical magnon modes occur for ferromagnetic and antiferromagnetic Kitaev coupling, if the field is changed as $h_{\text{FMK}} = h_{\text{AFK}} - 2/\sqrt{3}$.

honeycomb lattice, and infinite density renormalisation group (iDMRG) together with an matrix-product operator based time-evolution (tMPO). The latter extends the study in chapter 6 to higher fields. The method itself is explained in Sec. 3.1 and 3.3.

Figure 7.3 shows the numerically obtained dynamical spin-structure factor $\mathcal{S}(\mathbf{k}, \omega)$, cf. Eq. (3.28) in Sec. 3.3, for the bare antiferromagnetic Kitaev (AFK) coupling at fields $h = 1.15, 1.73$, and 2.31 . $\mathcal{S}(\mathbf{k}, \omega)$ is plotted along $\Gamma'-M-\Gamma-K-M'$ high-symmetry point in reciprocal space. The path and the corresponding geometries used are illustrated in Fig. 7.2. At $h = 2/\sqrt{3} \approx 1.15$, LSWT predicts a completely flat lower magnon band. However, iDMRG shows well defined magnon modes at finite energy.

The two magnon branches increase in energy as the field strength is raised. Both at $h = 1.73$ and $h = 2.31$, the magnon branches obtained using LSWT are shifted in

energy. Particularly, the upper branch shifts to lower energies, when interactions are considered. The lowest eigenvalues found using ED agree perfectly at all fields implying that finite size effects are negligible.

A symmetry between AFK and the ferromagnetic Kitaev coupling (FMK) within LSWT leads to similar magnon branches if the field is shifted as $h_{\text{FMK}} = h_{\text{AFK}} - 2/\sqrt{3}$. Thus, the LSWT magnon branches shown in Fig. 7.4(a) for FMK are equal to 7.3(b), and analogously 7.4(b) to 7.3(c). However, the numerically obtained $\mathcal{S}(\mathbf{k}, \omega)$ are different between AFK and FMK. In particular, the lower magnon branch is slightly reduced in energy for FMK, and the continuum is more pronounced.

Nonetheless, LSWT captures qualitative features like the minimal gap position and the position of the minimal gap between the two branches. A closer look at how interactions affect the LSWT results is given in [162] by performing spin-wave theory to next higher order including three and four magnon interactions. Already near the critical field, agreement between spin-wave theory and iDMRG improves significantly regarding the single magnon branches, but distinctions remain in the continuum.

7.4 Chirality on a Slab Geometry

Non-zero Chern numbers imply chiral edge modes. This motivates to employ the iDMRG + tMPO framework, cf. Ch. 3, on a slab geometry with one dimension being in the thermodynamic limit, $L_x \rightarrow \infty$, and one dimension being finite, $L_y = 12$. The boundaries in the finite dimension are open such that two edges exist at which the chiral edge modes may appear. The bulk $\mathcal{S}(\mathbf{k}, \omega)$, see Fig. 7.3 and Fig. 7.4, indicate that AFK provides a better test ground due to the larger gap in between the two magnon bands.

On a slab geometry, the Fourier transform along the finite dimension y is not well defined. Thus, in Fig. 7.5 the following quantity is plotted

$$\tilde{\mathcal{S}}^{\gamma\gamma}(k_x, \omega) = N \int dt e^{i\omega t} \sum_{a,b} e^{i(\mathbf{r}_b - \mathbf{r}_a) \cdot \hat{\mathbf{k}}_{\mathbf{x}} k_x} C_{ab}^{\gamma\gamma}(t), \quad (7.17)$$

where the spatial Fourier transform of the dynamical spin-spin correlation $C_{ab}^{\gamma\gamma}(t)$ is only carried out along the x direction. For the sake of comparison, Fig. 7.5(a) shows $\tilde{\mathcal{S}}^{\gamma\gamma}(k_x, \omega)$ on the cylinder geometry used before to obtain the bulk modes. However, the amount of modes increases due to an entire ring being the effective unit cell now. The gap in between the magnon modes is situated at $k_x = \pm 2\pi/3$. When changing to the slab geometry, Fig. 7.5(a), a mode within this gap appear. However, the presence of open boundaries shifts modes near the boundary in energy and increases the number of modes as the unit cell enlarges to a strip along the finite dimension. Up to $L_y = 12$ modes could appear of which some may overlap.

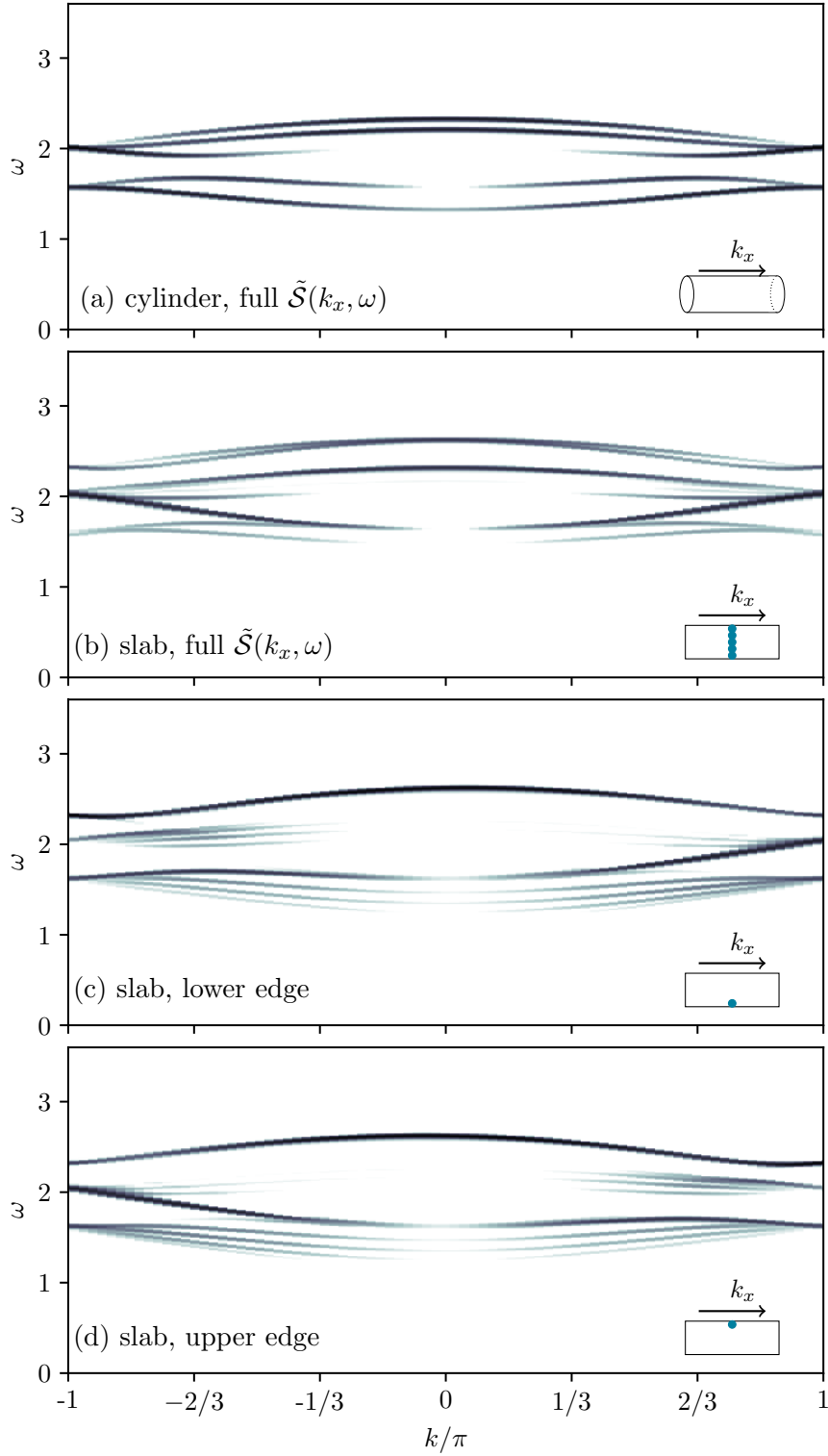


Figure 7.5: $\tilde{S}(k_x, \omega)$ as defined in Eq. (7.17) at $h = 1.73$ with antiferromagnetic Kitaev coupling for (a) cylinder geometry, (b) slab geometry, (c) slab geometry, but only exciting at the lower edge, and (d) at the upper edge. (b) presents the in-gap mode around $k_x = \pm 2\pi/3$ and $\omega = 1.8$, that clearly exhibits chirality as right moving mode (c) and left moving mode (d) depending on the edge considered.

Let us illustrate, that the in-gap mode has its support at the edges: the variable a in the sum, Eq. (7.17), is restricted to run only over the two sites of a fundamental (bulk) unit cell at the upper or the lower edge. The corresponding $\tilde{\mathcal{S}}^{\gamma\gamma}(k_x, \omega)$ are shown in Fig. 7.5(c) and Fig. 7.5(d). There, the chirality becomes apparent as an asymmetry in k_x of the spectral weight carried by the in-gap mode. On the lower edge, the right moving mode receives most of the spectral weight. Whereas on the upper edge it is the left moving mode that carries the majority of the spectral weight.

7.5 Extension to the $JK\Gamma\Gamma'$ -Model

The LSWT presented above translates over to the most general nearest neighbor model allowed by the symmetry of the edge-shared octahedral compounds [81, 82], where the octahedra form a honeycomb lattice. See section 2.3.8 and equation (2.46) in particular.

For fully polarized moments along [111], as used within LSWT, a mapping between the different couplings J, K, Γ , and Γ' together with a rescaling of the field h exists that leaves the magnon modes invariant within the non-interacting limit. Any combination of J, K, Γ, Γ' can be obtained from the Kitaev-Heisenberg model by using the replacement rules

$$\begin{aligned} K &\rightarrow K + \Gamma + \Gamma' \\ J &\rightarrow J - \Gamma \\ h &\rightarrow h - \sqrt{3}\Gamma S - 2\sqrt{3}\Gamma' S . \end{aligned} \tag{7.18}$$

Thus, at the non-interacting level any results of the Kitaev-Heisenberg model in a high [111] field carry over to the general model possibly describing the recently much studied Kitaev compounds. Note, however, this mapping does only apply on the level of LSWT and does not include possible interactions and any renormalisation of the magnon band the interactions may cause.

7.6 Conclusion

Spin-Orbit coupled magnetic compounds that exhibit Kitaev, Heisenberg, Γ , and Γ' interaction contain topologically non-trivial magnons in the high-field paramagnetic phase. Within linear spin-wave theory, the two magnon modes have a Chern number $C \pm 1$ implying chiral magnon modes at the surface. Based on this prediction, numerical simulations were presented verifying the chiral modes on a slab geometry. The topological edge modes are expected to exist in the whole parameter space of the $JK\Gamma\Gamma'$ -model (up to a few points) due to a mapping from the Kitaev-Heisenberg model to parameters in the $JK\Gamma\Gamma'$ -model. Thence, the findings here may be relevant in

magnetic compounds like Na_2IrO_3 , Li_2IrO_3 , and $\alpha\text{-RuCl}_3$ irrespective of their precise couplings.

On more general grounds, the Kitaev-Heisenberg model in a high-field along the [111] axis provides a concrete example of topological magnons implying edge modes, that due to a separation of energy scales survive interactions. By field-tuning the magnet within the paramagnetic phase, single magnon branches are gapped out, and their multi-magnon continuum is lifted resulting in a energy window where linewidths are suppressed.

The non-trivial Berry curvature and non-zero Chern number imply a thermal Hall effect studied already in a number of magnets [175, 179, 187–193]. Recent theoretical work predicts thermal Hall signatures in the Kitaev model in low fields within the topological non-abelian phase [194], which are claimed to be observed experimentally [195]. The thermal Hall signatures obtained in the paramagnetic phase are presented in [162] and it would be of interest to examine the experimental results of [195] within the context of topological magnons in the Kitaev model at high field.

Chapter 8

Polarization Plateaus in Hexagonal Water Ice

8.1 Introduction

Water exists in a huge variety of different phases including vapor, fluid, as well as numerous crystalline and amorphous phases. The most common crystalline phase of water on earth is the hexagonal phase *ice* I_h . Bernal and Fowler proposed that ice I_h is a molecular solid constructed out of H_2O molecules [9] obeying the *ice rules*. These ice rules are local constraints preventing ice I_h from ordering and leave a massively degenerate proton subsystem with a finite residual entropy [7, 8]. Consequently, ice I_h is considered to be an archetype of geometrical frustration. See Sec. 2.2 for more details. A similar constraint exists in *spin ice* materials, magnetic compounds where magnetic moments are aligned parallel or antiparallel to the links of a diamond lattice. Furthermore, they have to satisfy a modified ice rule constraint: two spins point into a tetrahedron and two point out. This is equivalent to the zero divergence condition of classical electrodynamics, Gauss' law, on a lattice and gives rise to emergent gauge fields, cf. Sec. 2.2.3.

The local constraints in ice-like materials manifest itself in certain features of scattering experiments. The ice rules cause an angle dependence of the scattering intensity around lattice Bragg points resulting in a bow-tie-like structure [45, 47, 196]. Such scattering maps contain information on proton-proton correlations, which have been computed for ice I_h using a large- N theory [197] or a projection operator approach [198].

At the lowest temperatures, quantum fluctuation may become important and result in a long-range ordered proton subsystem [199]. Experimental [200, 201] and theoretical work [198, 202] indicate that quantum fluctuations occur in the form of coherent many-body hopping of protons around a hexagonal plaquette.

In this chapter, we study the extensive classical degeneracy and how an external

field affects it. Generically, the degeneracy is expected to decrease upon applying an external field, but details depend on the direction of the field and which lattice symmetries it breaks. The degeneracy remains either extensive, e.g., when the field confines the remaining degrees of freedom to a stack of decoupled planar layers such as for pyrochlore spin ice in a [111] magnetic field [52, 55]. A small tilt of the field is needed to obtain an ordered state [55]. In contrast, spin ice in a field along [001] orders by an exotic three-dimensional Kasteleyn transition [51, 203, 204].

Here, an external electric field is applied which couples to the proton subsystem. We consider a minimal model describing the proton configuration: A proton can only take one of two positions on a link between two neighboring oxygen atoms and only a single proton per link exists. As such, the proton configurations can be described by Ising-like spins. If the field is applied along certain easy axes, it induces a partial ordering of the protons. The remaining degrees of freedom reside on decoupled layers mappable to hardcore dimer models. The field effectively reduces the dimensionality of the system from three to two. A slight tilt of the field lifts the remaining degeneracy within each layer and leads to an order-disorder transition first described by Kasteleyn [56].

In ice I_h , two qualitatively very different field directions exist: A field along [001] leads to decoupled layers with Ising-spin degrees of freedom on a honeycomb lattice. The local ice rules infer a mapping of the spins to dimers on the edges of the same lattice. This is in close analogy to the pyrochlore spin ice in a magnetic field along the [111] axis [55]. A second field direction along [010] results in decoupled layers of spins, which have an equivalent description as dimers on the edges of a square lattice. This direction has no analog in spin ice and, thence, receives more attention in this study.

Upon slightly tilting the field, the emergent dimers within the layers acquire different Boltzmann weights and, eventually, a Kasteleyn transition occurs [56, 57, 60, 205]. Using the theory introduced in Sec. 2.2.6, the emergent dimer models enable to compute thermodynamic quantities. Thence, the transition condition and its critical behaviour can be derived.

The structure of this chapter is as follows: In section 8.2, the ice I_h lattice and the model are introduced. An explanation of the numerical procedure and the directed worm Monte-Carlo method follows in section 8.3. Results based on thermodynamic observables are presented in section 8.4. A qualitative microscopic discussion of the emergent dimers is given in section 8.5, which is extended by a derivation of the dimer densities and polarizations. Section 8.6 contains diffuse scattering maps for comparison with experiments. We finish with concluding remarks in section 8.7.

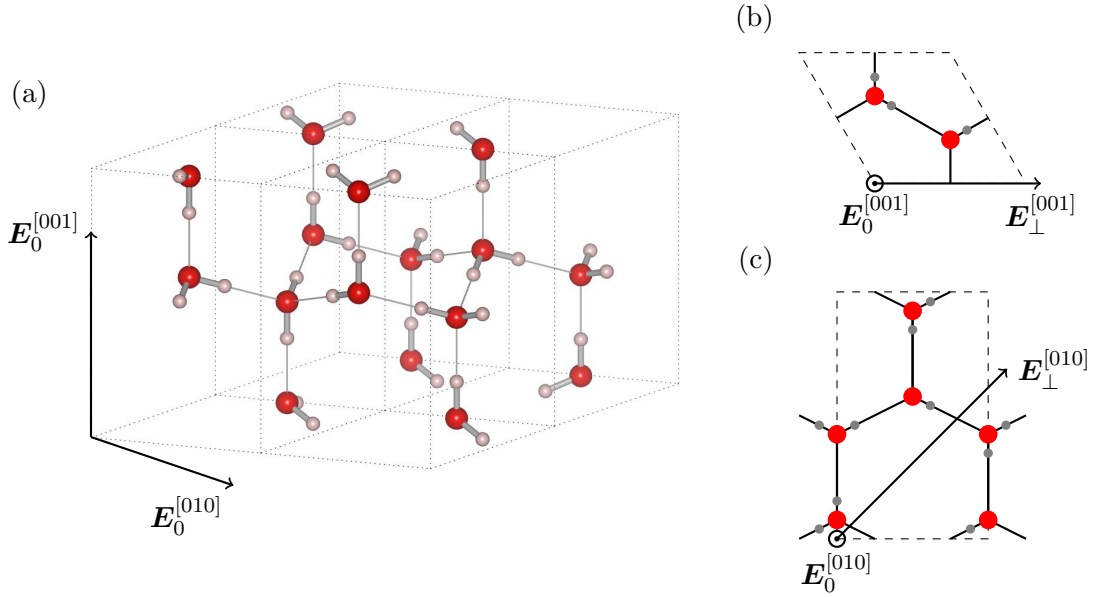


Figure 8.1: (a) Illustration of the structure of hexagonal ice I_h . An external field along $E_0^{[001]} \parallel [001]$ or $E_0^{[010]} \parallel [010]$ is applied with an additional tilt in the directions: (b) $E_\perp^{[001]} \parallel [100]$ and (c) $E_\perp^{[010]} \parallel [101]$. Oxygen ions are drawn in red, protons in gray.

8.2 Hexagonal Ice I_h Structure and Model

Ice I_h has a bipartite hexagonal lattice with four oxygen atoms and eight protons per primitive cell (Fig. 8.1). The oxygen atoms form a four-fold coordinated tetrahedral structure of class $P6_3/mmc$. The following symmetries exist: a sixfold rotation axis, a twofold rotation axis perpendicular to the z-axis and a horizontal reflection plane. The structure can be considered as a stacking of planes in an ABAB pattern, where B is the reflection of A with respect to a horizontal plane. This plane is perpendicular to the c-axis and is placed at the midpoint of the vertical links in Fig. 8.1(a).

Within the unit-cell, eight distinct oxygen-oxygen links exist. Each proton has two possible positions arranged symmetrically around the midpoint of a link. If we assume a single proton per link, which is one of the ice rules, the proton configuration can be represented as a configuration of electric dipoles \mathbf{d}_i

$$\mathbf{d}_i = s_i d \hat{\mathbf{e}}_i . \quad (8.1)$$

The dipoles are effective Ising spins s_i with respect to a local z-axis given by the direction $\hat{\mathbf{e}}_i$ of the oxygen-oxygen links. Such a mapping has been applied to spin ice in the reverse context. There the magnetic spins are represented as pairs of opposite charges forming *dumbbells* [14].

We consider the following minimal model in terms of electric dipoles or Ising spins, respectively. The Hamiltonian reads

$$H = J \sum_{\alpha} L_{\alpha}^2 - \sum_i s_i d \mathbf{E} \cdot \hat{\mathbf{e}}_i, \quad (8.2)$$

where $L_{\alpha} = \sum_{i \in \boxtimes_{\alpha}} s_i$ is the sum over effective the Ising spins on a tetrahedron \boxtimes_{α} . In choosing the limit $J \rightarrow \infty$, we restrict the dipole configuration to the ice-rule manifold. The second term is the coupling of the moment to an external field, which is named Stark coupling if an electric field is considered. The direction of the unit vectors $\hat{\mathbf{e}}_i$ along the links is chosen such that a positive s_i points from a site on sublattice A to a site on sublattice B. In the remainder, the constant d is set to unity.

The field is applied a) along the c-axis [001] and b) along [010] with respect to the orthorhombic unit cell, see Fig. 8.1 for an illustration. These field directions still leave an extensively degenerate ground state with finite entropy density. Therefore, a slight tilt of the field towards a) [100] and b) [101] is added, such that a single lowest energy state exist. For the remainder of this article, the notation $\mathbf{E} = \mathbf{E}_0 + \mathbf{E}_{\perp}$ is used for the external field. \mathbf{E}_0 is the component along the easy axis and \mathbf{E}_{\perp} denotes the tilt component with $\mathbf{E}_{\perp} \ll \mathbf{E}_0$.

8.3 Directed Loop Monte Carlo Sampling

The spin- or proton system is simulated numerically using a directed loop Monte-Carlo method [206]. Since a single spin flip would violate the second ice rule, loops of consecutive spins are created and flipped instead. In doing so, the simulation remains in the defect-free manifold. In order to keep the efficiency high, the sampling enters already at the loop creation: two defects are created by choosing a single spin randomly with uniform probability and flipping it. One of the defects executes a weighted random walk with weights depending on the energetics of the original local configuration and the possible new local configurations. As soon as that defect meets the other defect, the loop is closed and all corresponding spins will be flipped. This is also known as the long loop algorithm, which has the property of spanning on average a fraction of the whole system [207]. A loop which winds once or multiple times around the system connects different winding sectors.

The possibility of backtracking of a defect must also be considered to satisfy detailed balance. If the defect goes all the way back to its initial creation, no update occurs and a new initial spin is randomly chosen.

Usually, only the change of the local configuration on a single tetrahedron is taken into account when computing the probabilities to move the defect on site. However, this choice makes the algorithm highly inefficient for the field along [010]. Consider two

neighboring tetrahedra connected by a spin perpendicular to the field: the defect steps forward at the first tetrahedron with high probability as the change in configuration leads to a gain in energy. At the next tetrahedron, the defect has only a small probability to move forward as it would cost nearly the same energy and moving back is more likely. Thus, with decreasing temperature the probability of oscillating between the two vertices increases until the probability converges to one. This issue can be circumvented by considering double vertices of two neighboring tetrahedra sharing this particular spin perpendicular to the field. By doing so, the energy gain and cost are taken into account within one step.

The weighted random walk of the defect will be performed based on local heat bath sampling. Moving a defect through the smallest unit, either a single tetrahedron or a double tetrahedron, will change its local configuration from i to j . Its probability is given by

$$p(i \rightarrow j) = \frac{z(i \rightarrow j)}{\sum_k z(i \rightarrow k)},$$

where $z(i \rightarrow j) = e^{-\beta(\epsilon_j - \epsilon_i)}$ is the Boltzmann weight of a local configurational change. The sum in the denominator runs over all possible configurations k which can be achieved by forward steps and changing the local configuration ($i \neq k$) or by backtracking and retaining the local configuration ($i = k$). The energy ϵ_i of a local configuration is either given as

$$\epsilon_\alpha = -\frac{1}{2}\mathbf{E} \sum_{i \in \boxtimes_\alpha} s_i \hat{\mathbf{e}}_i,$$

where the sum runs over all links of a single tetrahedron \boxtimes_α , or, for the modified algorithm, as

$$\epsilon_\alpha = -s_{\alpha,\text{int}}\mathbf{E} \cdot \hat{\mathbf{e}}_{\alpha,\text{int}} - \frac{1}{2} \sum_{\text{ext } i \in D_\alpha} s_i \mathbf{E} \cdot \hat{\mathbf{e}}_i, \quad (8.3)$$

summing the Stark energy contribution from the internal spin of a double tetrahedron D_α . The (external) spins are weighted by a factor 1/2, since they are shared by two neighboring (double) tetrahedron.

The protocol for the simulation is as follows: The system is initialized in a configuration that obeys the ice rules everywhere. Loop creations and spin flips at infinite temperature are performed to randomize the initial state. Then follows an equilibration at a temperature of choice. The auto-correlation time is measured and determines how many loop iterations will be done between each measurement at the particular temperature. This procedure is repeated for all temperatures of interest. The field is held constant over the whole procedure. Simulations are done on systems with up to $160 \times 160 \times 80$ hexagonal unit cells and with periodic boundary conditions.

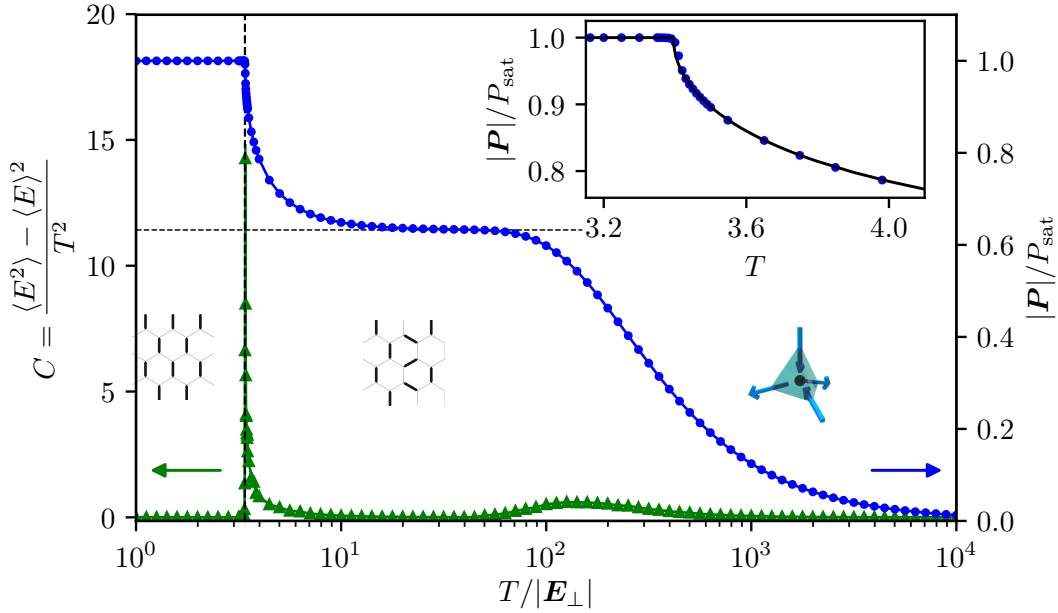


Figure 8.2: Relative polarization (blue dots) and specific heat (green triangles) versus temperature for a field applied along $\mathbf{E} = (1, 0, 100)$. The Kasteleyn transition occurs at $T_K = 3.396$ (vertical dashed line). The polarization in the intermediate plateau points along $[001]$ with magnitude $|\mathbf{P}|/P_{\text{sat}} = \frac{2}{\sqrt{10}} \approx 0.63$ (horizontal dashed line). The inset shows the relative polarization near the Kasteleyn transition of the effective dimers into a fully ordered state. The numerical data (blue dots) agrees with the polarization obtained analytically utilizing the Kasteleyn matrix (solid black line).

8.4 Polarization Plateaus

The numerically obtained polarization and the specific heat are shown in Fig. 8.2 for (A) \mathbf{E}_0 along $[001]$ with a tilt \mathbf{E}_\perp along $[100]$, and in Fig. 8.3 for (B) \mathbf{E}_0 along $[010]$ with a tilt \mathbf{E}_\perp along $[101]$. The exact values of the fields are

$$\begin{aligned} \text{(A)} \quad & \mathbf{E} = (1, 0, 100) \\ \text{(B)} \quad & \mathbf{E} = \left(\frac{1}{\sqrt{2}}, 100, \frac{1}{\sqrt{2}} \right) \approx (0.71, 100, 0.71) . \end{aligned}$$

$|\mathbf{E}_\perp|$ is set to be two orders of magnitude smaller than $|\mathbf{E}_0|$ in order to achieve a separation of the energy scales.

For temperatures $T \gg |\mathbf{E}_0|$ the physics are solely determined by the ice rules and, consequently, the polarization is close to zero. Upon cooling down to $|\mathbf{E}_\perp| \ll T < |\mathbf{E}_0|$, a crossover into an intermediate polarization plateau is observed. In the intermediate plateau, the spin sublattice with the maximal projection along the field gets pinned. The other spins remain free and form decoupled, two-dimensional layers. Thus, a

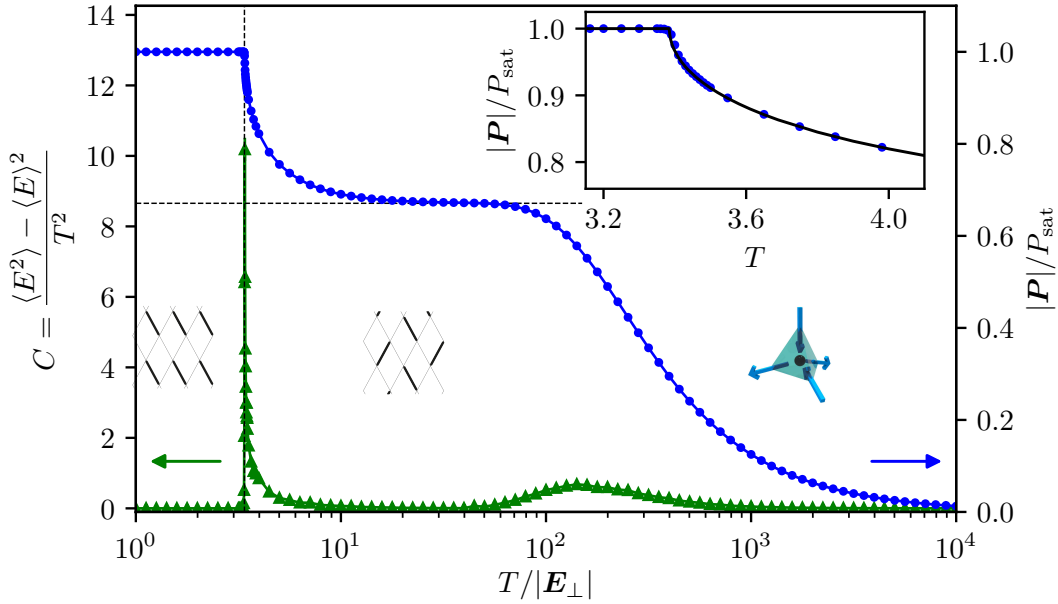


Figure 8.3: Relative polarization (blue dots) and specific heat (green triangles) versus temperature for a field applied along $\mathbf{E} = \left(\frac{1}{\sqrt{2}}, 100, \frac{1}{\sqrt{2}}\right) \approx (0.71, 100, 0.71)$. The Kasteleyn transition occurs at $T_K = 3.385$ (vertical dashed line). The polarization in the intermediate plateau points along $[010]$ with magnitude $|\mathbf{P}|/P_{\text{sat}} = \frac{3}{2\sqrt{5}} \approx 0.67$ (horizontal dashed line). The inset shows the relative polarization near the Kasteleyn transition of the effective dimers into a fully ordered state. The numerical data agrees with the polarization obtained analytically utilizing the Kasteleyn matrix (solid black line).

dimensional reduction of the physics from three to two dimensions occurs due to the external field. The polarization is determined by the fixed spins and is illustrated as horizontal dashed lines in Fig. 8.2 and 8.3.

The crossover between high-temperature and intermediate plateau has two qualitatively different regimes [34]. See Fig. 8.4. Due to the ice rules, the polarization can only be reduced by introducing string-defects of concurrent spins spanning the entire system. These string-defects flip spins that would be pinned by the field at lower temperatures. Thence, the two-dimensional layers which were decoupled at low temperatures, begin to interact and three-dimensionality gets restored. The crossover occurs once the entropic gain of a string-defect balances out the loss of internal energy. Multiple string defects exist at high temperature with an interaction of entropic origin. Once multiple string-defects exist, their interaction gets screened and a mean-field analysis can be applied to reveal a finite-size independent polarization [34]. Similar to spin ice, the polarization decreases exponentially as $\Delta P \propto \exp\left\{-\frac{32|\mathbf{E}|}{9T}\right\}$ upon raising the temperature [34, 55].

The occurrence of string-defects is suppressed exponentially in $\Delta E/T$, such that at low temperatures it is unlikely to have two or more string defects at a time. Equivalently

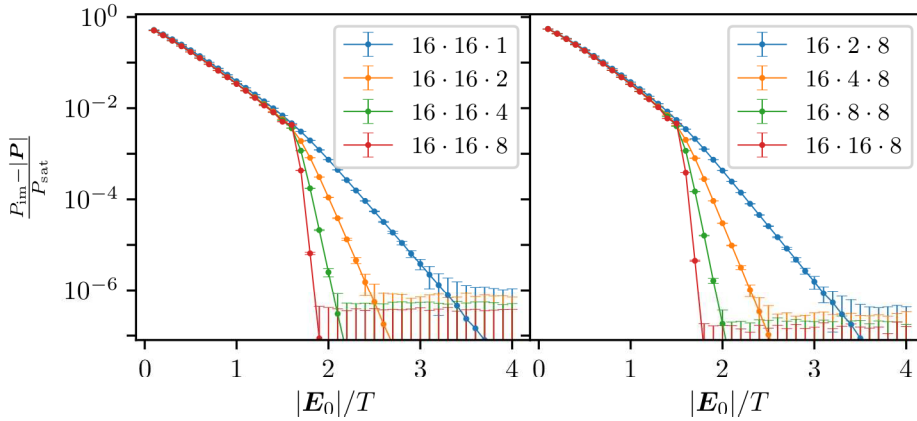


Figure 8.4: $P_{im} - |\mathbf{P}|$ over inverse temperature $T/|\mathbf{E}_0|$ normalized by the main field component. The left regime exhibits no size dependence, whereas the slope in the right regime depends on the systems size parallel to the field. The left column shows the data for $\mathbf{E}_0^{[001]}$, the right column for $\mathbf{E}_0^{[010]}$. A tilt, \mathbf{E}_\perp , has not been applied here.

for periodic boundary conditions, it is unlikely that a loop winds more than once around the system. As such, the interaction is not screened and the string-defect can explore the entire system. This results in finite-size depends both in the longitudinal and transverse size with respect to the field direction, cf. Fig. 8.4. Increasing the transverse size of the system increases the entropy gain due to a string defect. Thence, the crossover temperature gets shifted. The longitudinal dimension determines the energy cost of creating such a defect and, thus, increasing it results in a faster approach of the intermediate plateau. The latter implies a steeper decay of the difference of the polarization of the system and the polarization of the intermediate plateau, $|\mathbf{P}| - P_{im}$.

At low temperatures, a second polarization plateau with saturated polarization is approached. Near $T_K \approx 3.4$ the specific heat diverges for $T > T_K$, indicating a continuous phase transition. In contrast, the specific heat vanishes for $T < T_K$, which would indicate a first order phase transition. In fact, any fluctuations are suppressed below the transition as they are only caused by string defects spanning the entire system. This unconventional transition is known as a Kasteleyn transition [56], which appears for hardcore dimers at close packing.

We continue with a more detailed discussion of the intermediate plateau and the Kasteleyn-type transition into the fully polarized phase. A one-to-one mapping from spin configurations within the decoupled layers to hardcore dimers exists. The discussion of the emergent dimers is given separately for the two field directions studied. The first field direction (A) leads to decoupled layers of dimers on a hexagonal lattice, and the second field direction (B) gives rise to dimers on a square lattice.

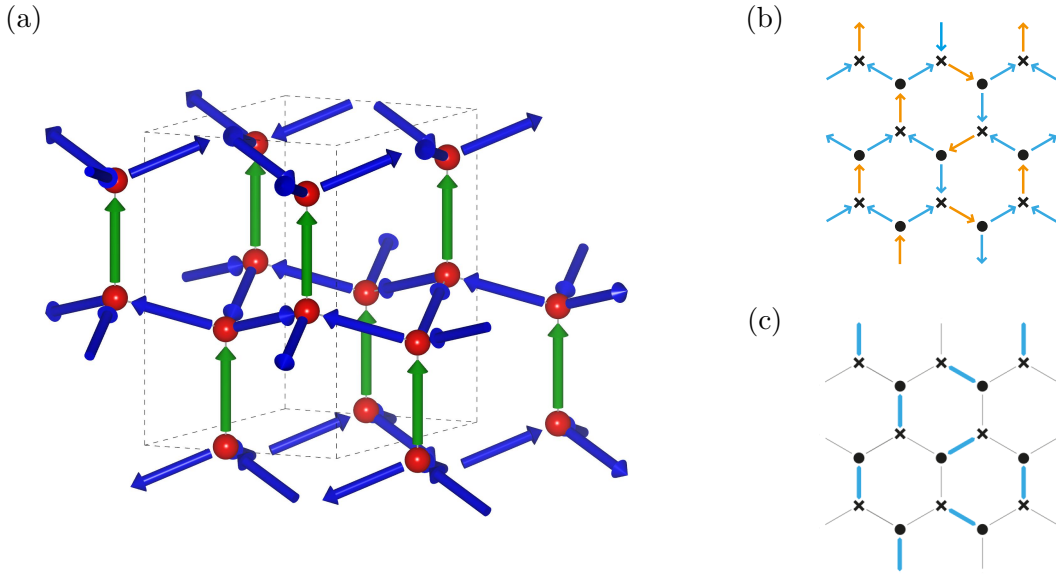


Figure 8.5: Upon applying a field along $[001]$ and lowering the temperature below the corresponding energy scale, the spins with the largest projection onto the field get pinned. These are highlighted as green spins in (a). The remaining degrees of freedom, blue spins in (a), form a bipartite honeycomb lattice with two-in-one-out or one-in-two-out configurations, see (b). A one-to-one map to dimers on the edges of a honeycomb lattice (c) exists.

(A) Intermediate Plateau: Dimer on an Hexagonal Lattice

Applying a field along $[001]$ pins the spins parallel to the field, the green spins in Fig. 8.5(a), as soon as the ratio $|\mathbf{E}_0|/T$ is sufficiently large. The remaining degrees of freedom, the blue spins, reside on the edges of two dimensional honeycomb lattices with alternating two-in-one-out or one-in-two-out vertices. We can map the blue spins to dimers on the same honeycomb lattice by assigning a dimer to each minority spin, which are highlighted in orange in Fig. 8.5(b). The hexagonal layers form an 'ABAB' stacking with inverted two-in-one-out or one-in-two-out vertices. Apart from the stacking, this intermediate state has a very close analogy to the $[111]$ magnetization plateau found in pyrochlore spin ice [34, 55].

Closely packed configurations of dimers on the edges of a honeycomb lattice exhibit a transition between a long-range ordered phase and a disordered phase [56]. The dimers are closely packed, if each site is occupied by a single dimer, yet no two dimers shall occupy the same site. This condition implies local constraints similar to the ice rules and results in an algebraic decay of two-point correlations. The transition occurs once the Boltzmann weight $e^{-\beta\epsilon_\alpha}$ of placing a dimer on one edge exceeds the sum of the weights on the other two edges, e.g., $a \geq b + c$. Here, β is the inverse temperature, $\beta = 1/k_B T$, with the Boltzmann constant k_B set to unity. $\epsilon_\alpha = -\sum_{i \in \alpha} s_i \hat{\mathbf{e}}_i \cdot \mathbf{E}_\perp$ is the

energy of the local configurations of spins on a tetrahedron α . The critical weight can be calculated by considering the corresponding spin configuration for each dimer and the direction of the tilt-component of the field. For the tilt field under consideration, $\mathbf{E}_\perp \parallel [100]$, the critical condition is

$$a_c = 1 + \frac{1}{a_c} \implies a_c = \frac{1}{2} (1 + \sqrt{5}) \approx 1.618 . \quad (8.4)$$

In the simulation, we normalize the dipole moment of the spin $\mathbf{d}_i = s_i \hat{\mathbf{e}}_i$. In doing so, the critical temperature T_K reads as

$$T_K = \frac{-\sum_i s_i \hat{\mathbf{e}}_i \cdot \mathbf{E}_\perp}{\log a_c} = \frac{\epsilon_a}{\log a_c} = 3.396 . \quad (8.5)$$

Here, ϵ_a is the energy of the spin configuration that is equivalent to energy of a dimer at the edge with weight a .

Since the case of emergent dimers on the honeycomb lattice has been studied extensively in the literature [34, 55, 56], we focus on the second field direction.

(B) Intermediate Plateau: Dimer on a Square Lattice

If the field is applied along $[010]$, the intermediate polarization plateau can be understood as layers of hardcore dimers on a rhombic lattice. Each layer is separated by the spin sublattice that is pinned by the field (green spins in Fig. 8.6(a)). Any remaining thermal fluctuations will happen within the two-dimensional layers. Each layer is composed of double vertices with two neighboring nodes of the same kind, either both of three-in-one-out or both of one-in-three-out configuration. See also Fig. 8.6(c). By combining two such nodes to a double vertex one internal spin and four external spins are obtained. Three of the external spins are pointing out (in) and one in (out). Thence, a one-to-one mapping to dimers exists by assigning a dimer to each minority spin. In doing so, one ends up with hardcore dimers on a rhombic lattice, see Fig. 8.6(c).

Such a dimer model still exhibits a set of ground states growing exponentially with system size. Consequently, the residual entropy remains finite, but is reduced in comparison to the residual entropy of ice I_h . A further introduction of a tilt field acting on the dimers within each layer reduces the entropy. Similar to hexagonal case above, a concrete condition for the ordering transition on the square lattice is known [205]. The dimers order once the Boltzmann weight $e^{-\beta\epsilon_i}$ of a dimer exceeds the sum of the weights of the other three dimer orientations. Note that due to the field, the dimers with the same orientation, horizontal or vertical, come in pairs with inverse weight. Swapping all spins of a given configuration leads to a change in sign of the energy and hence to an inverse weight.

Let us assume the ordering of weights $a > b \geq \frac{1}{b} > \frac{1}{a}$. Then, the critical condition

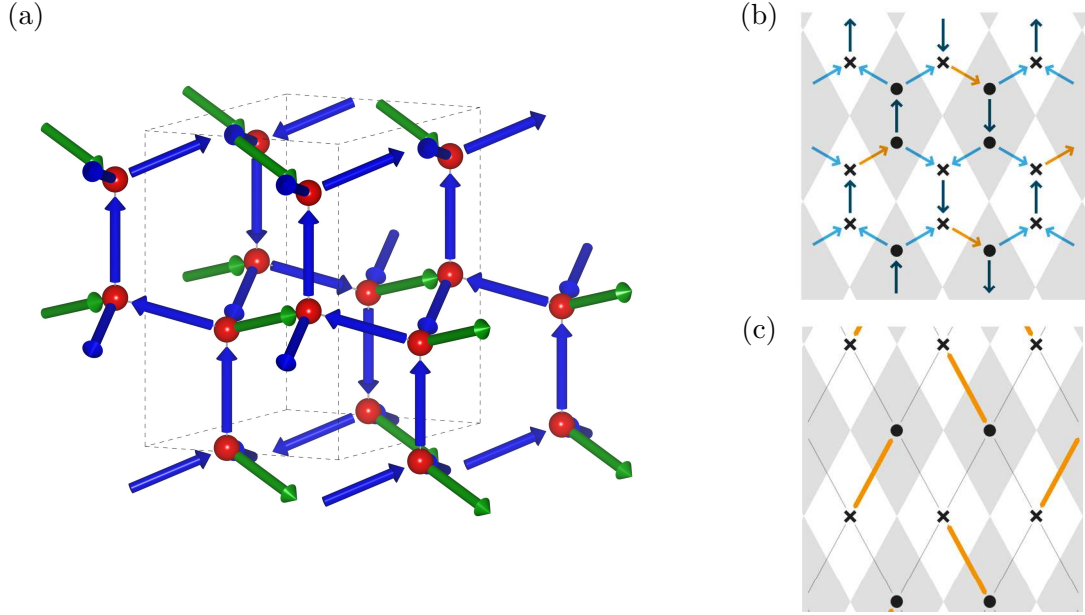


Figure 8.6: Upon applying a field along $[010]$ and lowering the temperature below the corresponding energy scale, the spins with the largest projection onto the field get pinned. These are highlighted as green spins in (a). The remaining degrees of freedom, blue spins in (a), form a non-bipartite honeycomb-like lattice with two neighboring vertices being of the same two-in-one-out configuration (or vice versa) as illustrated in (b). Upon contracting such a double vertex, a one-to-one map to dimers on the edges of a rhombic lattice (c) exists.

is $a = b + \frac{1}{b} + \frac{1}{a}$. By inserting the corresponding energies, cf. Eq. (8.3), one arrives at a transcendental equation

$$\sinh\left(-\frac{\epsilon_a}{k_B T_K}\right) = \cosh\left(-\frac{\epsilon_b}{k_B T_K}\right). \quad (8.6)$$

As before, k_B is set to one. For a tilt field \mathbf{E}_\perp applied along $[101]$, we get a critical temperature of

$$\frac{T_K}{E_\perp} \approx 3.385. \quad (8.7)$$

T_K is shown in the polarization plot, cf. Fig. 8.3, as a dashed vertical line and agrees with the simulation.

Extracted from the numerical simulations, we obtain a critical exponent of the heat above T_K extracted from numerics is $\alpha^+ \approx 0.53$, which is close to the expected value of $1/2$ [208]. Fluctuation are suppressed on the low T side of the transition and thus $\alpha^- = 0$. The difference of the polarization to the saturated value exhibits a critical exponent of $\beta^+ \approx 0.4$.

In the following section, the Kastelyn theory will be applied to obtain exact expres-

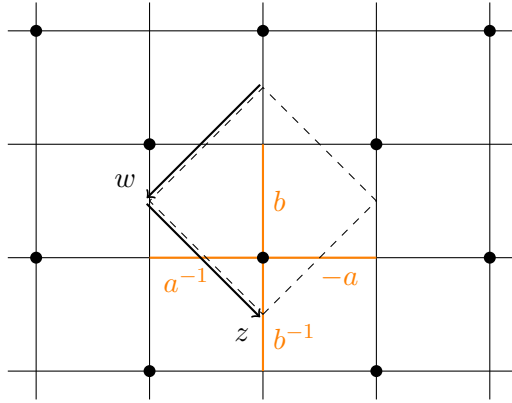


Figure 8.7: Unit cell convention for the computation of the partition sum utilizing a Kasteleyn matrix with bond weights and corresponding bonds highlighted in orange.

sions results for the effective dimer model.

8.5 Kasteleyn Transition for Dimers on a Square Lattice

As outlined in section 2.2.6, the partition sum of dimers on any planar graph can be derived by computing the Pfaffian of the Kasteleyn matrix, $\text{Pf } K$. The Kasteleyn matrix is the adjacency matrix of the lattice with an admissible orientation and weights determined by the Boltzmann factor of placing a dimer on that particular edge. For bipartite lattices, $\text{Pf } K$ is equivalent to the determinant of the reduced Kasteleyn matrix, \tilde{K} . The matrix \tilde{K} incorporates only the connections from even to odd sites.

Fig. 8.7 illustrates the convention of the fundamental unit cell and the edge weights used throughout this section. With this choice, the reduced Kasteleyn matrix is only a scalar and reads

$$\tilde{K} = b + \frac{zw}{b} - aw + \frac{z}{a} = \det \tilde{K} , \quad (8.8)$$

with complex variables $z = e^{i\phi}$ and $w = e^{i\psi}$

Following section 2.2.6 and using Eq. (2.23) therein, the partition sum, \mathcal{Z} , can be expressed as a double integral in the complex plane

$$\frac{1}{N} \log \mathcal{Z} = \frac{1}{(2\pi i)^2} \oint_{|w|=1} \frac{dw}{w} \oint_{|z|=1} \frac{dz}{z} \log \left(b + \frac{zw}{b} - aw + \frac{z}{a} \right) . \quad (8.9)$$

A direct computation of (8.9) for arbitrary weights a and b is difficult, if feasible at all. The logarithm, $\log z$, of a complex variable z has a branch cut for $\{z \in \mathbb{R}, z \leq 0\}$ and, thus, the residue theorem cannot be employed.

However, given the partition sum, thermodynamic quantities are defined as derivatives of $\log \mathcal{Z}$, resulting in terms suitable for the residue theorem. Let us focus on the

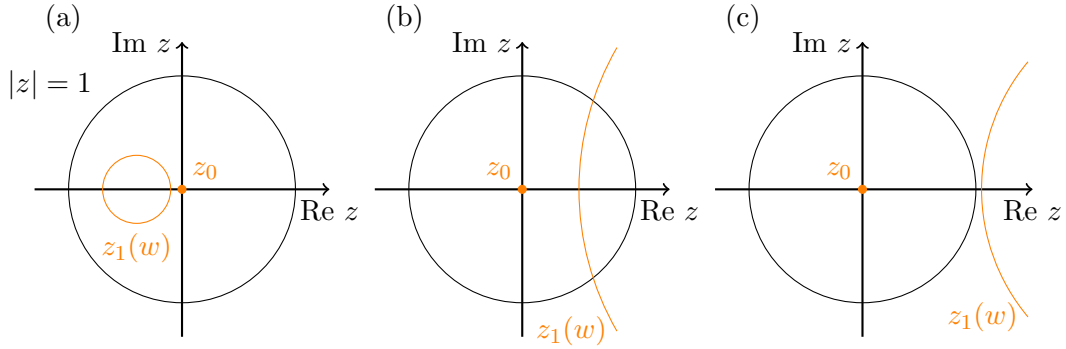


Figure 8.8: Poles of the integral (8.10) with respect to z . Three different cases exist depending on the choice of weights a, b : (a) $z_1(w)$ is completely inside, (b) $z_1(w)$ is partially inside, and (c) $z_1(w)$ is completely outside of the integration contour $|z|=1$.

density of dimers on a horizontal bond. If a dimer is placed right or left of an even site (filled dot in Fig. 8.7, its weight is inverted, $a \rightarrow a^{-1}$. Thence, the densities on either of the horizontal bond are correlated and its difference can be derived

$$\rho_a = \frac{N_a - N_{a^{-1}}}{N} = a \frac{\partial}{\partial a} \log \mathcal{Z} .$$

By moving the derivative $\partial/\partial a$ inside—the integration paths do not depend on a —we get

$$\rho_a = \frac{1}{(2\pi i)^2} \oint_{|w|=1} \frac{dw}{w} \oint_{|z|=1} \frac{dz}{z} \frac{-aw - \frac{z}{a}}{b + \frac{zw}{b} - aw + \frac{z}{a}} . \quad (8.10)$$

The inner integral with respect to z is performed using the residue theorem. First order poles are situated at

$$z_0 = 0 \quad z_1 = ab \frac{aw - b}{aw + b} , \quad (8.11)$$

of which z_0 is always within the integration path, and $z_1(w)$ depends on the second integration variable. Along the integration path, $|w|=1$, of the outer integral, $z_1(w)|_{|w|=1}$ is either completely inside, partially inside, or completely outside of the integration path, $|z|=1$, of the inner integration. See Fig. 8.8 for an illustration of the three different cases. Which of the three cases applies depends on the choice of the weights a, b . The cases of $z_1(w)$ being either completely inside or outside are trivial in that the residue theorem can also be applied for the integration with respect to w . These cases occur if one of the weights is larger than the three remaining ones, e.g., $a > b + \frac{1}{b} + \frac{1}{a}$, and the dimer configuration is long-range ordered. Consequently, the density ρ_a is

constant

$$\rho_a = \begin{cases} 1 & \text{if } (a > b + \frac{1}{b} + \frac{1}{a}) \\ 0 & \text{if } (b > \frac{1}{b} + a + \frac{1}{a}) \text{ or } (\frac{1}{b} > b + a + \frac{1}{a}) \\ -1 & \text{if } (\frac{1}{a} > b + \frac{1}{b} + a) . \end{cases} \quad (8.12)$$

In the remaining case, the choice of weights a and b results in the pole $z_1(w)$ being partially inside $|z| = 1$. Thence, the outer integral does only run along the path of w for which $z_1(w)$ is inside

$$\rho_a = \frac{1}{2\pi i} \oint_{|w|=1} \frac{dw}{w} \frac{aw}{b-aw} + \frac{1}{2\pi i} \int_{w_1}^{w_2} \frac{dw}{w} \frac{-aw}{aw-b} - \frac{b}{aw+b} . \quad (8.13)$$

Here, the first term comes from the residue at $z_0 = 0$, and the second term from the residue at $z_1(w)$. The first term is easily solved using the residue theorem again: a pole $w_0 = b/a$ is either inside or outside $|w| = 1$ and results in a step function $\Theta(x)$, which is zero if $x \leq 0$ and one if $x > 0$. For the second term, an expression of the indefinite integral exists. Consequently, the result of the definite integral is simply the difference of the indefinite integral at the final, $w_f = e^{i\phi_0}$, and the initial point, $w_i = e^{-i\phi_0}$, of the path. Thence,

$$\rho_a = \Theta\left(1 - \frac{b}{a}\right) - \frac{1}{\pi}\phi_0 + \frac{1}{2\pi i} \log \frac{b^2 - a^2 + 2iab \sin \phi_0}{b^2 - a^2 - 2iab \sin \phi_0} \quad (8.14)$$

with

$$\phi_0 = \arccos\left(\frac{(a^2 + b^2)(a^2b^2 - 1)}{2ab(a^2b^2 + 1)}\right) , \quad (8.15)$$

being the angle at which $z_1(e^{\pm i\phi})$ intersects with $|z| = 1$.

Figure 8.9 illustrates the dimer densities ρ_a and ρ_b as a function of the weight a for a fix choice of weight $b = 2.5$. Given the densities, the polarization can be computed exactly. The polarization is given as $\mathbf{P} = d \sum_i \langle s_i \rangle \hat{\mathbf{e}}_i$, where $\langle s_i \rangle$ is the thermal average of the Ising variable s_i , which depends on $\rho_a(a, b)$ and $\rho_b(a, b)$. Fig. 8.2 and 8.3 include both the numerical results and the exact values for the polarisation in the thermodynamic limit.

8.6 Correlations and Static Structure Factor

In this section, we study the static structure factor (SSF). The SSF is the Fourier transform of the equal-time two-point correlations and reveals details about the microscopic degrees of freedom. Furthermore, the SSF allows for comparison with scattering experiments like inelastic neutron scattering. Here, we focus on the diffuse part of the SSF

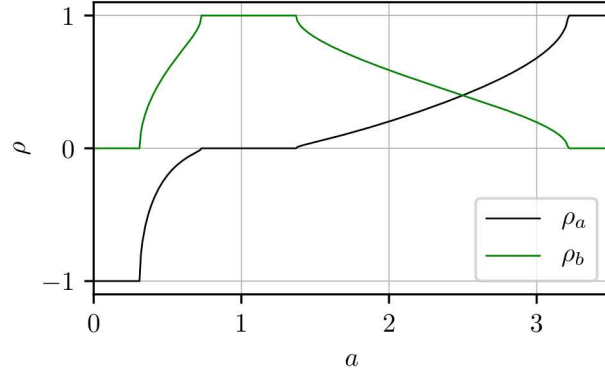


Figure 8.9: Density of dimers on horizontal edges ρ_a and on vertical edges ρ_b with fixed edge weight $b = 2.5$. In the region around $a \approx 1$, the dimer configuration is long-range ordered and dimers are only placed on the vertical edges with weight b (cf. Fig. 8.7). For $a > 3.2$ dimers are situated on the horizontal edges with weight a , whereas for $a < 0.3$ dimers are on the horizontal edges with weight a^{-1} . The dimer configurations are not ordered for the remaining values of a .

capturing the contribution from the proton disorder. The static oxygen lattice would only contribute to the Bragg peaks and is neglected.

Following the notation of [196] the general structure factor of the protons is

$$S_H(\mathbf{k}) \propto \left| \sum_{j \in \text{H sites}} n_j e^{i\mathbf{k} \cdot \mathbf{R}_j} \right|^2. \quad (8.16)$$

The sum runs over all proton sites, \mathbf{R}_j , of which two per link exist. n_j denotes the corresponding occupation number, which can either be zero or one.

By making use of the first ice rule, i.e. one proton per link, the proton configuration can be rewritten in terms of Ising variables s_j residing at the middle of a link, \mathbf{r}_j , and the proton shift distance combined with the direction of the link, $\mathbf{a}_{\gamma(j)}$. Here, $\gamma(j)$ maps the general label j of a link to one of the distinct links with label β within the unit-cell. Hence, $\mathbf{a}_{\gamma(j)}$ is a purely geometrical factor, whereas the Ising variables s_j contains all the information about the degrees of freedom and their correlations. Then, Eq. (8.16) becomes

$$S_H(\mathbf{k}) \propto \left| \sum_j s_j \sin(\mathbf{a}_{\gamma(j)} \cdot \mathbf{k}) e^{i\mathbf{k} \cdot \mathbf{r}_j} \right|^2, \quad (8.17)$$

where the sum runs over all links j . The sine factor leads to a suppression of any diffuse scattering within the first and partly the second Brillouin zone.

Eq. (8.17) simplifies by considering only effective Ising spins s_j and neglecting the

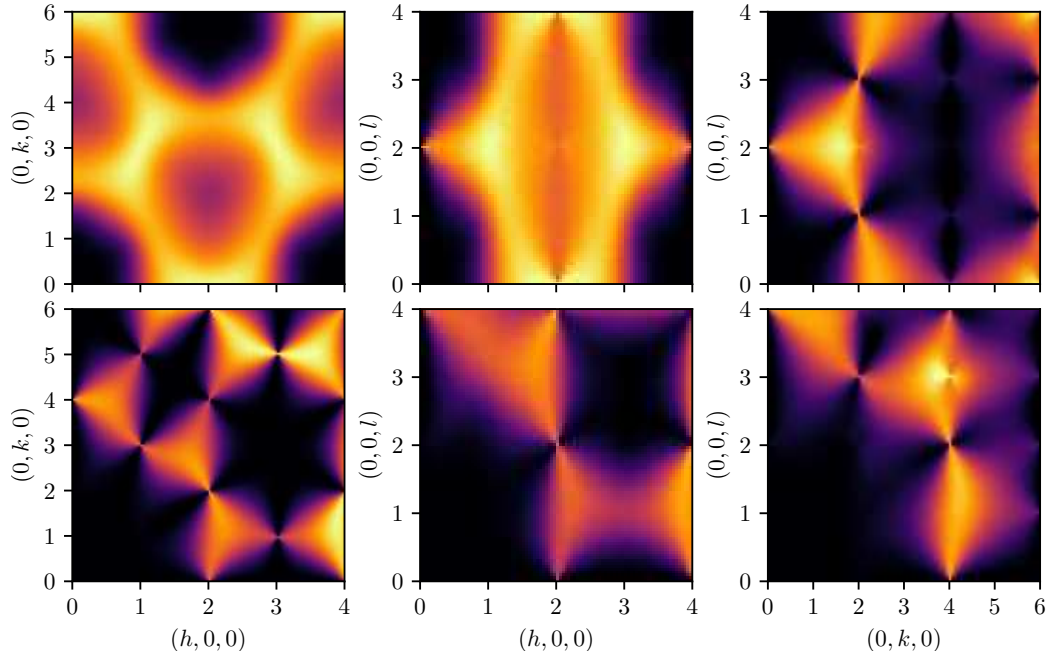


Figure 8.10: Diffuse part of the static structure factor at high temperatures or equivalently without external field. The upper row shows the $[hk0]$ -, $[0kl]$ - and the $[h0l]$ -plane for $S_I(\mathbf{k})$, see Eq. (8.18), of the effective spin model with Ising variables s_i . The lower row shows the same scattering planes for the proton system, $S_H(\mathbf{k})$ given in Eq. (8.17), which can be compared to experimental scattering data on ice I_h [196]. The local ice rule constraint results in pinch points with typical bow-tie features.

geometrical factor $\mathbf{a}_{\gamma(j)}$

$$S_I(\mathbf{k}) \propto \left| \sum_j s_j e^{i\mathbf{k}\cdot\mathbf{r}_j} \right|^2. \quad (8.18)$$

As a reminder, the convention for the s_j is such that a positive s_j refers to a spin pointing from a site on the sublattice A to a site on B.

Even though, both SSF look very different, they include the same information on the correlations and will exhibit similar scattering features. The SSF at high temperatures is shown in Fig. 8.10. At high temperatures thermal fluctuations exceed the Stark energy. Both SSF—that of the protons, $S_H(\mathbf{k})$, as well as that of the spins, $S_I(\mathbf{k})$ —exhibit pinch points with a bow tie structure of the intensity around lattice Bragg points, e.g. at $\mathbf{k} = (2, 2, 0)$ or $(0, 4, 2)$ for $S_H(\mathbf{k})$ and at $\mathbf{k} = (0, 2, 1)$ or $(0, 0, 2)$ for $S_I(\mathbf{k})$. The bow tie structure is typical for local constraints like the ice rules, cf. Sec. 2.2.3. The ice rules are equivalent to a divergence free condition on a lattice. In the continuum, it translates to Gauss law, $\nabla \cdot \mathbf{E} = 0$, that eliminates the longitudinal component of the field. Regarding the microscopic degrees, the ice rules project out any longitudinal

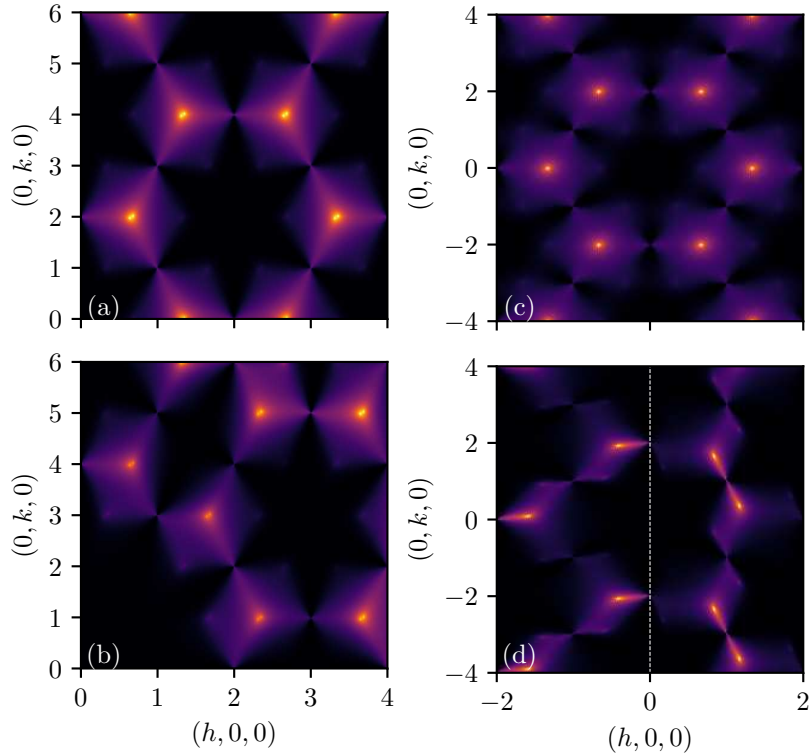


Figure 8.11: $[hk0]$ plane of the static structure factor within the intermediate plateau ($T = 40$) when a field is applied along $\mathbf{E} = (1, 0, 100)$ for: (a) effective spin model, (b) protons, (c) asymptotic correlations for dimers with equal weights on the hexagonal lattice [55], and (d) effective spin model at $T = 5$ within the plane formed by either the lower (left) or upper (right) spins of a unit cell. The splitting of the high-intensity points in (a) and (b) is caused by the small tilt component of the applied field. Lowering the temperature enhances the splitting as illustrated in (d). Furthermore, the splitting depends on the tilt direction relative to the lattice.

correlation of the otherwise unconstrained proton displacements. Additional broad features occur at $S_I(\mathbf{k})$ in the $[hk0]$ -plane, that become pinch points in the effective dimer model. They occur for example at $\mathbf{k} = (3, 0, 1)$ for $S_H(\mathbf{k})$ and at $\mathbf{k} = (1, 0, 1)$ for $S_I(\mathbf{k})$.

The SSF for high- T —or at (almost) zero field—agrees with experimental data based on neutron scattering [196] and theoretical analysis done by Wehinger et al. [209], Isakov et al. [197], and Benton et al. [198].

In the following, the SSF in the intermediate plateau is discussed. Thence, we separate the discussion depending on the field direction.

(A) SSF Within Intermediate Plateau: Field Along [001] Axis

In the intermediate plateau upon applying a field along the [001] axis, the SSF, cf. Fig. 8.11 exhibits the sixfold symmetry of the honeycomb lattice. Pinch points with bow ties survive the field. They occur due to the local constraints of dimers, which itself is a consequence of the initially imposed ice rules. More strikingly, the SSF exhibits peaks at $\mathbf{k} = (4/3, 0, 0)$ (in $S_I(\mathbf{k})$) and equivalent points generated by the C_6 symmetry. These peaks are not Bragg peaks which would signify order. Instead the peaks are caused by algebraically decaying correlations, $C(r) \propto \frac{1}{r^\alpha}$, with $\alpha = 2$ for classical dimers on the honeycomb lattice [55]. As such the intensity of these peaks grows logarithmically with system size. The correlations given in [55] lead to a similar SSF as in case of the effective spin model.¹ Compare Fig. 8.11 (a) and (c). When considering the SSF of the protons, cf. Fig. 8.11(b), the form factor due to the proton positions shift the pinch points and peaks. Yet, the qualitative features remain similar.

Upon lowering the temperature, the effect of the tilt field becomes apparent, cf. Fig. 8.11(d). The peaks split and shift towards a nearby pinch point. In fact, two peaks superimpose in the SSF. Remember, that two honeycomb layers are stacked in an ABAB pattern. A unit cell is cut by both planes and the planes are perpendicular to the [001] axis. The tilt field prefers different edges in the two layers. Consequently, one peak moves towards the $\mathbf{k} = (1, 1, 0)$ pinch point and a second peak moves towards the $\mathbf{k} = (2, 0, 0)$ pinch point. In figure 8.11(d), the SSF in the left half is obtained by summing only over the spin variables in the lower honeycomb plane, whereas the right half includes only the upper honeycomb plane. At the transition into the ordered state, the peaks annihilate at their corresponding pinch point.

(B) SSF Within Intermediate Plateau: Field Along [010] Axis

The SSF within the intermediate polarization plateau upon applying a field along the [010] axis is shown in Fig. 8.12. The SSF of the effective spin model, $S_I(\mathbf{k})$ as in Eq. (8.18), is shown in (a), and the SSF of the full proton system, $S_H(\mathbf{k})$ as in Eq. (8.17), is shown in (b). Regardless of the choice, pinch points with a bow-tie like structure occur as a sign of the ice rules. Some of the broad features previously mentioned sharpen and become pinch points as well, e.g., at $\mathbf{k} = (3, 0, 1)$ for $S_H(\mathbf{k})$ and at $\mathbf{k} = (1, 0, 1)$ for $S_I(\mathbf{k})$. Similar to the first field direction, the SSF exhibits peaks in between the pinch points, which are caused by the algebraic decay of correlations.

In order to make the similarity to a dimer model more striking, let us consider a SSF, where only the external spins of a double-vertex are considered. In doing so, the reduced SSF $S_{I,red}(\mathbf{k})$ becomes equivalent to the SSF of dimers on a square lattice [45, 210–

¹Yet, the structure factor plotted in [55] differs. The intensity at and near the peaks ($k = (4/3, 0, 0)$ and symmetry-equivalent points) is suppressed in their plot. We obtain the same SSF if we change a sign in the phase factor $e^{i\mathbf{k}\cdot\mathbf{r}}$ of the Fourier transform.

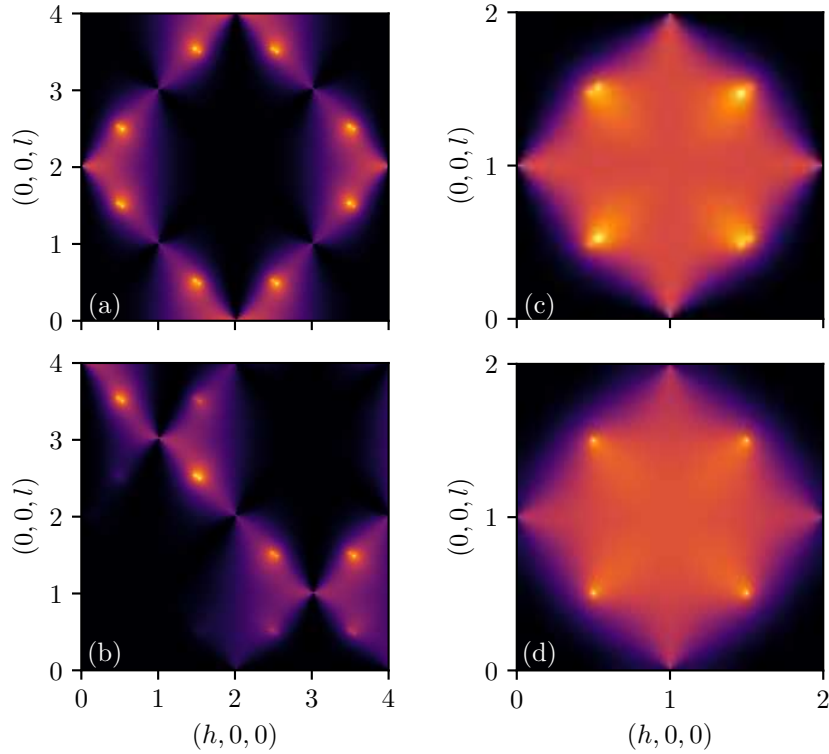


Figure 8.12: $[h0l]$ plane of the static structure factor within the intermediate plateau ($T = 40$) when a field is applied along $\mathbf{E} = (\sqrt{2}, 100, \sqrt{2})$ for: (a) effective spin model, (b) protons, (c) effective spin model without the intermediate spin, and (d) asymptotic correlations for dimers with equal weights on the square lattice [45]. The splitting of the high-intensity points in (a), (b), and (c) is caused by the small tilt component of the applied field. A bijective map exists from the double-vertices with three-in-one-out (one-in-three-out) spin configurations to dimers enabling to compare (c) and (d).

212]. The asymptotic correlations of dimers on a square lattice have been calculated for a smaller unit cell with only two Boltzmann weights, one for horizontal and one for vertical dimers [45]. Nevertheless, we can use the result in the limit of equal weights which corresponds to not applying a tilt field. Fig. 8.12 allows for a comparison of the structure factor based on our simulation (c) with the one based on the asymptotic correlations (d). Most notably, both show the peaks at $\mathbf{k} = (\frac{1}{2} + n, 0, \frac{1}{2} + m)$ with $n, m \in \mathbb{Z}$. They are caused by critical correlation of dimers of the same orientation [212] decaying algebraically with $1/r^2$. The broad square-like feature of increased intensity has its origin in the correlation of dimers of different orientation. Thus, we clearly find a dimensional reduction of the three-dimensional ice to a two-dimensional model of dimers on the edges of a square-like lattice.

As a remark, due to combining two oxygen nodes of different neighboring sublattices of the original ice I_h lattice, the initially defined orientation of two of the external spins

Table 8.1: Identification of several features in reciprocal space between different conventions.

scattering feature	\mathbf{k} in [212]	$\mathbf{k}_{I_h,or}$
S_{xx} log. peak	$(\pi, 0)$	$(\pi, 0, \pi)$
	$(\pi, 2\pi)$	$(3\pi, 0, -\pi)$
S_{xx} pinch point	(π, π)	$(0, 0, 2\pi)$

is opposite to the other two spins. This leads to a shift of 2π along the direction of alternation. In our case this shift occurs along [001] and has already been considered in Fig. 8.12(c). A second difference becomes apparent, when considering our enlarged unit cell. In earlier work, only two different Boltzmann weights are considered: one weight for horizontal and one weight for vertical dimers [45]. In ice I_h the bipartite property of the lattice reflects in the dimer weights and we have to double the unit cell consisting instead of two nodes and four inequivalent edges. A rotation of $\pi/4$ is needed in order to convert two of the small unit cells into the bigger one. The reciprocal lattice vectors change accordingly in length and direction. One can identify the position of the features in reciprocal space obtained in [212] with the positions in the reciprocal space of ice I_h , cf. table 8.1. Apart from a shift and a rotation, the diffuse scattering does not change due to the mapping.

Upon applying the tilt field, the (logarithmic) peaks splits into a pair of peaks. This is not captured by the asymptotic correlations of [45]. The unit cell needs to be doubled in order to see the splitting. Furthermore, the pair gets asymmetric in the sense, that one of the peaks is more pronounced. For understanding the asymmetry, recall that we have an extended unit-cell with four dimer and two of each orientation. One dimer of each orientation is energetically preferred. Thus its occupation number and the intensity of the corresponding peak increases.

By further reducing the temperature below the Kasteleyn temperature the system exhibits a transition into a single ordered configuration, which does not exhibit any diffuse scattering.

8.7 Conclusion

A minimal model of the proton subsystem of hexagonal water ice I_h coupled to an electric field has been studied. Upon applying an external (electric) field tilted slightly away from certain easy axes, the proton configuration enters a long-range ordered phase with the transition being of Kasteleyn-type. An intermediate plateau exists and is entered once the temperature is below the scale of the Stark energy caused by the main component of the field. The degrees of freedom within the intermediate plateau can be mapped to decoupled two-dimensional planes of hardcore dimers: (A) dimers

placed on the edges of a honeycomb lattice, if the field is applied along [001], and (B) dimers placed on the edges of a square lattice, if the field is applied along [010]. Case (A) is in close analogy to the intermediate magnetization plateau in spin ice with an magnetic field along [111]. Its transition to the ordered state is determined by the original work of Kasteleyn. The second case is a result of the structure of ice I_h and does not have an analogy to pyrochlore spin ice. Upon tilting the field, it exhibits a Kasteleyn transition into an ordered state.

In either case, the application of a field leads to a dimensional reduction of the thermally fluctuating degrees of freedom with a simultaneously reduced power in the algebraic correlations. In the effective two-dimensional models of dimers the correlations decay with $1/r^2$ and result in peaks in the static structure factor.

For a (sharp) Kasteleyn transition to occur, strings have to span the entire system along which the protons can be swapped without breaking the ice rules. Those dynamics are unlikely to occur in a realistic ice sample, as the energy barrier is too high. However, by introducing defects, i.e. doping with KOH, the necessary dynamics can be restored, but the defects will also round the unique cusp the polarization exhibits at the Kasteleyn transition [51].

The partial order within the intermediate polarization plateau may also restrict the quantum tunneling of protons into two dimensional layers. Such a tunneling has been discussed [198, 202] and may have been observed in an experiment [200]. Quantum tunneling would occur on the smallest loops with six protons, hexagonal plaquettes. In contrast to spin ice, where only one kind of plaquettes exist, ice I_h has two different hexagonal plaquettes either aligned perpendicular or along the c-axis. By applying a field along certain easy axis one can suppress the quantum tunneling around one of the two plaquettes and allow for tunneling only on the other. Hence, this would allow for studying the proton tunneling for each kind plaquette individually. The saturated plateau with full ordering does not exhibit any swappable six-proton-loop at all and quantum tunneling will be suppressed completely.

Chapter 9

Conclusion and Outlook

This thesis captures two important models exhibiting frustration and giving rise to numerous exotic physical phenomena like emergent gauge fields, topological bands, topological order, fractionalisation and (quantum) spin liquids.

Firstly, in the Kitaev model strongly anisotropic Ising exchange between spin- $\frac{1}{2}$ degrees of freedom results in a quantum spin liquid ground state that features a fractionalisation of an elemental spin excitation into Majoranas and \mathbb{Z}_2 -fluxes. The \mathbb{Z}_2 -fluxes are the vison excitations of a \mathbb{Z}_2 lattice gauge theory. Different perturbations motivated by recent experiments on Kitaev compounds were added. The Kitaev-Heisenberg model—initially considered as a minimal model for Iridates and α - RuCl_3 —exhibits two gapless quantum spin liquid regions around the pure Kitaev limits and several long-range ordered phases, namely FM, Néel, stripy, and zigzag. The quantum spin liquid phases are stable and remain gapless upon adding small perturbations by an Heisenberg spin-exchange. The dynamical spin-structure factor nearby the spin liquids, yet in the ordered phases, exhibits a broad continuum and a shift of weights to higher energies. The question arises, whether the high-energy excitations forming the continuum resemble to some extent the fractionalized quasiparticles of the nearby quantum spin liquid. If so, it may be legitimate to call α - RuCl_3 a proximate spin liquid. However, it was argued that interacting magnons may as well be the origin of the continuum [135].

A second perturbation presumably relevant in Kitaev compounds is the symmetric off-diagonal Γ -coupling. The phase diagram of the Kitaev- Γ model includes an extended long-range ordered phase in which the spins form a three-dimensional ordering pattern: the spins are pairwise antiparallel and aligned along one of the cubic axis. An extended quantum paramagnetic phase with large entanglement, presumably a spin-liquid phase, was found to span from close to the ferromagnetic Kitaev limit all the way to the antiferromagnetic Γ limit and slightly beyond. The eigenvalues of the transfer matrix—an object obtained from the infinite matrix-product state representation of the many-body ground state wave function—is consistent with a scenario of coherent

quasiparticle excitations. Such a finding would hint at a possible quantum spin liquid phase. However, a subtle transition, which may either be a finite size effect or of physical origin, raises the question, whether the Kitaev spin liquid and the extended quantum paramagnetic phase are in some sense related. For the Kitaev- Γ model in particular, finite-size effects due to the cylinder geometry are not negligible and more insight may be gained by utilizing intrinsically two-dimensional methods.

The Kitaev model in a field exhibits, as was verified in this thesis, a topological phase hosting non-abelian anyons. Depending on the sign of the Kitaev coupling, an intermediate, highly entangled, and possibly gapless phase exists in between the low-field topologically ordered phase and the high-field paramagnetic phase. The dynamical spin-structure factor was invoked to study the transition to the intermediate phase from both sites. Approaching from the topological phase, the dominant low-energy mode related to a fermion bound to a flux pair attains more structure and dispersion presumably due to the fluxes becoming mobile. As a result, the spectral gap decreases, yet a complete vanishing is not observed. From the paramagnetic field, a broad continuum forms ranging down to zero energy all over the reciprocal space signifying the unusual character of the intermediate phase. It is natural to ask about the nature of the intermediate phase. In a recent preprint Hickey and Trebst argue that the intermediate phase may be a gapless $U(1)$ spin-liquid [213]. Such an interpretation would be consistent with the numerical results presented in this thesis, however, it is certainly interesting to ask whether clear signatures in favor of—or against—the $U(1)$ spin-liquid could be obtained within the matrix-product states framework. Furthermore, it remains to be investigated, whether such an intermediate phase could be realized in Kitaev compounds. This includes the question about the stability of the intermediate phase under adding relevant spin exchanges.

On the numerical side, matrix-product state methods and the novel matrix-product operator based time-evolution have proven as a very beneficial and versatile numerical framework to study two-dimensional frustrated, and thus strongly correlated, systems in a non-perturbative and unbiased way. The dynamical spin-structure factors computed here provide a straightforward comparison to experimental data, i.e. from scattering experiments. On the contrary, the transfer-matrix spectra are a more theoretical tool, that contains information about the correlations. Its usefulness stems from the fact that it contains all possible correlations and not just particular correlations, e.g., spin-spin. Via a mapping from the correlations to the excitation spectrum, one can extract important knowledge like the position of the minimal gap in reciprocal space. In the context of matrix products states, this technique has only been applied to a small number of physical systems. Therefore, it is certainly interesting to study other problems in order to gain insight and intuition about the transfer matrix spectra.

Last but not least, a minimal model describing the proton configuration in hexagonal

water ice was studied. The ice rules leave an extensive ground state degeneracy. By applying an electric field, the ground state degeneracy reduces. Applying the field certain axes, the effective low-energy degrees of freedom can be described as dimer models confined to two-dimensional planes perpendicular to the field. A small tilt leads to an asymmetric transition of Kasteleyn-type, where fluctuations of the order parameter—polarization or magnetization—are suppressed on the low-temperature site of the transition as the excitations are required to span the entire system.

Bibliography

- [1] D. C. Tsui, H. L. Stormer, and A. C. Gossard: Two-Dimensional Magnetotransport in the Extreme Quantum Limit. *Physical Review Letters* **48**(22) (1982), 1559–1562. doi: 10.1103/PhysRevLett.48.1559.
- [2] R. B. Laughlin: Anomalous Quantum Hall Effect: An Incompressible Quantum Fluid with Fractionally Charged Excitations. *Physical Review Letters* **50**(18) (1983), 1395–1398. doi: 10.1103/PhysRevLett.50.1395.
- [3] S.-S. Chern and J. Simons: Characteristic Forms and Geometric Invariants. *Annals of Mathematics* **99**(1) (1974), 48–69. doi: 10.2307/1971013.
- [4] X.-G. Wen: *Quantum Field Theory of Many-Body Systems*. OUP Oxford, 2004. isbn: 978-0-19-853094-7.
- [5] C. Castelnovo, R. Moessner, and S. Sondhi: Spin Ice, Fractionalization, and Topological Order. *Annual Review of Condensed Matter Physics* **3**(1) (2012), 35–55. doi: 10.1146/annurev-conmatphys-020911-125058.
- [6] J. Villain: Insulating Spin Glasses. *Zeitschrift für Physik B Condensed Matter* **33**(1) (1979), 31–42. doi: 10.1007/BF01325811.
- [7] W. F. Giaque and J. W. Stout: The Entropy of Water and the Third Law of Thermodynamics. The Heat Capacity of Ice from 15 to 273°K. *Journal of the American Chemical Society* **58**(7) (1936), 1144–1150. doi: 10.1021/ja01298a023.
- [8] L. Pauling: The Structure and Entropy of Ice and of Other Crystals with Some Randomness of Atomic Arrangement. *Journal of the American Chemical Society* **57**(12) (1935), 2680–2684. doi: 10.1021/ja01315a102.
- [9] J. D. Bernal and R. H. Fowler: A Theory of Water and Ionic Solution, with Particular Reference to Hydrogen and Hydroxyl Ions. *The Journal of Chemical Physics* **1**(8) (1933), 515. doi: 10.1063/1.1749327.
- [10] P. W. Anderson: Ordering and Antiferromagnetism in Ferrites. *Physical Review* **102**(4) (1956), 1008–1013. doi: 10.1103/PhysRev.102.1008.
- [11] M. J. Harris, S. T. Bramwell, D. F. McMorrow, T. Zeiske, and K. W. Godfrey: Geometrical Frustration in the Ferromagnetic Pyrochlore $\text{Ho}_2\text{Ti}_2\text{O}_7$. *Physical Review Letters* **79**(13) (1997), 2554–2557. doi: 10.1103/PhysRevLett.79.2554.
- [12] A. P. Ramirez, A. Hayashi, R. J. Cava, R. Siddharthan, and B. S. Shastry: Zero-Point Entropy in ‘Spin Ice’. *Nature* **399**(6734) (1999), 333–335. doi: 10.1038/20619.

- [13] S. T. Bramwell and M. J. P. Gingras: Spin Ice State in Frustrated Magnetic Pyrochlore Materials. *Science* **294**(5546) (2001), 1495–1501. doi: 10.1126/science.1064761.
- [14] C. Castelnovo, R. Moessner, and S. L. Sondhi: Magnetic Monopoles in Spin Ice. *Nature* **451**(7174) (2008), 42–45. doi: 10.1038/nature06433.
- [15] K. I. Kugel and D. I. Khomskii: The Jahn-Teller Effect and Magnetism: Transition Metal Compounds. *Soviet Physics Uspekhi* **25**(4) (1982), 231. doi: 10.1070/PU1982v025n04ABEH004537.
- [16] A. Kitaev: Anyons in an Exactly Solved Model and Beyond. *Annals of Physics* **321**(1) (2006), 2–111. doi: 10.1016/j.aop.2005.10.005.
- [17] P. W. Anderson: Resonating Valence Bonds: A New Kind of Insulator? *Materials Research Bulletin* **8**(2) (1973), 153–160. doi: 10.1016/0025-5408(73)90167-0.
- [18] J. M. Leinaas and J. Myrheim: On the Theory of Identical Particles. *Il Nuovo Cimento B (1971-1996)* **37**(1) (1977), 1–23. doi: 10.1007/BF02727953.
- [19] F. Wilczek: Quantum Mechanics of Fractional-Spin Particles. *Physical Review Letters* **49**(14) (1982), 957–959. doi: 10.1103/PhysRevLett.49.957.
- [20] X. G. Wen: Vacuum Degeneracy of Chiral Spin States in Compactified Space. *Physical Review B* **40**(10) (1989), 7387–7390. doi: 10.1103/PhysRevB.40.7387.
- [21] A. Y. Kitaev: Fault-Tolerant Quantum Computation by Anyons. *Annals of Physics* **303**(1) (2003), 2–30. doi: 10.1016/S0003-4916(02)00018-0.
- [22] J. Knolle, D. L. Kovrizhin, J. T. Chalker, and R. Moessner: Dynamics of a Two-Dimensional Quantum Spin Liquid: Signatures of Emergent Majorana Fermions and Fluxes. *Physical Review Letters* **112**(20) (2014), 207203. doi: 10.1103/PhysRevLett.112.207203.
- [23] S. R. White: Density Matrix Formulation for Quantum Renormalization Groups. *Physical Review Letters* **69**(19) (1992), 2863–2866. doi: 10.1103/PhysRevLett.69.2863.
- [24] A. Klumper, A. Schadschneider, and J. Zittartz: Equivalence and Solution of Anisotropic Spin-1 Models and Generalized t-J Fermion Models in One Dimension. *Journal of Physics A: Mathematical and General* **24**(16) (1991), L955. doi: 10.1088/0305-4470/24/16/012.
- [25] A. Klümper, A. Schadschneider, and J. Zittartz: Groundstate Properties of a Generalized VBS-Model. *Zeitschrift für Physik B Condensed Matter* **87**(3) (1992), 281–287. doi: 10.1007/BF01309281.
- [26] D. Perez-Garcia, F. Verstraete, M. M. Wolf, and J. I. Cirac: Matrix Product State Representations. *arXiv:quant-ph/0608197* (2006).
- [27] L. J. Sandilands, Y. Tian, K. W. Plumb, Y.-J. Kim, and K. S. Burch: Scattering Continuum and Possible Fractionalized Excitations in α -RuCl₃. *Physical Review Letters* **114**(14) (2015), 147201. doi: 10.1103/PhysRevLett.114.147201.
- [28] A. Banerjee, J. Yan, J. Knolle, et al.: Neutron scattering in the proximate quantum spin liquid α -RuCl₃. *Science* **356**(6342) (2017), 1055–1059. doi: 10.1126/science.aah6015.

-
- [29] N. H. Fletcher: *The Chemical Physics of Ice*. London: Cambridge U.P., 1970. isbn: 978-0-521-07597-8.
- [30] K. Momma and F. Izumi: VESTA 3 for Three-Dimensional Visualization of Crystal, Volumetric and Morphology Data. *Journal of Applied Crystallography* **44**(6) (2011), 1272–1276. doi: 10.1107/S0021889811038970.
- [31] N. Bjerrum: Structure and Properties of Ice. *Science* **115**(2989) (1952), 385–390. doi: 10.1126/science.115.2989.385.
- [32] J. F. Nagle: Lattice Statistics of Hydrogen Bonded Crystals. I. The Residual Entropy of Ice. *Journal of Mathematical Physics* **7**(8) (1966), 1484. doi: 10.1063/1.1705058.
- [33] E. H. Lieb: Residual Entropy of Square Ice. *Physical Review* **162**(1) (1967), 162–172. doi: 10.1103/PhysRev.162.162.
- [34] S. V. Isakov, K. S. Raman, R. Moessner, and S. L. Sondhi: Magnetization Curve of Spin Ice in a [111] Magnetic Field. *Physical Review B* **70**(10) (2004), 104418. doi: 10.1103/PhysRevB.70.104418.
- [35] L. Vanderstraeten, B. Vanhecke, and F. Verstraete: Residual Entropies for Three-Dimensional Frustrated Spin Systems with Tensor Networks. *arXiv:1805.10598 [cond-mat]* (2018).
- [36] S. V. Isakov, R. Moessner, and S. L. Sondhi: Why Spin Ice Obeys the Ice Rules. *Physical Review Letters* **95**(21) (2005), 217201. doi: 10.1103/PhysRevLett.95.217201.
- [37] R. Moessner and J. T. Chalker: Properties of a Classical Spin Liquid: The Heisenberg Pyrochlore Antiferromagnet. *Physical Review Letters* **80**(13) (1998), 2929–2932. doi: 10.1103/PhysRevLett.80.2929.
- [38] R. Moessner and J. T. Chalker: Low-Temperature Properties of Classical Geometrically Frustrated Antiferromagnets. *Physical Review B* **58**(18) (1998), 12049–12062. doi: 10.1103/PhysRevB.58.12049.
- [39] C. L. Henley: Power-Law Spin Correlations in Pyrochlore Antiferromagnets. *Physical Review B* **71**(1) (2005), 014424. doi: 10.1103/PhysRevB.71.014424.
- [40] D. A. Huse, W. Krauth, R. Moessner, and S. L. Sondhi: Coulomb and Liquid Dimer Models in Three Dimensions. *Physical Review Letters* **91**(16) (2003), 167004. doi: 10.1103/PhysRevLett.91.167004.
- [41] C. L. Henley: The “Coulomb Phase” in Frustrated Systems. *Annual Review of Condensed Matter Physics* **1**(1) (2010), 179–210. doi: 10.1146/annurev-conmatphys-070909-104138.
- [42] M. Hermele, M. P. A. Fisher, and L. Balents: Pyrochlore photons: The $U(1)$ spin liquid in a $S = \frac{1}{2}$ three-dimensional frustrated magnet. *Physical Review B* **69**(6) (2004), 064404. doi: 10.1103/PhysRevB.69.064404.
- [43] S. V. Isakov, K. Gregor, R. Moessner, and S. L. Sondhi: Dipolar Spin Correlations in Classical Pyrochlore Magnets. *Physical Review Letters* **93**(16) (2004), 167204. doi: 10.1103/PhysRevLett.93.167204.

- [44] R. Youngblood and J. D. Axe: Neutron-Scattering Study of Short-Range Order in a Model Two-Dimensional Ferroelectric. *Physical Review B* **17**(9) (1978), 3639–3649. doi: 10.1103/PhysRevB.17.3639.
- [45] R. Youngblood, J. D. Axe, and B. M. McCoy: Correlations in Ice-Rule Ferroelectrics. *Physical Review B* **21**(11) (1980), 5212–5220. doi: 10.1103/PhysRevB.21.5212.
- [46] R. W. Youngblood and J. D. Axe: Polarization Fluctuations in Ferroelectric Models. *Physical Review B* **23**(1) (1981), 232–238. doi: 10.1103/PhysRevB.23.232.
- [47] T. Fennell, P. P. Deen, A. R. Wildes, et al.: Magnetic Coulomb Phase in the Spin Ice Ho₂Ti₂O₇. *Science* **326**(5951) (2009), 415–417. doi: 10.1126/science.1177582.
- [48] C. Lacroix, P. Mendels, and F. Mila, eds.: *Introduction to Frustrated Magnetism*. Vol. 164. Springer Series in Solid-State Sciences. Berlin, Heidelberg: Springer Berlin Heidelberg, 2011. isbn: 978-3-642-10588-3.
- [49] L. D. C. Jaubert: Topological Constraints and Defects in Spin Ice. Lyon, France: Ecole Normal Superieure de Lyon, 2009.
- [50] S.-i. Yoshida, K. Nemoto, and K. Wada: Ordered Phase of Dipolar Spin Ice under [110] Magnetic Field. *Journal of the Physical Society of Japan* **73**(7) (2004), 1619–1622. doi: 10.1143/JPSJ.73.1619.
- [51] L. Jaubert, J. Chalker, P. Holdsworth, and R. Moessner: Three-Dimensional Kasteleyn Transition: Spin Ice in a [100] Field. *Physical Review Letters* **100**(6) (2008). doi: 10.1103/PhysRevLett.100.067207.
- [52] K. Matsuhira, Z. Hiroi, T. Tayama, S. Takagi, and T. Sakakibara: A new macroscopically degenerate ground state in the spin ice compound Dy₂Ti₂O₇ under a magnetic field. *Journal of Physics: Condensed Matter* **14**(29) (2002), L559. doi: 10.1088/0953-8984/14/29/101.
- [53] A. S. Wills, R. Ballou, and C. Lacroix: Model of Localized Highly Frustrated Ferromagnetism: The Kagom\’e Spin Ice. *Physical Review B* **66**(14) (2002), 144407. doi: 10.1103/PhysRevB.66.144407.
- [54] M. Udagawa, M. Ogata, and Z. Hiroi: Exact Result of Ground-State Entropy for Ising Pyrochlore Magnets under a Magnetic Field along [111] Axis. *Journal of the Physical Society of Japan* **71**(10) (2002), 2365–2368. doi: 10.1143/JPSJ.71.2365.
- [55] R. Moessner and S. L. Sondhi: Theory of the [111] magnetization plateau in spin ice. *Physical Review B* **68**(6) (2003), 064411. doi: 10.1103/PhysRevB.68.064411.
- [56] P. W. Kasteleyn: Dimer Statistics and Phase Transitions. *Journal of Mathematical Physics* **4**(2) (1963), 287. doi: 10.1063/1.1703953.
- [57] R. Kenyon: Lectures on Dimers. *arXiv:0910.3129 [math-ph]* (2009).
- [58] E. W. Montroll: Lattice Statistics. *Applied Combinatorial Mathematics*. Ed. by E. F. Beckenbach. New York: J. Wiley, 1964, 96–143. isbn: 978-0-471-06125-0.
- [59] P. W. Kasteleyn: Graph Theory and Crystal Physics. *Graph Theory and Theoretical Physics*. Ed. by F. Harary. New York: Academic Press, 1967.

-
- [60] R. Kenyon, A. Okounkov, and S. Sheffield: Dimers and Amoebae. *Annals of mathematics* **163** (2006), 1019–1056. doi: 10.4007/annals.2006.163.1019.
- [61] G. Baskaran, D. Sen, and R. Shankar: Spin-S Kitaev Model: Classical Ground States, Order by Disorder and Exact Correlation Functions. *Physical Review B* **78**(11) (2008), 115116. doi: 10.1103/PhysRevB.78.115116.
- [62] S. Chandra, K. Ramola, and D. Dhar: Classical Heisenberg Spins on a Hexagonal Lattice with Kitaev Couplings. *Physical Review E* **82**(3) (2010), 031113. doi: 10.1103/PhysRevE.82.031113.
- [63] I. Rousochatzakis, U. K. Rössler, J. van den Brink, and M. Daghofer: Kitaev anisotropy induces mesoscopic \mathbb{Z}_2 vortex crystals in frustrated hexagonal antiferromagnets. *Physical Review B* **93**(10) (2016), 104417. doi: 10.1103/PhysRevB.93.104417.
- [64] X. Yao: The Expanded Triangular Kitaev–Heisenberg Model in the Full Parameter Space. *Physics Letters A* **378**(30) (2014), 2290–2294. doi: 10.1016/j.physleta.2014.05.037.
- [65] H. Yao and S. A. Kivelson: Exact Chiral Spin Liquid with Non-Abelian Anyons. *Physical Review Letters* **99**(24) (2007), 247203. doi: 10.1103/PhysRevLett.99.247203.
- [66] S. Mandal and N. Surendran: Exactly Solvable Kitaev Model in Three Dimensions. *Physical Review B* **79**(2) (2009), 024426. doi: 10.1103/PhysRevB.79.024426.
- [67] H.-D. Chen and Z. Nussinov: Exact Results on the Kitaev Model on a Hexagonal Lattice: Spin States, String and Brane Correlators, and Anyonic Excitations. *Journal of Physics A: Mathematical and Theoretical* **41**(7) (2008), 075001. doi: 10.1088/1751-8113/41/7/075001.
- [68] E. H. Lieb: Flux Phase of the Half-Filled Band. *Physical Review Letters* **73**(16) (1994), 2158–2161. doi: 10.1103/PhysRevLett.73.2158.
- [69] P. R. Wallace: The Band Theory of Graphite. *Physical Review* **71**(9) (1947), 622–634. doi: 10.1103/PhysRev.71.622.
- [70] A. H. Castro Neto, F. Guinea, N. M. R. Peres, K. S. Novoselov, and A. K. Geim: The Electronic Properties of Graphene. *Reviews of Modern Physics* **81**(1) (2009), 109–162. doi: 10.1103/RevModPhys.81.109.
- [71] C. Nayak, S. H. Simon, A. Stern, M. Freedman, and S. Das Sarma: Non-Abelian Anyons and Topological Quantum Computation. *Reviews of Modern Physics* **80**(3) (2008), 1083–1159. doi: 10.1103/RevModPhys.80.1083.
- [72] X. G. Wen: Topological Orders in Rigid States. *International Journal of Modern Physics B* **04** (02 1990), 239–271. doi: 10.1142/S0217979290000139.
- [73] L. Cincio and G. Vidal: Characterizing Topological Order by Studying the Ground States on an Infinite Cylinder. *Physical Review Letters* **110**(6) (2013), 067208. doi: 10.1103/PhysRevLett.110.067208.
- [74] A. Kitaev and J. Preskill: Topological Entanglement Entropy. *Physical Review Letters* **96**(11) (2006), 110404. doi: 10.1103/PhysRevLett.96.110404.

- [75] M. Levin and X.-G. Wen: Detecting Topological Order in a Ground State Wave Function. *Physical Review Letters* **96**(11) (2006), 110405. doi: 10.1103/PhysRevLett.96.110405.
- [76] H. Yao and X.-L. Qi: Entanglement Entropy and Entanglement Spectrum of the Kitaev Model. *Physical Review Letters* **105**(8) (2010), 080501. doi: 10.1103/PhysRevLett.105.080501.
- [77] B. Dóra and R. Moessner: Gauge Field Entanglement in Kitaev's Honeycomb Model. *Physical Review B* **97**(3) (2018), 035109. doi: 10.1103/PhysRevB.97.035109.
- [78] J. Knolle, D. L. Kovrizhin, J. T. Chalker, and R. Moessner: Dynamics of Fractionalization in Quantum Spin Liquids. *Physical Review B* **92**(11) (2015), 115127. doi: 10.1103/PhysRevB.92.115127.
- [79] J. Knolle: *Dynamics of a Quantum Spin Liquid*. Springer Theses. Springer International Publishing, 2016. isbn: 978-3-319-23953-8.
- [80] G. Jackeli and G. Khaliullin: Mott Insulators in the Strong Spin-Orbit Coupling Limit: From Heisenberg to a Quantum Compass and Kitaev Models. *Physical Review Letters* **102**(1) (2009), 017205. doi: 10.1103/PhysRevLett.102.017205.
- [81] V. M. Katukuri, S. Nishimoto, V. Yushankhai, et al.: Kitaev interactions between $j = \frac{1}{2}$ moments in honeycomb Na_2IrO_3 are large and ferromagnetic: insights from ab initio quantum chemistry calculations. *New Journal of Physics* **16**(1) (2014), 013056. doi: 10.1088/1367-2630/16/1/013056.
- [82] J. G. Rau, E. K.-H. Lee, and H.-Y. Kee: Generic Spin Model for the Honeycomb Iridates beyond the Kitaev Limit. *Physical Review Letters* **112**(7) (2014), 077204. doi: 10.1103/PhysRevLett.112.077204.
- [83] J. Chaloupka, G. Jackeli, and G. Khaliullin: Kitaev-Heisenberg Model on Honeycomb Lattice: Possible Exotic Phases in Iridium Oxides A_2IrO_3 . *Physical Review Letters* **105**(2) (2010), 027204. doi: 10.1103/PhysRevLett.105.027204.
- [84] H.-C. Jiang, Z.-C. Gu, X.-L. Qi, and S. Trebst: Possible proximity of the Mott insulating iridate Na_2IrO_3 to a topological phase: Phase diagram of the Heisenberg-Kitaev model in a magnetic field. *Physical Review B* **83**(24) (2011), 245104. doi: 10.1103/PhysRevB.83.245104.
- [85] J. Chaloupka, G. Jackeli, and G. Khaliullin: Zigzag Magnetic Order in the Iridium Oxide Na_2IrO_3 . *Physical Review Letters* **110**(9) (2013), 097204. doi: 10.1103/PhysRevLett.110.097204.
- [86] J. Osorio Iregui, P. Corboz, and M. Troyer: Probing the Stability of the Spin-Liquid Phases in the Kitaev-Heisenberg Model Using Tensor Network Algorithms. *Physical Review B* **90**(19) (2014), 195102. doi: 10.1103/PhysRevB.90.195102.
- [87] M. G. Yamada, H. Fujita, and M. Oshikawa: Designing Kitaev Spin Liquids in Metal-Organic Frameworks. *Physical Review Letters* **119**(5) (2017), 057202. doi: 10.1103/PhysRevLett.119.057202.

-
- [88] I. Affleck, T. Kennedy, E. H. Lieb, and H. Tasaki: Rigorous Results on Valence-Bond Ground States in Antiferromagnets. *Physical Review Letters* **59**(7) (1987), 799–802. doi: 10.1103/PhysRevLett.59.799.
- [89] J. Eisert, M. Cramer, and M. B. Plenio: Colloquium: Area Laws for the Entanglement Entropy. *Reviews of Modern Physics* **82**(1) (2010), 277–306. doi: 10.1103/RevModPhys.82.277.
- [90] P. Calabrese and J. Cardy: Entanglement Entropy and Quantum Field Theory. *Journal of Statistical Mechanics: Theory and Experiment* **2004** (06 2004), P06002. doi: 10.1088/1742-5468/2004/06/P06002.
- [91] Y. Zhang, T. Grover, A. Turner, M. Oshikawa, and A. Vishwanath: Quasiparticle Statistics and Braiding from Ground-State Entanglement. *Physical Review B* **85**(23) (2012), 235151. doi: 10.1103/PhysRevB.85.235151.
- [92] H.-C. Jiang, Z. Wang, and L. Balents: Identifying Topological Order by Entanglement Entropy. *Nature Physics* **8**(12) (2012), 902–905. doi: 10.1038/nphys2465.
- [93] L. Tagliacozzo, T. R. de Oliveira, S. Iblisdir, and J. I. Latorre: Scaling of Entanglement Support for Matrix Product States. *Physical Review B* **78**(2) (2008), 024410. doi: 10.1103/PhysRevB.78.024410.
- [94] F. Pollmann, S. Mukerjee, A. M. Turner, and J. E. Moore: Theory of Finite-Entanglement Scaling at One-Dimensional Quantum Critical Points. *Physical Review Letters* **102**(25) (2009), 255701. doi: 10.1103/PhysRevLett.102.255701.
- [95] G. M. Crosswhite and D. Bacon: Finite Automata for Caching in Matrix Product Algorithms. *Physical Review A* **78**(1) (2008), 012356. doi: 10.1103/PhysRevA.78.012356.
- [96] M. P. Zaletel, R. S. K. Mong, C. Karrasch, J. E. Moore, and F. Pollmann: Time-Evolving a Matrix Product State with Long-Ranged Interactions. *Physical Review B* **91**(16) (2015), 165112. doi: 10.1103/PhysRevB.91.165112.
- [97] U. Schollwöck: The Density-Matrix Renormalization Group in the Age of Matrix Product States. *Annals of Physics* **326**(1) (2011), 96–192. doi: 10.1016/j.aop.2010.09.012.
- [98] U. Schollwöck: Matrix Product State Algorithms: Dmrg, Tebd and Relatives. *Strongly Correlated Systems*. Springer, 2013, 67–98.
- [99] F. Verstraete and J. I. Cirac: Renormalization Algorithms for Quantum-Many Body Systems in Two and Higher Dimensions. *arXiv:cond-mat/0407066* (2004).
- [100] V. Zauner, D. Draxler, L. Vanderstraeten, et al.: Transfer Matrices and Excitations with Matrix Product States. *New J. Phys.* **17**(5) (2015), 053002. doi: 10.1088/1367-2630/17/5/053002.
- [101] M. B. Hastings: Locality in Quantum and Markov Dynamics on Lattices and Networks. *Physical Review Letters* **93**(14) (2004), 140402. doi: 10.1103/PhysRevLett.93.140402.
- [102] E. H. Lieb and D. W. Robinson: The Finite Group Velocity of Quantum Spin Systems. *Communications in Mathematical Physics* **28**(3) (1972), 251–257. doi: 10.1007/BF01645779.

- [103] G. Vidal: Efficient Classical Simulation of Slightly Entangled Quantum Computations. *Phys. Rev. Lett.* **91**(14) (2003), 147902. doi: 10.1103/PhysRevLett.91.147902.
- [104] E. Lieb, T. Schultz, and D. Mattis: Two Soluble Models of an Antiferromagnetic Chain. *Annals of Physics* **16**(3) (1961), 407–466. doi: 10.1016/0003-4916(61)90115-4.
- [105] S. Katsura: Statistical Mechanics of the Anisotropic Linear Heisenberg Model. *Physical Review* **127**(5) (1962), 1508–1518. doi: 10.1103/PhysRev.127.1508.
- [106] E. Barouch, B. M. McCoy, and M. Dresden: Statistical Mechanics of the XY Model. I. *Physical Review A* **2**(3) (1970), 1075–1092. doi: 10.1103/PhysRevA.2.1075.
- [107] E. Barouch and B. M. McCoy: Statistical Mechanics of the XY Model. II. Spin-Correlation Functions. *Physical Review A* **3**(2) (1971), 786–804. doi: 10.1103/PhysRevA.3.786.
- [108] U. Schmidt: The Excitation Spectrum of the One-Dimensional XY-Model in a Magnetic Field. *Z. Physik* **267**(4) (1974), 271–275. doi: 10.1007/BF01669447.
- [109] K. W. Plumb, J. P. Clancy, L. J. Sandilands, V. V. Shankar, Y. F. Hu, K. S. Burch, H.-Y. Kee, and Y.-J. Kim: α -RuCl₃: A spin-orbit assisted Mott insulator on a honeycomb lattice. *Phys. Rev. B* **90**(4) (2014), 041112. doi: 10.1103/PhysRevB.90.041112.
- [110] J. Knolle, G.-W. Chern, D. L. Kovrizhin, R. Moessner, and N. B. Perkins: Raman Scattering Signatures of Kitaev Spin Liquids in A₂ IrO₃ Iridates. *Physical Review Letters* **113**(18) (2014), 187201. doi: 10.1103/PhysRevLett.113.187201.
- [111] X.-Y. Song, Y.-Z. You, and L. Balents: Low-Energy Spin Dynamics of the Honeycomb Spin Liquid Beyond the Kitaev Limit. *Physical Review Letters* **117**(3) (2016), 037209. doi: 10.1103/PhysRevLett.117.037209.
- [112] D. Gotfryd, J. Rusnaifmmoddecelsěcko, K. Wohlfeld, G. Jackeli, J. Chaloupka, and A. M. Oleifmmodeseš: Phase Diagram and Spin Correlations of the Kitaev-Heisenberg Model: Importance of Quantum Effects. *Phys. Rev. B* **95**(2) (2017), 024426. doi: 10.1103/PhysRevB.95.024426.
- [113] T. Suzuki, T. Yamada, Y. Yamaji, and S.-i. Suga: Dynamical properties of the honeycomb-lattice iridates Na₂IrO₃. *Physical Review B* **92**(18) (2015), 184411. doi: 10.1103/PhysRevB.92.184411.
- [114] A. Banerjee, C. A. Bridges, J.-Q. Yan, et al.: Proximate Kitaev Quantum Spin Liquid Behaviour in a Honeycomb Magnet. *Nature Materials* **15**(7) (2016), 733–740. doi: 10.1038/nmat4604.
- [115] R. D. Johnson, S. C. Williams, A. A. Haghighirad, et al.: Monoclinic crystal structure of α – RuCl₃ and the zigzag antiferromagnetic ground state. *Physical Review B* **92**(23) (2015), 235119. doi: 10.1103/PhysRevB.92.235119.
- [116] H.-S. Kim and H.-Y. Kee: Crystal structure and magnetism in α – RuCl₃: An *ab initio* study. *Physical Review B* **93**(15) (2016), 155143. doi: 10.1103/PhysRevB.93.155143.

-
- [117] L. J. Sandilands, Y. Tian, A. A. Reijnders, H.-S. Kim, K. W. Plumb, Y.-J. Kim, H.-Y. Kee, and K. S. Burch: Spin-orbit excitations and electronic structure of the putative Kitaev magnet α -RuCl₃. *Physical Review B* **93**(7) (2016), 075144. doi: 10.1103/PhysRevB.93.075144.
- [118] L. J. Sandilands, C. H. Sohn, H. J. Park, S. Y. Kim, K. W. Kim, J. A. Sears, Y.-J. Kim, and T. W. Noh: Optical probe of Heisenberg-Kitaev magnetism in α -RuCl₃. *Physical Review B* **94**(19) (2016), 195156. doi: 10.1103/PhysRevB.94.195156.
- [119] J. Chaloupka and G. Khaliullin: Magnetic anisotropy in the Kitaev model systems Na₂IrO₃ and RuCl₃. *Physical Review B* **94**(6) (2016), 064435. doi: 10.1103/PhysRevB.94.064435.
- [120] F. Lang, P. J. Baker, A. A. Haghighirad, Y. Li, D. Prabhakaran, R. Valentí, and S. J. Blundell: Unconventional magnetism on a honeycomb lattice in α -RuCl₃ studied by muon spin rotation. *Physical Review B* **94**(2) (2016), 020407. doi: 10.1103/PhysRevB.94.020407.
- [121] G. B. Halász, N. B. Perkins, and J. van den Brink: Resonant Inelastic X-Ray Scattering Response of the Kitaev Honeycomb Model. *Physical Review Letters* **117**(12) (2016), 127203. doi: 10.1103/PhysRevLett.117.127203.
- [122] A. Koitzsch, C. Habenicht, E. Müller, et al.: J_{eff} Description of the Honeycomb Mott Insulator α – RuCl₃. *Physical Review Letters* **117**(12) (2016), 126403. doi: 10.1103/PhysRevLett.117.126403.
- [123] B. Dalla Piazza, M. Mourigal, N. B. Christensen, et al.: Fractional Excitations in the Square-Lattice Quantum Antiferromagnet. *Nature Physics* **11**(1) (2015), 62–68. doi: 10.1038/nphys3172.
- [124] E. Sela, H.-C. Jiang, M. H. Gerlach, and S. Trebst: Order-by-Disorder and Spin-Orbital Liquids in a Distorted Heisenberg-Kitaev Model. *Physical Review B* **90**(3) (2014), 035113. doi: 10.1103/PhysRevB.90.035113.
- [125] K. Shinjo, S. Sota, and T. Tohyama: Density-Matrix Renormalization Group Study of the Extended Kitaev-Heisenberg Model. *Physical Review B* **91**(5) (2015), 054401. doi: 10.1103/PhysRevB.91.054401.
- [126] S. Coleman: There Are No Goldstone Bosons in Two Dimensions. *Communications in Mathematical Physics* **31**(4) (1973), 259–264. doi: 10.1007/BF01646487.
- [127] M. Gohlke, R. Verresen, R. Moessner, and F. Pollmann: Dynamics of the Kitaev-Heisenberg Model. *Physical Review Letters* **119**(15) (2017), 157203. doi: 10.1103/PhysRevLett.119.157203.
- [128] J. A. Kjäll, F. Pollmann, and J. E. Moore: Bound states and E_8 symmetry effects in perturbed quantum Ising chains. *Physical Review B* **83**(2) (2011), 020407. doi: 10.1103/PhysRevB.83.020407.
- [129] H. N. Phien, G. Vidal, and I. P. McCulloch: Infinite Boundary Conditions for Matrix Product State Calculations. *Phys. Rev. B* **86**(24) (2012), 245107. doi: 10.1103/PhysRevB.86.245107.

- [130] V. Zauner, M. Ganahl, H. G. Evertz, and T. Nishino: Time Evolution within a Comoving Window: Scaling of Signal Fronts and Magnetization Plateaus after a Local Quench in Quantum Spin Chains. *Journal of Physics: Condensed Matter* **27**(42) (2015), 425602. doi: 10.1088/0953-8984/27/42/425602.
- [131] S. R. White and I. Affleck: Spectral function for the $S = 1$ Heisenberg antiferromagnetic chain. *Physical Review B* **77**(13) (2008), 134437. doi: 10.1103/PhysRevB.77.134437.
- [132] Z. Weihong, J. Oitmaa, and C. J. Hamer: Second-Order Spin-Wave Results for the Quantum XXZ and XY Models with Anisotropy. *Physical Review B* **44**(21) (1991), 11869–11881. doi: 10.1103/PhysRevB.44.11869.
- [133] R. Yadav, N. A. Bogdanov, V. M. Katukuri, S. Nishimoto, J. v. d. Brink, and L. Hozoi: Kitaev exchange and field-induced quantum spin-liquid states in honeycomb α - RuCl_3 . *Scientific Reports* **6** (2016), 37925. doi: 10.1038/srep37925.
- [134] W. Wang, Z.-Y. Dong, S.-L. Yu, and J.-X. Li: Theoretical investigation of magnetic dynamics in α - RuCl_3 . *Phys. Rev. B* **96**(11) (2017), 115103. doi: 10.1103/PhysRevB.96.115103.
- [135] S. M. Winter, K. Riedl, A. Honecker, and R. Valentí: Breakdown of Magnons in a Strongly Spin-Orbital Coupled Magnet. *Nature Communications* **8** (2017), 1152. doi: 10.1038/s41467-017-01177-0.
- [136] J. Zheng, K. Ran, T. Li, et al.: Gapless Spin Excitations in the Field-Induced Quantum Spin Liquid Phase of α - RuCl_3 . *Physical Review Letters* **119**(22) (2017), 227208. doi: 10.1103/PhysRevLett.119.227208.
- [137] S. M. Winter, Y. Li, H. O. Jeschke, and R. Valentí: Challenges in Design of Kitaev Materials: Magnetic Interactions from Competing Energy Scales. *Physical Review B* **93**(21) (2016), 214431. doi: 10.1103/PhysRevB.93.214431.
- [138] A. Catuneanu, Y. Yamaji, G. Wachtel, H.-Y. Kee, and Y. B. Kim: Realizing Quantum Spin Liquid Phases in Spin-Orbit Driven Correlated Materials. *arXiv:1701.07837 [cond-mat]* (2017).
- [139] I. Rousochatzakis and N. B. Perkins: Classical Spin Liquid Instability Driven By Off-Diagonal Exchange in Strong Spin-Orbit Magnets. *Physical Review Letters* **118**(14) (2017), 147204. doi: 10.1103/PhysRevLett.118.147204.
- [140] I. P. McCulloch: Infinite Size Density Matrix Renormalization Group, Revisited. *arXiv:0804.2509 [cond-mat]* (2008).
- [141] J. A. Kjäll, M. P. Zaletel, R. S. K. Mong, J. H. Bardarson, and F. Pollmann: Phase Diagram of the Anisotropic Spin-2 XXZ Model: Infinite-System Density Matrix Renormalization Group Study. *Phys. Rev. B* **87**(23) (2013), 235106. doi: 10.1103/PhysRevB.87.235106.
- [142] J. Chaloupka and G. Khaliullin: Hidden symmetries of the extended Kitaev-Heisenberg model: Implications for the honeycomb-lattice iridates A_2IrO_3 . *Physical Review B* **92**(2) (2015), 024413. doi: 10.1103/PhysRevB.92.024413.

-
- [143] Y.-C. He, M. P. Zaletel, M. Oshikawa, and F. Pollmann: Signatures of Dirac Cones in a DMRG Study of the Kagome Heisenberg Model. *Physical Review X* **7**(3) (2017), 031020. doi: 10.1103/PhysRevX.7.031020.
- [144] M. Gohlke, G. Wachtel, Y. Yamaji, F. Pollmann, and Y. B. Kim: Quantum Spin Liquid Signatures in Kitaev-like Frustrated Magnets. *Physical Review B* **97**(7) (2018), 075126. doi: 10.1103/PhysRevB.97.075126.
- [145] W. Witczak-Krempa, G. Chen, Y. B. Kim, and L. Balents: Correlated Quantum Phenomena in the Strong Spin-Orbit Regime. *Annual Review of Condensed Matter Physics* **5**(1) (2014), 57–82. doi: 10.1146/annurev-conmatphys-020911-125138.
- [146] Z. Nussinov and J. van den Brink: Compass Models: Theory and Physical Motivations. *Reviews of Modern Physics* **87**(1) (2015), 1–59. doi: 10.1103/RevModPhys.87.1.
- [147] J. G. Rau, E. K.-H. Lee, and H.-Y. Kee: Spin-Orbit Physics Giving Rise to Novel Phases in Correlated Systems: Iridates and Related Materials. *Annual Review of Condensed Matter Physics* **7** (2016), 195–221. doi: 10.1146/annurev-conmatphys-031115-011319.
- [148] S. M. Winter, A. A. Tsirlin, M. Daghofer, J. van den Brink, Y. Singh, Philipp Gegenwart, and R. Valentí: Models and Materials for Generalized Kitaev Magnetism. *Journal of Physics: Condensed Matter* **29**(49) (2017), 493002. doi: 10.1088/1361-648X/aa8cf5.
- [149] J. A. Sears, M. Songvilay, K. W. Plumb, J. P. Clancy, Y. Qiu, Y. Zhao, D. Parshall, and Y.-J. Kim: Magnetic order in α -RuCl₃: A honeycomb-lattice quantum magnet with strong spin-orbit coupling. *Phys. Rev. B* **91**(14) (2015), 144420. doi: 10.1103/PhysRevB.91.144420.
- [150] L. Janssen, E. C. Andrade, and M. Vojta: Honeycomb-Lattice Heisenberg-Kitaev Model in a Magnetic Field: Spin Canting, Metamagnetism, and Vortex Crystals. *Physical Review Letters* **117**(27) (2016), 277202. doi: 10.1103/PhysRevLett.117.277202.
- [151] L. Janssen, E. C. Andrade, and M. Vojta: Magnetization processes of zigzag states on the honeycomb lattice: Identifying spin models for α -RuCl₃ and Na₂IrO₃. *Physical Review B* **96**(6) (2017), 064430. doi: 10.1103/PhysRevB.96.064430.
- [152] J. A. Sears, Y. Zhao, Z. Xu, J. W. Lynn, and Y.-J. Kim: Phase diagram of α -RuCl₃ in an in-plane magnetic field. *Physical Review B* **95**(18) (2017), 180411. doi: 10.1103/PhysRevB.95.180411.
- [153] S. M. Winter, K. Riedl, D. Kaib, R. Coldea, and R. Valentí: Probing α -RuCl₃ Beyond Magnetic Order: Effects of Temperature and Magnetic Field. *Physical Review Letters* **120**(7) (2018), 077203. doi: 10.1103/PhysRevLett.120.077203.
- [154] N. Janša, A. Zorko, M. Gomilšek, et al.: Observation of Two Types of Fractional Excitation in the Kitaev Honeycomb Magnet. *Nature Physics* (2018), 1. doi: 10.1038/s41567-018-0129-5.
- [155] A. N. Ponomaryov, E. Schulze, J. Wosnitza, et al.: Unconventional spin dynamics in the honeycomb-lattice material α -RuCl₃: High-field electron spin resonance studies. *Physical Review B* **96**(24) (2017), 241107. doi: 10.1103/PhysRevB.96.241107.

- [156] A. U. B. Wolter, L. T. Corredor, L. Janssen, et al.: Field-induced quantum criticality in the Kitaev system α -RuCl₃. *Physical Review B* **96**(4) (2017), 041405. doi: 10.1103/PhysRevB.96.041405.
- [157] Z. Wang, S. Reschke, D. Hübner, et al.: Magnetic Excitations and Continuum of a Possibly Field-Induced Quantum Spin Liquid in α -RuCl₃. *Physical Review Letters* **119**(22) (2017), 227202. doi: 10.1103/PhysRevLett.119.227202.
- [158] A. Banerjee, P. Lampen-Kelley, J. Knolle, et al.: Excitations in the field-induced quantum spin liquid state of α -RuCl₃. *npj Quantum Materials* **3**(1) (2018), 8. doi: 10.1038/s41535-018-0079-2.
- [159] P. Lampen-Kelley, S. Rachel, J. Reuther, et al.: Anisotropic susceptibilities in the honeycomb Kitaev system α -RuCl₃. *arXiv:1803.04871 [cond-mat]* (2018).
- [160] R. Hentrich, A. U. Wolter, X. Zotos, et al.: Unusual Phonon Heat Transport in α -RuCl₃: Strong Spin-Phonon Scattering and Field-Induced Spin Gap. *Physical Review Letters* **120**(11) (2018), 117204. doi: 10.1103/PhysRevLett.120.117204.
- [161] Z. Zhu, I. Kimchi, D. N. Sheng, and L. Fu: Robust Non-Abelian Spin Liquid and a Possible Intermediate Phase in the Antiferromagnetic Kitaev Model with Magnetic Field. *Physical Review B* **97**(24) (2018), 241110. doi: 10.1103/PhysRevB.97.241110.
- [162] P. A. McClarty, X.-Y. Dong, M. Gohlke, J. G. Rau, F. Pollmann, R. Moessner, and K. Penc: Topological Magnons in Kitaev Magnets at High Fields. *arXiv:1802.04283 [cond-mat]* (2018).
- [163] M. B. Hastings and X.-G. Wen: Quasiadiabatic Continuation of Quantum States: The Stability of Topological Ground-State Degeneracy and Emergent Gauge Invariance. *Physical Review B* **72**(4) (2005), 045141. doi: 10.1103/PhysRevB.72.045141.
- [164] M. P. Zaletel, R. S. K. Mong, and F. Pollmann: Topological Characterization of Fractional Quantum Hall Ground States from Microscopic Hamiltonians. *Physical Review Letters* **110**(23) (2013), 236801. doi: 10.1103/PhysRevLett.110.236801.
- [165] K. Meichanetzidis, M. Cirio, J. K. Pachos, and V. Lahtinen: Anatomy of Fermionic Entanglement and Criticality in Kitaev Spin Liquids. *Physical Review B* **94**(11) (2016), 115158. doi: 10.1103/PhysRevB.94.115158.
- [166] S. D. Geraedts, M. P. Zaletel, R. S. K. Mong, M. A. Metlitski, A. Vishwanath, and O. I. Motrunich: The Half-Filled Landau Level: The Case for Dirac Composite Fermions. *Science* **352**(6282) (2016), 197–201. doi: 10.1126/science.aad4302.
- [167] H. Théveniaut and M. Vojta: Bound States of Fractionalized Excitations in a Modulated Kitaev Spin Liquid. *Physical Review B* **96**(5) (2017), 054401. doi: 10.1103/PhysRevB.96.054401.
- [168] V. Lahtinen and J. K. Pachos: Topological Phase Transitions Driven by Gauge Fields in an Exactly Solvable Model. *Physical Review B* **81**(24) (2010), 245132. doi: 10.1103/PhysRevB.81.245132.
- [169] V. Lahtinen: Interacting Non-Abelian Anyons as Majorana Fermions in the Honeycomb Lattice Model. *New Journal of Physics* **13**(7) (2011), 075009. doi: 10.1088/1367-2630/13/7/075009.

-
- [170] D. G. Joshi: Topological Excitations in the Ferromagnetic Kitaev-Heisenberg Model. *arXiv:1803.01515 [cond-mat]* (2018).
- [171] G. Seibold, F. Becca, and J. Lorenzana: Theory of Antibound States in Partially Filled Narrow Band Systems. *Physical Review Letters* **100**(1) (2008), 016405. doi: 10.1103/PhysRevLett.100.016405.
- [172] B. A. Bernevig: *Topological Insulators and Topological Superconductors*. In collab. with T. L. Hughes. Princeton University Press, 2013. isbn: 978-0-691-15175-5.
- [173] M. Z. Hasan and C. L. Kane: Colloquium: Topological Insulators. *Reviews of Modern Physics* **82**(4) (2010), 3045–3067. doi: 10.1103/RevModPhys.82.3045.
- [174] R. Shindou, R. Matsumoto, S. Murakami, and J.-i. Ohe: Topological Chiral Magnonic Edge Mode in a Magnonic Crystal. *Physical Review B* **87**(17) (2013), 174427. doi: 10.1103/PhysRevB.87.174427.
- [175] A. Mook, J. Henk, and I. Mertig: Magnon Hall Effect and Topology in Kagome Lattices: A Theoretical Investigation. *Physical Review B* **89**(13) (2014), 134409. doi: 10.1103/PhysRevB.89.134409.
- [176] A. Mook, J. Henk, and I. Mertig: Edge States in Topological Magnon Insulators. *Physical Review B* **90**(2) (2014), 024412. doi: 10.1103/PhysRevB.90.024412.
- [177] S. A. Owerre: A First Theoretical Realization of Honeycomb Topological Magnon Insulator. *Journal of Physics: Condensed Matter* **28**(38) (2016), 386001. doi: 10.1088/0953-8984/28/38/386001.
- [178] S. A. Owerre: Noncollinear Antiferromagnetic Haldane Magnon Insulator. *Journal of Applied Physics* **121**(22) (2017), 223904. doi: 10.1063/1.4985615.
- [179] J. Romhányi, K. Penc, and R. Ganesh: Hall Effect of Triplons in a Dimerized Quantum Magnet. *Nature Communications* **6** (2015), 6805. doi: 10.1038/ncomms7805.
- [180] P. A. McClarty, F. Krüger, T. Guidi, S. F. Parker, K. Refson, A. W. Parker, D. Prabhakaran, and R. Coldea: Topological Triplon Modes and Bound States in a Shastry–Sutherland Magnet. *Nature Physics* **13**(8) (2017), 736–741. doi: 10.1038/nphys4117.
- [181] K. Nakata, S. K. Kim, J. Klinovaja, and D. Loss: Magnonic Topological Insulators in Antiferromagnets. *Physical Review B* **96**(22) (2017), 224414. doi: 10.1103/PhysRevB.96.224414.
- [182] A. L. Chernyshev and P. A. Maksimov: Damped Topological Magnons in the Kagome-Lattice Ferromagnets. *Physical Review Letters* **117**(18) (2016), 187203. doi: 10.1103/PhysRevLett.117.187203.
- [183] T. Holstein and H. Primakoff: Field Dependence of the Intrinsic Domain Magnetization of a Ferromagnet. *Physical Review* **58**(12) (1940), 1098–1113. doi: 10.1103/PhysRev.58.1098.
- [184] J.-P. Blaizot: *Quantum Theory of Finite Systems*. In collab. with G. Ripka. Cambridge, Mass.: MIT Press, 1986. isbn: 978-0-262-02214-9.

- [185] J. R. Schrieffer and P. A. Wolff: Relation between the Anderson and Kondo Hamiltonians. *Physical Review* **149**(2) (1966), 491–492. doi: 10.1103/PhysRev.149.491.
- [186] M. V. Berry: Quantal Phase Factors Accompanying Adiabatic Changes. *Proc. R. Soc. Lond. A* **392**(1802) (1984), 45–57. doi: 10.1098/rspa.1984.0023.
- [187] H. Katsura, N. Nagaosa, and P. A. Lee: Theory of the Thermal Hall Effect in Quantum Magnets. *Physical Review Letters* **104**(6) (2010), 066403. doi: 10.1103/PhysRevLett.104.066403.
- [188] Y. Onose, T. Ideue, H. Katsura, Y. Shiomi, N. Nagaosa, and Y. Tokura: Observation of the Magnon Hall Effect. *Science* **329**(5989) (2010), 297–299. doi: 10.1126/science.1188260.
- [189] R. Matsumoto and S. Murakami: Rotational Motion of Magnons and the Thermal Hall Effect. *Physical Review B* **84**(18) (2011), 184406. doi: 10.1103/PhysRevB.84.184406.
- [190] R. Matsumoto, R. Shindou, and S. Murakami: Thermal Hall Effect of Magnons in Magnets with Dipolar Interaction. *Physical Review B* **89**(5) (2014), 054420. doi: 10.1103/PhysRevB.89.054420.
- [191] T. Ideue, Y. Onose, H. Katsura, Y. Shiomi, S. Ishiwata, N. Nagaosa, and Y. Tokura: Effect of Lattice Geometry on Magnon Hall Effect in Ferromagnetic Insulators. *Physical Review B* **85**(13) (2012), 134411. doi: 10.1103/PhysRevB.85.134411.
- [192] S. Murakami and A. Okamoto: Thermal Hall Effect of Magnons. *Journal of the Physical Society of Japan* **86**(1) (2016), 011010. doi: 10.7566/JPSJ.86.011010.
- [193] D. Watanabe, K. Sugii, M. Shimozawa, et al.: Emergence of Nontrivial Magnetic Excitations in a Spin-Liquid State of Kagomé Volborthite. *Proceedings of the National Academy of Sciences* **113**(31) (2016), 8653–8657. doi: 10.1073/pnas.1524076113.
- [194] J. Nasu, J. Yoshitake, and Y. Motome: Thermal Transport in the Kitaev Model. *Physical Review Letters* **119**(12) (2017), 127204. doi: 10.1103/PhysRevLett.119.127204.
- [195] Y. Kasahara, K. Sugii, T. Ohnishi, et al.: Unusual Thermal Hall Effect in a Kitaev Spin Liquid Candidate α - RuCl_3 . *Physical Review Letters* **120**(21) (2018), 217205. doi: 10.1103/PhysRevLett.120.217205.
- [196] J. C. Li, V. M. Nield, D. K. Ross, R. W. Whitworth, C. C. Wilson, and D. A. Keen: Diffuse Neutron-Scattering Study of Deuterated Ice Ih. *Philosophical Magazine B* **69**(6) (1994), 1173–1181. doi: 10.1080/01418639408240187.
- [197] S. V. Isakov, R. Moessner, S. L. Sondhi, and D. A. Tennant: Analytical theory for proton correlations in common-water ice I_h . *Physical Review B* **91**(24) (2015), 245152. doi: 10.1103/PhysRevB.91.245152.
- [198] O. Benton, O. Sikora, and N. Shannon: Classical and Quantum Theories of Proton Disorder in Hexagonal Water Ice. *Physical Review B* **93**(12) (2016), 125143. doi: 10.1103/PhysRevB.93.125143.
- [199] A. H. Castro Neto, P. Pujol, and E. Fradkin: Ice: A Strongly Correlated Proton System. *Physical Review B* **74**(2) (2006), 024302. doi: 10.1103/PhysRevB.74.024302.

-
- [200] L. E. Bove, S. Klotz, A. Paciaroni, and F. Sacchetti: Anomalous Proton Dynamics in Ice at Low Temperatures. *Physical Review Letters* **103**(16) (2009), 165901. doi: 10.1103/PhysRevLett.103.165901.
- [201] F. Yen and T. Gao: Dielectric Anomaly in Ice near 20 K: Evidence of Macroscopic Quantum Phenomena. *The Journal of Physical Chemistry Letters* **6**(14) (2015), 2822–2825. doi: 10.1021/acs.jpcllett.5b00797.
- [202] C. Drechsel-Grau and D. Marx: Quantum Simulation of Collective Proton Tunneling in Hexagonal Ice Crystals. *Physical Review Letters* **112**(14) (2014), 148302. doi: 10.1103/PhysRevLett.112.148302.
- [203] S. Powell and J. T. Chalker: Classical to Quantum Mappings for Geometrically Frustrated Systems: Spin-Ice in a [100] Field. *Physical Review B* **78**(2) (2008), 024422. doi: 10.1103/PhysRevB.78.024422.
- [204] D. J. P. Morris, D. A. Tennant, S. A. Grigera, et al.: Dirac Strings and Magnetic Monopoles in the Spin Ice $\text{Dy}_2\text{Ti}_2\text{O}_7$. *Science* **326**(5951) (2009), 411–414. doi: 10.1126/science.1178868.
- [205] H. Cohn, R. Kenyon, and J. Propp: A Variational Principle for Domino Tilings. *Journal of the American Mathematical Society* **14**(2) (2001), 297–346. doi: 10.1090/S0894-0347-00-00355-6.
- [206] G. T. Barkema and M. E. J. Newman: Monte Carlo Simulation of Ice Models. *Physical Review E* **57**(1) (1998), 1155–1166. doi: 10.1103/PhysRevE.57.1155.
- [207] L. D. C. Jaubert, M. Haque, and R. Moessner: Analysis of a Fully Packed Loop Model Arising in a Magnetic Coulomb Phase. *Physical Review Letters* **107**(17) (2011). doi: 10.1103/PhysRevLett.107.177202.
- [208] S. M. Bhattacharjee, J. F. Nagle, D. A. Huse, and M. E. Fisher: Critical Behavior of a Three-Dimensional Dimer Model. *Journal of Statistical Physics* **32**(2) (1983), 361–374. doi: 10.1007/BF01012715.
- [209] B. Wehinger, D. Chernyshov, M. Krisch, S. Bulat, V. Ezhov, and A. Bosak: Diffuse Scattering in Ih Ice. *Journal of Physics: Condensed Matter* **26**(26) (2014), 265401. doi: 10.1088/0953-8984/26/26/265401.
- [210] M. E. Fisher and J. Stephenson: Statistical Mechanics of Dimers on a Plane Lattice. II. Dimer Correlations and Monomers. *Physical Review* **132**(4) (1963), 1411–1431. doi: 10.1103/PhysRev.132.1411.
- [211] E. Fradkin, D. A. Huse, R. Moessner, V. Oganesyan, and S. L. Sondhi: Bipartite Rokhsar-Kivelson Points and Cantor Deconfinement. *Physical Review B* **69**(22) (2004), 224415. doi: 10.1103/PhysRevB.69.224415.
- [212] Y. Tang, A. W. Sandvik, and C. L. Henley: Properties of Resonating-Valence-Bond Spin Liquids and Critical Dimer Models. *Physical Review B* **84**(17) (2011), 174427. doi: 10.1103/PhysRevB.84.174427.
- [213] C. Hickey and S. Trebst: Gapless Visons and Emergent $U(1)$ Spin Liquid in the Kitaev Honeycomb Model: Complete Phase Diagram in Tilted Magnetic Fields. *arXiv:1805.05953 [cond-mat]* (2018).

Acknowledgments

In the past years, I have enjoyed the support of several people, who contributed in various ways in the successful completion of this thesis. First and foremost, I like to thank my advisor Prof. Dr. Roderich Moessner for his guidance and stimulating discussions. I am also very grateful to Prof. Dr. Frank Pollmann who shared many insights into various valuable numerical techniques, without which this work wouldn't have been possible.

I would like to thank my collaborators and colleagues Xiaoyu Dong, Voitech Kaiser, Yong-Baek Kim, Paul McClarty, Karlo Penc, Jeffrey G. Rau, Nic Shannon, Ruben Verresen, Gideon Wachtel, and Youhei Yamaji, with whom I had the pleasure to work and discuss with.

I also like to thank the Max-Planck-Institute for the Physics of Complex Systems, in particular the IT department, for the assistance and the resources they provided. I would like to acknowledge support from the International Max Planck Research School for Many Particle Systems in Structured Environments and from Deutsche Forschungsgemeinschaft via SFB 1143.

Finally and most importantly, I like to give thanks to my family and friends for assistance and distraction whenever needed. Many thanks go to my wife Maria Gohlke for all the advice and help on how to present science, for creating the cover of this thesis, but also for organizing my life whenever physics took over my mind. Last but not least, I thank Ijon Erik Gohlke for his patience with his father.

Versicherung

Hiermit versichere ich, Matthias Gohlke, dass ich die vorliegende Arbeit ohne unzulässige Hilfe Dritter und ohne Benutzung anderer als der angegebenen Hilfsmittel angefertigt habe; die aus fremden Quellen direkt oder indirekt übernommenen Gedanken sind als solche kenntlich gemacht. Die Arbeit wurde bisher weder im Inland noch im Ausland in gleicher oder ähnlicher Form einer anderen Prüfungsbehörde vorgelegt. Diese Arbeit wurde unter der wissenschaftlichen Betreuung von Prof. Dr. Roderich Moessner am Max-Planck Institut für Physik komplexer Systeme in Dresden angefertigt. Ich erkläre hiermit, dass keine früheren erfolglosen Promotionsverfahren stattgefunden haben. Ich erkenne die Promotionsordnung der Fakultät für Mathematik und Naturwissenschaften der Technische Universität Dresden an.

Ort, Datum:

Unterschrift:
